

Distribution Agreement

In presenting this thesis or dissertation as a partial fulfillment of the requirements for an advanced degree from Emory University, I hereby grant to Emory University and its agents the non-exclusive license to archive, make accessible, and display my thesis or dissertation in whole or in part in all forms of media, now or hereafter known, including display on the world wide web. I understand that I may select some access restrictions as part of the online submission of this thesis or dissertation. I retain all ownership rights to the copyright of the thesis or dissertation. I also retain the right to use all or part of this thesis or dissertation in future works (such as articles or books).

Signature:

Sk Aysha Rashid

Date

**Utilizing DNA Nanotechnology to Unveil the Effects of Receptor Forces on Cell
Maturation and Function**

By

Sk Aysha Rashid

Doctor of Philosophy

Chemistry

Khalid Salaita

Advisor

Bill Wuest

Committee Member

Yonggang Ke

Committee Member

Accepted:

Kimberly Jacob Arriola, Ph.D, MPH

Dean of the James T. Laney School of Graduate Studies

Date

**Utilizing DNA Nanotechnology to Unveil the Effects of Receptor Forces on Cell
Maturation and Function**

By

Sk Aysha Rashid

B.S., Bangladesh University of Engineering and Technology, 2016

M.Sc, Georgia State University, 2017

Advisor: Khalid Salaita, Ph.D

An abstract of

A dissertation submitted to the faculty of the
James T. Laney School of Graduate Studies of Emory University
in partial fulfillment of the requirements for the degree of

Doctor of Philosophy

in Chemistry

2023

Abstract

Utilizing DNA Nanotechnology to Unveil the Effects of Receptor Forces on Cell Maturation and Function

By

Sk Aysha Rashid

This dissertation examines the fundamental biological processes of cell differentiation and maturation, which are mediated by piconewton forces that cells transmit to their receptors. However, the challenge of substrate dependency in the cell-generated forces poses a significant obstacle to studying and understanding these processes. This study utilizes a range of innovative DNA-based tension-sensing techniques to measure and modulate receptor forces to address this issue. This approach provides new insights into the impact of molecular forces and rigidity on complex phenomena, such as cardiac muscle maturation and stem cell differentiation. The dissertation is structured into five chapters, which explore topics such as cardiac mechanobiology, the development and expansion of DNA-based sensors, and a novel cell sorting technique based on mechanical phenotypes. Moreover, this study presents a hydrogel-based matrix that overcomes the limitations of non-physiologically relevant stiff substrates in the field of mechanotransduction. In summary, this dissertation represents a significant contribution to the scientific understanding of the mechanics of biological processes and holds great promise for future research in this field.

**Utilizing DNA Nanotechnology to Unveil the Effects of Receptor Forces on Cell
Maturation and Function**

By

Sk Aysha Rashid

B.S., Bangladesh University of Engineering and Technology, 2016

M.Sc, Georgia State University, 2017

Advisor: Khalid Salaita, Ph.D

A dissertation submitted to the faculty of the
James T. Laney School of Graduate Studies of Emory University
in partial fulfillment of the requirements for the degree of
Doctor of Philosophy
in Chemistry
2023
Abstract

Acknowledgments

Throughout my life, I have harbored an unwavering aspiration to pursue a career in the scientific field. However, I am acutely aware that this noble endeavor would have been rendered unattainable were it not for the invaluable support and affection bestowed upon me by my cherished family, friends, and esteemed mentors.

Firstly I want to Thank Dr. Khalid Salaita. I am deeply indebted to my advisor for his exceptional support and guidance throughout my Ph.D. program. His profound expertise, endless encouragement, and unwavering patience were indispensable in helping me navigate the intricate and often challenging landscape of academic research. He was always there to provide me with thoughtful and constructive feedback on my work, to answer my many questions, and to offer inspiration when I felt discouraged or unsure. His dedication to my success was unwavering and inspiring, and he played an instrumental role in shaping my academic and personal growth.

I am also very thankful to my committee members, Dr. Bill Wuest and Dr. Yonggang Ke, who gave me precious advice and motivated my research to improve it. I was fortunate to have a committee of supportive and dedicated individuals who helped me to get my projects off the ground. Their guidance, feedback, and encouragement were essential to my success, and I could not have done it without them. Each member brought a unique perspective and area of expertise that complemented my own, and they worked together

to provide me with the resources and tools I needed to succeed. Additionally, Dr. Wuest's guidance on biotech consulting was particularly impactful. His insights and experience in the field helped me navigate the complex world of biotech and provided me with valuable knowledge and skills to serve me well in my future career. I am also thankful to my excellent collaborators and mentors, Dr. Cho, Dr. Xu, Dr. Parvin, Dr. Qu, and Natasha. I am also thankful to collaborate with Dr. Leo on the astrocytes project.

I would also like to thank the current members and alumni of the Salaita lab for their support and kindness over the past few years. You've made this challenging and sometimes frustrating journey colorful and fun. (Kim, Jing, Victor Ma, Jessica, Han, Roxy, Aaron, Jiahui, Rong, Alisina, Dale, Brendan, Yixiao, Anna, Allison, Hiroaki, Alex, Rachel, Yuxin, Arventh, Radhika, Yuesong, Selma, Thea, Steven, Sarah, Yusha, Shuhong, Tharindu, Jhordan, Krista, Joseph, Hus, Luna, Tianyi, Maia, Vageesha and Thomas). I thank Dr. Kornelia Galior and Dr. Roxanne Glazier for their mentorships during my early Ph.D. years. I thank Dr. Hanquan and Dr. Kim, who were always kind to me and helped me with microscopy training and any science problems. I am also grateful to Dr. Allison Ramey-Ward; she was a great help in the lab and a good friend. I am grateful to Dale and Dr. Aaron, who were great collaborators and friends. I especially want to thank Dale for being a great friend and mentor and always being there whenever I had a bad day. I also want to thank my friends Yixiao, Yuesong, Selma, Arventh, Yuxin, Rong, and Hiroaki for providing the support I needed to survive and thrive at the same time. I want to especially thank Yixiao for being my best buddy and a fantastic collaborator. I thank Selma and Yuesong for being amazing friends and great people who helped create many wonderful memories. You guys were so awesome and made these five years one of the best years

of my life even with all the struggles. I thank my homie Yusha and Shuhong for being there for me. I thank Arventh and Gokul for being my friends and also helping me with life when I was not doing great. I am incredibly grateful for all the people I met and befriended. I want to cherish and flourish in these friendships in years to come.

Finally, I would like to give my thanks to my family. I thank my mom and dad, who provided everything and loved me. Especially my mom, who always told me the sky is the limit. She was my support, and because of her, I never thought anything is impossible. I thank them for supporting me in any situation. I thank my sister, Easha apu, for all the support and love. I won't be who I am without them. Also, I want to thank Nahian bhaiya and Eva apu; you were my rock. Eva apu you are my sister from another mother; you were a godsend and one of my biggest blessings. I also want to thank my nephews and niece, Aronnok, Neeladri, and Zohair. You guys are all rock stars. I want to also thank Ivey apu and Zubair bhaiya for being there for us. And my cats, all eight of you- Pusheen, Phoebe, Pikachu, Pistachio, Pearl, Pascal, Penny, and Pinocchio. Your unconditional love made me who I am today.

Last but not least, I want to thank my husband, Tausif. You and I are a team. And when we are together, we can make anything possible.

TABLE OF CONTENTS

List of abbreviations	3
CHAPTER 1. INTRODUCTION.....	8
1.1 Cardiomyocyte mechanotransduction.....	9
1.2 Stem cell mechanics and tissue regeneration.....	28
1.3 Different techniques to measure and manipulate cellular forces	37
1.4 Mechanotagging and its importance	50
1.5 Aim and scope of this dissertation	52
References.....	54
CHAPTER 2. DNA tension sensors show cardiac muscle maturation is sensitive to pN receptor force	69
2.1 Abstract.....	70
2.2 Introduction.....	71
2.3 Results and discussions	74
2.4 Conclusions.....	92
2.5 Materials and methods	95
2.6 Appendix	101
Reference.....	132
CHAPTER 3. Mechanically sorting cells using TaCT probes	144
3.1 Abstract.....	145
3.2 Introduction.....	146
3.3 Results and discussions	147
3.4 Conclusions.....	156
3.5 Materials and methods	157
3.5 Appendix	163

Reference.....	172
CHAPTER 4. HYDROGEL-BASED CELLULAR TENSION-SENSING MATRIX.....	177
4.1 Abstract	178
4.2 Introduction.....	179
4.3 Results and discussions	182
4.4 Conclusions.....	196
4.5 Materials and methods	194
4.6 Appendix	202
Reference.....	220
CHAPTER 5. SUMMARY AND OUTLOOKS	228
5.1 Summary	229
5.2 Perspective.....	232
5.3 Other contributions	233
5.4 Outlook	239

List of Abbreviations

Abbreviation	Full Name
pN	piconewton
ECM	extracellular matrix
TM	transmembrane
RGD	peptide arginine-glycine-aspartic acid
FA	focal adhesions
VWF	Willebrand Factor
BC	bent closed
EC	extended closed
EO	extended open
SRA	serotonin release assay
AFM	Atomic force microscopy

WLC	worm-like-chain
GFP	green fluorescent protein
TGT	tension gauge tether
SLB	supported lipid bilayers
MFM	molecular force microscopy
DNA-PAINT	DNA-Points Accumulation for Imaging in Nanoscale Topography
MTFM	molecular tension fluorescence microscopy
ELISA	enzyme-linked immunoassay
PCR	polymerase chain reaction
RCA	rolling circle amplification
RICM	reflection interference contrast microscopy
TIRF	total internal reflection fluorescence
FISH	fluorescence in situ hybridization
HPLC	high-performance liquid chromatography
SPR	surface plasmon resonance

SERS	surface-enhanced Raman scattering
Ca ²⁺	Calcium flux
PEG	Polyethylene glycol
kPa	Kilo pascal
GPa	Giga pascal
MPa	Mega pascal
aTF	transcription factors
LOD	limit of detection
CMCs	Cardiac muscle cells
hiPSC	Human induced pluripotent stem cells
hMSC	Human mesenchymal stem cells
hESC	Human embryonic stem cells
Serca2A	Serca2a calcium pump protein
IC ₅₀	half maximal inhibitory concentration
RT	room temperature
SRRF	super-resolution radial fluctuations
MLC	Myosin light chain

COX	cyclooxygenase
S/N	Signal to noise ratio
FRET	Fluorescence Resonance Energy Transfer
PGE-1	prostaglandin E1
MEF	Mouse embryonic fibroblasts
SUB	Small unilamellar vesicles
cRGDfk	cyclo-Arg-Gly-Asp-Phe-Lys
BHQ2	Black hole quencher 2
GP	glycoprotein
Fib	Fibronectin
CF	Cardiac fibroblasts
NA	numerical aperture
DMEM	Dulbecco's Modified Eagle Medium
Ex	excitation
Em	emission
S.E.M.	Standard error of the mean

S.D.	Standard deviation
LatB	Latrunculin B
APC	antigen-presenting cells
YAP	Yes associated protein
APTES	(3-Aminopropyl) triethoxysilane
ADP	Adenosine 5'-diphosphate
FN	Fibronectin

Chapter-1 Introduction to Cardiac cells mechanotransduction, stem cell mechanics and different techniques to manipulate and measure mechanical forces exerted by cells.

1.1 Cardiomyocyte mechanotransduction

1.1.1 Cardiac muscle cells

The human body consists of three diverse muscle types - cardiac muscle, also known as myocardium, smooth muscle, and skeletal muscle.¹ The myocardium also known as cardiac muscle cells (CMCs) is like a skeletal muscle in that it is made of sarcomeres, allowing it to contract.^{2, 3} Yet, its control differs from skeletal muscle as it operates under involuntary regulation.⁴⁻⁶

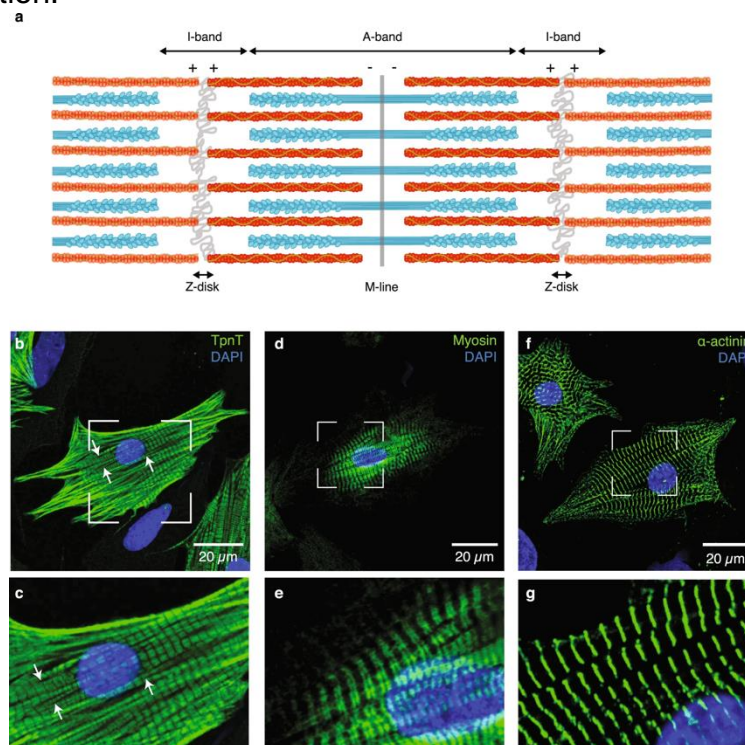


Figure 1.1. a. Schematic representation of adjoining micrometer-sized sarcomeres within a myofibril, showing the organization of the thick (cyan) and thin (red) filaments in this basic contractile unit of striated muscle. Neonatal rat cardiomyocytes were labeled with antibodies specific for troponin T (TpnT; **b, c**), the heavy chain of myosin (Myosin; **d, e**), and α -actinin (**f, g**), respectively. Thin (**b, c**) and thick (**d, e**) filaments assemble into myofibrils, which align along the main axes of the star-like shaped cells and display regularly spaced Z-disks (**f, g**). Myofibril branching is indicated with white arrows. **c, e, g** Zoomed-in views of the framed regions in **b, d, f**, respectively. A minimum of three biologically independent experiments were performed in each case. The image is reused from reference 11 with permission from the publisher.

The heart comprises three layers: the pericardium, myocardium, and endocardium. ⁴ The endocardium, which lines the inner chambers and valves of the heart, ⁷ is not part of the cardiac muscle but is made of simple squamous epithelial cells. ⁸ The pericardium, a fibrous membrane encasing the heart, consists of several components, including the epicardium, pericardial space, the parietal pericardium, and the fibrous pericardium. ^{9, 10}

The cardiac muscle holds great responsibility as it powers the heart's beating, ensuring blood flow meets the entire body's metabolic needs. ⁴ This process is called cardiac output, calculated as the product of heart rate and stroke volume. It depends on the cardiac muscle's contractile force and activation frequency, with changes in metabolic demand leading to alterations in the contractility of the heart. The contractile unit that helps cardiac muscle with coordinated beating is its sarcomere, made with multiple proteins (Figure-1.1).¹¹ In this chapter, we will discuss the importance of the mechanotransduction of CMCs and our motivation to use CMC as a cell model to understand how mechanical forces affect the functional maturation of cardiac cells.

1.1.2 Cardiac mechanotransduction

Mechanotransduction refers to cells' ability to sense and respond to mechanical forces such as compression, strain, and flow stress by triggering intracellular signaling pathways and resulting in a change in phenotype.¹² This process is relevant in developmental biology and morphogenesis and is now recognized as a critical factor in pathophysiology.¹³ The cells in the cardiovascular system are constantly exposed to various mechanical stimuli and can detect even small changes in the stiffness of their

surrounding environment.^{14, 15} This leads to intracellular activation and a shift towards pro-inflammatory and profibrotic phenotypes.¹²

Integrins play a crucial role in the ability of cells in the cardiovascular system to translate mechanical signals into biochemical signals, a process known as mechanotransduction.¹⁶ This allows the extracellular matrix (ECM) to affect cell and tissue development and overall cellular function.¹⁷ Cardiac costameres, vinculin-containing, rib-like bands are another key players in this process.¹⁸ Changes in the load-bearing molecules at these adhesion-rich regions, triggered by mechanical forces, result in stress-dependent remodeling and signal transduction.¹⁹ These forces can reach the nucleus through the cytoskeleton, potentially altering chromatin organization, DNA replication, gene transcription, and RNA processing.^{19, 20} This integrin-mediated sarcolemma-nuclear connection can have rapid intracellular effects faster than typical chemical changes via

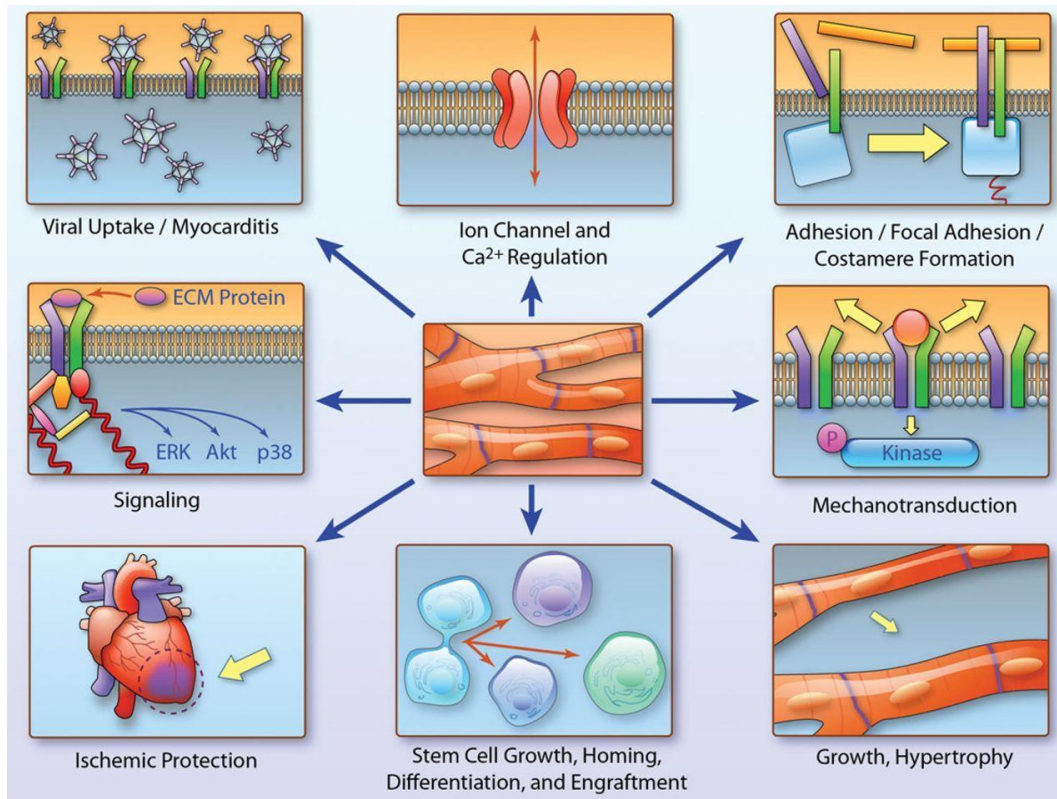


Figure 1.2. Schematic representation of function of integrins in the cardiac myocyte (cm). integrins can have a wide variety of functions. These include ubiquitous ones such as adhesion, formation of extracellular matrix–cytoskeletal junctions, signaling or viral uptake. There are also ones that are not as well understood and that are important in the cm, such as modification of ion channel function, or stem cell growth and engraftment; hypertrophic growth, mechanotransduction, and ischemic protection. Erk indicates extracellular signal–regulated kinase. Ben Smith. The image is reused from reference 16 with permission from the publisher.

membrane receptor signaling. Specific signaling molecules, such as melusin, are activated by integrin binding, allowing CMs to respond to hemodynamic load¹⁶. In this way, CMs may use integrin-mediated mechanochemical pathways to increase their sensitivity to mechanical stresses from the ECM.

Integrins are mechanotransducers, translating mechanical signals to biochemical information, making them particularly relevant for a contracting muscle cell.¹⁷ Unfortunately, very little is known regarding cardiac muscle-specific integrin tension and how the CMCs' contraction modulates their biochemical response.²¹ Literature precedent revealed that such mechano-chemical signaling leads to changes in their structure and function, such as rhythmic myocardial contractility. Its dysregulation promotes the progression of various heart diseases.^{22, 23}

1.1.2 Different proteins involved in cardiac muscle mechanotransduction.

1.1.2.1 Sarcomeric alpha-actinin

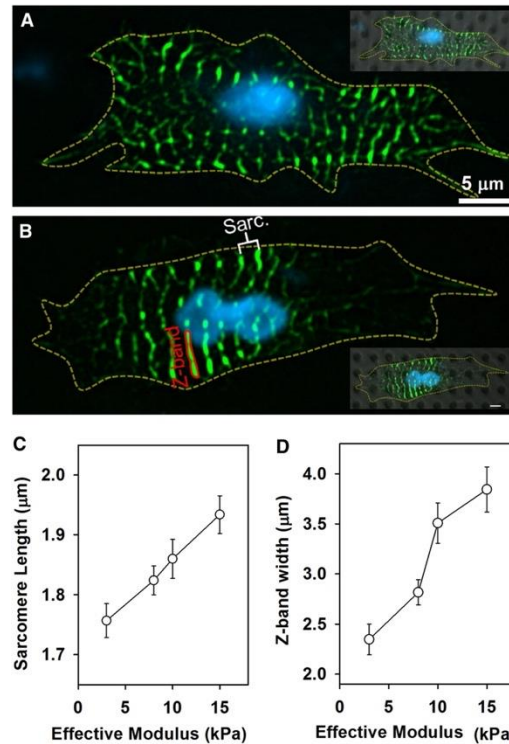


Figure 1.3. Resting sarcomere length and z-band width increase with stiffness. Cells on the (a) softest arrays (3 kPa) and on the (b) stiffest arrays (15 kPa) were fixed and stained for α -actinin (green) and nuclei (blue). (insets) same cell with a bright-field image showing the micro-posts. (c) sarcomere length and (d) z-band width increased with substrate stiffness (ANOVA $p < 0.001$). Error bars represent the 95% confidence intervals. Scale bars, 5 μm . Figure reused from reference 28 with permission from the publisher.

Sarcomeric α -actinin is a versatile protein that plays a critical role in maintaining the structural integrity of sarcomeres in skeletal and cardiac muscle cells.^{24, 25} It modulates receptors and channels and serves as a platform for various signaling pathways. This protein is essential for linking actin filaments from neighboring sarcomeres, forming the Z-disk, and promoting proper muscle function.^{26, 27}

Previous work has reported how changing substrate stiffness can affect the sarcomeric structure of CMCs. Studies have plated CMCs in varying stiffness and reported elongated sarcomeres when CMCs are cultured on stiff substrates to determine whether the changing stiffness affects the biomechanical changes in myofibril structure. They showed (Figure 3) how z bandwidth and sarcomere were manipulated due to the cell culture microenvironment. These studies helped us determine matrix/molecular markers of CMC maturation.^{2, 28-30}

1.1.2.2 Cardiac myosin and mechanotransduction

The heart's beating action is powered by cardiac myosin, a molecule that transforms chemical energy from ATP into mechanical force.¹² The heart's output must be controlled carefully to satisfy the body's requirements. Recent studies across all levels, from molecules to tissues, have uncovered intricate mechanisms that adjust heart contraction.¹⁶ Myosin not only generates power but also takes an active role in regulating it, adapting, and being influenced by the mechanical environment. These studies have shown that the tension generated by myosin also affects processes beyond muscle contraction. Scientists have extensively studied innovative regulatory mechanisms and the significance of myosin-based force generation and mechanotransduction in development and disease.^{13, 31} They explored the crucial interactions within and between molecules that control myosin contractility and the impact of mechanical forces on myosin's performance.³² The rising utilization of cardiac myosin as a target for heart failure drugs and the possibility of creating precision medicine treatments aimed at contractility and mechanotransduction are essential. Research to enhance our understanding of myosin's functions and regulation is needed in the cardiovascular field.

1.1.2.3 SERCA-2A calcium pump protein

The central aspect of single cardiomyocyte function is its ability to handle calcium, with the trigger for contraction being calcium-induced calcium release. This release is rapidly cleared from the cell by SERCA2a pumps and NCX.³³ In contrast, human pluripotent stem cell-derived cardiomyocytes (hiPSC-CMs) have poorly developed calcium handling, relying on both calcium release from the sarcoplasmic reticulum and trans-sarcolemma calcium influx for contraction.³⁴ This is due to a lack of t-tubule systems and limited regulatory component expression, decreasing calcium release and uptake rates. However, the functional maturation of hiPSC-CMs can be partially improved through the expression of missing adult proteins or hormonal treatment.

The performance of hiPSC-CMs is closely linked to the maturation and organization of

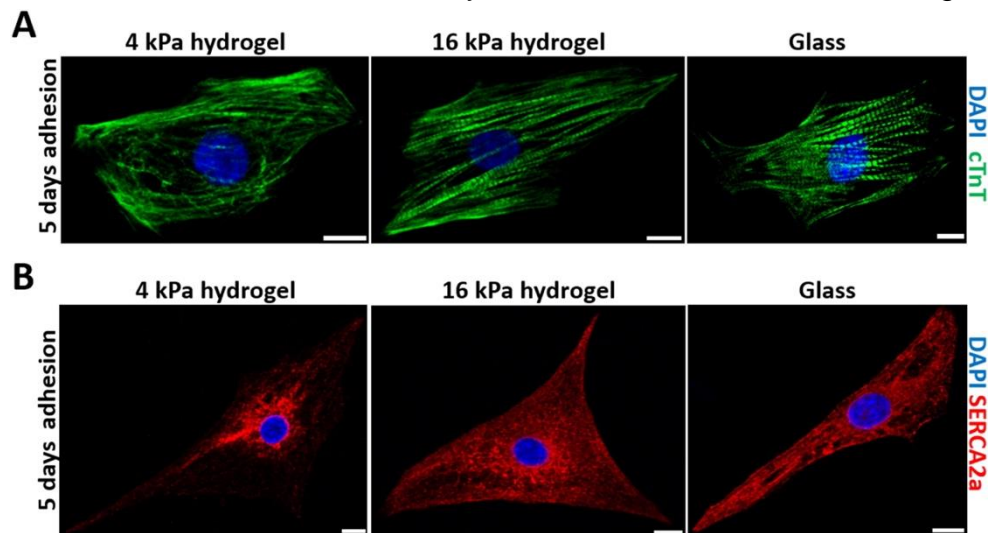


Figure 1.4. Serca2A expression of hiPSC derived CMCs on different substrate stiffness. CMCs have more structured and aligned sarcomeres and SERCA expression on a stiffer substrate compared to a soft substrate. Image reused from reference 34 with permission from the publisher.

the sarcoplasmic reticulum, which serves as the primary calcium store in mature cells and

contains critical components for calcium cycling, such as RyR channels and SERCA2a pumps. Recent studies have revealed a connection between SERCA2a pumps and integrin structures, indicating that the mechanical environment of the cardiomyocyte can impact SR organization and function. This connection is further supported by evidence of mechanotransduction signaling regulation of SERCA2a transcripts.

Studies have revealed the essential role of the RhoA/ROCK pathway in reorganizing human pluripotent stem cell-derived cardiomyocytes after they are plated for adhesion.³⁵ These structural alterations profoundly impact the distribution of SERCA2 pumps, which improves calcium cycling. The initiation of this transformation occurs when the cells interact with the culture substrate, and mechanical cues guide the alignment of sarcomeres. The redistribution of SERCA2a pumps from a perinuclear to a more widespread location. The mechanical properties of the substrate control this reorganization, as seen when the process fails when hiPSC-CMs are cultured on soft 4 kPa hydrogels instead of the stiffer 16 kPa hydrogels or glass.³⁴ These findings prompted us to utilize SERCA2a as a maturity matrix for this thesis.

1.1.2.4 Mechanotransduction and action potentials

The cardiac action potential represents the cell membrane potential over time, which is altered as ions such as Na^+ , Ca^{2+} , and K^+ move across the cell membrane during each cardiac cycle.^{36, 37} The ionic pathways that control this movement are tightly regulated and influenced by factors such as voltage gating, ligand binding, second messengers,

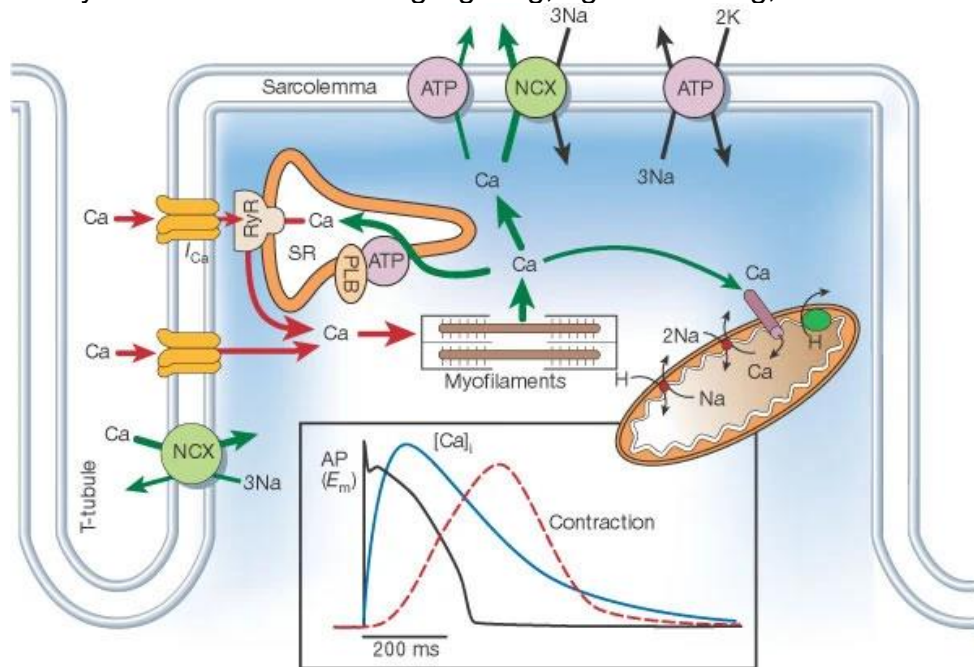


Figure 1.5. Schematic showing CMC membrane currents generating a typical action potential. Resting (4), upstroke (0), early repolarization (1), plateau (2), and final repolarization are the 5 phases of the action potential. A decline of potential at the end of phase 3. The image is taken from reference 37 with permission.

and post-translational modification. These ionic pathways can be impacted by both standard physiological factors and pathological stressors, leading to changes in channel behavior and the potential for arrhythmic activity.³⁸

The cardiac action potential is divided into phases, each reflecting unique ionic movements. During diastole, the resting membrane potential in working cardiomyocytes is maintained by baseline ionic and charge gradients established across the sarcolemma membrane, which is driven by pumps and transporters, particularly the Na⁺, K⁺-ATPase.³⁹ This energy-dependent electrogenic pump facilitates the exchange of Na⁺ ions for K⁺ ions, leading to opposing Na⁺ and K⁺ ion gradients. At rest, K⁺ channels are open, but those for Na⁺ or Ca²⁺ are minimally permeable, allowing K⁺ ions to flow out of the cell until the excess negative charge within the cell balances the diffusional forces and an electrochemical equilibrium is reached.¹⁹

The heart can regulate its beating rhythm through the automaticity of its cardiac cells. The contraction of these cardiomyocytes is driven by the cardiac action potential, which consists of two phases: the resting phase, also known as the polarized phase, and the active phase. During the resting phase, the cell membrane potential is maintained by the resting potential of ions such as sodium, potassium, and calcium, which are separated by the beating. The cardiomyocyte also can depolarize spontaneously, allowing sodium ions to enter the cell until reaching a point of depolarization. Calcium ions then extend the depolarization further. After calcium ions stop moving inward, potassium ions slowly move out and repolarize the cell.⁴⁰ Despite various methods to measure the contraction cycle of myocytes, the relationship between molecular tension and contraction remains largely unknown.

1.1.3 Podosomes and their implication on cardiomyocytes biology

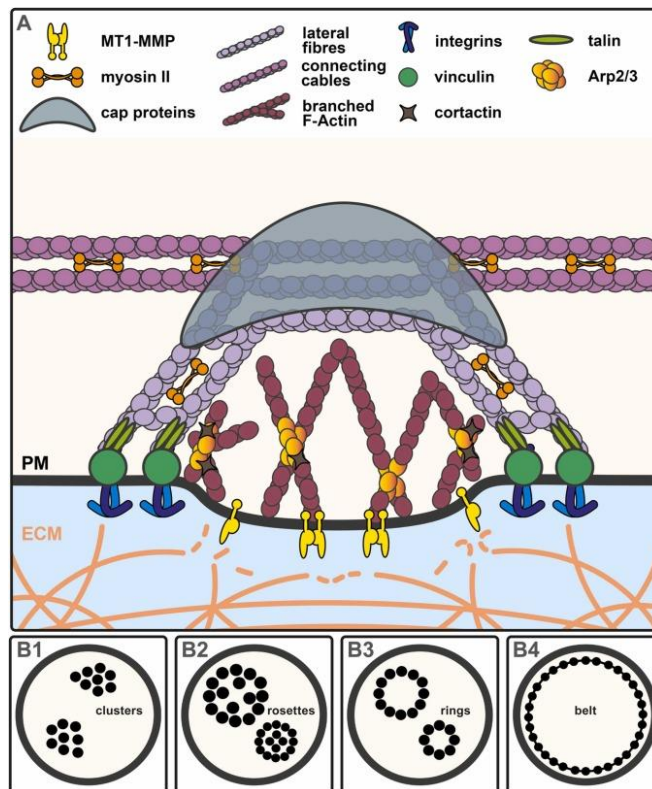


Figure 1.6 Schematic representation of podosome architecture. Podosomes feature several substructures, including i) an F-actin-rich core which is based on Arp2/3 complex-dependent actin nucleation and contains numerous actin-regulatory proteins such as cortactin, ii) a ring structure that mediates binding to the extracellular matrix through integrins, as well as linkage to the cytoskeleton via adhesion plaque proteins such as talin and vinculin, iii) a cap structure on top of the actin core that features several actomyosin regulatory proteins such as LSP1 or fascin, iv) a set of lateral actin cables that also contains myosin IIA and connects the top of the core with the ring structure, v) a second set of unbranched actin filaments, the connecting cables, that are extensively decorated by myosin II A and integrate individual podosomes into superstructures, as well as vi) a basal structure containing transmembrane proteins such as MT1-MMP. PM: plasma membrane, ECM: extracellular matrix. For individual elements, see the legend. Extracellular space in light blue, with filaments of the extracellular matrix in orange. (B1-B4) The appearance of podosome superstructures, including clusters (B1), rosettes (B2), and rings (B3). and belts (B4). Image taken from reference 42 with permission.

Cardiomyocytes, the cells responsible for heart muscle contraction, have been observed to exhibit morphological and biochemical changes under certain conditions. These changes include the formation of actin-rich assemblies known as podosomes, which have different levels of rigidity. ^{41, 42}

Previous research has shown that neonatal rat cardiomyocytes form ring-shaped vinculin and become actin-rich under stress caused by hypoxic conditions, as opposed to their typical striated distribution of proteins in optimal conditions. ^{43, 44} Podosomes have been described in various cell types, including all three vertebrate muscle lineages. They have been intensively studied in smooth muscle cells but less in cardiac and skeletal muscle cells. ⁴¹

A study by the Hilenski group found the presence of podosomes in cardiomyocytes. It indicated that these assemblies are only formed on collagen-coated substrates, with actin-rich cores and cortex domains containing vinculin, α -actinin, and β 1 integrins. These cells formed up to 20 structures with a diameter of 0.15 - 0.6 μ m. ⁴³ However, there is limited evidence of how podosomes play a role in the cardiac muscle cell. ⁴⁵

In this dissertation, we show that the formation of podosomes can be influenced by molecular rigidity and was observed only in lower force threshold surfaces (<12 pN). This suggests that the molecular rigidity of the substrate may play a role in forming these assemblies.

1.1.4 Different techniques to study and modulate the effect of mechanotransduction of CMCs.

Various techniques have been applied to examine the tension exerted by heart muscle cells through their integrin receptors during contraction. Traction force microscopy, atomic force microscopy, and optical edge detection have shown that a single cardiomyocyte can generate forces in the nano-Newton range. However, these methods are either sequential or have limited spatial and force resolution. Studies have also attempted to determine the contractile properties of cardiomyocytes by culturing them in three-dimensional structures. However, this method only provides an estimate of the average mechanical properties of the cells, and the individual contractile force produced by each cell is brutal to determine due to the influence of the rigidity of the bulk tissue and cell-cell contacts. Additionally, these three-dimensional and nonplanar structures make it challenging to observe individual cells using microscopy.

1.1.4.1 Substrate stiffness control the functional maturation of neonatal CMCs.

The maturation of cardiac cells occurs during the first postnatal week, along with changes in the mechanical properties of the extracellular environment. To examine the impact of these mechanical changes on cardiomyocyte maturation, neonatal rat ventricular myocytes were cultured for 7 days on polyacrylamide gels coated with collagen and having varying elastic moduli.⁴⁶ The results showed that cardiomyocytes grown on gels with a 10 kPa developed aligned sarcomeres. In contrast, cells grown on stiffer substrates

displayed unaligned sarcomeres, including stress fibers, which are not typically seen in vivo.⁴⁴

Furthermore, cells grown on 10 kPa gels exhibited the most significant mechanical force compared to those grown on stiffer or softer substrates. Additionally, cardiomyocytes grown on 10 kPa gels exhibited the highest levels of calcium transients, sarcoplasmic calcium stores, and sarcoplasmic/endoplasmic reticular calcium ATPase2a expression, while there was no difference in contractile protein.⁴⁷

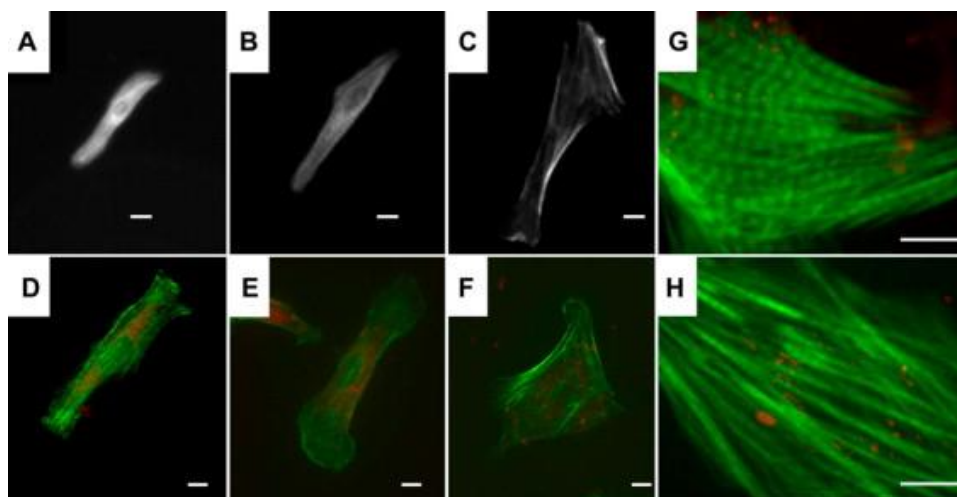


FIGURE 1.7 NRVMs on polyacrylamide gels and labeled for α -actin have poorly defined striations on soft 1 kPa substrates (A), well-defined and aligned striations on 10 kPa substrates (B), and unaligned striations with long, large stress fibers on stiff 50 kPa gels (C). NRVMs plated on polyacrylamide gels and labeled with phalloidin (*green*), and Dil (*red*) shows an axially aligned cytoskeleton throughout the cell on 1 kPa (D) and 10 kPa (E) gels. Still, F-actin concentrated on the periphery and nucleus and no axial alignment on 50 kPa gels (F). Zoomed-in confocal images of NRVMs on 10 kPa gels (G) and 50 kPa gels (H) better show differences in sarcomeric structure and alignment. Scale bars = 10 μ m. The image is reused from reference 46 with permission.

To determine if inhibiting stress fiber formation could improve myocyte maturation on stiffer substrates, maturing cardiomyocytes were treated with hydroxy fasudil, a RhoA

kinase inhibitor known to prevent stress fiber formation. This treatment led to an increase in force generation on the stiffest gels. ⁴⁸

In conclusion, extracellular stiffness near that of the native myocardium plays a crucial role in enhancing the maturation of neonatal rat ventricular myocytes. Deviations from this ideal stiffness result in lower expression of sarcoplasmic/endoplasmic reticular calcium ATPase, decreased stored calcium, smaller calcium transients, and reduced force generation. On very stiff substrates, this adaptation appears to involve RhoA kinase.

49

1.1.4.2 Muscle and non-muscle myosin in CMC rigidity sensing

The mechanical properties of a cell's environment play a crucial role in many biological processes and can profoundly impact cellular behavior, especially in the heart. During development, changes in the extracellular matrix composition and cross-linking can result in the stiffening of the microenvironment surrounding cardiomyocytes, affecting their

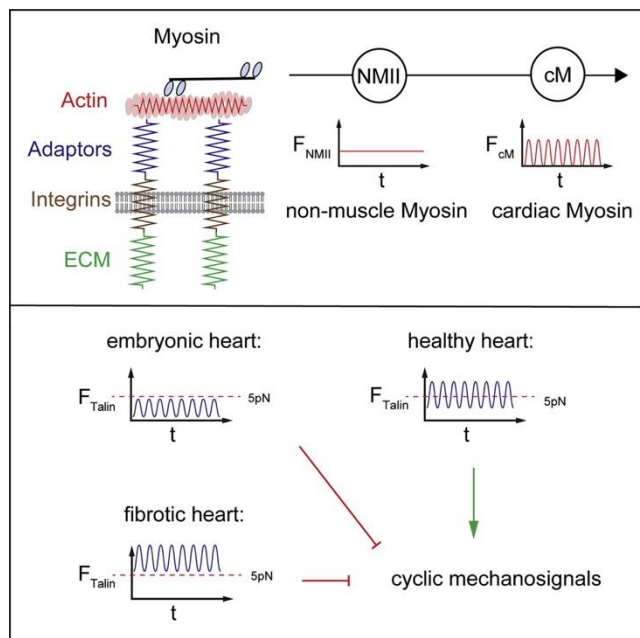


FIGURE 1.8 Schematic image showing myosin's role in the embryonic, healthy, and fibrotic heart. The image is taken from reference 32 with permission from the publisher.

behavior. Similarly, myocardial infarction and cardiomyopathies lead to fibrosis and a stiffer cellular environment, impacting the function of these cells. ^{15, 49}

Previous research has revealed that single cardiomyocyte adhesions sense mechanical changes through fast-oscillating cardiac muscle and slow non-muscle myosin contractions. ¹² On substrates with a stiffness like healthy adult heart tissue, these contractions lead to oscillating tension on the mechanosensitive adaptor protein talin. In contrast, no such tension is observed on substrates with either embryonic heart or fibrotic stiffness. ³²

Additionally, scientists have discovered that activation of the protein kinase C (PKC) leads to the induction of cardiomyocyte hypertrophy in a stiffness-dependent manner through the activation of non-muscle myosin. This highlights the importance of mechanically sensitive signaling pathways in regulating cardiac cell behavior. ¹² The research has shown that PKC and non-muscle myosin are upregulated at the costameres in heart disease, suggesting that aberrant mechanosensing may contribute to long-term remodeling and heart failure. ³²

1.1.4.3 Tunable substrates to study maturation and differentiation of CMs

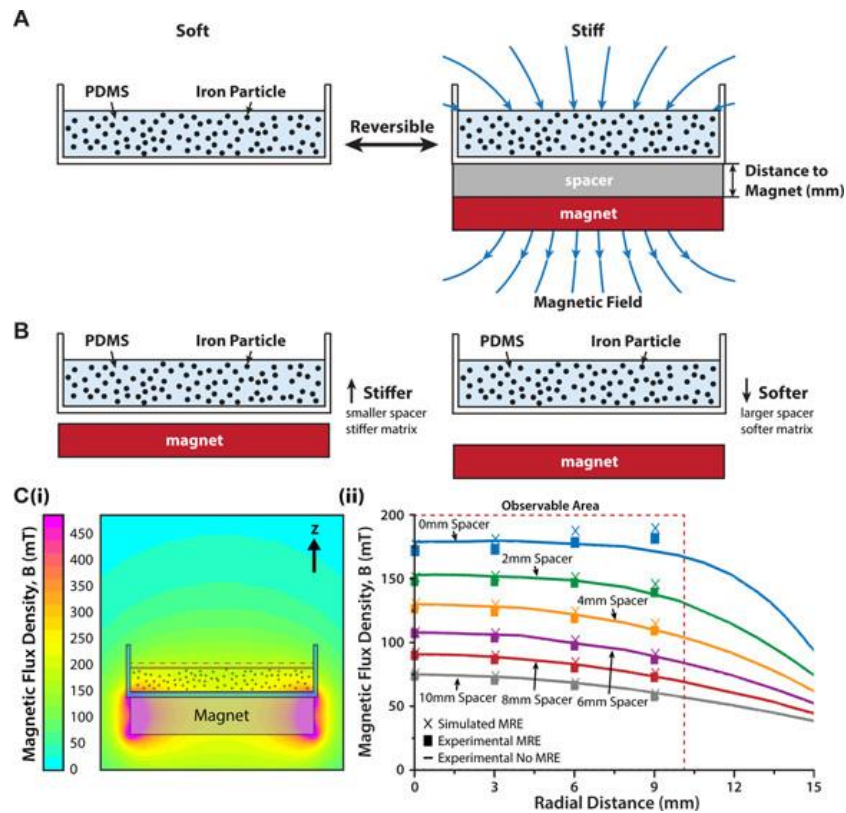


Figure 9 Overview of the magnetorheological elastomer. (A) Composite consisting of the polymer matrix and iron particles. When a magnetic field is applied, the particles rearrange and cause a change in the material stiffness. (B) Dynamic control of the matrix stiffness is possible by varying the magnetic field gradient by adding spacers between the magnet and the substrate. The material stiffens as the magnet is placed close to the material and softens as spacers are added, and there is a greater distance between the fabric and the magnet. (C) (i) Simulation showing the magnetic flux density of the magnet with a shadow drawing of the placement of the MRE within a 35 mm dish and the dashed box indicating the location of cells on the surface. (ii) Line snapshots from the simulation show the z-component of the magnetic flux density at the surface of the MRE measured along the radial direction at the specified spacer distances between the base of the dish and the magnet. Image reused from reference 52 with permission.

The physical properties of the extracellular matrix (ECM) play a crucial role in cellular processes, particularly in cardiomyocytes and cardiac fibroblasts.⁴⁴ Stiffness and viscoelasticity of the ECM impact cell spreading, fibroblast activation, cardiomyocyte contractility, Yes-associated protein activation, and actin filament organization.^{50, 51} The ECM is dynamic and changes normal and diseased tissues, with cells responding to their mechanical environment through topographic cues, material stress relaxation, and memory of past environments. Studying the mechanical regulation of cells at different time scales is essential in understanding cellular signaling. However, nonphysiologically, stiff materials have limited our understanding of these processes in vitro.

Recently, there has been an uptick in interest in creating in vitro systems that can adjust their material stiffness through various methods, such as exposure to light, changes in temperature or pH, or adding biomolecules. One approach for controlling stiffness is using hydrogels that can stiffen or soften through phototunable crosslinking or degradation. However, these methods are limited in that they can only make permanent, unidirectional changes in stiffness or in some cases, offer bidirectional changes only once.

Researchers have presented a novel solution to these limitations in previous studies by introducing a magnetorheological elastomer (MRE) that can control stiffness through applied magnetic fields. The MRE is an elastomeric polymer that contains embedded iron particles. When subjected to magnetic field gradients, it rapidly stiffens and relaxes back to its soft state when the magnetic field is removed. This stiffness control is reversible, tunable and allows for varying stiffnesses by adjusting the magnitude of the applied magnetic field gradient.⁵²

1.1.5 Limitations of these techniques and gap in knowledge

In the past few years, our lab^{53, 54, 41} and others in^{53, 55} have pioneered the development of molecular force sensors (MFSs) and revealed that the individual integrin receptors of cells actively engage their cognate ligands and indeed transmit low pico-Newton forces in real-time. These forces are essential for the differentiation and development of functional CMCs. Current literature suggests that the differentiation and development of mature CMC may change when cultured on gel substrates with different global stiffness. The variability in substrate stiffness was found to alter the cell's ability to transmit forces, as observed by the change of their spread area, sarcomeric structure, actin dynamics, and contractility in the long term (7-10 days post-culture)^{30, 56}. Despite rigorous, long-term studies, very little is known about how mechanical inputs regulate the biochemical signaling of CMCs at early time frames (~hours to days).

1.2.1 Stem cells and their role in tissue regeneration

Stem cells are a distinctive type characterized by their capacity to divide and differentiate into various cell types, making them crucial for tissue repair and regeneration. There are two main types: embryonic stem cells from the inner cell mass of the blastocyst during early embryonic development, which are pluripotent and able to differentiate into any cell type, and adult stem cells found in different tissues, which are multipotent and capable of

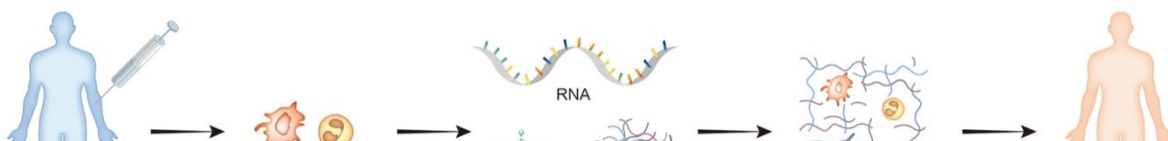


Figure 10 Flow chart of stem cell therapeutic strategy from extraction to transplantation. Image is taken from reference 59 with permission.

producing several cell types. Stem cells divide either symmetrically to create two identical daughter cells or asymmetrically to create a differentiated cell and a new stem cell.^{57, 58}

Stem cell differentiation is controlled by signals such as hormones, growth factors, and the local environment. Stem cells play a crucial role in tissue repair and regeneration and hold great potential for treating diseases. The workings of stem cells include self-renewal, where they divide and produce identical copies of themselves to maintain a pool of unspecialized stem cells. Additionally, stem cells can differentiate into specific cell types such as muscle, bone, or blood cells, through a process known as differentiation. Some stem cells, such as mesenchymal stem cells, display plasticity, enabling them to change into multiple cell types, thus contributing to the versatility of tissue regeneration. Lastly, stem cells can be regulated through internal and external signaling pathways, such as hormones, cytokines, and growth factors, to control their self-renewal and differentiation. The mechanics of stem cells require a careful balance between maintaining a supply of undifferentiated cells and guiding their differentiation into specific cell types for tissue repair and regeneration.⁵⁹

1.2.2 Biophysical and mechanical influence on stem cells in living systems.

Physical and mechanical cues are crucial in tissue formation and maintenance throughout the human body. This includes embryonic development, where ESCs (Embryonic Stem Cells) respond to biophysical cues to self-renew and differentiate, leading to proper organ formation.⁶⁰ These cues remain essential for adult stem cells, where cell-cell and cell-matrix interactions are necessary to maintain potency. Physical and mechanical forces

during embryonic development, such as cell contractions and early muscle twitches, can dictate gene expression and cell viability, leading to asymmetric development if not typical.⁵⁷ Additionally, maternal movements and muscle activity provide important mechanical cues for normal skeletal development in the embryo. In the rudimentary heart, cardiac cell contractions play a critical role in tissue deformation and blood flow, leading to a functioning heart with its chambers and valves.⁶¹ Throughout life, biophysical cues are essential in maintaining normal adult tissues, and changes in the extracellular mechanical environment or cellular mechanisms to sense stimuli can lead to pathological conditions.⁵⁸

1.2.3 Stem cell mechanics and implications in regenerative therapies.

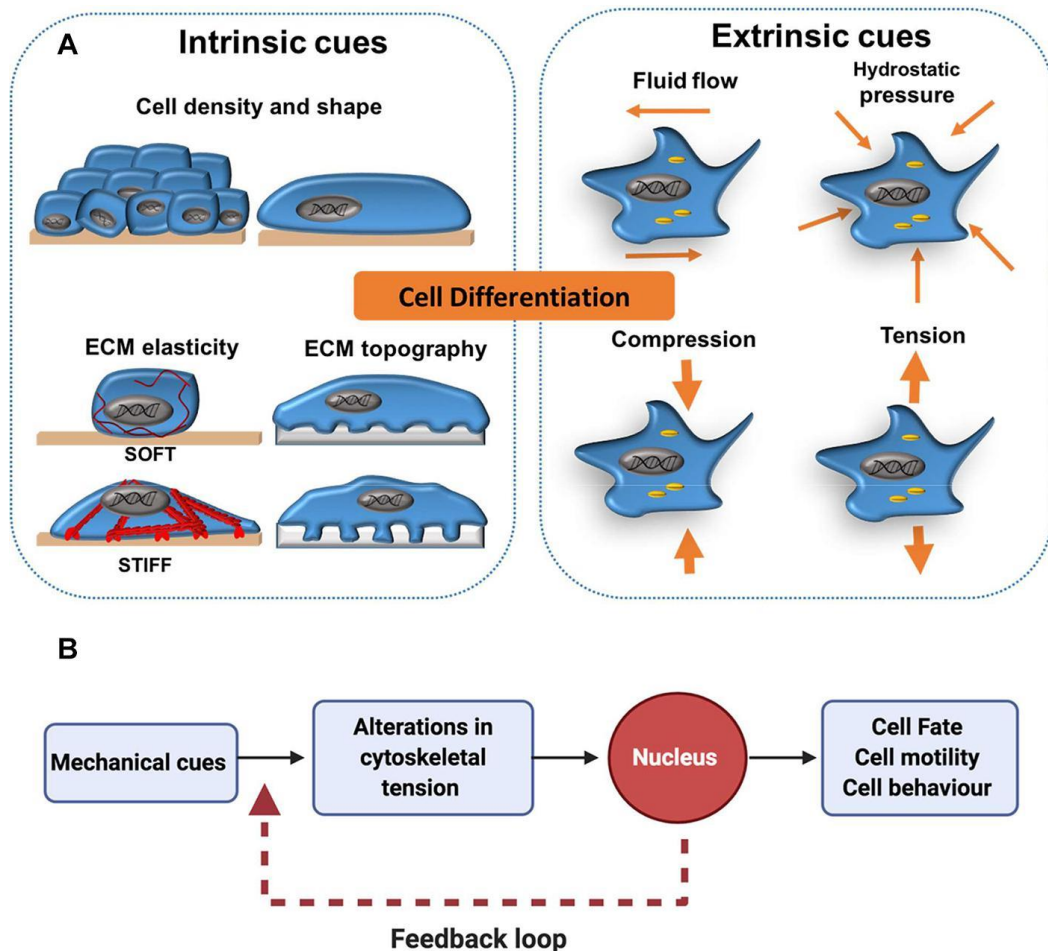


Figure 1. 11 Schematic of the physical cues on stem cells mechanics. **(A)** Cell differentiation has been shown to be affected by mechanical forces external to the cell (extrinsic) such as shear stress from fluid flow and more local mechanical cues (intrinsic) such as cell density, shape, and elasticity of the surrounding extracellular matrix (ECM). **(B)** As a general concept, mechano-transduction involves the transfer of mechanical cues from the cell surface to the nucleus via the cytoskeleton. This activates downstream cell signaling cascades, which can influence cell fate decisions. In addition, a transcriptional feedback loop allows cells to maintain a cytoskeletal equilibrium that is responsive to changes in their mechano-environment. This is particularly important for processes like cell migration, in which continual cytoskeletal remodeling is required for persistent cell motility. The image is reused from reference 61 with permission from the publisher.

Stem cells, known for their ability to regenerate tissues and differentiate into specialized cells, have been extensively researched for their potential in treating various medical conditions. Stem cells can be obtained from both embryonic and adult tissues and are identified by markers such as CD13, CD44, and others, while the absence of markers such as CD11b, CD14, and others indicates their presence.⁶² Exposing stem cells to biochemical cues such as growth factors, genetic regulators, and bioactive molecules can have stimulated them to differentiate into specific tissues.⁵⁸

Biophysical cues also play a crucial role in regulating stem cell behavior, impacting proliferation, differentiation, gene expression, and apoptosis. Biophysical environments, such as matrix architecture, topographical guidance, electrical stimulation, and mechanical strength, affect stem cell biology.⁶³

Various techniques have been developed to control biomaterials' physical and mechanical properties, including 2D stiffness and 3D scaffold properties, to study the impact of biophysical cues. Computational models have also been created better to

understand the interaction between stem cells and biomaterials. There is a continued need to understand the biophysical cues that promote stem cell differentiation for successful clinical applications.⁶⁴

1.2.4 Different techniques to manipulate stem cell mechanotransduction.

The success of regenerative medicine relies on the ability to recreate the molecular processes that enable stem cells to heal damaged tissue or organs. To achieve this goal, biomaterials are designed to possess properties that can guide stem cell fate in a controlled and physiologically relevant manner. This is based on the understanding that stem cells are sensitive to physical forces and can convert mechanical stimuli into chemical responses. This chapter will focus on the recent advancements in the interaction between stem cells and biomaterials, emphasizing the impact of mechanical stimulation, also known as mechanotransduction.^{58, 63}

1.2.4.1 2D substrate and its effect on stem cell differentiation

The stiffness of the substrate can play a significant role in shaping the differentiation of stem cells. Studies have found that stem cells cultured on stiff substrates exhibit a higher expression of specific markers. For example, mesenchymal stem cells (MSCs) on a stiff (15 kPa) substrate show higher expression of smooth muscle cell markers, while on a soft (1 kPa) substrate, there is increased expression of chondrogenic and adipogenic markers.⁶⁵

In studies on human embryonic stem cells (hESCs), a stiff (10 kPa) substrate activated the nuclear localization of YAP/TAZ, while a soft (0.7 kPa) substrate resulted in low levels of YAP/TAZ.⁶⁶ Meanwhile, osteogenic differentiation of bone marrow-derived stem cells (BMSCs) was inhibited by either depletion of YAP and TAZ, culturing cells on a soft extracellular matrix (ECM), or incubating cells with a Rho inhibitor.⁶⁷

On the other hand, osteogenic differentiation of ESCs was enhanced on stiff substrates compared to soft ones, with increased expression of genes involved in early mesendoderm differentiation. The substrate stiffness was also found to affect the expansion and maintenance of undifferentiated mouse hematopoietic stem cells (HSCs) and human HSCs when cultured on tropoelastin.⁶⁸ However, the biological effects of tropoelastin were lost when the substrates were cross-linked with glutaraldehyde or when the mechanotransduction was inhibited.⁶⁹

1.2.3.2 Effect of using different ligands on stem cells differentiation

The study of stem cell behavior in response to different substrate stiffnesses has revealed intriguing results. For instance, osteogenic differentiation of MSCs has been observed to increase with increased substrate stiffness, with the highest levels of differentiation achieved on high-stiffness collagen-I coated gels.⁷⁰ Similarly, myogenic differentiation occurred on all gel-protein combinations with a stiffness greater than 9 kPa, with the best results observed on fibronectin-coated gels with a modulus of 25 kPa.⁷¹

The mechanical properties of the ECM also influenced hiPSC, with increasing ECM stiffness resulting in increased colony spread area but not affecting self-renewal. Soft matrices, on the other hand, promoted neural differentiation and increased the number of

neurons and dopaminergic neurons.⁷² The YAP nuclear translocation was found to occur at a lower density for fibronectin, collagen I, and collagen IV but at a higher density for laminin. It was linked to different levels of osteogenic commitment depending on the ECM.⁶⁴

Soft PEG hydrogels with stiffness close to that of native muscle elasticity were found to promote self-renewal in muscle stem cells and enhanced muscle regeneration when transplanted into mice. This was not observed in stem cells cultured on stiff tissue culture plastic. Additionally, migration velocity was found to increase in stem cells cultured on stiff PEG hydrogels compared to softer matrices.⁷³

The softness of the substrate was also found to impact human MSC behavior. MSCs seeded on soft hydrogels showed reduced cell attachment and spreading, while those seeded on stiff hydrogels spread with high spatial coverage, with the effect dependent on RGD concentration and isoform. On the other hand, diminished contractility of hMSCs was observed on soft substrates, with cell spreading and osteogenic differentiation only occurring on soft hydrophobic PDMS and not on soft hydrophilic PEO-PDMS.⁵⁸

In conclusion, substrate stiffness plays a crucial role in the behavior and differentiation of stem cells, and different ECM types and mechanical properties have distinct effects on cell fate.

1.2.3.3 Micropost array to measure stem cell mechanics.

The stiffness of the matrix plays a crucial role in the differentiation of stem cells. Previous studies incorporating micro-post arrays showed that when human mesenchymal stem cells (hMSCs) were cultured on a rigid matrix with a modulus of 1,556 nN μm^{-1} , they

strongly preferred osteogenic differentiation.⁷⁴ Conversely, when hMSCs were cultured on a softer matrix with a modulus of $1.90 \text{ nN } \mu\text{m}^{-1}$, they showed a greater inclination towards adipogenic differentiation. It was also observed that hMSCs undergoing osteogenic differentiation had higher traction forces than those without. Similarly, non-differentiating hMSCs exhibited higher contractility compared to those undergoing adipogenic differentiation. The osteogenic potential of hMSCs was suppressed following inhibition of the Rho-ROCK pathway.⁷⁵

On the other hand, 20% of human embryonic stem cells (hESCs) cultured on a rigid matrix remained undifferentiated compared to cells cultured on a soft matrix. The cytoskeletal contractility of hESCs was seen to increase with increased matrix rigidity. A soft matrix with a modulus of 5 kPa was found to promote the neuroepithelial conversion of hESCs. In addition, the purity and yield of functional motor neurons derived from neural progenitors were higher on soft matrices.⁷⁶

1.2.3.4 3D materials to study stem cell mechanotransduction

The mechanical properties of 3D culture systems significantly impact the behavior and fate of stem cells. These systems, which imitate the in vivo environment in terms of the architecture and biological roles of the extracellular matrix (ECM), provide a more complex environment for cell growth and differentiation than traditional 2D cultures. Therefore, researchers have studied the effects of various mechanical properties on stem cell behavior, such as stiffness and porosity.⁷⁷

Tissue engineering scaffolds offer a 3D platform for cell attachment and proliferation while providing mechanical stability to mimic the in vivo environment. Porosity and 3D

architecture can be achieved through various methods, including freeze-drying, electrospinning, solvent extraction of porogen templates, material degradation, or 3D printing.⁷⁸ This leads to complex 3D mechanical environments determined by the stiffness of the bulk material, topographical features, and specific characteristics of the porous architecture, such as porosity, pore size, and strut thickness.⁷⁹

Studies have investigated the impact of ECM rigidity on MSC phenotype by encapsulating

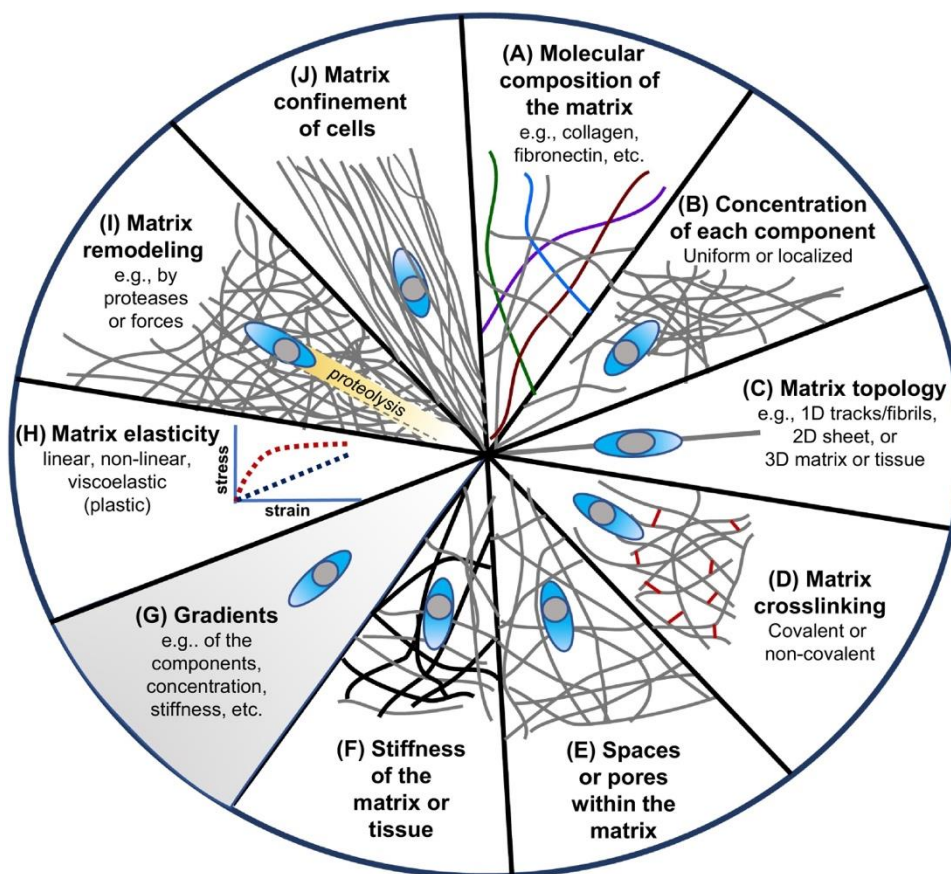


Figure 1.12 Biochemical or mechanical properties of the extracellular matrix (ECM) governing cell–ECM interactions. Image reused from reference 78 with permission.

cells in PEGDM polymers with varying weight percent and photo-crosslinking them in the presence of acryloyl-PEG-GRGDS2. Results showed moderate stiffness 3D hydrogels (11-30 kPa) favored osteogenic differentiation, while hydrogels in the 2.5-5 kPa range

promoted adipogenesis. However, stem cell and nuclear morphology were not strongly correlated with the mechanical properties of the 3D hydrogels in the specific ranges studied. Matrix stiffness was found to regulate integrin binding and adhesion ligand reorganization through cell contractility and inhibiting RGD binding to integrins reduced osteogenesis.⁸⁰

Additionally, the adhesion, shape, and cytoskeletal organization of MSCs have been shown to depend on the stiffness (0-40 kPa) of 3D cross-linked hyaluronic acid and 2D PA substrates.⁸¹ Stiffer matrices were found to promote cell spreading, while stem cells embedded in hyaluronic acid matrices were constrained to spherical shapes and assembled a predominantly cortical cytoskeleton. Inhibition of myosin-II contractility with Blebbistatin prevented the spreading of MSCs.⁸²

These studies highlight the complex relationship between ECM stiffness and stem cell behavior, with mechanical properties influencing adhesion, shape, cytoskeleton assembly, and differentiation.

1.3.1 Methods to measure cell-generated forces.

Cell-generated forces shape tissue development and homeostasis and control cellular functions like receptor signaling, transcription, differentiation, and proliferation. Despite their importance, only a few of these forces have been fully characterized. Unlike the different molecular genetic tools available to investigate the expression, regulation, and activity of specific proteins, the current understanding of the impact of mechanical force on cell biology is limited.⁸³ This chapter succinctly evaluates the established techniques for measuring cell-generated forces, highlighting their advantages and disadvantages.⁸⁴

This section of the chapter is a helpful guide for seeking to understand the various options available to study the role of mechanical force in cell biology.

1.3.1.1 Traction force microscopy

Traction forces (TFs) are a unique type of tension generated by cells, which they exert on either the extracellular matrix (ECM) or the surface they are on (as illustrated in Fig. 13 A&B).⁸⁵ These forces are initiated within the cell, but their influence extends to the cell's environment, affecting cell spreading and migration processes. These forces are transferred through focal adhesions (FAs), which act as a bridge between the ECM proteins and the cell's cytoskeleton, primarily composed of actin filaments.⁸⁶ FAs comprise internal components, such as paxillin, vinculin, Talin, and actin, and external components, like integrins and proteoglycans.⁸⁷ Determining the presence and strength of TFs offers valuable insight into cell movement and the alteration of cell phenotype due to mechanical and chemical changes in the cell microenvironment.⁸⁸

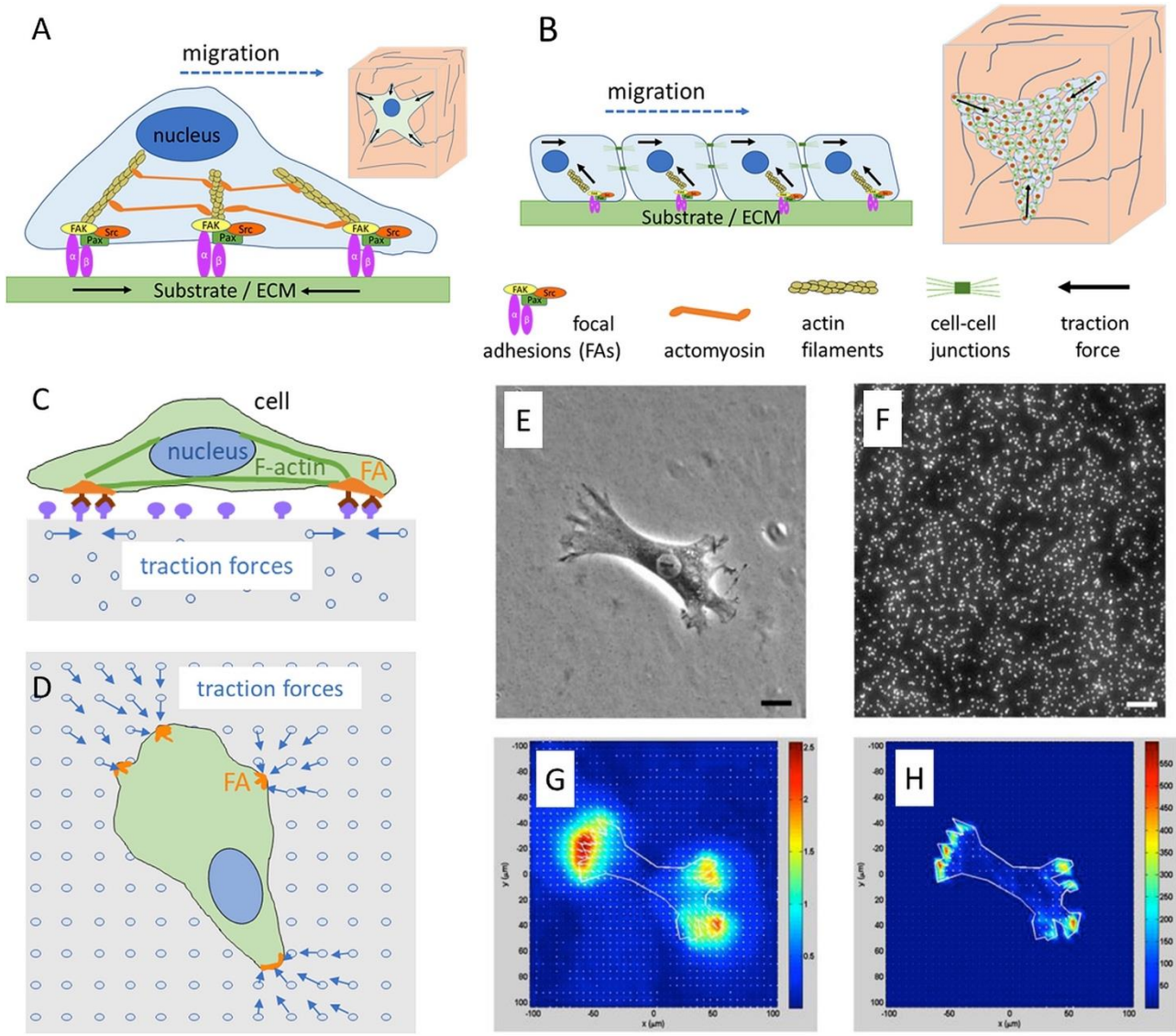


Figure 1.13 Schematic representation of workflow of traction force microscopy. Image reused from reference 88 with permission.

The measurement of traction forces (TFs) exerted by a cell on a soft surface is performed using Traction Force Microscopy (TFM).^{79, 89} This process involves calculating forces at each contact point between the cell and the substrate by analyzing the deformation field created by the cell. To achieve this, the substrate is embedded with tiny fluorescent beads that act as displacement markers, allowing for the deformation tracking and calculation of the displacement field. Bead positions are recorded before and after cell detachment and

compared to determine the displacement field. However, it's worth noting that TFs are not measured directly but are reconstructed from the cell's induced deformation of its surroundings.^{90,91} To ensure accurate results, the mechanical properties of the substrate must remain unchanged by the presence of the beads, and the assumption is made that TFs acting perpendicular to the substrate surface are negligible.⁹² A vital factor in TFM is the ability to track the lateral motion of the beads, as demonstrated in Fig. 1.13. Many studies have been deployed to use traction force microscopy to measure both 2D and 3D matrices.⁸⁵

1.3.1.2 Micro-post array to measure cellular force.

Micro posts, treated as cylindrical vertical cantilever beams, serve as a tool to quantify cell traction forces.⁹³ The micro post has one end fixed to a substrate and the other free. Any force applied to the free end will result in a bending of the micro post.⁷⁴ As a cell's contractile machinery relaxes or contracts, it changes its traction forces. For a cell attached to the top of the micro post, these mechanical changes become apparent as directional deflections of the micro post.^{74,94}

In the linear regime, the micro post behaves like a spring, with deflection directly proportional to the applied force. Hence, the traction forces can be determined by calculating the deflection of each micro post. The relationship between force, F , and free end displacement, x , can be calculated using Euler-Bernoulli Beam Theory. The spring constant of the micropost can be modified by altering its size or Young's modulus of the PDMS used.⁹⁵ To find the optimal micropost with the appropriate stiffness, the post diameter can be varied in ranges of micrometers. The spacing between the micro-posts

can also be adjusted to create a different density of micro-post arrays. The measurement of forces using micro post arrays is restricted to a two-dimensional setting, which doesn't accurately reflect the three-dimensional surroundings of cells in real-life environments,

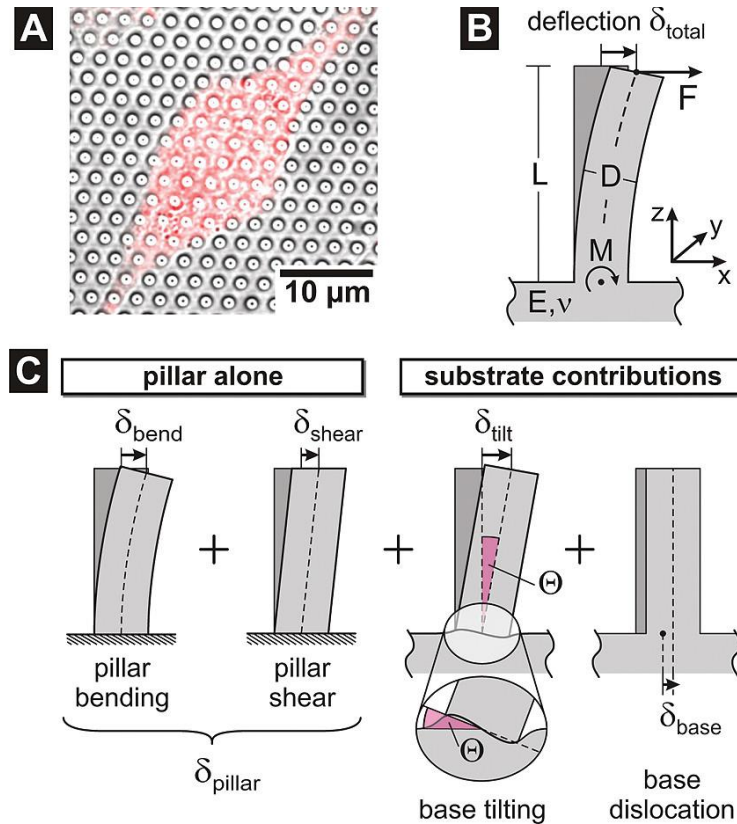


Figure 1.14 Elastic pillar deflections induced by lateral force. (A) Fibroblasts on micropillar array. Overlay of a DIC image with fluorescence from a Dil membrane stain. (B) Relevant parameters of the system: the pillar has height L , diameter D , Young's modulus E , and Poisson ratio ν . A force F directed in the positive x direction causes a deflection δ_{total} of the pillar top and induces a momentum $M = FL$ at its bottom. (C) The total deflection comprises contributions from the bending and shear of the pillar, as well as tilting and a lateral displacement of the base beneath the pillar. Reused from reference 95 with permission.

leading to a loss of some physiological significance. The analysis of these micro-posts is also limited by optical measurements, causing potential constraints in spatial and temporal resolution. ^{95, 96}

1.3.2 Molecular traction force microscopy to measure cell forces.

Mechanical forces play a crucial role in various biological activities, including cell migration, differentiation, and adhesion, through mechanotransduction, where cells respond to physical stimuli. Receptor-ligand bonds on the cell membrane transmit piconewton mechanical forces modulated by the cytoskeleton. Two main techniques to measure cell receptor forces are traction force microscopy (TFM) and single molecule force spectroscopy (SMFS). Recently, molecular tension fluorescence microscopy (MTFM) has been introduced as a new method to measure receptor mechanics in living cells. This method combines aspects of TFM and SMFS to optically report receptor forces with pN sensitivity by using MTFM probes that consist of an extendable linker and fluorophore/quencher. The fluorescence emission from MTFM probes measures the extension and force. In this chapter, we review the design of MTFM probes, including the extendable linker, spectroscopic ruler, surface immobilization chemistry, and ligand design strategies.⁹⁷ This chapter also extensively discusses the strengths and weaknesses of different versions of MTFM probes and present case studies of the pN forces involved in various signaling pathways. We incorporated DNA-based MTFM probes for the entirety of this thesis.

1.3.2.1 DNA-based molecular tension probes

As the primary carrier of our genetic information, DNA has enormous potential as a tool for biophysical studies. In addition to its well-known properties, DNA's behavior under mechanical forces has been extensively studied using a worm-like chain (WLC) model. Characterizing DNA using optical tweezers, AFM, and magnetic tweezers lays the

foundation for its use as a molecular tension probe. Based on the mechanical properties of DNA molecules, DNA-based force probes have been developed to study the forces mediated by cellular receptors. These probes can be divided into two categories based on the signal it detects: reversible DNA probes based on DNA hairpin structures and irreversible DNA probes based on DNA duplex structures.⁹⁸

1.3.2.1.1 Irreversible DNA tension probes

Usually, the irreversible tension sensors consist of a DNA duplex that can be unhybridized based on force application. In the Tension-Gauge Tether (TGT) probes, a ligand-conjugated double-stranded DNA (dsDNA) is anchored to a solid surface using biotin-streptavidin linkage. When cells are placed on the surface, the cellular receptor interacts with the ligand, applying force to the dsDNA. If the force exceeds the dsDNA's rupture force, the dsDNA will break and deactivate the receptor. If the force is weaker, the dsDNA remains intact, activating the receptor. The critical force required for dsDNA rupture depends on the application geometry, with lower forces needed for unzipping and higher for shearing. Wang and Ha were the first reporters of first-generation TGT probes.⁹⁹ Later, Salaita and a coworker upgraded the system to measure the turn-on signal.¹⁰⁰ To monitor cell activation, TGT probes were developed that either monitor the activation signal (first-gen TGT) or visualize the ligand distribution (2015 TGT with a fluorescently labeled dsDNA). Limitations of TGT include its irreversible nature and the possibility of quenching being misinterpreted as dsDNA rupture. To overcome these issues, alternatives such as Integrative Tension Sensors (ITS) and Quenched TGT (q-TGT) have been developed, as well as reversible tension probes and force sensors.

Two types of TGT designs exist - unzipping and shearing - with varying levels of tension tolerance (T_{tol}), depending on the placement of the anchor and ligand about each other on the DNA molecule (as shown in Figure 1.6b). T_{tol} is the force required to break a DNA duplex within two seconds. Previous studies have indicated that the rupture force of different TGTs can be calculated using the following equation:

$$F = 2f_c \left[\chi^{-1} \tanh\left(\chi \frac{L}{2}\right) + 1 \right]$$

where f_c represents the force needed to break a single bond ($f_c = 3.9$ pN), L stands for the number of DNA base pairs between the two anchor points, and the value represents the finite length over which the force is distributed ($= 6.8$).^{98, 101} Compared to DNA probes that can be reversed, TGTs can detect a broader range of forces. However, TGTs typically break after a mechanical event, making them irreversible probe that records the tension history. To address this issue, the Salaita lab developed a reversible TGT by attaching a DNA duplex probe to a single-stranded strand anchored to the surface (Figure 1.15). We utilized this probe in the second chapter of this thesis.

1.3.2.1.2 Reversible DNA tension probes

The reversible DNA tension probe design utilizes a dye-quencher pair and a ligand-labeled DNA hairpin to target specific receptors and measure mechanical forces (Figure-). The probes feature a functional group for surface immobilization and a hairpin sequence that can be adjusted for a range of force thresholds, from 4.7 pN to 19 pN. When the targeted receptors apply force to the hairpin, mechanical melting occurs, leading to a substantial increase in fluorescent signal. This approach has been used to study a variety of mechanotransduction pathways, including cell adhesion and platelet activation, with its high temporal resolution and low force threshold making it a valuable tool for these studies.^{97, 101} However, it may not be suitable for receptors that exert significantly higher forces.

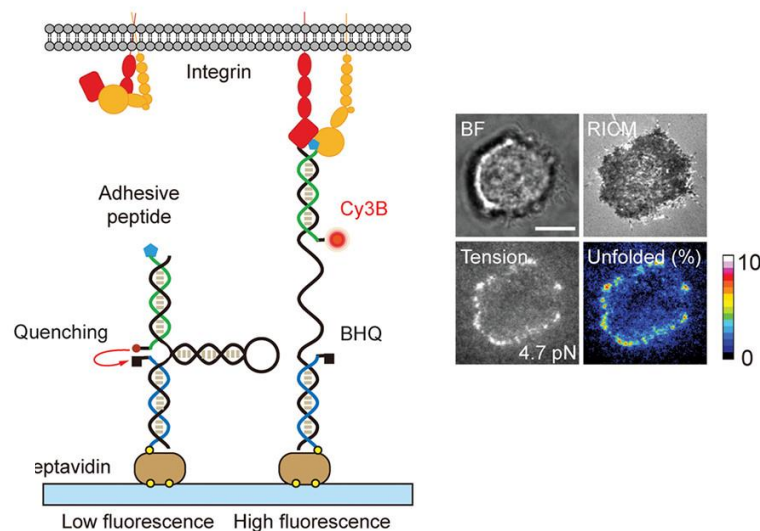


Figure 1.15 Schematic representation of DNA hairpin probes on gold nanoparticle. Image reused from reference 97 with permission.

1.3.2.2 PEG-based molecular tension probes

The first PEG-based MTFM probes were designed to measure the mechanical forces associated with endocytosis of the epidermal growth factor receptor (EGFR) and its impact on cell survival, proliferation, and differentiation (Figure-1.17). The probes could detect punctate force signals during EGFR engagement and link them to cadherin recruitment. Following this, a similar probe was created to examine the forces generated

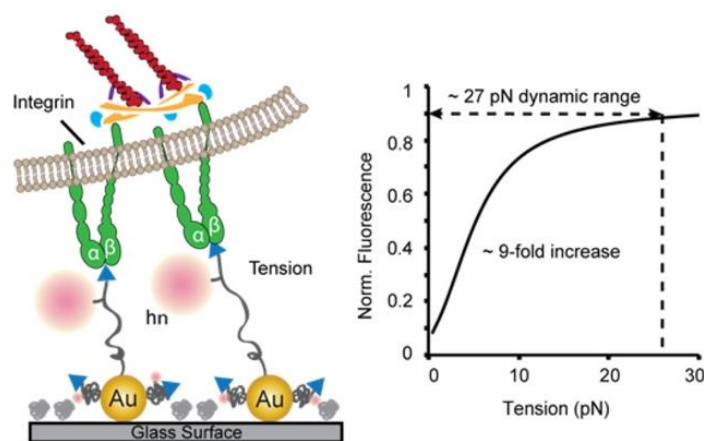


Figure 1.16 Schematic representation of PEG molecular tension sensors on gold nanoparticle. The image is reused from reference 97 with permission from the publisher. by integrin receptors. The biological ligand in this probe was modified with a cyclic RGD peptide that has a high affinity to the $\alpha\beta3$ and $\alpha5\beta1$ integrins. The study found that the integrin receptors exerted forces strong enough to dissociate streptavidin–biotin complexes, one of the strongest noncovalent interactions.¹⁰²

To overcome the biotin–streptavidin dissociation, a gold nanoparticle (AuNP) based MTFM sensor was developed to detect integrin-mediated forces with a ten-fold fluorescence increase (Figure 1.17). This sensor was anchored to the AuNP surface through a bond that ruptured at around 0.6-1 nN. The researchers also combined AuNP-

based MTFM with block copolymer micelle nanolithography to create substrates with arrays of precisely spaced tension probes. This allowed them to examine the impact of receptor nano clustering on force transmission. The study found that a critical ligand spacing of less than 60 nm was necessary to sustain high integrin forces in focal adhesion maturation. In comparison, loosely spaced ligand arrays above 100 nm destabilized focal adhesion formation and reduced integrin forces. These findings provide new mechanistic insights into the role of integrin clustering in focal adhesion formation and suggest that the cellular mechanism of sensing nanoscale ligand spacing is force mediated.⁵⁴

1.3.2.3 Protein-based molecular tension probes

Previous literature has suggested that the tension exerted by certain cells (cancer cells, muscle cells, cardiac cells) is higher than the tension magnitude of the hairpin probes. Researchers employed protein-based mechanical tension force microscopy (MTFM) probes to test the strength of integrin-mediated forces. To better understand these forces, researchers utilized a molecular tension probe composed of the I27 domain of cardiac titin, a fluorophore, and a gold nanoparticle (Figure 1.18). The results of cellular experiments indicate that integrin forces are strong enough to unfold the I27 domain, with estimates suggesting values greater than 80 pN.¹⁰³

To accurately measure these forces, the researchers introduced a disulfide bridge into the I27 probe which "clamped" it, preventing mechanical unfolding. The addition of a reducing agent allowed for the disulfide bridge to be broken, unclamping the I27 and allowing for the measurement of applied forces. This analysis showed that a subset of

integrins applies tension far greater than previously reported, with estimates suggesting values of 110 ± 15 pN. These findings are supported using nanoparticle titin tension.

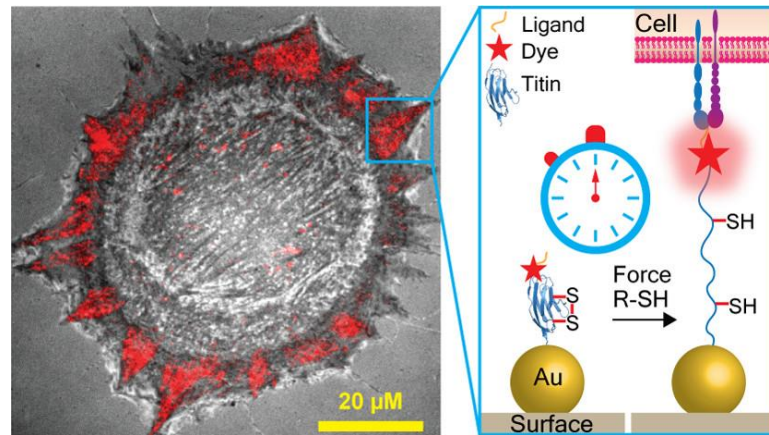


Figure 1.17 Schematic representation of titin-based protein tension sensors on gold nanoparticle. Image is reused from reference 103 with permission.

sensors and the kinetic analysis of unfolding. Galior and coworkers created a series of I27-based tension probes that either displayed an RGD polypeptide or recombinant fibronectin 9-10th protein domains with both RGD and the PHSRN synergy site (Figure 6A). Remarkably, integrin-mediated forces were found to cause the I27 domain and super folder GFP to unfold within minutes of cell engagement, indicating that integrin forces may be even greater than 30 pN. However, the exact magnitude of these forces is difficult to determine since the mechanical loading rate of integrin receptors within focal adhesions is unknown. To overcome this limitation, a covalent disulfide bridge was engineered within I27 to clamp the probe and prevent mechanical unfolding. The bridge could be unclamped by adding a reducing agent DTT, and the kinetics of protein unfolding could then be monitored to estimate the relative tension applied by different subtypes of integrins. This

approach provides a unique method for inferring the forces within stable focal adhesions, although the results are dependent on the parameters determined in previously published work.^{54, 104}

1.3.2.4 Other development and limitations of the MTFM probes

Recent advancements have expanded the application of the previously described DNA tension probe design. For instance, researchers have developed DNA origami structures containing multiple reversible DNA probes to investigate the relationship between receptor forces and clustering.¹⁰⁵ DNA tension probes have been utilized with supported lipid bilayers to simulate receptor forces on cell membranes.¹⁰⁶ To further explore forces at cell-cell junctions, the probes have been anchored on cell membranes with cholesterol.¹⁴ Molecular force microscopy (MFM) has also been developed by combining fluorescence polarization microscopy with DNA hairpin probes to study receptor force orientation, revealing the involvement of lateral forces in platelet activation.^{14, 106} Using PNA to increase DNA probe stability has shown promise in studying cancer cell mechanics.¹⁰⁷ Furthermore, combining DNA-Points Accumulation for Imaging in Nanoscale Topography (DNA-PAINT) with DNA tension probes has allowed researchers to achieve a spatial resolution in the tens of nanometers.¹⁰⁸ We have also had development in creating reversible TGT probes where research showed reversible control of mechanical force could affect cell function and biology.¹⁰⁹⁻¹¹²

Even with many advances in DNA tension probes, one major limitation of DNA tension probes is that the substrate utilized is too rigid and the tension measurement lacks

physiological relevance.^{101, 113} Given the biological tissues have substrate stiffness in the kPa range and glass substrate is tens of thousands fold more rigid. Incorporating these tension sensors in the soft substrate is therefore desirable in the field of molecular mechanobiology field. In Chapter-4, we describe how we created a hydrogel-based tension sensor to tackle this issue. This dissertation will describe the methods we developed to solve this challenge.

1.4 Functional cell sorting assays.

Separating and classifying cells from mixed and diverse samples is vital in several biology, biotechnology, and medicine areas. Cell classification is often utilized to refine cell samples into well-defined groups to increase productivity in research and development processes. Additionally, it serves as a critical step in various diagnostic and therapeutic procedures, such as separating hematopoietic stem cells for self-transplant treatments. The need to classify cells is rapidly growing to accommodate the isolation of rarer target populations, including circulating tumor cells, hematopoietic stem cells, and circulating fetal cells from the blood. Meanwhile, the increasing interest in personalized medicine and theragnostic, where treatments are customized based on patient diagnoses, further boosts the demand for rapid and efficient cell classification.^{114, 115}

The first commercially available cell classifier, using a method known as fluorescence-activated cell sorting (FACS), was invented in 1969 by Herzenberg and others. Shortly after its introduction, FACS was optimized and transformed into a useful technology that has now become the standard for modern cell classification devices. Today, FACS technologies are automated, sturdy, and capable of precise classification using multiple

morphological and fluorescent cell markers (such as cell surface labels, size, and granularity). These systems can also perform multiplexed detection, analysis, and classification speeds of up to 50,000 cells per second. Magnetic-activated cell sorting devices, which generally divide labeled cells from unlabeled cells using a permanent magnet in a column, are also widely used due to their rapid batch processing capabilities.

116

1.4.1 Mechanical cell sorting and its impact in the biological field.

The importance of developing new methods and technologies for cell separation, sorting, isolation, or enrichment has increased with the growth of precision medicine research. Precision medicine refers to treatments tailored to the unique characteristics of each patient, such as their genetic makeup or biomarker profile. For precision medicine to become a reality in medical practice, advances must be made in analyzing disease-related cells obtained from complex samples.¹¹⁷

Cell mechanics can serve as a biophysical marker that complements the biochemical profile of cells. Flow cytometry methods have been developed to measure cell deformation and provide insights into the mechanical properties of cells. However, these methods face a challenge because cell deformation is influenced by several parameters, including cell volume, membrane composition, cytoskeletal dynamics, and cell cycle. Molecular markers of mechanotransduction can help overcome this challenge by offering a more precise and informative approach to mechanophenotyping. While high-resolution fluorescence microscopy is currently used to detect molecular forces generated by cells,

there is a need for flow cytometry or FACS-like techniques that can tag cells based on the magnitude of molecular forces generated. Overall, the development of mechanophenotyping platforms that incorporate molecular markers of mechanotransduction would enhance our understanding of cell mechanics and facilitate clinical applications.

1.5 Scope and aim of the dissertation.

The development of DNA-based tension probes has significantly broadened our knowledge of how cell mechanics affect the essential biological process. We utilized these sensors to study different biological processes; however, muscle cell mechanotransduction and stem cell receptor forces and its implication on cell differentiation are poorly understood. Different techniques have been adopted to study cardiac cell mechanics and how the mechanical stiffness of the environment can modulate cell fate but only on a global scale. It is unknown how molecular rigidity can affect cell differentiation and maturation. There is also a need to utilize mechanical forces to sort and tag functional cells. It is vastly known that cell mechanics are different based on cellular function. Like how CMCs will exert weaker forces compared to CFs (cardiac fibroblasts). Using mechanical force as a cell tagging technique can open new avenues for mechano-molecular therapeutics. Current DNA-based force measurement techniques lack physiological relevance due to using glass-like platforms. In this dissertation, we aim to utilize previously published DNA probes to understand how molecular rigidity can induce and modulate muscle cell differentiation and maturation. We aim to answer the following questions: (1) If cardiomyocytes can sense pN forces exerted by integrin and if these forces can control and manipulate the functional maturation of CMCs (2) how can

we optimize those techniques to be used with primary and hiPSC derived cardiac cell types and receptors? (3) Can we develop techniques to sort cells from complex tissue types? (4) How can we utilize the tool kit to sort and separate different cells based on their mechanical property? (5) And lastly can we mimic the tissue environment and utilize PEG-based soft substrates to study integrin-mediated receptor forces?

During my Ph.D. research, I've developed and applied multiple techniques to fulfill the aims of this dissertation. More specifically,

In **Chapter 2**, I'll describe how receptor forces can affect CMC biology. We utilized irreversible tension probes with varying force thresholds (12-160 pN) and showed that early CMC maturation can detect and modulate its functional maturation based on integrin-ligand interaction. **Chapter 3** We will discuss the design and application of peeling probes in mechanotagging. In **Chapter 4**, I will discuss the hydrogel-based DNA tension matrix to measure cellular tension. Finally, **Chapter 5** will summarize the development of tension measurement and outline promising directions in future development and applications.

References

1. Noto, R. E.; Leavitt, L.; Edens, M. A., Physiology, Muscle. In *StatPearls*, Treasure Island (FL), 2022.
2. Mukund, K.; Subramaniam, S., Skeletal muscle: A review of molecular structure and function, in health and disease. *Wiley Interdiscip Rev Syst Biol Med* **2020**, *12* (1), e1462.
3. Schiaffino, S.; Reggiani, C., Fiber types in mammalian skeletal muscles. *Physiol Rev* **2011**, *91* (4), 1447-531.
4. Ripa, R.; George, T.; Sattar, Y., Physiology, Cardiac Muscle. In *StatPearls*, Treasure Island (FL), 2022.
5. Saxton, A.; Tariq, M. A.; Bordoni, B., Anatomy, Thorax, Cardiac Muscle. In *StatPearls*, Treasure Island (FL), 2022.
6. Lindskog, C.; Linne, J.; Fagerberg, L.; Hallstrom, B. M.; Sundberg, C. J.; Lindholm, M.; Huss, M.; Kampf, C.; Choi, H.; Liem, D. A.; Ping, P.; Varemo, L.; Mardinoglu, A.; Nielsen, J.; Larsson, E.; Ponten, F.; Uhlen, M., The human cardiac and skeletal muscle proteomes defined by transcriptomics and antibody-based profiling. *BMC Genomics* **2015**, *16* (1), 475.
7. Arackal, A.; Alsayouri, K., Histology, Heart. In *StatPearls*, Treasure Island (FL), 2022.
8. Dye, B.; Lincoln, J., The Endocardium and Heart Valves. *Cold Spring Harb Perspect Biol* **2020**, *12* (12).

9. Sebastiani, M.; Manfredi, A.; Ferri, C., Chapter 14 - Cardiac Involvement in Systemic Vasculitis. In *Handbook of Systemic Autoimmune Diseases*, Atzeni, F.; Doria, A.; Nurmohamed, M.; Pauletto, P., Eds. Elsevier: 2017; Vol. 14, pp 335-382.
10. Zhang, H.; Lui, K. O.; Zhou, B., Endocardial Cell Plasticity in Cardiac Development, Diseases and Regeneration. *Circ Res* **2018**, *122* (5), 774-789.
11. Burbaum, L.; Schneider, J.; Scholze, S.; Bottcher, R. T.; Baumeister, W.; Schwille, P.; Plitzko, J. M.; Jasnin, M., Molecular-scale visualization of sarcomere contraction within native cardiomyocytes. *Nat Commun* **2021**, *12* (1), 4086.
12. Barrick, S. K.; Greenberg, M. J., Cardiac myosin contraction and mechanotransduction in health and disease. *J Biol Chem* **2021**, *297* (5), 101297.
13. Lyon, R. C.; Zanella, F.; Omens, J. H.; Sheikh, F., Mechanotransduction in cardiac hypertrophy and failure. *Circ Res* **2015**, *116* (8), 1462-1476.
14. Brockman, J. M.; Salaita, K., Mechanical Proofreading: A General Mechanism to Enhance the Fidelity of Information Transfer Between Cells. *Frontiers in Physics* **2019**, *7* (14).
15. Liao, H.; Qi, Y.; Ye, Y.; Yue, P.; Zhang, D.; Li, Y., Mechanotransduction Pathways in the Regulation of Mitochondrial Homeostasis in Cardiomyocytes. *Front Cell Dev Biol* **2020**, *8*, 625089.
16. Israeli-Rosenberg, S.; Manso, A. M.; Okada, H.; Ross, R. S., Integrins and integrin-associated proteins in the cardiac myocyte. *Circ Res* **2014**, *114* (3), 572-586.
17. Ross, R. S.; Borg, T. K., Integrins and the myocardium. *Circ Res* **2001**, *88* (11), 1112-9.

18. Samarel, A. M., Costameres, focal adhesions, and cardiomyocyte mechanotransduction. *Am J Physiol Heart Circ Physiol* **2005**, 289 (6), H2291-301.
19. Hidalgo, C.; Donoso, P., Cell signaling. Getting to the heart of mechanotransduction. *Science* **2011**, 333 (6048), 1388-90.
20. Haack, T.; Abdelilah-Seyfried, S., The force within: endocardial development, mechanotransduction and signalling during cardiac morphogenesis. *Development* **2016**, 143 (3), 373-86.
21. Moiseeva, E. P., Adhesion receptors of vascular smooth muscle cells and their functions. *Cardiovascular Research* **2001**, 52 (3), 372-386.
22. Grskovic, M.; Javaherian, A.; Strulovici, B.; Daley, G. Q., Induced pluripotent stem cells--opportunities for disease modelling and drug discovery. *Nat Rev Drug Discov* **2011**, 10 (12), 915-29.
23. Duncker, D. J.; Bache, R. J., Regulation of coronary blood flow during exercise. *Physiol Rev* **2008**, 88 (3), 1009-86.
24. Fan, X.; Hughes, B. G.; Ali, M. A.; Cho, W. J.; Lopez, W.; Schulz, R., Dynamic Alterations to alpha-Actinin Accompanying Sarcomere Disassembly and Reassembly during Cardiomyocyte Mitosis. *PLoS One* **2015**, 10 (6), e0129176.
25. Ladha, F. A.; Thakar, K.; Pettinato, A. M.; Legere, N.; Cohn, R.; Romano, R.; Meredith, E.; Chen, Y.-S.; Hinson, J. T., Identifying cardiac actinin interactomes reveals sarcomere crosstalk with RNA-binding proteins. *bioRxiv* **2020**, 2020.03.18.994004.
26. Martin, T. G.; Myers, V. D.; Dubey, P.; Dubey, S.; Perez, E.; Moravec, C. S.; Willis, M. S.; Feldman, A. M.; Kirk, J. A., Cardiomyocyte contractile impairment in heart

failure results from reduced BAG3-mediated sarcomeric protein turnover. *Nat Commun* **2021**, *12* (1), 2942.

27. Hein, S.; Block, T.; Zimmermann, R.; Kostin, S.; Scheffold, T.; Kubin, T.; Klovekorn, W. P.; Schaper, J., Deposition of nonsarcomeric alpha-actinin in cardiomyocytes from patients with dilated cardiomyopathy or chronic pressure overload. *Exp Clin Cardiol* **2009**, *14* (3), e68-75.

28. Rodriguez, A. G.; Han, S. J.; Regnier, M.; Sniadecki, N. J., Substrate stiffness increases twitch power of neonatal cardiomyocytes in correlation with changes in myofibril structure and intracellular calcium. *Biophys J* **2011**, *101* (10), 2455-64.

29. Ribeiro, M. C.; Slaats, R. H.; Schwach, V.; Rivera-Arbelaez, J. M.; Tertoolen, L. G. J.; van Meer, B. J.; Molenaar, R.; Mummery, C. L.; Claessens, M.; Passier, R., A cardiomyocyte show of force: A fluorescent alpha-actinin reporter line sheds light on human cardiomyocyte contractility versus substrate stiffness. *J Mol Cell Cardiol* **2020**, *141*, 54-64.

30. Ribeiro, A. J.; Ang, Y. S.; Fu, J. D.; Rivas, R. N.; Mohamed, T. M.; Higgs, G. C.; Srivastava, D.; Pruitt, B. L., Contractility of single cardiomyocytes differentiated from pluripotent stem cells depends on physiological shape and substrate stiffness. *Proc Natl Acad Sci U S A* **2015**, *112* (41), 12705-10.

31. McCain, M. L.; Parker, K. K., Mechanotransduction: the role of mechanical stress, myocyte shape, and cytoskeletal architecture on cardiac function. *Pflugers Arch* **2011**, *462* (1), 89-104.

32. Pandey, P.; Hawkes, W.; Hu, J.; Megone, W. V.; Gautrot, J.; Anilkumar, N.; Zhang, M.; Hirvonen, L.; Cox, S.; Ehler, E.; Hone, J.; Sheetz, M.; Iskratsch, T.,

Cardiomyocytes Sense Matrix Rigidity through a Combination of Muscle and Non-muscle Myosin Contractions. *Dev Cell* **2018**, *44* (3), 326-336 e3.

33. Lipskaia, L.; Chemaly, E. R.; Hadri, L.; Lompre, A. M.; Hajjar, R. J., Sarcoplasmic reticulum Ca(2+) ATPase as a therapeutic target for heart failure. *Expert Opin Biol Ther* **2010**, *10* (1), 29-41.

34. Martewicz, S.; Serena, E.; Zatti, S.; Keller, G.; Elvassore, N., Substrate and mechanotransduction influence SERCA2a localization in human pluripotent stem cell-derived cardiomyocytes affecting functional performance. *Stem Cell Res* **2017**, *25*, 107-114.

35. Periasamy, M.; Kalyanasundaram, A., SERCA pump isoforms: their role in calcium transport and disease. *Muscle Nerve* **2007**, *35* (4), 430-42.

36. Grant, A. O., Cardiac ion channels. *Circ Arrhythm Electrophysiol* **2009**, *2* (2), 185-94.

37. Bers, D. M., Cardiac excitation-contraction coupling. *Nature* **2002**, *415* (6868), 198-205.

38. Chin, I. L.; Hool, L.; Choi, Y. S., A Review of in vitro Platforms for Understanding Cardiomyocyte Mechanobiology. *Front Bioeng Biotechnol* **2019**, *7*, 133.

39. Zhang, Y.; Su, S. A.; Li, W.; Ma, Y.; Shen, J.; Wang, Y.; Shen, Y.; Chen, J.; Ji, Y.; Xie, Y.; Ma, H.; Xiang, M., Piezo1-Mediated Mechanotransduction Promotes Cardiac Hypertrophy by Impairing Calcium Homeostasis to Activate Calpain/Calcineurin Signaling. *Hypertension* **2021**, *78* (3), 647-660.

40. Takahashi, K.; Kakimoto, Y.; Toda, K.; Naruse, K., Mechanobiology in cardiac physiology and diseases. *J Cell Mol Med* **2013**, *17* (2), 225-32.

41. Bernadzki, K. M.; Rojek, K. O.; Proszynski, T. J., Podosomes in muscle cells and their role in the remodeling of neuromuscular postsynaptic machinery. *Eur J Cell Biol* **2014**, *93* (10-12), 478-85.
42. Weber, K.; Hey, S.; Cervero, P.; Linder, S., The circle of life: Phases of podosome formation, turnover and reemergence. *Eur J Cell Biol* **2022**, *101* (2), 151218.
43. Hilenski, L. L.; Terracio, L.; Borg, T. K., Myofibrillar and cytoskeletal assembly in neonatal rat cardiac myocytes cultured on laminin and collagen. *Cell Tissue Res* **1991**, *264* (3), 577-87.
44. Guo, Y.; Pu, W. T., Cardiomyocyte Maturation: New Phase in Development. *Circ Res* **2020**, *126* (8), 1086-1106.
45. Sheehy, S. P.; Grosberg, A.; Parker, K. K., The contribution of cellular mechanotransduction to cardiomyocyte form and function. *Biomech Model Mechanobiol* **2012**, *11* (8), 1227-39.
46. Jacot, J. G.; McCulloch, A. D.; Omens, J. H., Substrate stiffness affects the functional maturation of neonatal rat ventricular myocytes. *Biophys J* **2008**, *95* (7), 3479-87.
47. Korner, A.; Mosqueira, M.; Hecker, M.; Ullrich, N. D., Substrate Stiffness Influences Structural and Functional Remodeling in Induced Pluripotent Stem Cell-Derived Cardiomyocytes. *Front Physiol* **2021**, *12*, 710619.
48. Querceto, S.; Santoro, R.; Gowran, A.; Grandinetti, B.; Pompilio, G.; Regnier, M.; Tesi, C.; Poggesi, C.; Ferrantini, C.; Pioner, J. M., The harder the climb the better the view: The impact of substrate stiffness on cardiomyocyte fate. *J Mol Cell Cardiol* **2022**, *166*, 36-49.

49. Kannan, S.; Kwon, C., Regulation of cardiomyocyte maturation during critical perinatal window. *J Physiol* **2020**, *598* (14), 2941-2956.
50. Byun, J.; Del Re, D. P.; Zhai, P.; Ikeda, S.; Shirakabe, A.; Mizushima, W.; Miyamoto, S.; Brown, J. H.; Sadoshima, J., Yes-associated protein (YAP) mediates adaptive cardiac hypertrophy in response to pressure overload. *J Biol Chem* **2019**, *294* (10), 3603-3617.
51. Del Re, D. P.; Yang, Y.; Nakano, N.; Cho, J.; Zhai, P.; Yamamoto, T.; Zhang, N.; Yabuta, N.; Nojima, H.; Pan, D.; Sadoshima, J., Yes-associated protein isoform 1 (Yap1) promotes cardiomyocyte survival and growth to protect against myocardial ischemic injury. *J Biol Chem* **2013**, *288* (6), 3977-88.
52. Corbin, E. A.; Vite, A.; Peyster, E. G.; Bhoopalam, M.; Brandimarto, J.; Wang, X.; Bennett, A. I.; Clark, A. T.; Cheng, X.; Turner, K. T.; Musunuru, K.; Margulies, K. B., Tunable and Reversible Substrate Stiffness Reveals a Dynamic Mechanosensitivity of Cardiomyocytes. *ACS Appl Mater Interfaces* **2019**, *11* (23), 20603-20614.
53. Liu, Y.; Yehl, K.; Narui, Y.; Salaita, K., Tension Sensing Nanoparticles for Mechano-Imaging at the Living/Nonliving Interface. *Journal of the American Chemical Society* **2013**, *135* (14), 5320-5323.
54. Liu, Y.; Galior, K.; Ma, V. P.-Y.; Salaita, K., Molecular Tension Probes for Imaging Forces at the Cell Surface. *Accounts of Chemical Research* **2017**, *50* (12), 2915-2924.
55. Huebsch, N.; Loskill, P.; Mandegar, M. A.; Marks, N. C.; Sheehan, A. S.; Ma, Z.; Mathur, A.; Nguyen, T. N.; Yoo, J. C.; Judge, L. M.; Spencer, C. I.; Chukka, A. C.; Russell, C. R.; So, P. L.; Conklin, B. R.; Healy, K. E., Automated Video-Based Analysis of Contractility and Calcium Flux in Human-Induced Pluripotent Stem Cell-Derived

Cardiomyocytes Cultured over Different Spatial Scales. *Tissue Eng Part C Methods* **2015**, *21* (5), 467-79.

56. Boothe, S. D.; Myers, J. D.; Pok, S.; Sun, J.; Xi, Y.; Nieto, R. M.; Cheng, J.; Jacot, J. G., The Effect of Substrate Stiffness on Cardiomyocyte Action Potentials. *Cell Biochem Biophys* **2016**, *74* (4), 527-535.

57. Dimarino, A. M.; Caplan, A. I.; Bonfield, T. L., Mesenchymal stem cells in tissue repair. *Front Immunol* **2013**, *4*, 201.

58. Naqvi, S. M.; McNamara, L. M., Stem Cell Mechanobiology and the Role of Biomaterials in Governing Mechanotransduction and Matrix Production for Tissue Regeneration. *Front Bioeng Biotechnol* **2020**, *8*, 597661.

59. Kwon, S. G.; Kwon, Y. W.; Lee, T. W.; Park, G. T.; Kim, J. H., Recent advances in stem cell therapeutics and tissue engineering strategies. *Biomater Res* **2018**, *22*, 36.

60. Nourian Dehkordi, A.; Mirahmadi Babaheydari, F.; Chehelgerdi, M.; Raeisi Dehkordi, S., Skin tissue engineering: wound healing based on stem-cell-based therapeutic strategies. *Stem Cell Res Ther* **2019**, *10* (1), 111.

61. Petzold, J.; Gentleman, E., Intrinsic Mechanical Cues and Their Impact on Stem Cells and Embryogenesis. *Front Cell Dev Biol* **2021**, *9*, 761871.

62. D'Angelo, F.; Tiribuzi, R.; Armentano, I.; Kenny, J. M.; Martino, S.; Orlicchio, A., Mechanotransduction: tuning stem cells fate. *J Funct Biomater* **2011**, *2* (2), 67-87.

63. Raman, N.; Imran, S. A. M.; Ahmad Amin Noordin, K. B.; Zaman, W.; Nordin, F., Mechanotransduction in Mesenchymal Stem Cells (MSCs) Differentiation: A Review. *Int J Mol Sci* **2022**, *23* (9).

64. Gerardo, H.; Lima, A.; Carvalho, J.; Ramos, J. R. D.; Couceiro, S.; Travasso, R. D. M.; Pires das Neves, R.; Graos, M., Soft culture substrates favor stem-like cellular phenotype and facilitate reprogramming of human mesenchymal stem/stromal cells (hMSCs) through mechanotransduction. *Sci Rep* **2019**, *9* (1), 9086.
65. Schmidt, S.; Lilienkampf, A.; Bradley, M., New substrates for stem cell control. *Philos Trans R Soc Lond B Biol Sci* **2018**, *373* (1750).
66. Eroshenko, N.; Ramachandran, R.; Yadavalli, V. K.; Rao, R. R., Effect of substrate stiffness on early human embryonic stem cell differentiation. *J Biol Eng* **2013**, *7* (1), 7.
67. Hamouda, M. S.; Labouesse, C.; Chalut, K. J., Nuclear mechanotransduction in stem cells. *Curr Opin Cell Biol* **2020**, *64*, 97-104.
68. Witkowska-Zimny, M.; Walenko, K.; Wrobel, E.; Mrowka, P.; Mikulska, A.; Przybylski, J., Effect of substrate stiffness on the osteogenic differentiation of bone marrow stem cells and bone-derived cells. *Cell Biol Int* **2013**, *37* (6), 608-16.
69. Kang, E. S.; Kim, D. S.; Suhito, I. R.; Lee, W.; Song, I.; Kim, T. H., Two-dimensional material-based bionano platforms to control mesenchymal stem cell differentiation. *Biomater Res* **2018**, *22*, 10.
70. El-Rashidy, A. A.; El Moshy, S.; Radwan, I. A.; Rady, D.; Abbass, M. M. S.; Dorfer, C. E.; Fawzy El-Sayed, K. M., Effect of Polymeric Matrix Stiffness on Osteogenic Differentiation of Mesenchymal Stem/Progenitor Cells: Concise Review. *Polymers (Basel)* **2021**, *13* (17).

71. Yuan, H.; Zhou, Y.; Lee, M. S.; Zhang, Y.; Li, W. J., A newly identified mechanism involved in regulation of human mesenchymal stem cells by fibrous substrate stiffness. *Acta Biomater* **2016**, *42*, 247-257.
72. Rowlands, A. S.; George, P. A.; Cooper-White, J. J., Directing osteogenic and myogenic differentiation of MSCs: interplay of stiffness and adhesive ligand presentation. *Am J Physiol Cell Physiol* **2008**, *295* (4), C1037-44.
73. Gilbert, P. M.; Havenstrite, K. L.; Magnusson, K. E.; Sacco, A.; Leonardi, N. A.; Kraft, P.; Nguyen, N. K.; Thrun, S.; Lutolf, M. P.; Blau, H. M., Substrate elasticity regulates skeletal muscle stem cell self-renewal in culture. *Science* **2010**, *329* (5995), 1078-81.
74. Beussman, K. M.; Rodriguez, M. L.; Leonard, A.; Taparia, N.; Thompson, C. R.; Sniadecki, N. J., Micropost arrays for measuring stem cell-derived cardiomyocyte contractility. *Methods* **2016**, *94*, 43-50.
75. Yang, M. T.; Fu, J.; Wang, Y. K.; Desai, R. A.; Chen, C. S., Assaying stem cell mechanobiology on microfabricated elastomeric substrates with geometrically modulated rigidity. *Nat Protoc* **2011**, *6* (2), 187-213.
76. Devine, D.; Vijayakumar, V.; Wong, S. W.; Lenzini, S.; Newman, P.; Shin, J. W., Hydrogel Micropost Arrays with Single Post Tunability to Study Cell Volume and Mechanotransduction. *Adv Biosyst* **2020**, *4* (11), e2000012.
77. Vining, K. H.; Mooney, D. J., Mechanical forces direct stem cell behaviour in development and regeneration. *Nat Rev Mol Cell Biol* **2017**, *18* (12), 728-742.
78. Yamada, K. M.; Doyle, A. D.; Lu, J., Cell-3D matrix interactions: recent advances and opportunities. *Trends Cell Biol* **2022**, *32* (10), 883-895.

79. Franck, C.; Maskarinec, S. A.; Tirrell, D. A.; Ravichandran, G., Three-dimensional traction force microscopy: a new tool for quantifying cell-matrix interactions. *PLoS One* **2011**, *6* (3), e17833.
80. Yang, B.; Wei, K.; Loebel, C.; Zhang, K.; Feng, Q.; Li, R.; Wong, S. H. D.; Xu, X.; Lau, C.; Chen, X.; Zhao, P.; Yin, C.; Burdick, J. A.; Wang, Y.; Bian, L., Enhanced mechanosensing of cells in synthetic 3D matrix with controlled biophysical dynamics. *Nat Commun* **2021**, *12* (1), 3514.
81. Zonderland, J.; Moroni, L., Steering cell behavior through mechanobiology in 3D: A regenerative medicine perspective. *Biomaterials* **2021**, *268*, 120572.
82. Baker, B. M.; Chen, C. S., Deconstructing the third dimension: how 3D culture microenvironments alter cellular cues. *J Cell Sci* **2012**, *125* (Pt 13), 3015-24.
83. Kolb, P.; Schundner, A.; Frick, M.; Gottschalk, K. E., In Vitro Measurements of Cellular Forces and their Importance in the Lung-From the Sub- to the Multicellular Scale. *Life (Basel)* **2021**, *11* (7).
84. Polacheck, W. J.; Chen, C. S., Measuring cell-generated forces: a guide to the available tools. *Nat Methods* **2016**, *13* (5), 415-23.
85. Maskarinec, S. A.; Franck, C.; Tirrell, D. A.; Ravichandran, G., Quantifying cellular traction forces in three dimensions. *Proc Natl Acad Sci U S A* **2009**, *106* (52), 22108-13.
86. Javanmardi, Y.; Colin-York, H.; Szita, N.; Fritzsche, M.; Moeendarbary, E., Quantifying cell-generated forces: Poisson's ratio matters. *Commun Phys* **2021**, *4*, 237.
87. Sugimura, K.; Lenne, P. F.; Graner, F., Measuring forces and stresses in situ in living tissues. *Development* **2016**, *143* (2), 186-96.

88. Lekka, M.; Gnanachandran, K.; Kubiak, A.; Zielinski, T.; Zemla, J., Traction force microscopy - Measuring the forces exerted by cells. *Micron* **2021**, *150*, 103138.
89. Huang, Y.; Schell, C.; Huber, T. B.; Simsek, A. N.; Hersch, N.; Merkel, R.; Gompper, G.; Sabass, B., Traction force microscopy with optimized regularization and automated Bayesian parameter selection for comparing cells. *Sci Rep* **2019**, *9* (1), 539.
90. Schwarz, U. S.; Soine, J. R., Traction force microscopy on soft elastic substrates: A guide to recent computational advances. *Biochim Biophys Acta* **2015**, *1853* (11 Pt B), 3095-104.
91. Style, R. W.; Boltyanskiy, R.; German, G. K.; Hyland, C.; MacMinn, C. W.; Mertz, A. F.; Wilen, L. A.; Xu, Y.; Dufresne, E. R., Traction force microscopy in physics and biology. *Soft Matter* **2014**, *10* (23), 4047-55.
92. Zancla, A.; Mozetic, P.; Orsini, M.; Forte, G.; Rainer, A., A primer to traction force microscopy. *J Biol Chem* **2022**, *298* (5), 101867.
93. Cheng, Q.; Sun, Z.; Meininger, G.; Almasri, M., PDMS Elastic Micropost Arrays for Studying Vascular Smooth Muscle Cells. *Sens Actuators B Chem* **2013**, *188*, 1055-1063.
94. Sniadecki, N. J.; Anguelouch, A.; Yang, M. T.; Lamb, C. M.; Liu, Z.; Kirschner, S. B.; Liu, Y.; Reich, D. H.; Chen, C. S., Magnetic microposts as an approach to apply forces to living cells. *Proc Natl Acad Sci U S A* **2007**, *104* (37), 14553-8.
95. Schoen, I.; Hu, W.; Klotzsch, E.; Vogel, V., Probing cellular traction forces by micropillar arrays: contribution of substrate warping to pillar deflection. *Nano Lett* **2010**, *10* (5), 1823-30.

96. Shi, Y.; Sivarajan, S.; Crocker, J. C.; Reich, D. H., Measuring Cytoskeletal Mechanical Fluctuations and Rheology with Active Micropost Arrays. *Curr Protoc* **2022**, 2 (5), e433.
97. Liu, Y.; Galior, K.; Ma, V. P.; Salaita, K., Molecular Tension Probes for Imaging Forces at the Cell Surface. *Acc Chem Res* **2017**, 50 (12), 2915-2924.
98. Ma, V. P.; Salaita, K., DNA Nanotechnology as an Emerging Tool to Study Mechanotransduction in Living Systems. *Small* **2019**, 15 (26), e1900961.
99. Wang, X.; Ha, T., Defining single molecular forces required to activate integrin and notch signaling. *Science* **2013**, 340 (6135), 991-4.
100. Zhang, Y.; Qiu, Y.; Blanchard, A. T.; Chang, Y.; Brockman, J. M.; Ma, V. P.; Lam, W. A.; Salaita, K., Platelet integrins exhibit anisotropic mechanosensing and harness piconewton forces to mediate platelet aggregation. *Proc Natl Acad Sci U S A* **2018**, 115 (2), 325-330.
101. Ma, R.; Kellner, A. V.; Ma, V. P.-Y.; Su, H.; Deal, B. R.; Brockman, J. M.; Salaita, K., DNA probes that store mechanical information reveal transient piconewton forces applied by T cells. *Proceedings of the National Academy of Sciences* **2019**, 116 (34), 16949-16954.
102. Liu, Y.; Medda, R.; Liu, Z.; Galior, K.; Yehl, K.; Spatz, J. P.; Cavalcanti-Adam, E. A.; Salaita, K., Nanoparticle tension probes patterned at the nanoscale: impact of integrin clustering on force transmission. *Nano Lett* **2014**, 14 (10), 5539-46.
103. Galior, K.; Liu, Y.; Yehl, K.; Vivek, S.; Salaita, K., Titin-Based Nanoparticle Tension Sensors Map High-Magnitude Integrin Forces within Focal Adhesions. *Nano Lett* **2016**, 16 (1), 341-8.

104. Galior, K.; Ma, V. P.; Liu, Y.; Su, H.; Baker, N.; Panettieri, R. A., Jr.; Wongtrakool, C.; Salaita, K., Molecular Tension Probes to Investigate the Mechanopharmacology of Single Cells: A Step toward Personalized Mechanomedicine. *Adv Healthc Mater* **2018**, *7* (14), e1800069.
105. Dutta, P. K.; Zhang, Y.; Blanchard, A. T.; Ge, C.; Rushdi, M.; Weiss, K.; Zhu, C.; Ke, Y.; Salaita, K., Programmable multivalent DNA-origami tension probes for reporting cellular traction forces. *Nano letters* **2018**, *18* (8), 4803-4811.
106. Glazier, R.; Brockman, J. M.; Bartle, E.; Mattheyses, A. L.; Destaing, O.; Salaita, K., DNA mechanotechnology reveals that integrin receptors apply pN forces in podosomes on fluid substrates. *Nature Communications* **2019**, *10* (1), 4507.
107. Zhao, Y.; Sarkar, A.; Wang, X., Peptide nucleic acid based tension sensor for cellular force imaging with strong DNase resistance. *Biosensors and Bioelectronics* **2020**, *150*, 111959.
108. Brockman, J. M.; Su, H.; Blanchard, A. T.; Duan, Y.; Meyer, T.; Quach, M. E.; Glazier, R.; Bazrafshan, A.; Bender, R. L.; Kellner, A. V.; Ogasawara, H.; Ma, R.; Schueder, F.; Petrich, B. G.; Jungmann, R.; Li, R.; Mattheyses, A. L.; Ke, Y.; Salaita, K., Live-cell super-resolved PAINT imaging of piconewton cellular traction forces. *Nature Methods* **2020**, *17* (10), 1018-1024.
109. Bender, R. L.; Ogasawara, H.; Kellner, A. V.; Velusamy, A.; Salaita, K., Unbreakable DNA tension probes show that cell adhesion receptors detect the molecular force-extension curve of their ligands. *bioRxiv* **2022**, 2022.04.04.487040.
110. Baek, K. Y.; Kim, S.; Koh, H. R., Molecular Tension Probes to Quantify Cell-Generated Mechanical Forces. *Mol Cells* **2022**, *45* (1), 26-32.

111. Liu, J.; Le, S.; Yao, M.; Huang, W.; Tio, Z.; Zhou, Y.; Yan, J., Tension Gauge Tethers as Tension Threshold and Duration Sensors. *ACS Sens* **2023**.
112. Liu, J.; Le, S.; Yao, M.; Huang, W.; Tio, Z.; Zhou, Y.; Yan, J., The mechanical stability of Tension Gauge Tethers. *bioRxiv* **2022**, 2022.03.11.483943.
113. Gaudet, C.; Marganski, W. A.; Kim, S.; Brown, C. T.; Gunderia, V.; Dembo, M.; Wong, J. Y., Influence of type I collagen surface density on fibroblast spreading, motility, and contractility. *Biophys J* **2003**, *85* (5), 3329-35.
114. Sun, G.; Teng, Y.; Zhao, Z.; Cheow, L. F.; Yu, H.; Chen, C. H., Functional Stem Cell Sorting via Integrative Droplet Synchronization. *Anal Chem* **2020**, *92* (11), 7915-7923.
115. Rabinovitch, P. S.; Robinson, J. P., Overview of functional cell assays. *Curr Protoc Cytom* **2002**, *Chapter 9*, Unit 9 1.
116. Miwa, H.; Dimatteo, R.; de Rutte, J.; Ghosh, R.; Di Carlo, D., Single-cell sorting based on secreted products for functionally defined cell therapies. *Microsyst Nanoeng* **2022**, *8*, 84.
117. Castagnola, S.; Cazareth, J.; Lebrigand, K.; Jarjat, M.; Magnone, V.; Delhay, S.; Brau, F.; Bardoni, B.; Maurin, T., Agonist-induced functional analysis and cell sorting associated with single-cell transcriptomics characterizes cell subtypes in normal and pathological brain. *Genome Res* **2020**, *30* (11), 1633-1642.

Chapter 2: DNA nanotechnology shows cardiac muscle cells maturation is sensitive to pN force exerted by integrins.

Dr. Blanchard helped with automatic Calcium analysis. Dale Combs contributed with actinin puncta analysis. Dr. Dong helped with one control experiment with CMCs on gel matrix. Dr. Cho lab provided the primary cells for this study and Natasha helped with cell isolation. More detailed Authors contribution for the manuscript can be found in acknowledgement section.

This chapter is adapted from DNA tension probes, show that cardiomyocyte maturation is sensitive to the pN traction forces transmitted by integrins; Rashid, Sk Aysha; Blanchard, Aaron; Combs, J Dale; Dong, Yixiao Fernandez, Natasha; Cho, Hee Cheol ; and Salaita, Khalid*; *ACS Nano*, 2022 with permission.

2.1 Abstract

Cardiac muscle cells (CMCs) are the unit cells that comprise the heart. CMCs go through different stages of differentiation and maturation pathways to fully mature into beating cells. These cells can sense and respond to mechanical cues through receptors such as integrins which influence maturation pathways. For example, cell traction forces are important for the differentiation and development of functional CMCs, as CMCs cultured on varying substrate stiffness function differently. Most work in this area has focused on understanding the role of bulk ECM (extracellular matrix) stiffness in mediating the functional fate of CMC. Since stiffness sensing mechanisms are mediated by individual integrin receptors, an essential question in this area pertains to the specific magnitude of integrin piconewton (pN) forces that can trigger CMC functional maturation. To address this knowledge gap, we used DNA adhesion tethers that rupture at specific thresholds of force (~12, ~56, and ~160 pN) to test whether capping peak integrin tension to specific magnitudes affects CMC function. The work shows that adhesion tethers with greater force tolerance led to functionally mature CMCs as determined by morphology, twitching frequency, transient calcium flux measurements, and protein expression (F-actin, vinculin, α -actinin, YAP, and SERCA2). Additionally, sarcomeric actinin alignment and multinucleation were significantly enhanced as the mechanical tolerance of integrin tethers was increased. Taken together, the results show that CMCs harness defined pN integrin forces to influence early-stage development. This study represents an essential step toward the biophysical characterization of the contribution of pN forces in early-stage cardiac differentiation.

2.2 Introduction

The development of the heart is a complex and dynamic process that can be categorized into two main phases. The first is the differentiation of neonatal stem cells into various cardiac cell lineages such as cardiac progenitor cells and crescent cells.¹⁻³ The second is the subsequent maturation of these lineages into functional cells such as fibroblasts and different types of mature cardiac muscle cells (CMCs) that achieve rhythmic beating.⁴ Maturation is the final phase of this dynamic process where the CMCs undergo extensive structural, functional and metabolic changes as the heart develops from the fetal to adult stage.⁵⁻⁷ Developing a fundamental understanding of CMC maturation is important as it impacts many areas, including developing therapies to treat heart disease. For example, during a major cardiac insult, the heart can lose an enormous number of cardiomyocytes.⁸ As a treatment, current therapeutic strategies are heavily focused on repairing the damaged tissue using cardiac lineage stem cells.⁹⁻¹¹ However, this approach tends to exhibit limited efficacy because only a small fraction (~3%) of the therapeutic stem cells mature appropriately.^{12, 13} The mechanisms of CMC maturation remain unclear and hence, a major motivation for studying this process is to improve CMC potency as a therapeutic for myocardial regeneration.¹⁴⁻¹⁷

A key area of particular interest is understanding how physical and biochemical cues can alter and influence CMC developmental fate.¹⁸⁻²⁰ While there is a significant body of literature investigating how different chemical cues can modulate CMC fate, there is relatively less known about the role of mechanical cues in controlling maturation despite evidence that it influences the development and function of heart tissue.^{4,11, 21} Irregularities in mechanotransduction can result in stiffening of the cardiac tissue, a

precursor to multiple cardiac diseases, such as cardiac fibrosis, congenital heart defects, and arrhythmia.^{14, 22} Therefore, developing tools to understand better how mechanical cues modulate CMC function is critical to improving the efficacy of stem-cell-based therapeutics.

Prior studies of neonatal rat ventricular muscle (NRVM) cells, a subtype of CMC, have reported that CMCs display greater yields of functional maturation showing higher peak calcium, aligned sarcomeres, and higher expression of the associated proteins on surfaces with the appropriate Young's modulus^{19, 23-29}. One of the most studied markers of maturation is the sarcomere, the fundamental unit of mechanical contractility in CMCs. Each mature sarcomere consists of actin filaments and sarcomeric α -actinin proteins, with elongated and aligned z-lines.^{19,23,30} Another marker of CMC maturation is the SERCA-2A calcium pump which tunes the rate of calcium transport and hence the amplitude and frequency of calcium transients. These reports show a link between substrate stiffness and CMC function indicating the importance of adhesion receptor mechanotransduction in CMC maturation.^{31, 32}

To study how mechanical cues influence CMC maturation, the field has generally measured CMCs maturation for cells grown on hydrogels of differing stiffness.^{16,20} This past work showed “goldilocks” like relation between substrate stiffness and CMC maturation, where intermediate levels of substrate stiffness enhance functional maturation of CMCs.^{18,16,24} For example, NRVM cells cultured on PDMS gels matured optimally when the substrate stiffness was 10-20 kPa as quantified using different markers such as, CMC morphology, SERCA-2A, YAP and myosin heavy chain (MHC) expression as well as sarcomeric organization and Ca^{2+} signaling.^{15,24,40} This

demonstrates how tuning bulk mechanical properties, like stiffness, controls cardiomyocyte maturation through a mechanosensing response. However, all past work in this area has focused on tuning the bulk mechanical properties of the substrate and it remains unknown how the force magnitude transmitted through individual adhesion receptors contributes to the events of CMC maturation.^{19, 23, 32, 33} Therefore, a remaining challenge in this area is to manipulate the traction forces applied by CMCs with molecular resolution (piconewton, pN) and to study how these individual molecular forces modulate maturation.

Here, we address this challenge by using cell adhesion ligands that can rupture mechanically at different thresholds. We use variants of the tension gauge tether (TGT) and the biotin-streptavidin rupture tether to control the maximum threshold of integrin tension and to study how these thresholds control CMC maturation.^{30, 31, 34, 35} We find that CMC integrins show sensitivity to pN forces ranging from ~12 pN -160 pN, thereby modulating their maturation fate. The findings suggest that CMCs can sense pN forces through their adhesion receptors, and threshold forces that exceed 12 pN lead to functional maturation, elongated morphology, synchronized twitching and more coordinated Ca^{2+} peaks. Integrin threshold forces greater than 12 pN also lead to increased expression of proteins associated with contractility such as SERCA and YAP. This report represents a step toward studying the relationship of pN integrin forces and functional maturation of cardiomyocytes.

2.3 Results and Discussion

2.3.1 DNA probes to control CMC integrin tension.

The rupture probes we used here comprise a DNA duplex anchored to a surface using a “bottom” oligonucleotide that is complementary to a “top” strand presenting an integrin ligand. In this work, we used the cyclic arginine-glycine-aspartic acid-*D*-phenylalanine-lysine (cRGDfK) ligand (**Figure 2.1b**) which mimics fibronectin and primarily binds to the $\alpha_5\beta_1$ integrin receptors. These integrin receptors are highly expressed by neonatal cardiomyocytes and shown to be important for development and growth.³⁶⁻³⁹ Additionally neonatal cardiomyocytes display the greatest adhesion to fibronectin compared to that of collagen and laminin.⁴⁰ Therefore, the cRGDfK peptide (referred to as the RGD-ligand) was ideally suited for our current investigation of neonatal cardiomyocytes. When the rupture probes experience mechanical forces that exceed its tension tolerance (T_{tol}), the DNA duplex will rupture, thus terminating the mechanotransduction between the integrin and ligand. In this way, the rupture probes cap the maximum tension experienced by the integrin receptor. Importantly, the magnitude of the T_{tol} is time-dependent and can be tuned from ~12 pN up to ~56 pN (for a 2 sec force duration) by changing the location of the anchoring group on the bottom strand relative to the ligand position on the top strand (**Figure 2.1**).³⁰ For example, TGT probes with the ligand and the anchoring groups on the same terminus of the duplex have a $T_{\text{tol}} = 12$ pN, while shearing probes that present the ligand and anchoring groups on opposite ends of the duplex display a $T_{\text{tol}} = 56$ pN (**Figure 1a**). To record probe rupture events, we conjugated the anchor strand with a fluorophore (Cy3b), while the ligand strand was conjugated with a quencher (BHQ2) (**Figure S1 &**

S2, Supplementary table-1,2). With this fluorophore-quencher pair, mechanical melting of the duplex results in a turn-on signal with a 10-fold enhancement in fluorescence intensity (**Figure S3**).³¹ This fluorescence intensity reports on the accumulation of mechanical events with $F > T_{\text{tol}}$. To extend the T_{tol} to greater values, we designed another type of duplex where the RGD-ligand strand is directly anchored to the surface. Because the probe is anchored using biotin-streptavidin we estimate an effective T_{tol} (2 sec) of ~160 pN (**Figure 2.1c**).⁴¹ All three types of DNA probes surfaces were prepared from streptavidin-modified glass slides and yielded nearly identical probe densities of ~1400 molecules/mm² (**Figure S4**). Most prior studies using TGTs use T_{tol} values estimated using a 2 sec duration. Still, in our case, given that CMC maturation occurs over longer durations (~hrs), we plotted the expected T_{tol} for longer time durations in **Figure 2.1c (SI methods 1)**. Assuming that the applied force magnitude is steady, the 2 sec T_{tol} of 12, 56, and 160 pN reported previously are shifted to 6, 28, and 80 pN, respectively, for the 1000 sec time duration. We still refer to the 2 sec T_{tol} values in the text for clarity, but with the understanding that the actual applied forces may vary drastically based on the mechanical history of the bond given that cell forces are highly dynamic.

2.3.2 Cardiomyocytes display elongated morphology with integrin-ligand tension > 12pN.

In our work, we used neonatal rat CMCs as a model for CMC maturation. This is a well-studied and established model of CMC maturation.^{4,19,23,24} We first used CMC morphology

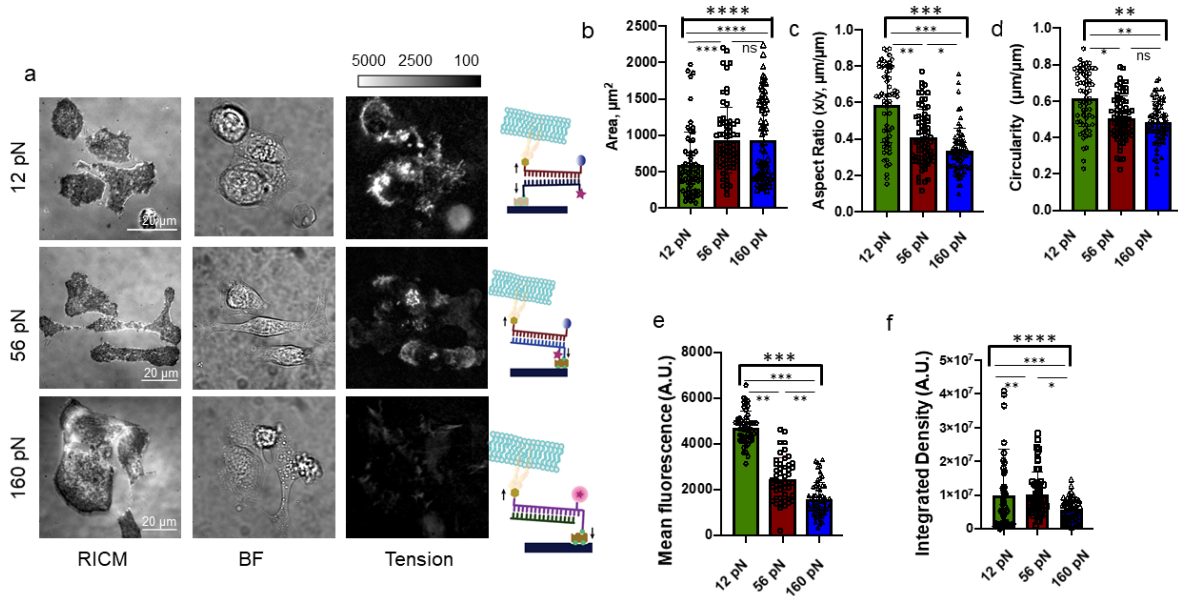


Figure 2.2. Cardiomyocytes display elongated morphology with integrin-ligand tension > 12pN. (a) CMCs on 12, 56, and 160 pN rupture probe surfaces, the leftmost panel (RICM) channel shows the outline of the attached cells, middle panel (Bright Field), TRITC channel shows the signal increase of Cy3B Fluorescence due to probe rupture for 12 and 56 pN probes and the inverted fluorescence loss for 160 pN probes.(t=6-8hrs) (b-f) Bar graphs show the spread area, aspect ratio (x/y), circularity, mean fluorescent under the cells, and integrated fluorescent density obtained from CMCs that were cultured on 12, 56, and 160 pN probes. Each data point represents a single cell while the bar shows the average. ****, ***, **, *, and ns indicate p<0.0001, p<0.001, p<0.01, p<0.05, and not significant respectively, as determined from one-way ANOVA. Error bars show the standard deviation for N>3, where each experiment was averaged from three or more different cell isolations with three different sets of surface preparations. Scale bar= 20 μm

as an indicator of maturation. This is because CMCs spreading area and cell shape are correlated with maturation. CMCs grow by elongating,^{19,21} which facilitates the arrangement of contractile proteins in CMCs and results in enhanced contraction capabilities.^{4,11} Moreover, the morphology of CMCs is easily measured and strongly correlated to their maturation and fate.

Initially, we screened the seeding density of these cells to identify an optimal density of 38,000-45,000 cells/cm². Images were taken at 2 hrs. intervals to measure spreading and the initiation of beating/twitching. To investigate the influence of morphology on cell function we waited for the cardiac cells to start beating and imaged cells to measure the spread area, aspect ratio, and circularity (**Figure 2.1 a-d**). We observed that CMCs display twitching ~6-8 hrs. after seeding on these rupture probe surfaces regardless of T_{tol} and used this time point to measure cell morphology. We found that cells adhered poorly on the 12 pN T_{tol} surface compared to the 56 and 160 pN probe surfaces and we generally found fewer attached cells on the 12 pN surfaces (**Figure 2.2a**). Moreover, cells were more elongated on 56 and 160 pN surfaces and had an average spreading area of 700 μm^2 , significantly greater (ANOVA, $P < 0.001$) than cells on 12 pN substrates (**Figure 2.2b**). Aspect ratio and circularity measurements confirmed that CMCs were more elongated on the 56 and 160 pN surfaces compared to the 12 pN surface (**Figures 2.2c and 2.2c**).

We also measured the fluorescence intensity under each cell as a quantitative readout of the accumulated mechanical events where $F > T_{tol}$ under the cell (**Figure S5**). Note that this signal is a lower bound estimate of the tension signal as there is DNA loss due to the

activity of nucleases³⁵, proteases, and the inherent k_{off} rate of biotin-streptavidin⁴¹ (**Figure S6**). Representative fluorescence images show that the weaker 12-pN rupture probe displayed more excellent fluorescence and dissociation (2.5-fold difference) than the 56-pN rupture probes (**Figure 2.2e**). For the 160 pN probes, we fluorescently tagged the biotinylated strand; hence, the readout is a loss of signal due to the disassociation of the biotin-streptavidin bond (**Figures 2.2e and 2.2f**).³¹ We observed CMCs reach the tension threshold before they started twitching. They reached maximum rupture events after 4-6 hours of incubation (**Figure S7**). In general, we found that the spatial distribution of integrin tension for the 56 pN rupture probes was localized at the center of the cells in fluorescent tension puncta (**Figure 2.2a**), with nuclear staining showing the location to be around the nucleus (**Figure S8**). The tension signal seems inconsistent with the cytoskeleton and adhesion structures because DNA probe rupture is irreversible, hence the tension signal represents a history of past mechanical events (**Figure S9**).

To confirm that the change in morphology and tension is due to integrin mechanotransduction, we treated the cells with eptifibatide, RGD binding integrin inhibitor⁴², for 30 mins before seeding. The cells had no difference in morphology, and their tension was significantly reduced (70-75%) (**Figure S10**) suggesting the phenomena observed here are directly connected with integrin Mechanotransduction. To evaluate the role of the ROCK and myosin II pathways we treated the cells with y-27632(Rho kinase inhibitor) and blebbistatin (myosin II inhibitor). Treated CMCs had similar morphology and significantly lower tension and contractility (**Figure S11 & S12**). We also investigated the effect of ligand density in force sensing of CMC by controlling the ligand density (**Figure S13**). This experiment confirmed the ligand loss or differential ligand density between 12,

56, 160 pN surfaces is not the major reason for poor attachment or differences in functional maturation of CMCs on 12 pN surfaces.

2.3.3 Cardiomyocytes display contractile behavior and calcium profiles consistent with greater maturation on surfaces with $T_{\text{tol}} = 56$ and 160 pN

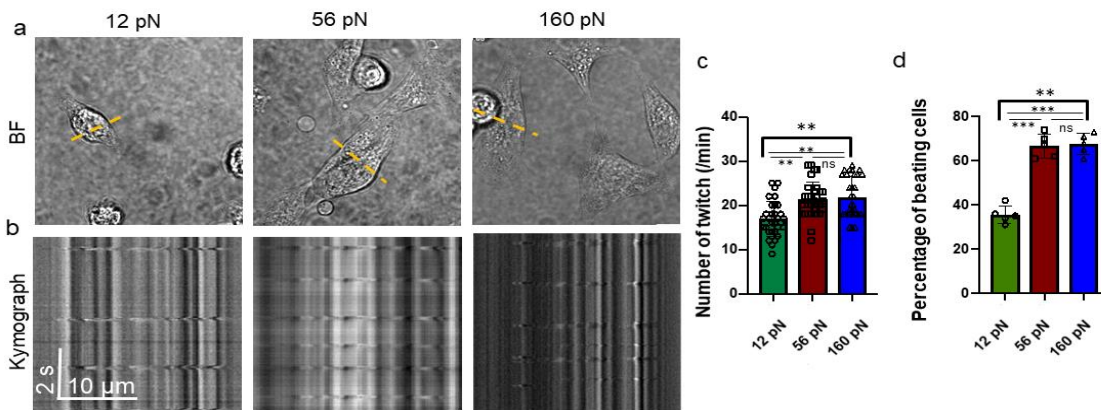


Figure 2.3. Cardiomyocytes display contractile profile consistent with greater maturation on surfaces with $T_{\text{tol}} = 56$ and 160 pN (a) Brightfield images from time-lapse of cardiomyocytes twitching on different probes ($t = 8-10$ hrs), dashed yellow line shows the major axis of Kymograph, (b) Kymographs of representative cells along the yellow dashed line. the y-axis of the graphs is elapsed time (t), and x shows the displacement, $t = 2$ s, $x = 10 \mu\text{m}$, (c) Bar graphs showing the average number of twitches per cell where for each replicate. Ten 1 min long videos were analyzed in BF, the error bar shows the standard deviation for $N=3$. Error bar shows standard deviation for $N=3$. ****, ***, **, * and ns indicate $p < 0.0001$, $p < 0.001$, $p < 0.01$, $p < 0.05$ and not significant respectively, as determined from one-way ANOVA. (d) Bar graph shows the percentage of attached cells measured from 11 videos per replicate and was calculated by the percentage of cells that had contractility, error bar shows the standard error of the mean for $N=5$. Scale bar= $10 \mu\text{m}$.

Compared to other muscle cells, cardiac muscle cells are unique in their ability to generate synchronized beating and spontaneous twitching. As CMC matures, the magnitude and frequency of beating increase. Hence, the twitching profile of CMCs is often used as another parameter to quantify maturation.^{24, 25} To characterize twitching rate in our experiments, neonatal rat cardiomyocytes were plated on rupture surfaces with different T_{tol} . Cells displayed spontaneous twitching on all rupture probe surfaces tested at 8 hrs. after seeding. However, we did note that spontaneous twitching could be observed at shorter time points (4-6 hrs.) for $T_{\text{tol}} = 56$ and 160 pN. Twitch frequency for individual cells were measured using kymographs obtained from time-lapse videos of CMCs (**Figure 23a, b**). The axis of twitching was assigned based on the direction of the twitch, which was typically the long axis of the cells, then the twitch frequency was calculated by measuring the time interval of contraction and dividing it by the time frame (**Figure S14**). We found that CMCs have higher twitching frequency on 56 and 160 pN (**Figure 2.3c**) surfaces. Moreover, a significantly (ANOVA, $P < 0.005$) greater population of CMCs were twitching and exhibited spontaneous beating (synchronized twitching

within neighboring cells) on the 56 pN and 160 pN rupture probe compared to 12 pN substrates (**Figure 3d and SI Video 1-3**).

Calcium (Ca^{2+}) is a critical intrinsic modulator of functional cardiomyocytes and plays a role in connecting the electrical signals which illicit muscle contraction and rhythmic

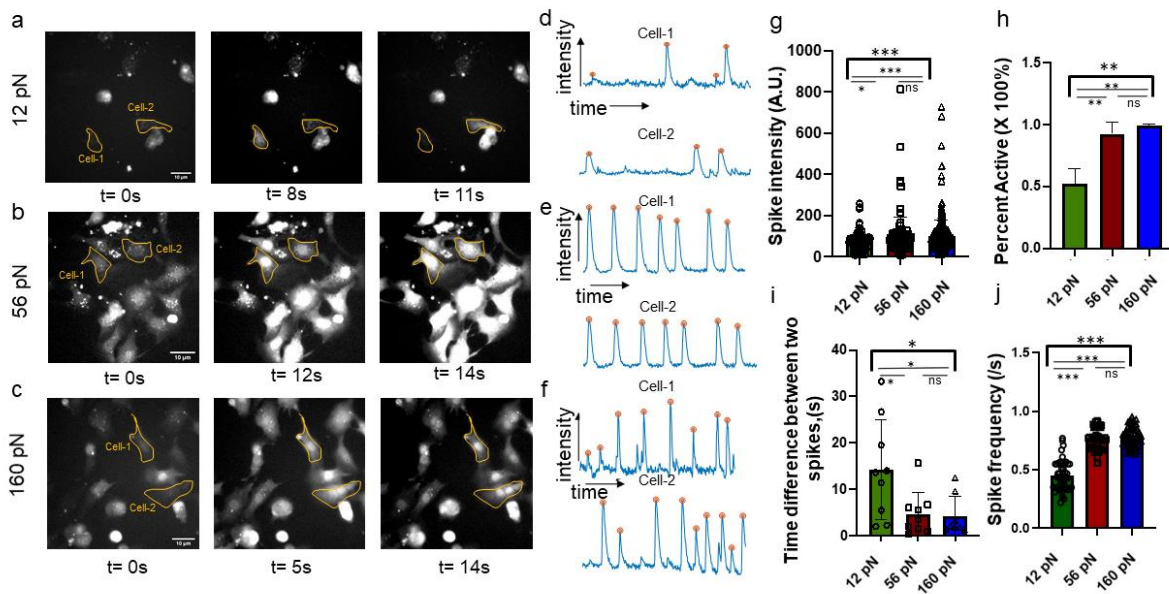


Figure 2.4. Cardiomyocytes display calcium profile consistent with greater maturation on surfaces with $T_{\text{tot}} = 56$ and 160 pN (a-c) FITC images of CMCs on 12, 56, and 160 pN rupture probes stained with Fluo-4. Images were taken from time-lapse to measure transient Ca^{2+} spark. (t=12-14hrs) (d-f) Transient Ca^{2+} flux profile of the outlined CMCs on 12, 56, and 160 pN probes. The dotted yellow line shows if the Ca^{2+} sparks have the same τ for the outlined cells. (g-j). The bar graph shows spike intensity, percent active, the time difference between two spikes, and spike frequency obtained from Fluo-4-stained CMCs on 12, 56, and 160 pN probes****, ***, **, * and ns indicate $p < 0.0001$, $p < 0.001$, $p < 0.01$, $p < 0.05$ and not significant respectively, as determined from one-way ANOVA. Scale bar=10 μm .

beating of the heart, gene transcription, and various other functions. Previous studies showed that CMCs had higher transient Ca^{2+} flux and more regular spikes on 10 kPa PDMS substrates compared to 5 kPa and 50 kPa.^{23,24} To evaluate the Ca^{2+} response as a function of the T_{tol} , cells were grown on the substrates for ~8 hrs. and then stained with the Fluo-4 Ca^{2+} indicator for 2 hrs. After dye incubation, transient Ca^{2+} spikes, which coincided with twitching, were measured by time-lapse videos in the Fluo-4 channel (**Figure 2.4 a-c and SI video 4-6**). The spike intensity was significantly higher in 56 and 160 pN substrates than that of 12 pN (**Figure 2.4d-f, g**). NRVMs also had more synchronized Ca^{2+} spikes on 56 and 160 pN substrates, with more cells exhibiting spontaneous beating (**Figure 2.4h-j**). This shows that integrin traction forces greater than 12 pN contribute to more contractile and matured Ca^{2+} profiles in CMCs.

2.3.4 Cardiomyocytes have aligned sarcomeres at a higher integrin force.

CMC's functional maturation is closely related to the spatial organization of the sarcoplasmic reticulum (SR), which harbors key elements for calcium cycling, such as RyR channels that release Ca^{2+} and SERCA2a pumps for Ca^{2+} uptake.^{43, 44} Specifically, elongation and alignment of the SR indicates CMC maturation.^{24, 32, 45} Moreover, recent studies have shown that SERCA 2A organization is substrate dependent and the expression levels is upregulated in functional CMCs.^{32, 45, 46}

To understand how molecular cell traction forces, influence the SERCA2A expression, we plated the NRVMs on different rupture probe surfaces with varied T_{tol} . As described above, cells were incubated on the 12, 56 and 160 pN DNA rupture surfaces for 6-8 hrs. The cells were then fixed and stained with a SERCA2A antibody. It was observed that

SERCA2A was clustered around the nucleus on the 56 and 160 pN surfaces in contrast to the 12 pN surfaces which had more diffuse (**Figure 2.5a**). Quantifying the total SERCA2A from fluorescence microscopy images showed that the total and average SERCA2A expression was significantly higher (2-3-fold greater) on the 56pN and 160pN substrates compared to the 12 pN substrates (**Figure 2.5b-c**). It was also observed that SERCA2a organization was different in CMCs seeded on 12 pN surface compared to 56 and 160 pN surfaces (**Figure S15**). This data is consistent with the previously discussed Ca^{2+} flux and supports the conclusion that the functional maturation of CMCs is enhanced by stronger integrin-ECM ligand bonds.^{19,23}

CMCs were seeded on rupture probes to measure the SR morphology and stained for sarcomeric α -actinin. Fluorescence microscopy showed CMCs with organized and aligned SR on 56pN and 160pN surfaces which contrasts with the 12pN surfaces that displayed disorganized and punctate sarcomeric α -actinin (**Figure 2.5e**). The total expression of α -actinin was not found to be different among the different thresholds of rupture (**Figure S16**), which is consistent with previous studies growing NRVMs on gels of differing young's moduli. Upon measuring the length of the z-band known as myofibril width and sarcomere length, the stained NRVMs showed almost two-fold longer myofibril width and SR length on 56 and 160 pN surfaces compared to 12pN surfaces (**Figure 2.5d-f**). Total number of α -actinin bands measured by particle tracking showed lower numbers for CMCs plated on 12 pN surface compared to the 56 and 160 pN surfaces (**Figure S15**). These data show nearly identical cell response on the 56 and 160 pN probe

surfaces in contrast to the 12 pN surface, and thus suggest that integrin forces > 12 pN result in more matured SR organization in NRVMs which is essential for CMC function.

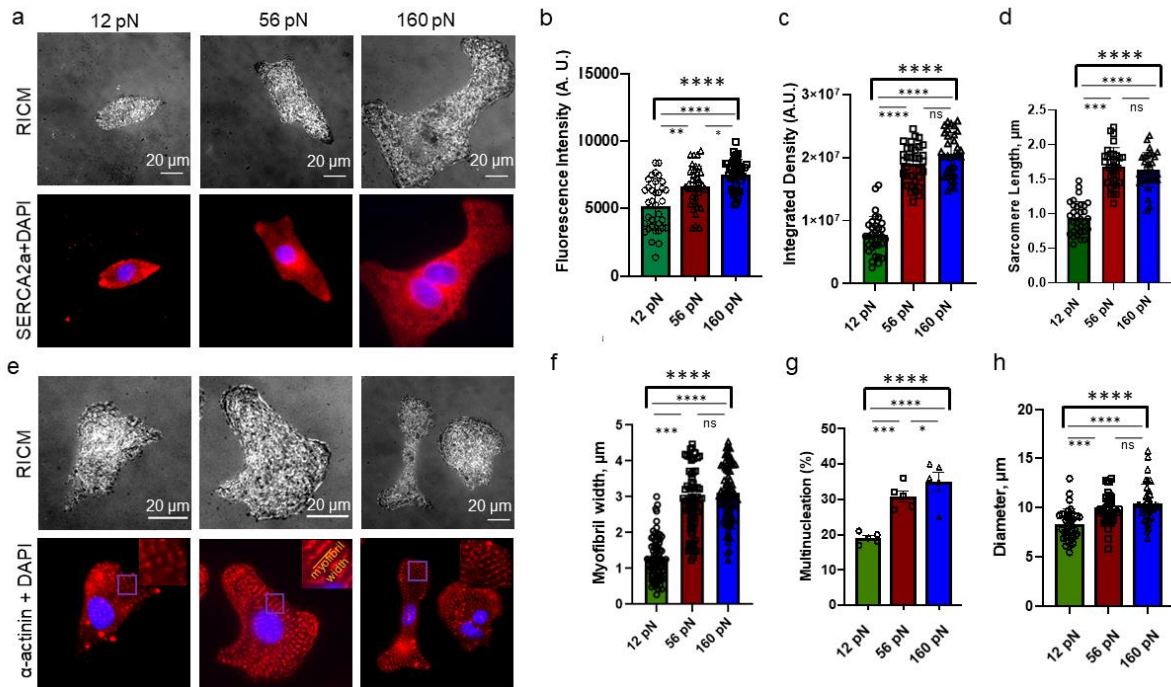


Figure 2.5. Cardiomyocytes have aligned sarcomeres at higher integrin force (a) SERCA2a calcium pump protein expression, representative cells (RICM), overlay image showing SERCA2a and DAPI expression, (t= 10-12hrs) (b) SERCA2a expression measured by mean fluorescence intensity, (c) total SERCA2a expression. (d) sarcomere length of CMCs on 12, 56, and 160 pN probes. (e) sarcomeric α -actinin expression, the yellow dashed line showing the length of individual z band. (f) Bar graph showing myofibril width of CMCs. (g) Percentage of cells containing multiple (>1) nucleus, where each dot represents one replicate and error bars show the standard error of mean. (N=5) (h) average nuclear diameter of the cells measured by averaging two major axes, each data point represents a single cell while the bar shows the average. ****, ***, **, * and ns indicate $p < 0.0001$, $p < 0.001$, $p < 0.01$, $p < 0.05$ and not significant respectively, as determined from one-way ANOVA. Error bars show the standard deviation for $n > 3$, where each experiment was averaged from three or more different cell isolations with three different sets of surface preparations. Scale bar=20 μm

Even though adult CMCs are mostly mononucleated, they are shown to have multinucleation in the postnatal development stage.^{47, 48} Multinucleation and polyplody

have been reported as essential for the CMC cell cycle and early development.⁴⁹⁻⁵¹ We observed CMCs have increased amounts of multinucleation when the receptor and ligand attachment is more stable. CMCs showed an increased nuclear diameter, eccentricity, area, and increased multinucleation on 56 and 160 pN surfaces compared to the 12 pN surfaces (**Figure 2.5 g, h & Figure S17**). This is due to greater T_{tol} of the receptor bond facilitating attachment of multinucleated CMCs on 56 and 160 pN surfaces compared to the 12 pN probe.

2.3.5 YES, associated protein (YAP) is upregulated when integrin F>12 pN

YAP is a well-known transcription factor that is mechano-sensitive and regulated by integrin mechanotransduction.^{52, 53, 54} Past reports showed upregulated nuclear YAP translocation with increasing ECM rigidity in various cell lines.⁵⁵ YAP plays an important role in the HIPPO pathway which controls the proliferation of CMCs and is vital in controlling organ development during mammalian gestation. Increased YAP expression is essential in early CMC maturation, which increases the need to understand the role of YAP in CMC maturation.^{46, 56, 57} A recent study using human induced pluripotent stem cells derived cardiomyocytes (hiPSC-CMs) observed higher nuclear YAP levels for cells cultured on stiffer substrates compared to softer substrates for CMCs.⁴⁶

We examined YAP upregulation and nuclear translocation using immunofluorescence and found upregulated YAP expression on 56 and 160 pN compared to the 12 pN rupture probes (**Figure 2.6 a, b, c**). However, no difference in YAP nuclear/cytosolic ratio was observed across all the surfaces tested after 8-10 hours of attachment (**Figure S18**). These results were surprising, as previous studies observed YAP nuclear translocation

in non-myocytes and in stem cell-derived CMCs.⁴⁶ To validate our conclusion, we incubated CMCs on the rupture probe surfaces for additional time (10-12 hrs., 12-14hrs, and 14-16 hrs.). We observed CMCs to have higher nuclear YAP on 56 and 160 pN surfaces compared to 12 pN probes when incubated on the surface for a prolonged period (12-14hrs) (**Figure 2.6d**). This suggests YAP translocation is highly dynamic and requires longer incubation. Additionally, we measured YAP expression and colocalization in cardiac fibroblasts (CF) derived from the same NRVM isolation protocol. Briefly, CF cells were co-cultured with CMCs on 12, 56 and 160 pN substrates for 6-8 hours and then stained for YAP protein expression. We found that CF total YAP levels were similar for the three probe surfaces tested. However, in agreement with the literature, we found that YAP accumulated in the nucleus at levels that corresponded with the mechanical stiffness of the ECM, and 160 pN substrates had the greatest YAP nuclear localization followed by 56 and 12 pN surfaces (**Figure S19**).

Next, we focused on studying the effectors of YAP upregulation in CMCs. Prior literature linked integrin mechanotransduction to YAP translocation/upregulation via the ERK/MAPK pathway.^{57, 58} MEK (mitogen-activated protein kinase) is a key regulator of the ERK/MAPK pathway which controls the cytosolic YAP expression and nuclear YAP translocation.^{59, 60} It has also shown that inhibition of MEK resulted in significantly lower YAP expression.^{61, 62} To better understand the role of MEK in mediating integrin traction forces and YAP mechanosensing, we treated NRVMs with U0126, a MEK inhibitor field^{62, 63}. The treated cells had a significantly lower spread area and rupture density for all three probes tested (**Figure S20**). There was also a significant reduction of YAP expression as

a result of U0126 treatment in CMCs (**Figure S21**). These results suggest that upregulation of YAP expression is tuned by the magnitude of integrin tension likely through signaling from mature focal adhesions (**Figure 2.6e**).

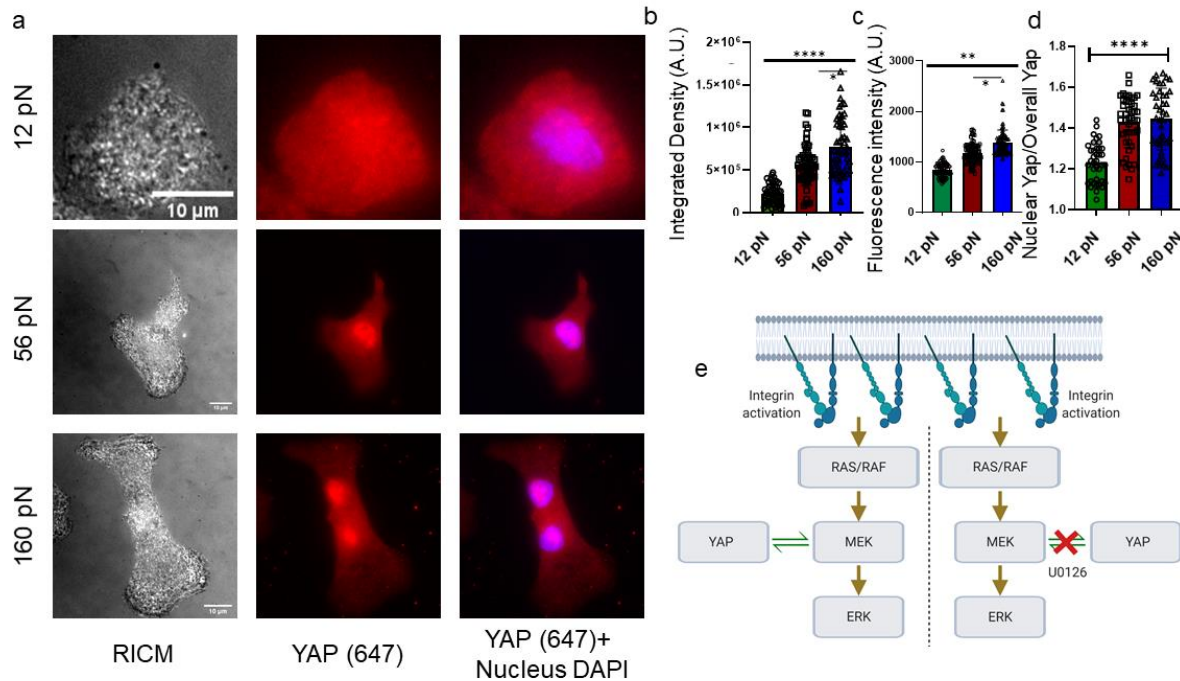


Figure 2.6. YES, associated protein (YAP) is upregulated when integrin $F > 12$ pN. (a) CMCs Stained for YAP-1 antibody 10-12hrs after seeding. RICM channel showing cell of interest, DAPI stain for nucleus, the rightmost channel showing the overlay of YAP+DAPI. Bar graphs show- (b) Total expression of YAP measured by immunostaining, (c) Average YAP expression, (d) Fraction of Nuclear YAP expression over total cellular YAP expression, each data point represents a single cell while the bar shows the average. ****, ***, **, * and ns indicate $p < 0.0001$, $p < 0.001$, $p < 0.01$, $p < 0.05$ and not significant respectively, as determined from one-way ANOVA. Error bars show standard deviation for $N > 3$, where each experiment was averaged from three or more different cell isolations with three different sets of surface preparations. Scale bar=10 μm . (e) Proposed mechanism of YAP upregulation due to integrin activation.

2.3.6 Podosomes as an early maturation marker in CMCs

Prior studies have shown that NRVMs form ring-shaped actomyosin and vinculin-rich structures under stress due to hypoxic conditions (O₂ deprivation).⁶⁴ These structures were described as “rosettes” and more recently as podosomes: structures of 0.15 –1 μm in diameter with actin-rich cores and cortex domains that contain vinculin, α-actinin, and β₁ integrins.⁶⁴ Podosomes are found in numerous cell types including dendritic cells, T-cells, and vascular smooth muscle cells, and have been intensively studied field⁶⁵⁻⁶⁸. Nonetheless, little is known about their functional roles in cardiac cells and what cues trigger podosome formation.⁶⁹⁻⁷¹ There has been some speculation that podosomes play an active role in the neuromuscular junction's developmental remodeling. However, more work is needed to support this claim.^{69,71} Moreover, some earlier investigations have suggested neural and dendritic cells form podosomes at earlier stages of maturation.⁷²

We discovered that ~30% of NRVMs seeded on the 12 pN surface formed ring-like patterns of probe rupture with micron-scale dimensions and these patterns appeared near the nucleus (**Figure 2.7a**). Interestingly, these tension patterns resembled the tension patterns observed for podosome assemblies reported by Glazier *et al.*⁷³ Podosomes are most often identified by immunostaining of F-actin (central core), vinculin, and talin (at the rim). To verify whether the observed tension pattern was generated by podosomes, cells were stained with both the F-actin stain phalloidin and with vinculin antibodies after culture on probe surfaces of varying mechanical stability (**Figure 2.7a, Figure S23**). Puncta showed the characteristic F-actin core surrounded by a rim of vinculin and integrin tension, thus suggesting the formation of podosomes (**Figure S22,23**). Podosomes were predominantly observed for cells on 12 pN surfaces with an average of 4 per cell

compared to the 56 and 160 pN surfaces that displayed an average of 1-2 podosome per cell (**Figure 2.7a, b**). We found that 30% of cells on the 12 pN surfaces had podosomes compared to ~10% of cells on the 56 and 160 pN surfaces that showed podosomes (**Figure 2.7c**). These two observations suggest that deficiency in integrin tension and focal adhesion formation is highly correlated with podosome formation. This is consistent with the observation by Yu and Sheetz *et al.* that fibroblasts cultured on fluid membranes show enhanced podosome formation.⁷⁴ Podosome size was also correlated with integrin tension, and podosomes on 12 pN surfaces showed larger diameters (**Figure 2.7d**). Further confirming that podosome formation is mechanosensitive, we found that treatment with ROCK inhibitor led to enhanced formation of podosomes in all substrates tested (**Figure S13a**). Surprisingly, we also found a strong correlation between podosome formation and twitching. While only ~30% of cells cultured on 12 pN surfaces were beating (**Figure 2.3b**), the majority (>90%) of this subpopulation were beating (**Figure S24**). This result along with the literature suggest that podosomes provide alternate adhesion signaling to compensate for weak focal adhesions.

Subsequently, we focused on identifying the timeline of podosome formation. We wanted to know if podosome formation occurs early in NRVM adhesion, and then these structures mediate twitching or alternatively do podosomes form in cells that may be more functional and already twitching. To answer this question, we performed time-lapse imaging after seeding cells and noticed that podosome-like puncta formed in cells on 12 pN surfaces at early time points (2-3 hours after seeding, **Figure S25a**). Podosomes seemed to form even before full cell spreading, which may indicate their role in aiding in cell spreading on substrates with labile adhesion sites and weak focal adhesion formation. Moreover, prior

studies have postulated a role for podosomes in cell-cell junctions.^{69,70} To test if cell-cell interactions increase podosome assembly, we plated cells at higher densities to find out if there is more podosome formation with cells which are in proximity. We seeded 76,000 cells/cm² and imaged at the 6-8 h time point (**Figure S25b**). We found that cells plated at higher densities displayed more podosome-like structures. Podosome size and number

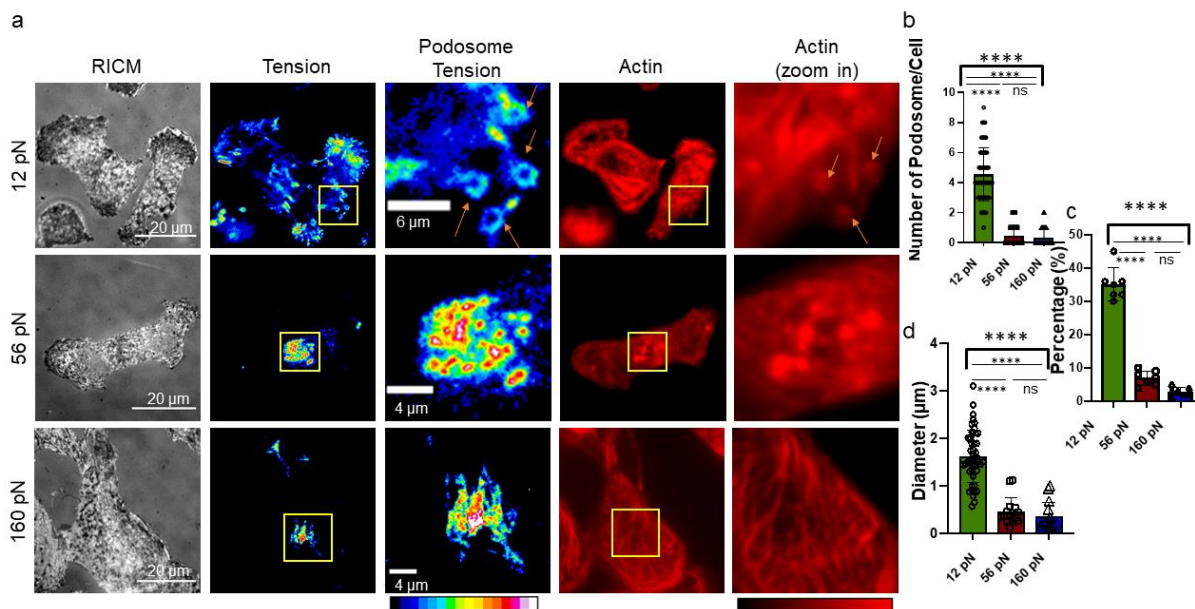


Figure 2.7. Podosomes/podosome like organelles as an early maturation marker in CMCs. (a) Representative images of CMCs having podosome like structure on 12 pN surface (t=8-10hrs), RICM showing cell of interest, TRITC channel showing podosome tension ring, Phalloidin staining confirming colocalization of actin in the structure. Scale bar= 20 μm (First column) and 4 μm (third column). (b) Number of podosomes in rupture probe surfaces, (c) Percentage of cells having podosomes (where each dot represents one biological replicate, $N=5$). (d) Diameter distribution of podosomes. Each data point represents a single cell while the bar shows the average. ****, ***, **, * and ns indicate $p < 0.0001$, $p < 0.001$, $p < 0.01$, $p < 0.05$ and not significant respectively, as determined from one-way ANOVA. Error bars show standard deviation for $N > 3$, where each experiment was averaged from three or more different cell isolations with three different sets of surface preparations.

were correlated to cell density, and isolated cells displayed the smallest podosomes compared to cells that were in proximity to their neighboring cells (**Figure S25 c, d**). We

observed that CMCs have an increase in podosome formation when tension is inhibited (Figure S26). Taken together, we find podosome formation is highly mechanosensitive, upstream of the twitching phenotype, and sensitive to cell-cell contact.

2.4 Conclusion

Biomechanical stimuli can determine the physiological structure of cells and tissues, particularly in cardiac development.^{20, 75, 76} These stimuli control not only regular cardiovascular maturation and differentiation but also play essential roles in disease homeostasis. Here we describe how tuning integrin forces with pN resolution can alter and modulate early CMC maturation. We utilize nucleic acid-based probes conjugated to fibronectin mimic peptides to target integrins expressed in NRVMs and CMCs. We generated three different rupture probes with distinctive mechanical tolerance T_{tol} (~12, ~56 and ~160 pN) by changing the position of where forces are applied to the probe. The 12 and 56 pN probes have been commonly used, and these DNA duplexes denature under tension, in contrast, the 160 pN probe only ruptures upon biotin-streptavidin dissociation. The greater the mechanical stability of the probe leads to stable integrin-RGD bonds that transmit more tension, and thus facilitates focal adhesion maturation. CMCs display more elongated morphology, higher spreading area, more periodic and synchronized beating as well as Ca^{2+} transients on 56 and 160 pN surfaces in contrast to the 12 pN surfaces.

CMCs were found to have elongated z-band and had higher sarcomere distancing, also known as sarcomere length. The data suggested CMCs when plated on 56 pN and 160 pN surfaces showed more aligned SR compared to the 12 pN surface. YAP is another regulator that play an important role in cardiac regeneration but very little is known on

how subcellular integrin forces can control YAP signaling on CMCs.⁶³ Our finding suggests that pN integrin forces control YAP expression and YAP enhancement modulate functional maturation of CMCs. We have specifically focused on parameters that are directly correlated with functional maturation of CMCs (NRVMs). The SR is the contractile unit of cardiomyocytes.³² Elongated, and well aligned SR is important for proper contraction of CMCs. Previous literature has shown that, in addition to the matrix stiffness affecting the calcium dynamics, SR organization and contractility of CMCs.^{19,,23,24,25,32,46} These studies showed that NRVMs seeded on PDMS gels coated with collagen and displaying an elastic modulus (measured by atomic force microscopy) of 10 kPa showed well-defined SR compared to gels with 1 and 5 kPa modulus.^{19,23} Moreover, prior reports have quantified the striation of CMCs using PDMS gels and micro-post arrays and showed that SR spacing is a sign of myofibril maturity and an indicator for force output.^{24,46} Tunable PDMS gel with micro posts also have shown CMCs on a softer substrate had un-aligned SR distribution by quantifying the sarcomeric α -actinin alignment.⁴⁶ Together, this data demonstrates that the specific magnitude of pN integrin forces functionally control the early maturation of CMCs.

During a heart failure a significant number of CMCs die and are lost.^{77, 78} The native heart has a limited capacity to recover from the loss by regenerating CMCs from CFs. To facilitate efficient cardiac regeneration after a cardiac arrest, researchers recently have focused on the stem cell-based therapeutics.⁷⁶ However, these stem cell-based therapeutics fail to recapitulate the loss myocytes efficiently.⁷⁷⁻⁷⁹ There is a growing interest in understanding the maturation and differentiation of CMCs to properly mimic the environment of native myocardium.^{4, 79} NRVMs have been used profusely in studies to

understand maturation and development of cardiovascular system. This report can address how single molecule forces can influence the early maturation of CMCs and the knowledge gathered is useful for increasing the functional efficacy of stem cells-based therapeutics.

Although previous work suggested that CMCs can form podosomes like organelles on only collagen and laminin substrate⁶⁴, the mechanism behind the formation is still unknown. Our work reveals that CMC can form podosome like structure on fibronectin as well. It also demonstrates how the threshold of pN integrin forces can have an effect of podosome formation. The result also suggest that CMCs mainly form podosome like structures when the integrin force threshold is low (<12 pN) indicating there might be a correlation between podosome formation and CMC maturation. Inhibition of ROCK signaling resulted in podosome formation on all the three substrates. This report shows that CMC's podosome formation is dependent on the bond strength of the receptors and ROCK signaling. In the future we plan to investigate how specific integrin heterodimers (e.g., β_1 , β_3) influence podosome formation and their specific role in CMCs.

In summary, we have identified the role of integrin forces on functional maturation of CMCs. One limitation of the current study is that the DNA probes rupture irreversibly; hence, the probe influences the biology and reports cumulative signals over the period. Therefore, rupture density cannot be directly compared to other measures of force such as traction force microscopy or the reversible DNA probes that can measure the steady state tension applied by cells without controlling or capping tension. These rupture forces are best suited to control tension rather than to measure it. Also, as the probes are DNA based, there is some signal loss due to nuclease activity and spontaneous DNA duplex

and biotin-streptavidin bond dissociation. Nonetheless, the work represents an essential step toward developing a molecular-level understanding of how adhesion receptor forces tune the process of CMC maturation as measured through physiological and biochemical markers. The general strategy can also be applied to other stem cell subtypes and may be broadly helpful in that capacity.

2.5 Methods

2.5.1 DNA probes synthesis and preparation

Rupture probes used in this project were adapted from previously published work.^{34,35} Cyclic peptide RGDfK was first coupled to the 5' end of rupture probe (TGT) top strand (12/56 pN ligand strand) *via copper-catalyzed cycloaddition* reaction. cRGDfK-azide was conjugated onto the top strand in 25 μ L of reaction mixture containing 5 mM of sodium ascorbate and 0.1 μ M pre-formed Cu-THPTA complex. The mixture was allowed to react for 2h, and the product was purified by reverse-phase HPLC. The biotin bottom strands were coupled to Cy3B NHS ester *via NHS-amine coupling*. For biotin rupture probe cRGD was coupled first following HPLC purification, and subsequently, Cy3B-NHS was conjugated and purified using HPLC.

2.5.2 Surface Preparation

All the DNA probes were immobilized to the surface using biotin-streptavidin interactions. The glass slides were covalently functionalized with the biotin group and further incubated with streptavidin by using previously published literature procedures. Glass coverslips (number 2, 25-mm diameter; VWR) were sonicated in EtOH and subsequently with

Nanopure water for 10 min and then etched in piranha (a 3:1 mixture of sulfuric acid and hydrogen peroxide) for 10-15 min. The glass coverslips were washed several times with Nanopure water and EtOH and then incubated in 1% (3-aminopropyl) triethoxysilane (APTES) in EtOH for 1 hr. The substrates were immersed in EtOH three times, rinsed with EtOH, and dried under nitrogen. Subsequently, substrates were baked in an oven (~100 °C) for 10 min. After cooling, the samples were incubated with NHS-biotin (Thermo Fisher) at 2 mg/ml in DMSO overnight. The substrates were washed with EtOH and dried in the oven for 20 mins. The biotin-functionalized glass substrates were assembled into cell chambers and flushed with 1× PBS (3 × 5 ml) and incubated with 0.1% BSA (EMD Chemicals, 100 µg/µL, 30 min), and washed again with 1× PBS (3 × 5 ml). Streptavidin was added (5 µg/ml 45 min, room temperature) followed by washing with 1× PBS (3 × 5 ml). The chambers were then incubated with the rupture probes (150 nM) for 1 h and rinsed before CMC experiment and imaging.

2.5.3 Cell Isolation

NRVMs were isolated from 2- to 3-day-old neonatal rat pups and cultured as a monolayer as described previously^{78, 80, 81}. Only the lower one third of the heart (from the apex to the midline) was excised in order to minimize contaminating atrioventricular nodal cells. For each of the biological replicate cells were isolated from ~20 neonatal rat pups. For all in vitro experiments, NRVMs were plated at a density of 25,000-30,000 cells per surface chamber (circular coverslip with a diameter of 16 mm exposed; area = 804 mm²). The cells were cultured in 2% serum for all experiments.

2.5.4 Immunostaining

For staining on rupture probes, CMCs were fixed and stained on 12, 56 and 160 pN probes following 8-10hrs of cell spreading. Cells were fixed in 2–4% formaldehyde in 1x PBS for 8–10 min. Cells were permeabilized for 3 min with 0.1% Triton X-100 and were blocked with BSA for 30 min. Staining was performed for 1 h at room temperature with 1:1000 Alexa 488-Phalloidin (ab176753, Abcam), 1:50 Vinculin Antibody SF9 647 (sc-73614 AF647, Santa Cruz Biotechnology), 1:50 Phospho-Paxillin (Tyr1888) Polyclonal Antibody (PA5-17828, Thermo Fisher) followed by 1:5500 Alexa Fluor 555 goat anti-rabbit (A21147, Thermo Fisher), or 10 µg/mL α -actinin Antibody(PA5-17308) from Invitrogen, Thermo fisher), 10 µg/mL Serca2A Antibody,(SC-376235) from Santa Cruz antibody, or YAP1 (SC 376830) followed by 1:1000 Alexa Fluor 647 or 488 goat anti-mouse IgG2b (γ 2b) (A28175 or A28181) or goat anti-rabbit secondary antibody(A27034 or A27080) from Thermo Fisher as indicated in the experiment details. Immunostained cells were imaged using total internal reflection fluorescence microscopy (TIRFM).

2.5.6 Drug treatment

CMCs were pretreated for (>1hr @RT) with various inhibitors before seeding. Cells were either treated with 25 µM Y27632 dihydrochloride (Y0503, Millipore Sigma) for 30 min or with 10 µM eptifibatide (Cas no- 881997-860) or with 10µM Blebbistatin (18-521, Fisher Sci) for 30 mins or with 15 µM of U1026 (PD 98059, cell signaling) for 30min. We used DMSO as a solvent vehicle for the control group.

2.5.7 Optical Microscopy

Live NRVM's were imaged in 2% serum buffer at 25 °C using a Nikon Eclipse Ti microscope driven by the Elements software package. The microscope is equipped with Evolve electron-multiplying charge-coupled device (Photometrics), an Intensilight epifluorescence source (Nikon), and a CFI Apo 100× NA 1.49 objective (Nikon). It also includes a TIRF launcher with three laser lines: 488 nm (10 mW), 561 nm (50 mW), and 638 nm (20 mW). The microscope also has a perfect focus system which can lock the focus to assist in capturing multipoint and time-lapse images without losing focus. All of the reported experiments were performed using the following Chroma filter cubes: DAPI, TIRF 488, TIRF 561, FITC, TRITC, Cy5, BF, and RICM.

2.5.8 Calcium staining and automated analysis of ROI calcium intensity

CMCs were stained with Fluo-4 (F14210, Thermofisher) using the previously published protocol.⁸² After staining CMCs were left in the incubator for two hours to restore spontaneous twitching. Time lapses were taken in the FITC channel. ROIs were manually selected at the area of calcium sparks. ROIs were analyzed using an automated code in MATLAB 2019b. The average fluorescence intensity and 99th percentile fluorescence intensity of each ROI was both quantified at each timepoint. The 99th percentile was used to check for saturation of the camera; if any timepoint for a given ROI had a 99th percentile fluorescence intensity equivalent to the maximum of the detector (255 arbitrary units), the ROI was discarded. ROIs with zero-value 99th percentiles were also discarded.

For each remaining ROI, calcium spikes were identified using a peak-finding process. First, the average intensity was normalized to a 901-point median filter with truncated edges using MATLAB's built-in "medfilt" command. Next, MATLAB's built-in "findpeaks"

function was used to identify fluorescence intensity spikes with the “MinPeakDistance” and “MinPeakHeight” settings set to 200 and 1.2, respectively (SUPP FIG REF). Finally, peaks that occurred at least 100 points after the initial time point and 200 points before the final time point were stored. Specifically, 100 points before the peak and 200 points after the peak were saved.

Peak dynamics were measured by fitting an equation to the saved 301-point intensity vs. time curves

$$I = (I_{max} - I_0) \left(\left(1 - \exp \left(-\frac{t - t_{start}}{\tau_{rise}} \right) \right) u(t - t_{start}) - \left(\exp \left(-\frac{(t - t_{start} - t_{end})}{\tau_{fall}} \right) \right) u(t - t_{start} - t_{fall}) \right) + I_0$$

Where I_{max} is the maximum peak intensity (i.e. spike height), I_0 is the baseline intensity, t is the time, t_{start} and t_{end} are the times at which the spikes begins rising and falling, respectively, τ_{rise} and τ_{fall} are the spike rising and falling time constants, respectively, and $u(x)$ is the Heaviside function denoting initiation at time x . Fitting of the parameter set $[I_{max}, I_0, t_{start}, t_{end}, \tau_{start}, \tau_{end}]$ was performed using MATLAB’s built-in “simultaneous” function with initial guesses of the maximum intensity, the minimum intensity, 50 timepoints, 100 timepoints, 5 timepoints, and 20 timepoints, respectively. All fit parameters were given a lower and upper bound of 0 and ∞ intensity units, respectively, and fitting was performed with the “HybridFcn” setting set to “fmincon” and all other settings set to their default values.

2.5.9 Illustration and statistical analysis

Either adobe illustrator or BioRender.com prepared all the illustrations of this manuscript.

Statistical analyses were performed in GraphPad, imagej and MATLAB.

2.6 Appendix

1) Determination of rupture probability

Rupture probability (p_{rup}) vs. force plots shown in Fig. 1c were calculated from the force-induced rupture rate, k_{rup} :

$$p_{rup} = 1 - \exp(-k_{rup}\Delta t)$$

where Δt is the duration of constantly applied force. The parameter k_{rup} was approximated using Bell's model⁸³:

$$k_{rup} = k_0 \exp\left(\frac{F x_{tst}}{k_B T}\right)$$

where F is the applied force, $k_B T = 4.114 \text{ pN nm}$ is the thermal energy at room temperature, k_0 is the zero-force off rate, and x_{tst} is the distance to transition state parameter. T_{tol} is generally defined as the constantly applied force that results in $p_{rup} = 0.5$ when $\Delta t = 2 \text{ s}$, which can be solved for by re-arranging the previous two equations and substituting T_{tol} for F :

$$T_{tol} = \frac{k_B T}{x_{tst}} \ln\left(\frac{\ln(2)}{k_0(2 \text{ s})}\right)$$

For all three tension sensors, we used $k_0 = 10^{-6}$ to reflect a very low rate of dissociation at zero force^{84, 85} and calculated x_{tst} as the value that produced the previously calibrated T_{tol} when $\Delta t = 2 \text{ s}$.

2) Determination of DNA surface density

We followed a previously reported surface density measurement assay to measure the DNA density on the surface.⁴ The protocol allows one to convert the raw fluorescence intensity of the surface to the molecular density of fluorescent molecules. In this assay, lipid membranes were used as calibrated fluorescence standards, based on the known documented molecular density of phospholipids within membranes. In this calibration, the intensity of labeled oligonucleotides and small unilamellar vesicles (SUVs) in solution are compared to determine the F factor, which relates the molecular brightness of the two fluorophores. The concentration of rupture probes on the surface was calculated using F factor. It was done by a calibration curve that was generated by imaging known concentrations of supported lipid bilayers (SLBs). To prepare SLBs, SUVs were prepared by mixing 99.9 mol% 1,2-dioleoyl-sn-glycero-3-phosphocholine (DOPC) and 0.1 mol% Texas Red 1,2 dihexadecanoyl-sn-glycero-3-phosphoethanolamine, triethylammonium salt (TR-DHPE, T1395MP, Thermofisher Scientific) in a round bottom flask with chloroform. Lipids were dried for 30 min under rotary evaporation followed by an ultra-high-purity nitrogen stream to remove residual chloroform. The dried lipid film was hydrated with nanopure water (2 mg/mL) before conducting three freeze-thaw cycles. The mixture was then passed through 10mL LIPEX® thermobarrel extruder 10 times (Evonik Industries, Essen, Germany) using a 80 nm polycarbonate filter. We then prepared known concentrations of labeled oligonucleotides and SUVs in solution to compare the fluorescence intensity with density. Glass was passivated with 0.1% BSA in PBS for 20-30 min. The quality of the calibration curve for DNA and SUVs was assessed by measuring the linear regression

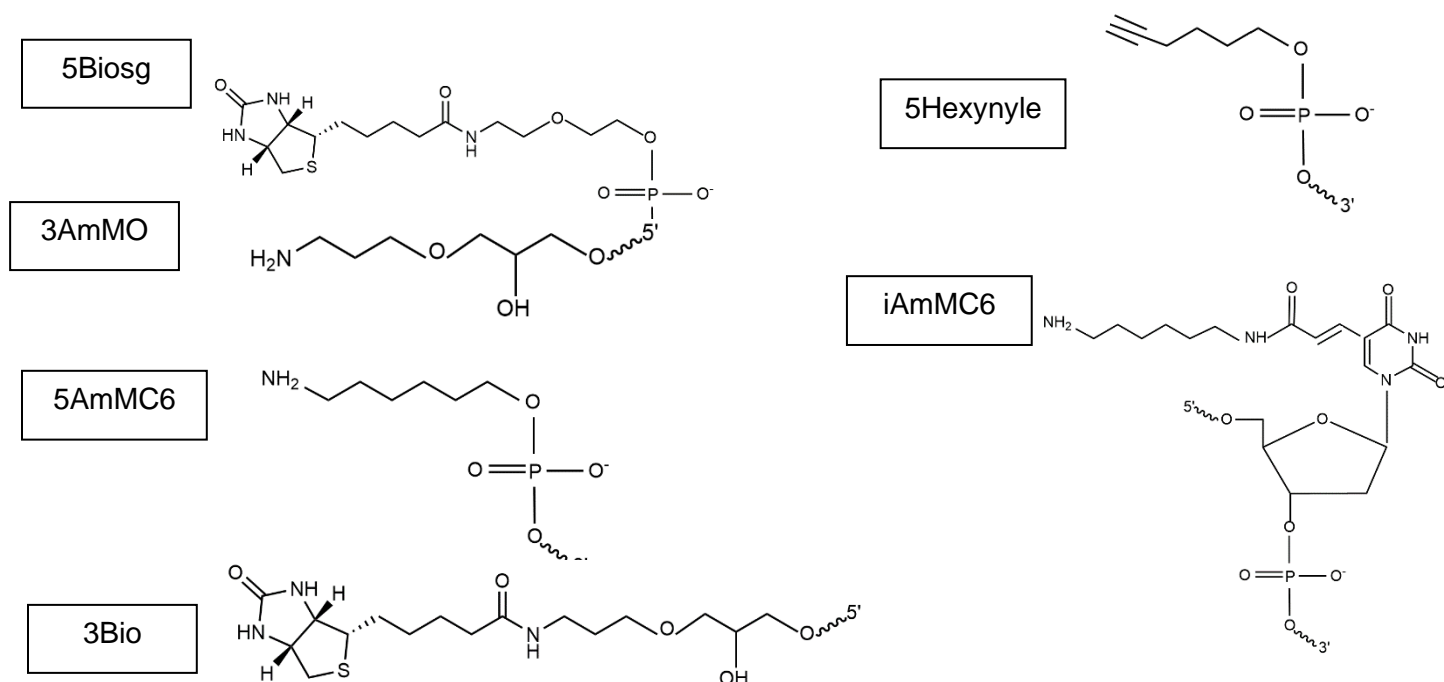
between the concentration of the known oligonucleotide (or the SUV sample) and its fluorescence intensity, as deviations can indicate nonspecific adsorption. The ratio of the calibration curve slopes was used to determine the “F factor” for the labeled oligonucleotide and the SUV samples. The F-factor was calculated as follows: $F = I_{\text{Cy3B-DNA}} / I_{\text{TR-DHPE}}$, where $I_{\text{Cy3B-DNA}}$ and $I_{\text{TR-DHPE}}$ represent the fluorescence intensities of the DNA and SUV samples, respectively. To prepare SUVs in glass bottom plates, the glass was treated with a 2 M NaOH etching solution. It was then thoroughly washed with water and 1x PBS. To create a fluorescence calibration curve, SLBs with varying fluorophore concentration were prepared by adding mixtures of labeled and unlabeled SUVs in known stoichiometries. Excess SUVs were rinsed using 1XPBS. The intensity of the SLBs was measured using epifluorescence microscopy. Using the known lipid footprint⁸⁶ (0.72 nm²), the generated graph was used to relate the density of fluorophores to arbitrary fluorescence units. The equation of the calculation generated for **Figure S4**, is $\text{DNA density} = \text{intensity} \div (F \times \text{slope})$. This equation was then used to convert the fluorescence intensity of DNA to probes density per μm^2 .

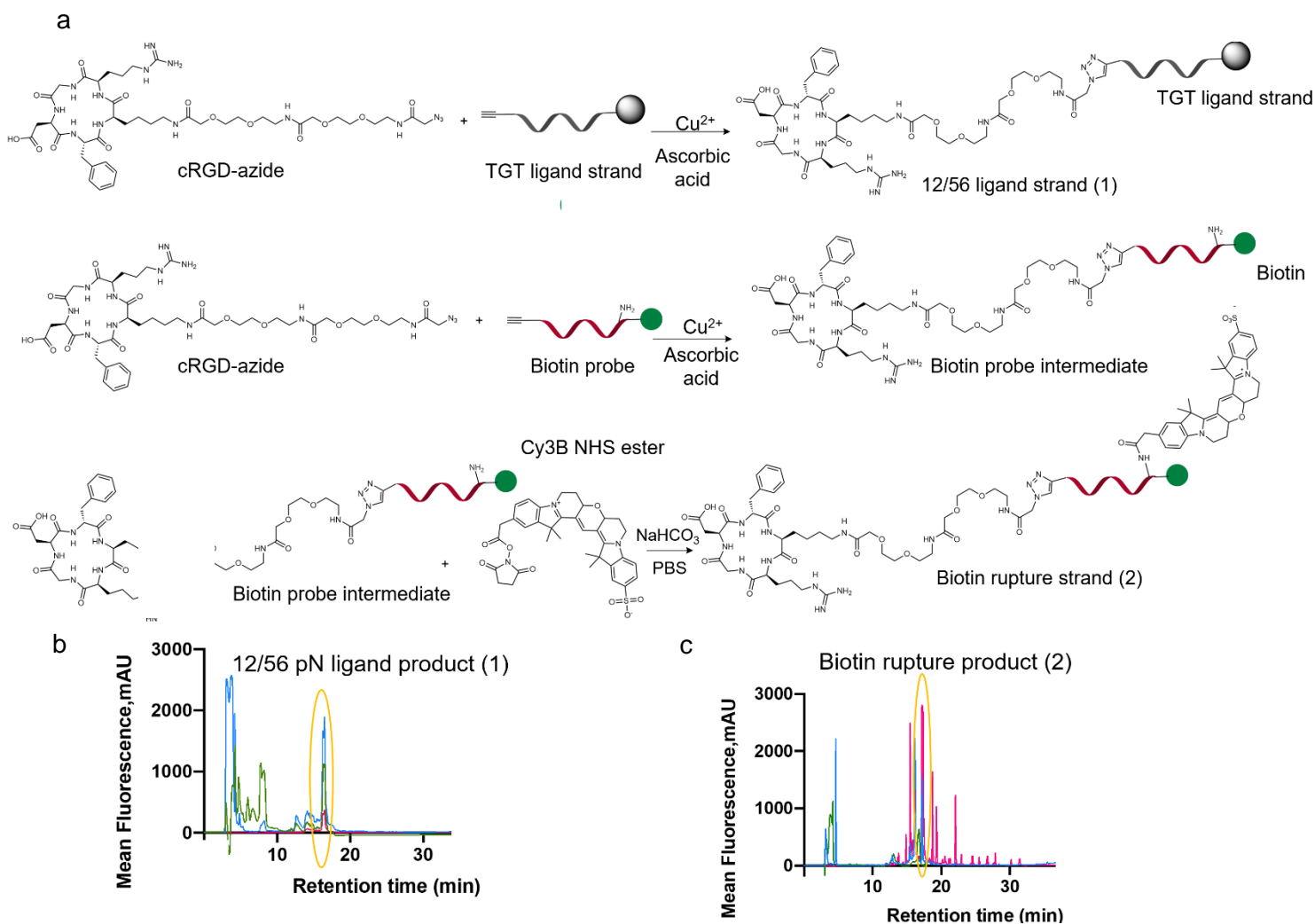
3) α -actinin puncta analysis

Fluorescent α -actinin micrographs were subjected to image analysis using the Fiji ImageJ distribution (NIH). α -actinin micrographs were first subjected to a rolling ball background subtraction using a 15-pixel radius. Images were then converted to 8-bit greyscale images. The setAutoTHreshold ("Default dark") function was executed to enhance the contrast of the fluorescent micrograph. Next, the cell RICM ROI was selected, and the run ("Clear Outside") function was carried out to remove fluorescent signal outside of the cell area. Images were then set between 35 and 255 greyscale units. Then the run ("Convert to Mask") function was carried out, followed by the run("Watershed") function. Actinin puncta were then identified by using the "Analyze Particles" function, selecting particles between 8- and 350-pixel units. The list of actinin puncta ROIs within the cell were then saved. Finally, the number of identified puncta per cell were counted.

Table 1: Identification and sequence of oligonucleotides used in this work.

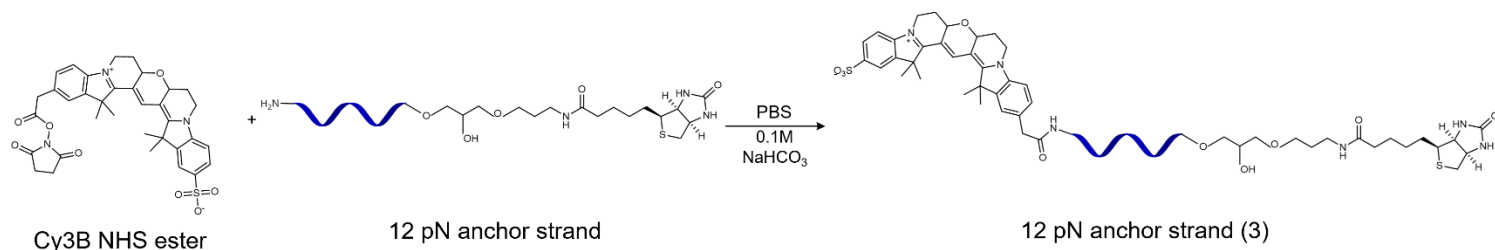
ID	DNA Sequence (5'-3')
12/56 pN ligand strand	/5Hexynyl/GTG AAA TAG CGC ACA GAT GCG /3AmMO/
56 pN anchor strand	/5Biosg/TTT/iAmMC6T/C GCA TCT GTG CGG TAT TTC AC/3/
12 pN anchor strand	/5AmMC6/CGC ATC TGT GCG GTA TTT CAC TTT/3Bio/
Biotin rupture strand	/5Hexynyl/CGC ATC TGT GCG GTA TTT CAC /iAmMC6T/TT T/3Bio/
Biotin rupture strand complement	/5/GTG AAA TAG CGC ACA GAT GCG /3/



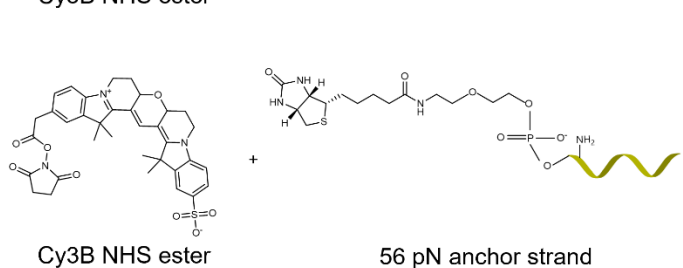


Supplementary Figure 1. Synthesis of ligand strands. a) Synthesis of 12/56 pN ligand strands. Schematic illustration of the Cu^{2+} catalyzed click reaction between the cRGD-azide and alkyne modified DNA. To prepare the biotin 12/56 pN ligand strand, the RGD peptide was first coupled to the nucleic acid followed by HPLC purification and then coupling of the peptide-nucleotide product to Cy3B dye. b) and c) Representative chromatograms of products **1** and **2**. HPLC was used to isolate and purify the products which were confirmed by mass spectrometry.

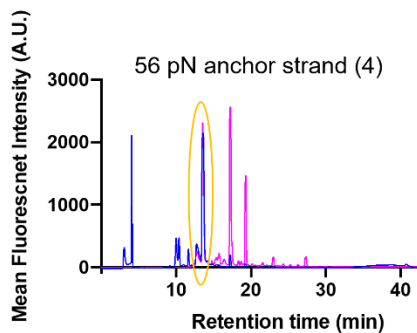
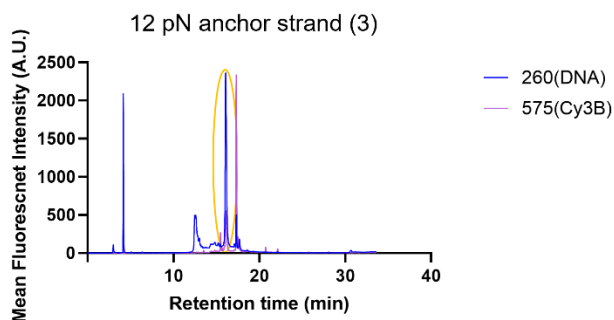
a



b



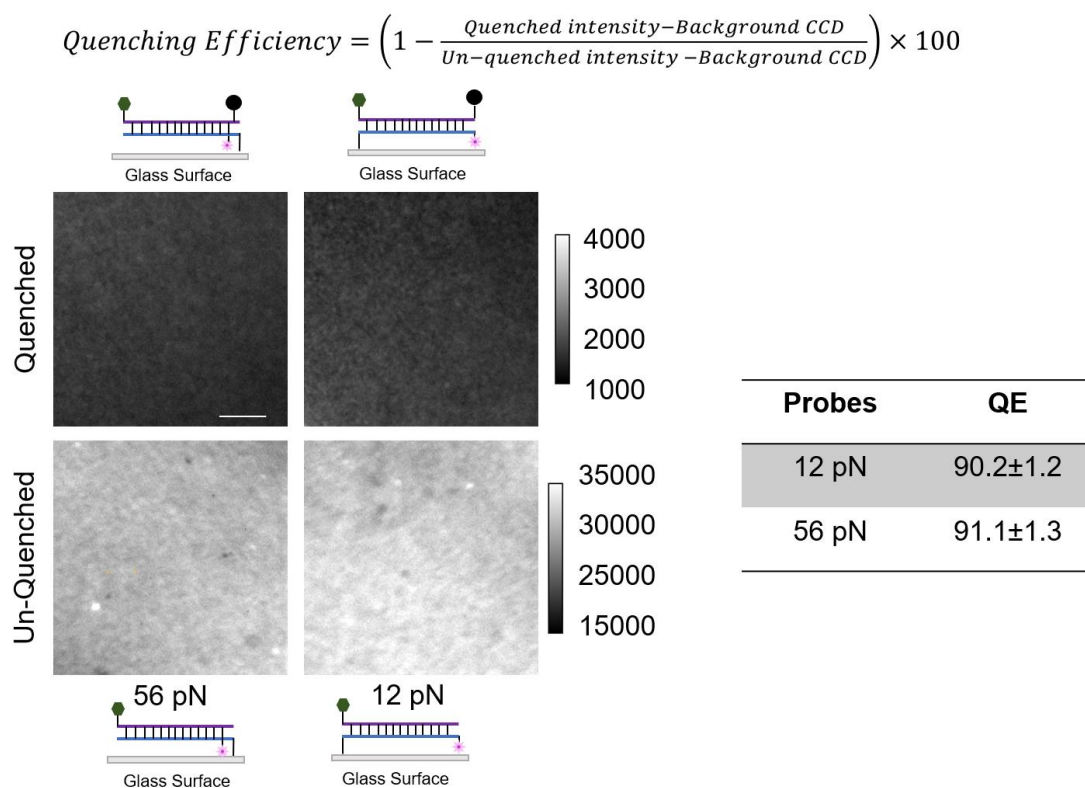
c



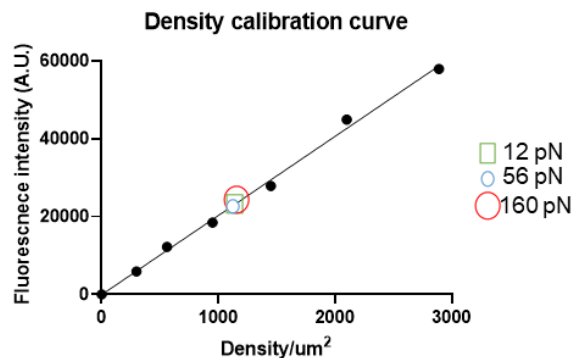
Supplementary Figure 2: Synthesis of anchor strands. Schematic illustration of the NHS-NH₂ coupling reaction between 12 and 56 pN anchor strands and Cy3B-NHS ester. b) and c) Representative chromatograms of products **3** and **4**. HPLC was used to isolate and purify the products which were confirmed by mass spectrometry.

Supplementary Table 2: Expected and calculated mass of oligonucleotides

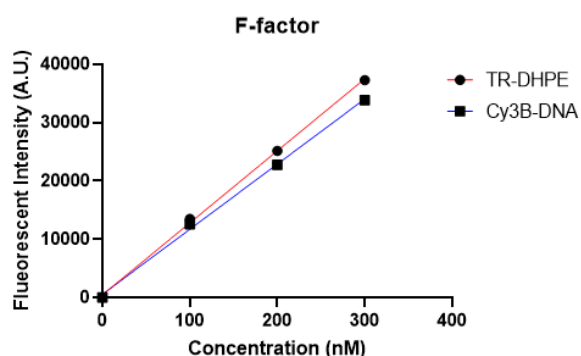
Oligo ID	Theoretical Mass	Calculated Mass (From Mass Spec)	Percent Error (%)
12 pN anchor strand	8460.6	8456.608	0.00047
56 pN anchor strand	10271.9	10266.872	0.00048
12/56 pN ligand strand	9880.9	9871.87	0.00091
Biotin rupture strand	8195.7	8190.788	0.00060



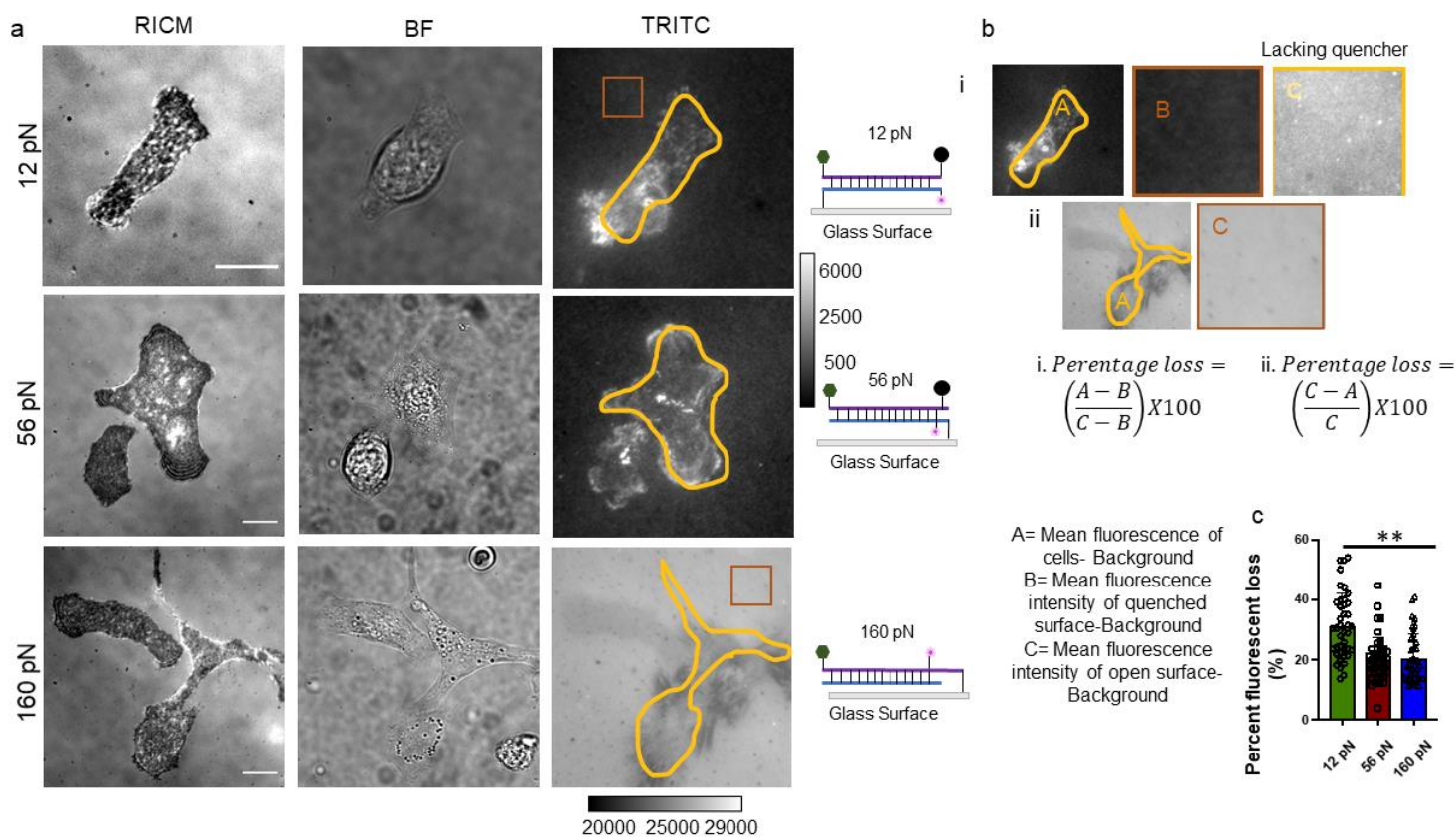
Supplementary Figure 3. Quenching efficiency measurement. Equation used to determine the quenching efficiency of 12 and 56 pN DNA probes. The quenched intensity was measured from the intensity of a uniform monolayer of probe with the Cy3B-BHQ-2 pair. The un-quenched intensity was determined from an identical monolayer of DNA probes lacking the BHQ-2 quencher. Intensities were background corrected. Scale bar = 10 μm . The error represents the standard deviation and was measured from 9 different substrates that were generated from three separate preparations.



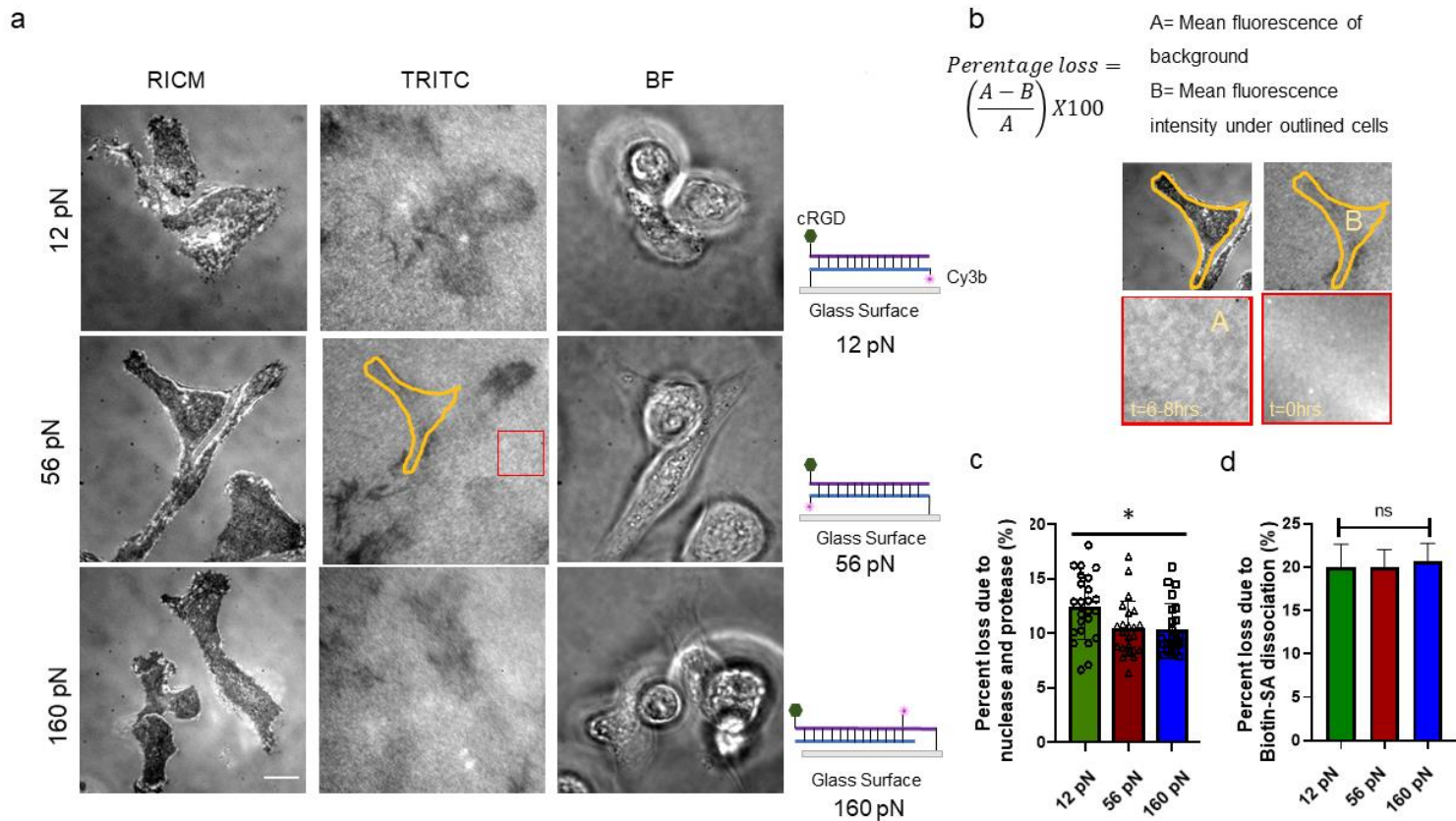
Type of TGT	Density
12 pN	1289.5 ± 55
56 pN	1238.3 ± 63
160 pN	1395.8 ± 75



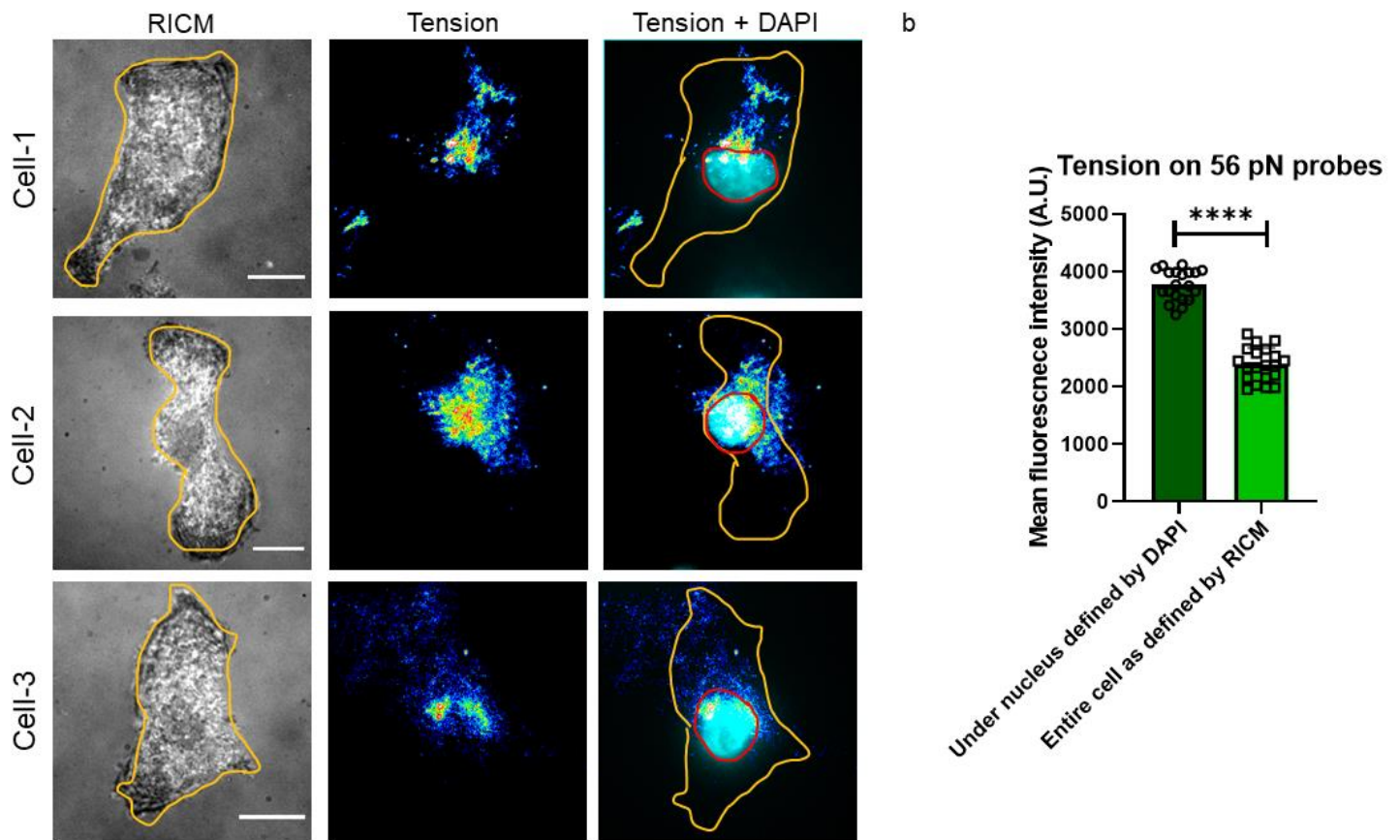
Supplementary Figure 4. Calibration curve used for determining molecular density of probes. Plot shows a calibration curve relating the fluorescence intensity of TR-DHPE – doped supported lipid membranes as a function of dye density. The density was calculated based on the mol % of the dye and by using the published density of DOPC reported using neutron scattering experiments. An F factor was also measured by comparing the calibration curve for TR-DHPE against a calibration curve for the Cy3B DNA probe. Finally, by using the TR-DHPE calibration curve along with the F factor, we were able to infer the molecular density of the 12 pN, 56 pN and 160 pN DNA probes (shown in the table). The errors signify the SD (standard deviation) from three individual replicates.



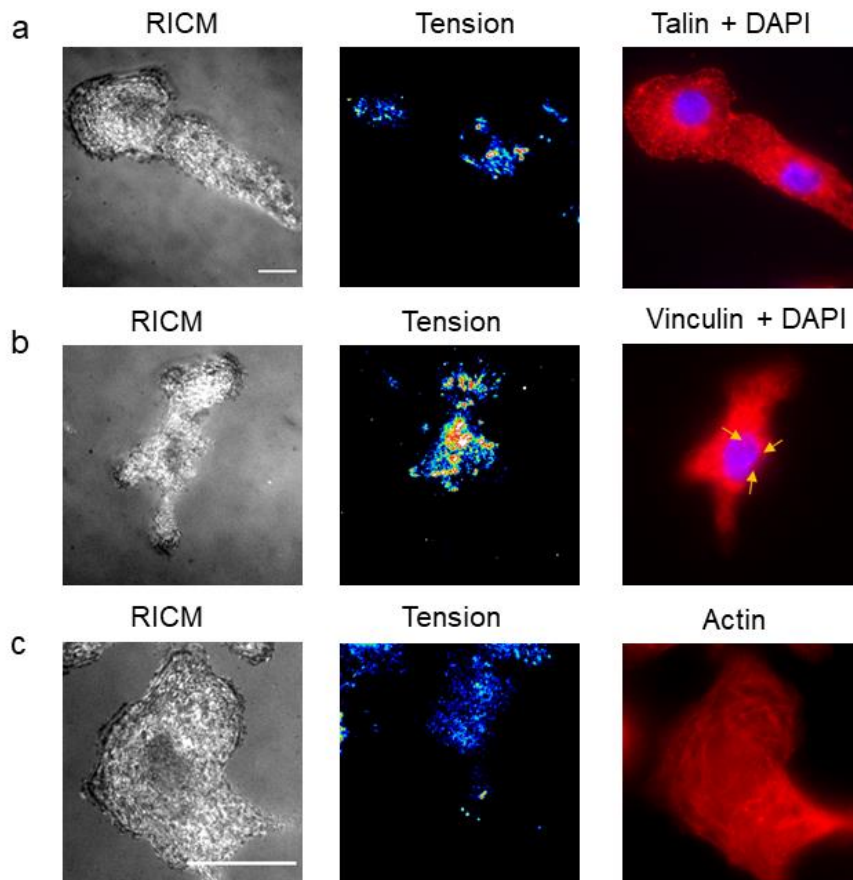
Supplementary Figure 5. Determination of fraction of DNA denatured under cells. a. representative RICM, brightfield and tension (TRITC) images of CMCs on 12, 56 and 160 pN surfaces. b. i. Representative images showing the workflow used to determine the fraction of DNA ruptured under cells on 12 and 56 pN probes. We created an ROI manually based on the RICM image (A) and also a second ROI corresponding to the signal intensity of a surface lacking quencher(C). The background regions surrounding the cell correspond to 0% ruptured probe(B), while (C) provides the mean intensity corresponding to 100% ruptured probe. Using the equation (i) we measured the loss of ligand. ii. For 160 pN probe we measured the loss of ligand by using (ii). c. Bar graph plotting the percentage of DNA probes ruptured on 12, 56 and 160 pN surfaces. Error bars represent the standard deviation from $n = 3$ independent surfaces for each group. Scale bar = 12 μ m.



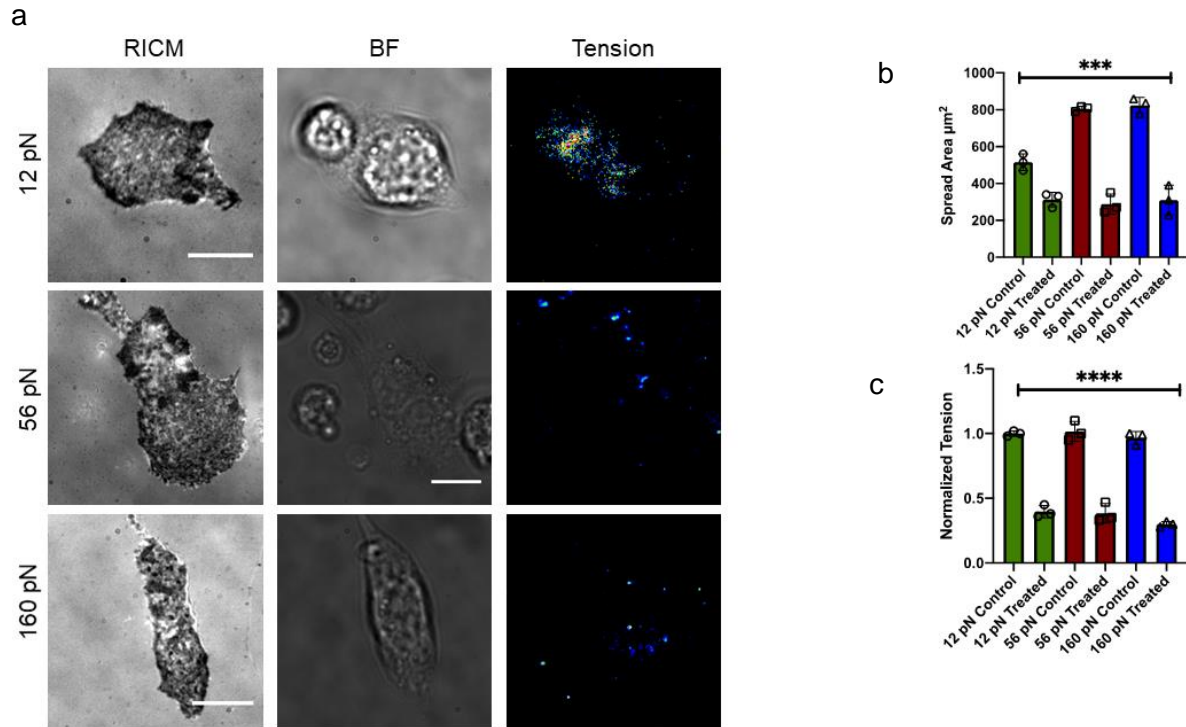
Supplementary Figure 6. Non-force-induced loss of DNA probes. a. Representative RICM, Cy3B and brightfield images of CMCs cultured on 12, 56 and 160 pN surfaces for 6-8 hrs on probes lacking quencher (100% Cy3B). b. Representative images showing the workflow and the equation used to determine the probe loss due to non-mechanical events. c. Bar graph plotting DNA loss on 12, 56 and 160 pN surfaces after 6-8 hrs of incubation. This value was determined by drawing an ROI of the cell based on the RICM channel and then averaging the signal under the cell compared to the signal outside of the cell. Because DNA rupture does not lead to loss of Cy3B signal, we ascribe this loss of signal to nuclease or protease activity as well as the spontaneous dissociation of biotin-streptavidin. d. Bar graph plotting loss of signal due to biotin-streptavidin dissociation over t= 6-8hrs. (**** indicates $p < 0.0001$ respectively from one way ANOVA.) Error bars show standard deviation for $n=3$ where the experiments were conducted from three different cell isolation with three different sets of surface preparation. Scale bar = 12 μm .



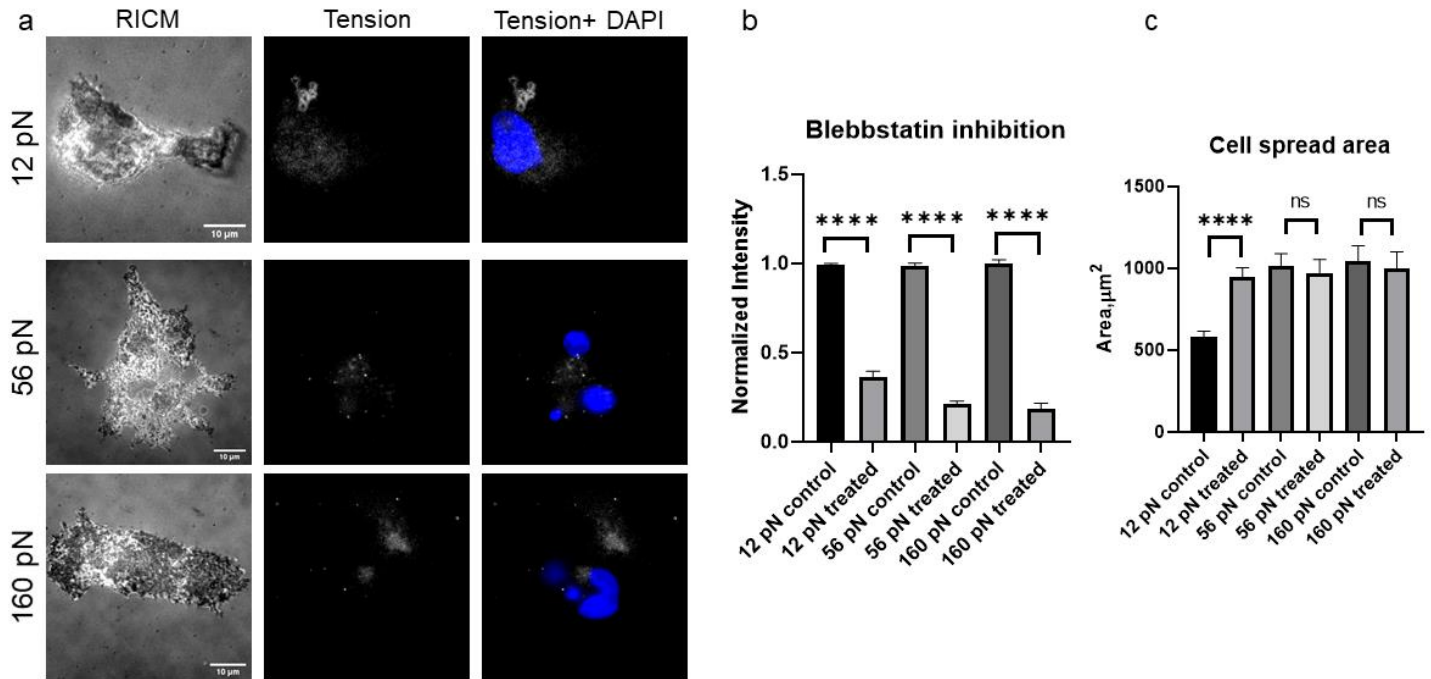
Supplementary Figure 7. Nuclear staining confirms tension puncta localization under nucleus on 56 pN probe. a) Three representative RICM, tension and tension + DAPI images of CMCs on 56 pN rupture probes. Nuclear ROI (red) was selected from DAPI channel and tension was measured by mean fluorescent intensity. For total tension cell outline was selected from RICM channel and mean fluorescent intensity was measured in the tension channel. b) Bar graph showing the comparison of nuclear tension vs peripheral tension, **** represents $p < 0.001$, $N = 3$. Scale bar = 10 μm .



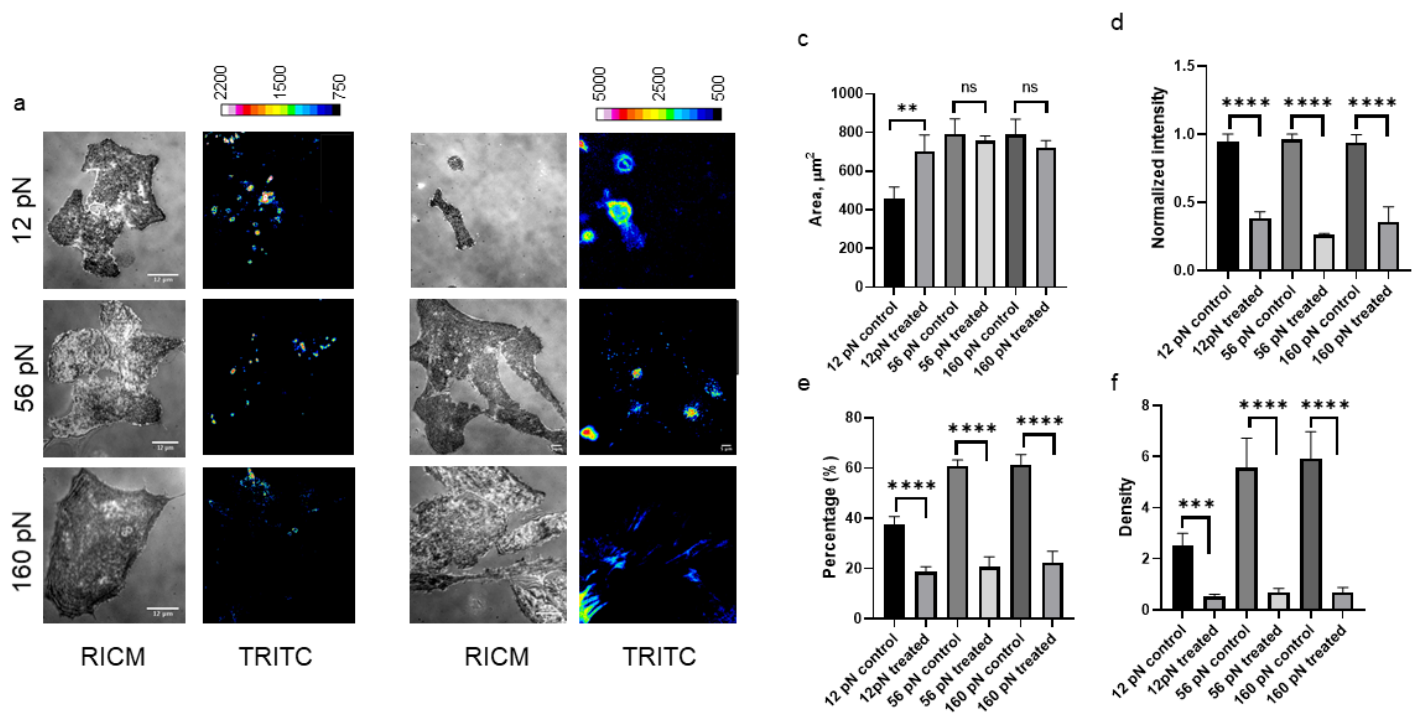
Supplementary Figure 8. Tension colocalization with Actin, talin and vinculin on 56 pN rupture probe. a-c. Representative RICM, tension and immunostaining for talin (a), vinculin (b) and actin (c). Scale bar= 30 μm .



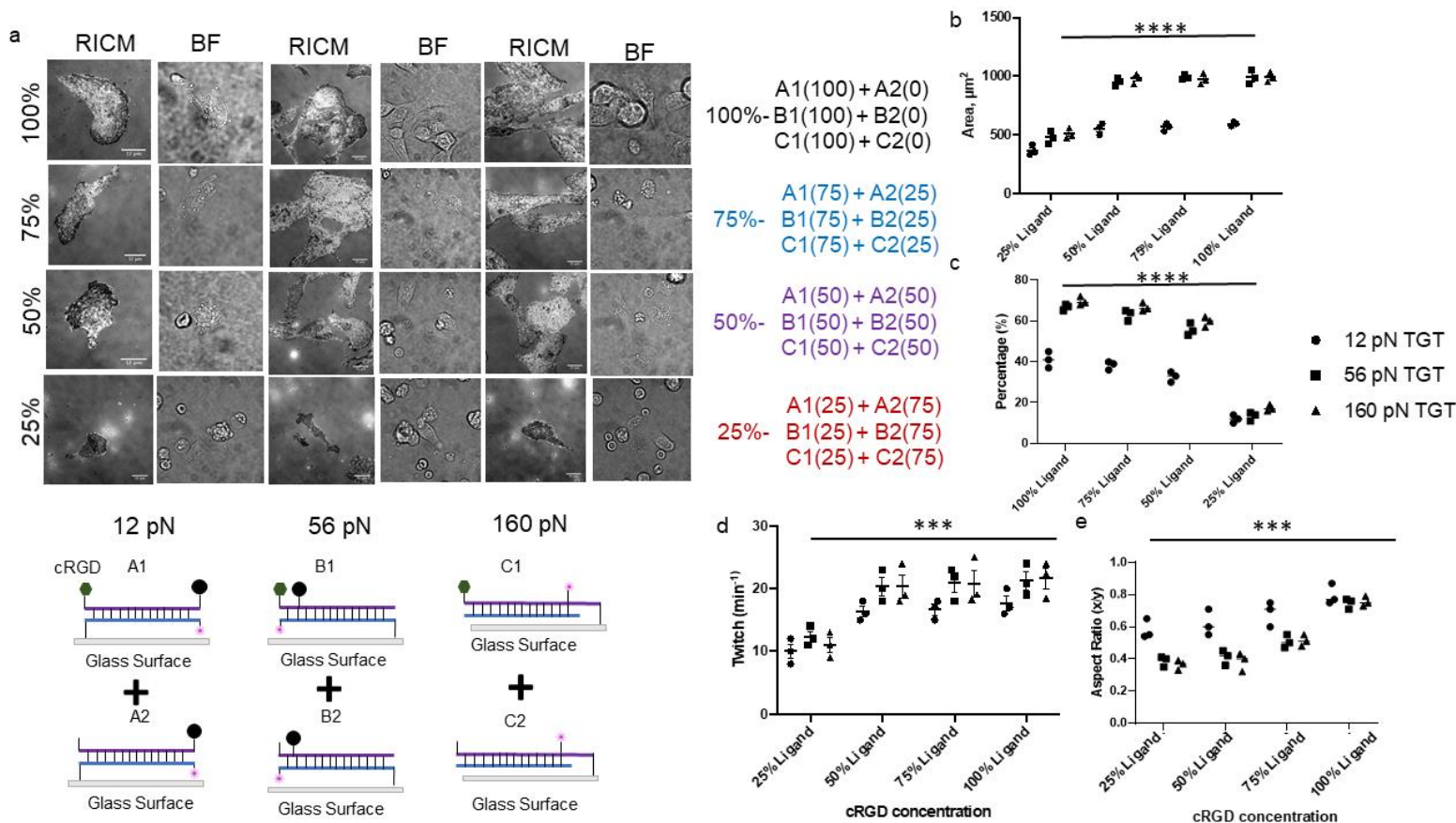
Supplementary Figure 9. Integrin inhibition (Eptifibatide) results in loss of force dependent functional maturation. a. Representative RICM, BF and Tension images of CMC on 12, 56, 160 pN probes treated with 10uM eptifibatide. b-c. Bar graphs showing the spread area and normalized tension (normalized to 12 pN control group) obtained from CMCs that were cultured on 12, 56 and 160 pN probes. Each data point represents a single cell while the bar shows the average. **** and *** indicate $p < 0.0001$, $p < 0.001$ respectively, as determined from one-way ANOVA. Error bars show standard deviation for $n=3$, where each experiment was averaged from three different cell isolations with three different sets of surface preparations. Scale bar=12 μm .



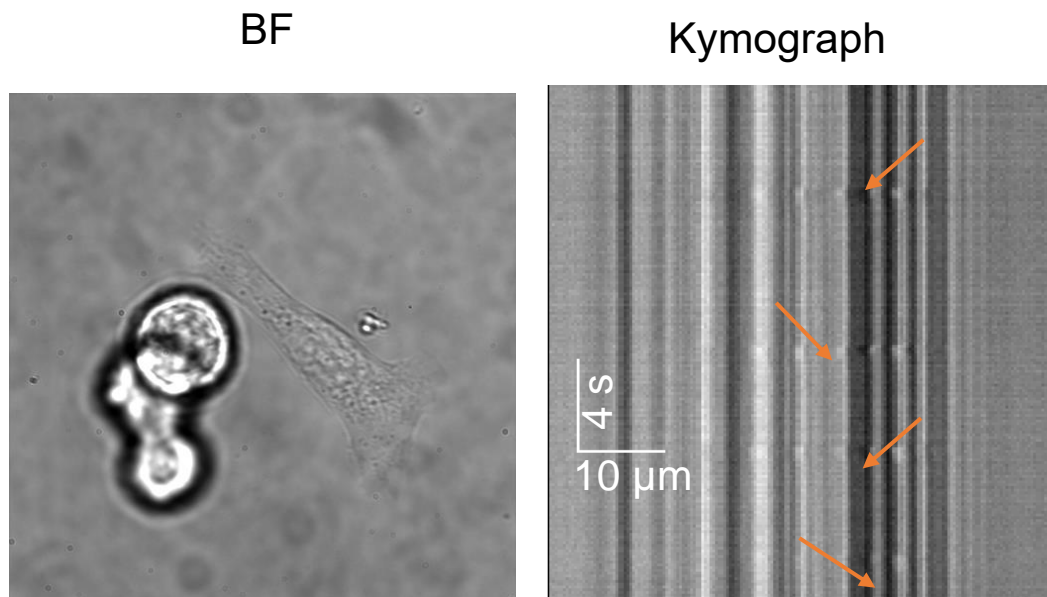
Supplementary Figure 10. Blebbistatin inhibition results in loss of force sensing driven functional maturation of CMCs. a. Representative RCM and Tension (TRITC) images of CMC on 12, 56, 160 pN probes treated with 25 μM Y-27632. b-d. Bar graphs showing the spread area, aspect ratio, and the percentage of beating cells obtained from CMCs that were cultured on 12, 56 and 160 pN probes. Each data point represents a single cell while the bar shows the average. ****, ***, **, and * indicate $p < 0.0001$, $p < 0.001$, $p < 0.01$ and $p < 0.05$, respectively, as determined from one-way ANOVA. Error bars show standard deviation for $n=3$, where each experiment was averaged from three different cell isolations with three different sets of surface preparations. Scale bar=12 μm .



Supplementary Figure 11. ROCK inhibition results in loss of force sensing driven functional maturation of CMCs. a-b. Representative RICM and Tension (TRITC) images of CMC on 12, 56, 160 pN probes treated with and without(control) 25uM Y-27632. b-e. Bar graphs showing the spread area, normalized tension, the percentage of beating cells and density of attached cells obtained from CMCs that were cultured on 12, 56 and 160 pN probes. Each data point represents a single cell while the bar shows the average. ****, ***, **, and * indicate $p < 0.0001$, $p < 0.001$, $p < 0.01$ and $p < 0.05$, respectively, as determined from one-way ANOVA. Error bars show standard deviation for $n=3$, where each experiment was averaged from three different cell isolations with three different sets of surface preparations. Scale bar= $12 \mu\text{m}$.

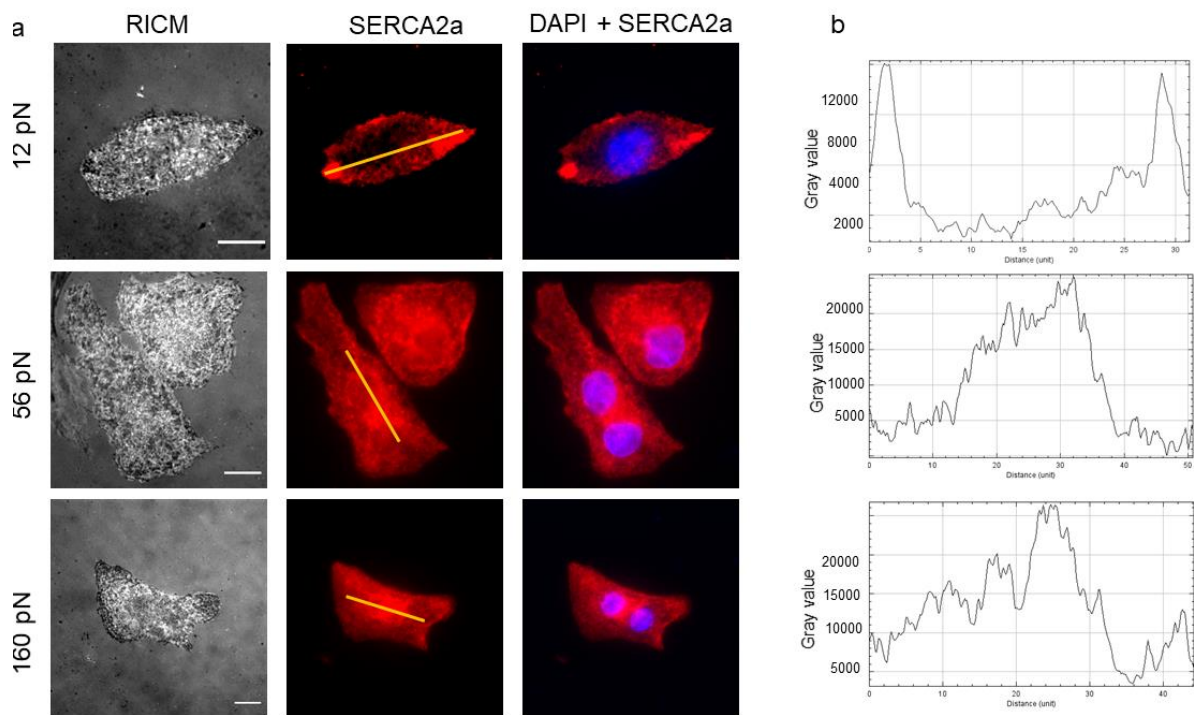


Supplementary Figure 12. Effect of ligand density on cell spreading area and beating frequency. **a.** Representative RICM and BF images of CMC on 12, 56 and 160 pN probes with four different ligand densities (100%, 75%, 50% and 25%). The different ligand densities were achieved by incubating the surface with a binary mixture of two probes: one lacking and the second displaying the RGD ligand. The total concentration of the probes was held at 150 nM to keep a constant DNA density on these surfaces. **b.** Scatter plot showing spread area of CMCs on 12, 56 and 160 pN probes having 100%, 75%, 50% and 25% ligand. The spread area was measured using RICM. **** indicates $p < 0.0001$ from one-way ANOVA. Error bars show standard error of the mean for $n=3$, where each experiment was conducted from three different cell isolations with three different sets of surface preparations. Each experiment included over 20 cells that were analyzed. **c-e.** Scatter plot showing the percentage of beating CMCs, beating frequency and aspect ratio on surfaces of differing ligand density and rupture force (**** indicates $p < 0.0001$ and *** indicates $p < 0.01$, Error bars shows standard deviation for $n=3$, where each experiment was conducted from three different cell isolations with three different sets of surface preparations). Scale bar = 12 μm .

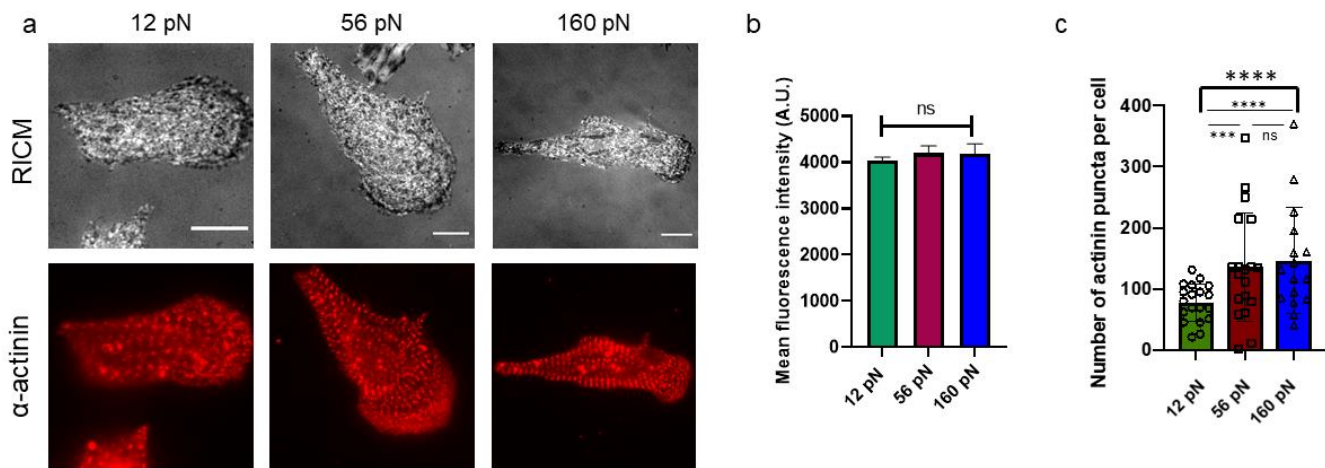


4 beats in 30s timelapse

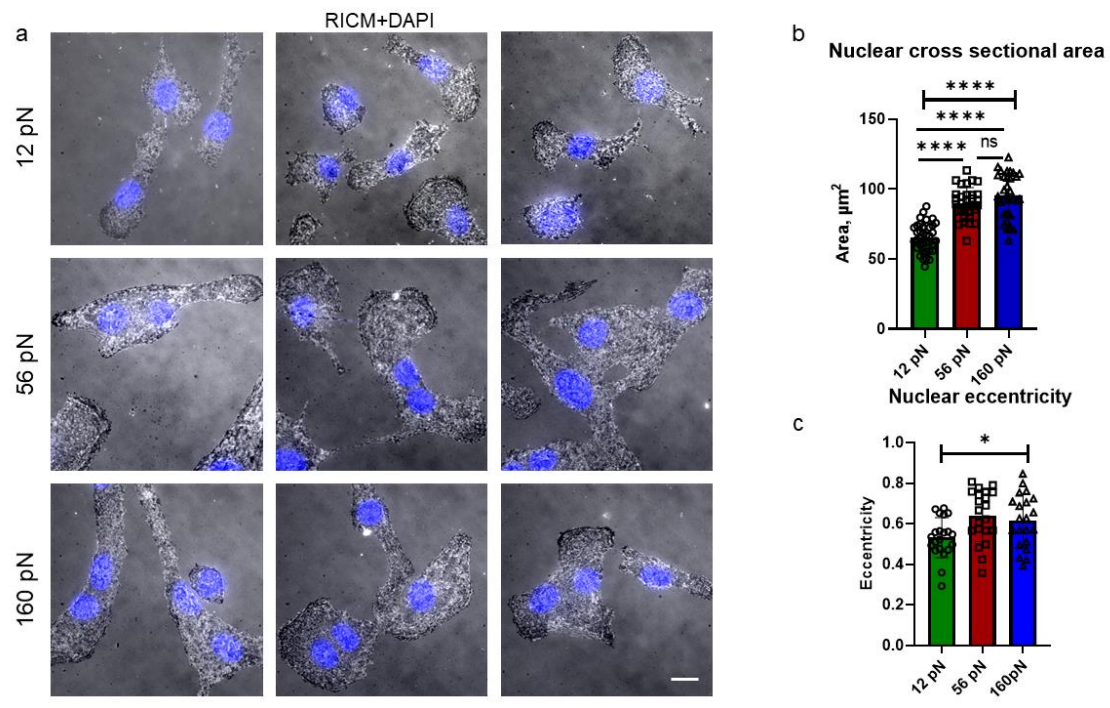
Supplementary Figure 13. Twitching frequency measurement. To measure the twitching frequency, we acquired a time-lapse video of CMC grown on the different DNA probe surfaces and determined the twitching frequency by using kymograph analysis. The data is reported in main **Figure 3b**. Here we show a snapshot from the time-lapse as well as a representative kymograph plot. The twitching frequency of the cells was measured by the “Multikymograph plot” plugin in ImageJ. To use the plugin, a line was drawn in the BF time-lapse image at the center of the twitching cells in the avi acquisition (towards the long axis). The horizontal line (indicated by the arrow) indicates the twitching of cell. the vertical distance is measured in unit of time(s) and the horizontal measurement shows displacement. Each horizontal line is counted as one beat and the time required was calculated by measuring the distance (vertical) from two neighboring lines. From each kymograph we measured three twitching frequencies (twitch/min) and averaged those values for each ROI.



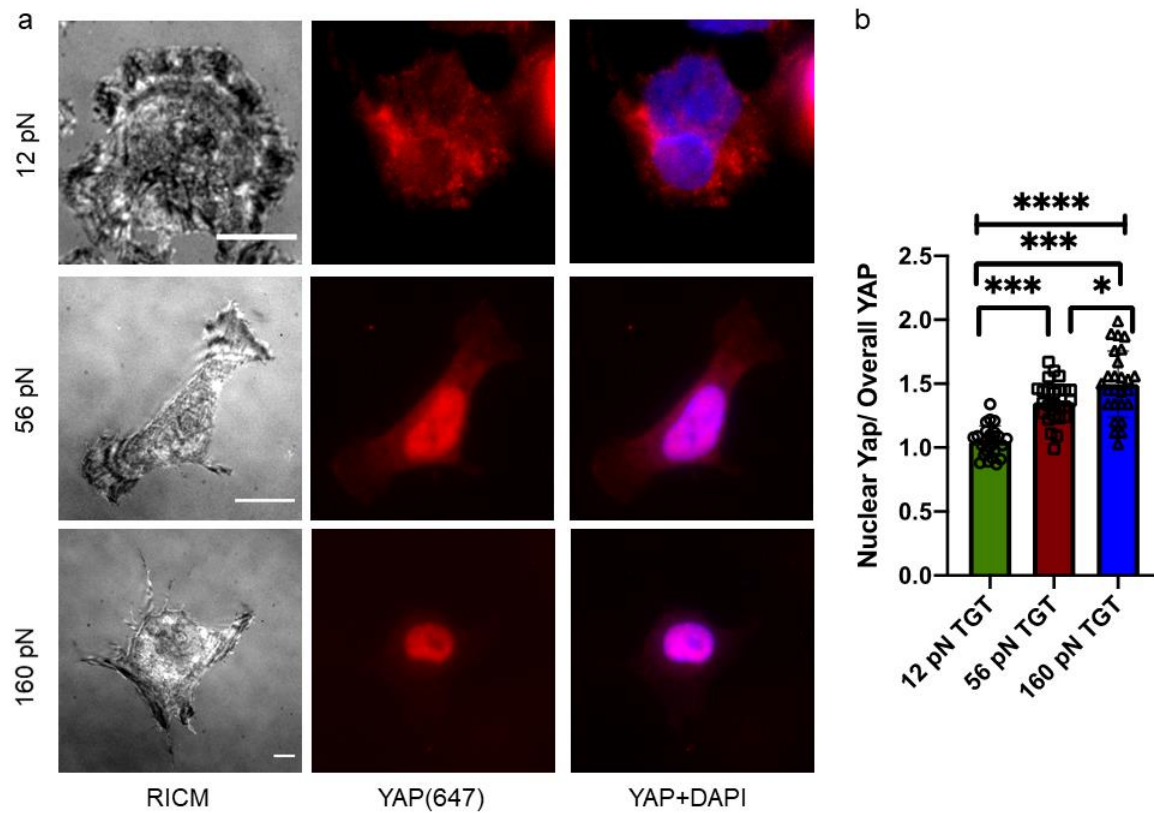
Supplementary Figure 14. Distribution of SERCA2a. a) Representative RICM, SERCA2a, SERCA2a+DAPI images of CMCs on 12 pN, 56 pN and 160 pN rupture probes. b) Line scan of the SERCA2a intensity (yellow line) shows SERCA is mostly localized in the center in CMCs on 56 and 160 pN rupture probes. Scale bar= 12 μ m.



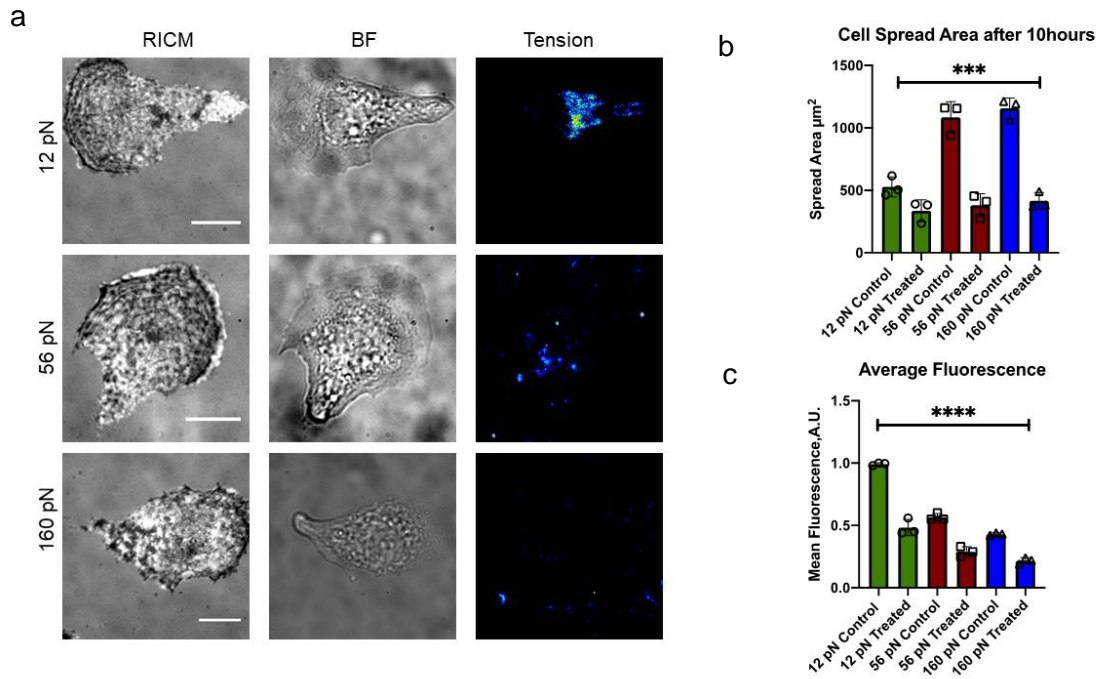
Supplementary Figure 15. α -actinin expression of CMCs on rupture probes a) Representative RICM and α -actinin images of CMCs on 12, 56 and 160 pN surfaces. Bar graph showing mean α -actinin expression. b) bar graph showing number of α -actinin puncta on 12, 56 and 160 pN rupture probes. $N=3$. Scale bar= 10 μ m. c) Number of actinin puncta per cell as measured by supplementary method 3.



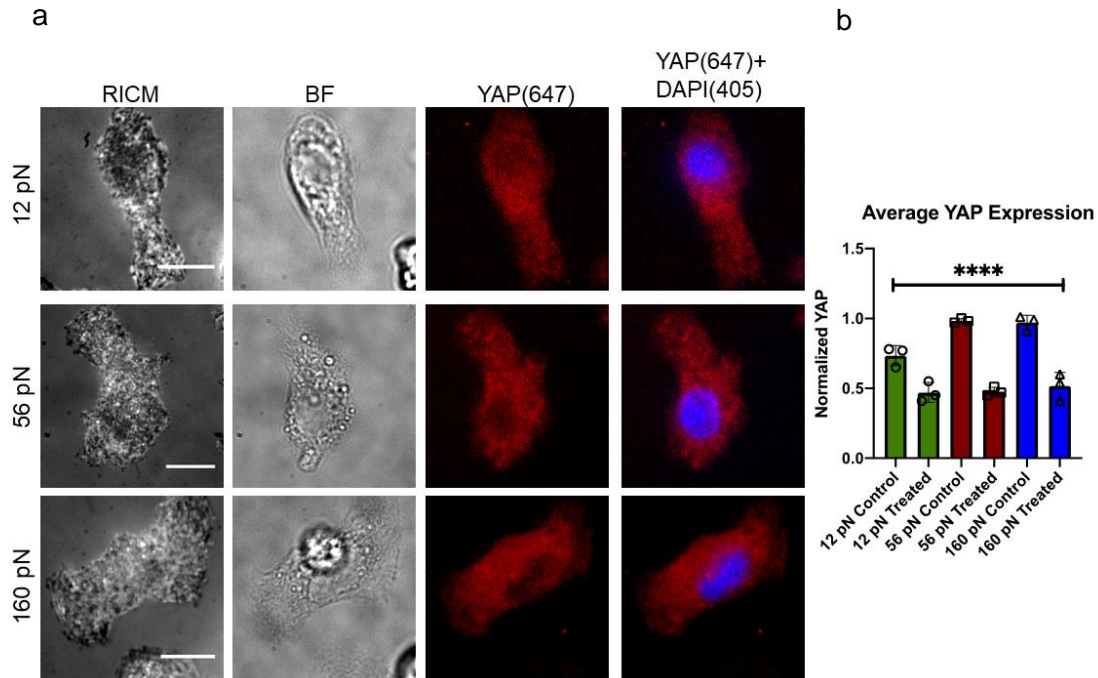
Supplementary Figure 16. Multinucleation on 56 and 160 pN probes. a. Representative RICM, BF and DAPI images of CMC on 12, 56, 160 pN probes stained with nucBlue for nucleus. CMCs on 56 and 160 pN surfaces had higher nuclear diameter and increased multinucleation. Scale bar=15 μm .



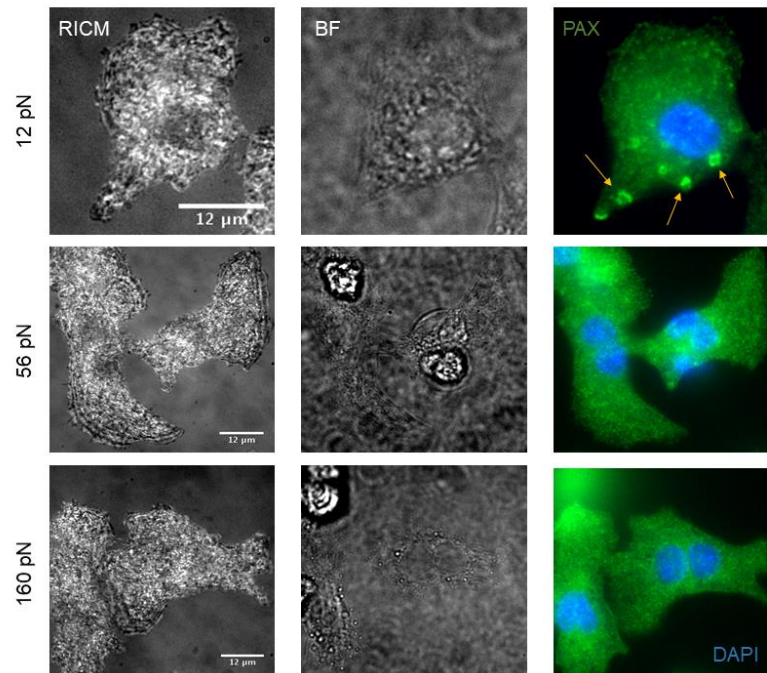
Supplementary Figure 17. CFs have an increased nuclear YAP on 160 and 56 pN probes with greater nuclear YAP signal on 160 pN probes compared to 12 pN probe. a. Representative RICM, YAP (647) and overlay of the DAPI (405) and YAP (647) images of CFs cultured on 12, 56, 160 pN probes. b. Bar graph plotting YAP nuclear translocation calculated by nuclear YAP/ overall YAP for CFs on 12, 56 and 160 pN probes. ****, *** and * indicates $p < 0.0001$, $p < 0.001$ and $p < 0.05$ respectively, from one-way ANOVA. Error bars show the standard error of the mean for $n=3$, where each n experiment was obtained from unique cell isolations. Scale bar=5 μm .



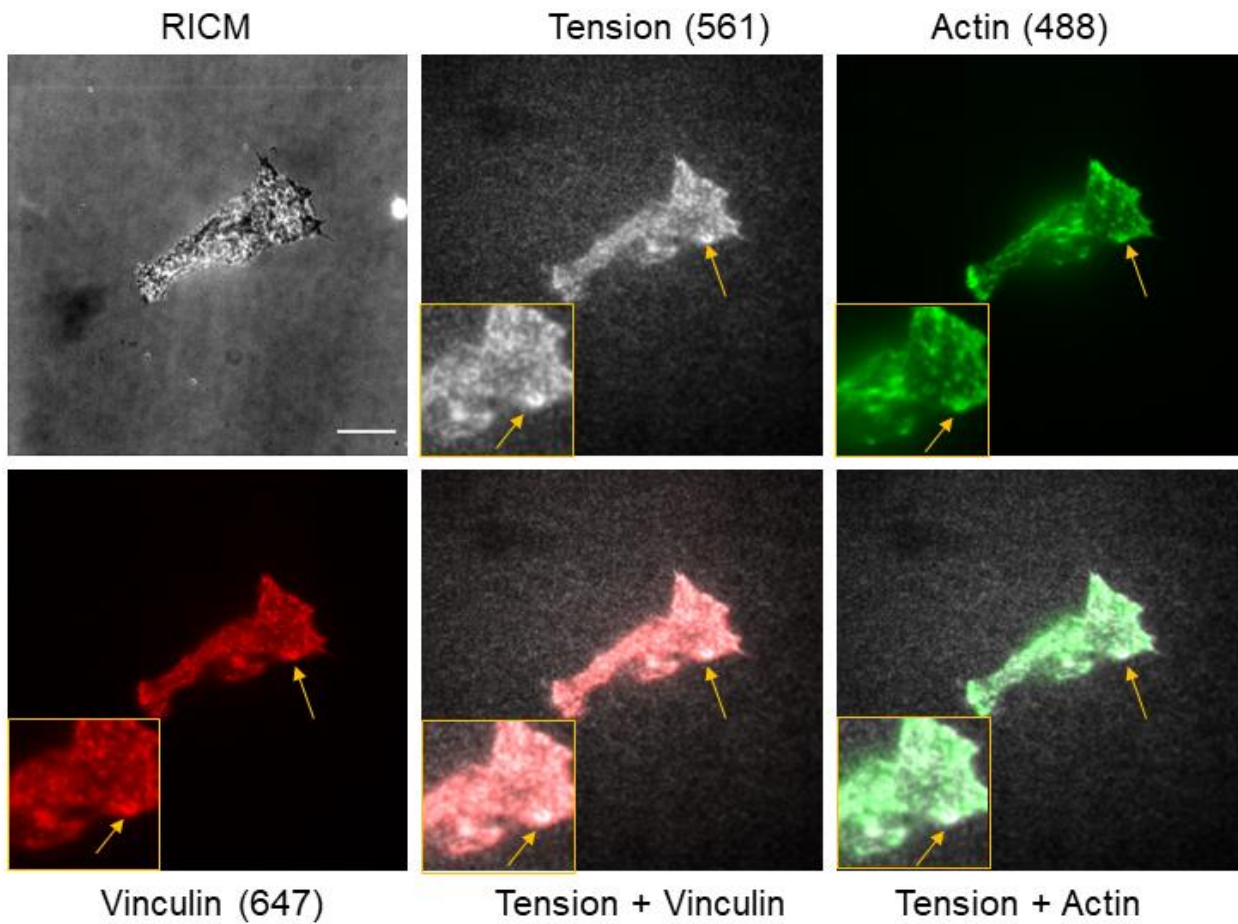
Supplementary Figure 18. MEK inhibition dampens integrin tension and force sensing of CMCs a. Representative RICM, BF and tension images of CMCs grown on 12, 56, 160 pN probe surfaces for cells pre-treated with 10 mM u1026. Cells were pretreated with drug for 30 min. b. Bar graph plotting the spread area of CMCs on three different probes. c. Bar graphs show the normalized tension (normalized with untreated CMCs tension on 12 pN probes). **** and *** indicates $p < 0.0001$ and $p < 0.001$ respectively, from one-way ANOVA. Error bars show standard error of the mean for $n=3$, where each experiment was obtained from a unique cell isolation. Scale bar= 10 µm.



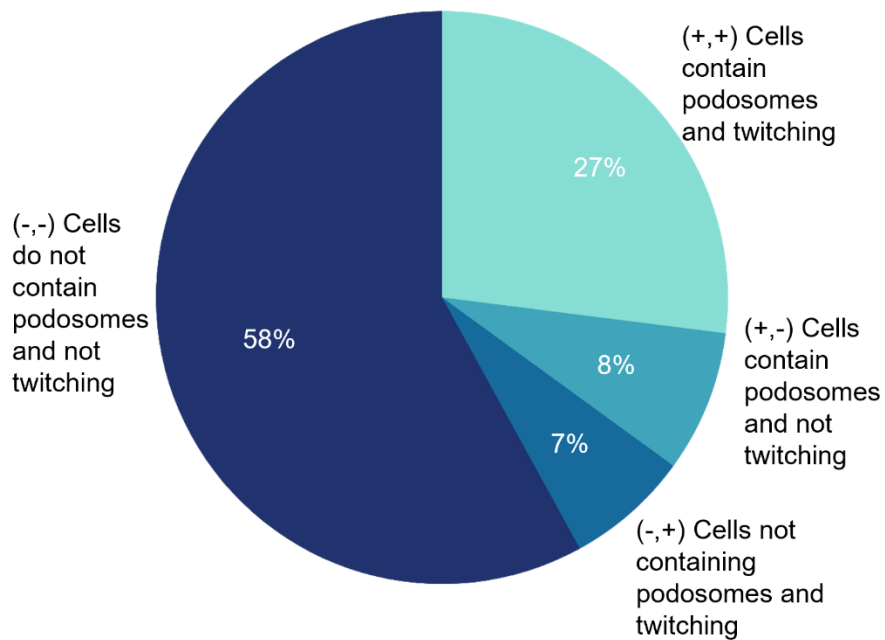
Supplementary Figure 19. MEK inhibition downregulates YAP expression of CMCs on all three different probes a. Representative RICM, BF, YAP (cy5) and overlay of DAPI and YAP images of CMCs on 12, 56, 160 pN probes. Cells were pre-treated with 10 mM u1026 for 30 min prior to plating. c. Bar graph shows the normalized YAP expression (normalized to untreated cells on the 160 pN probes). **** indicates $p < 0.0001$ from one-way ANOVA. Error bars show standard error of the mean for $n=3$, where each experiment was obtained from a unique cell isolation. Scale bar=10 μm .



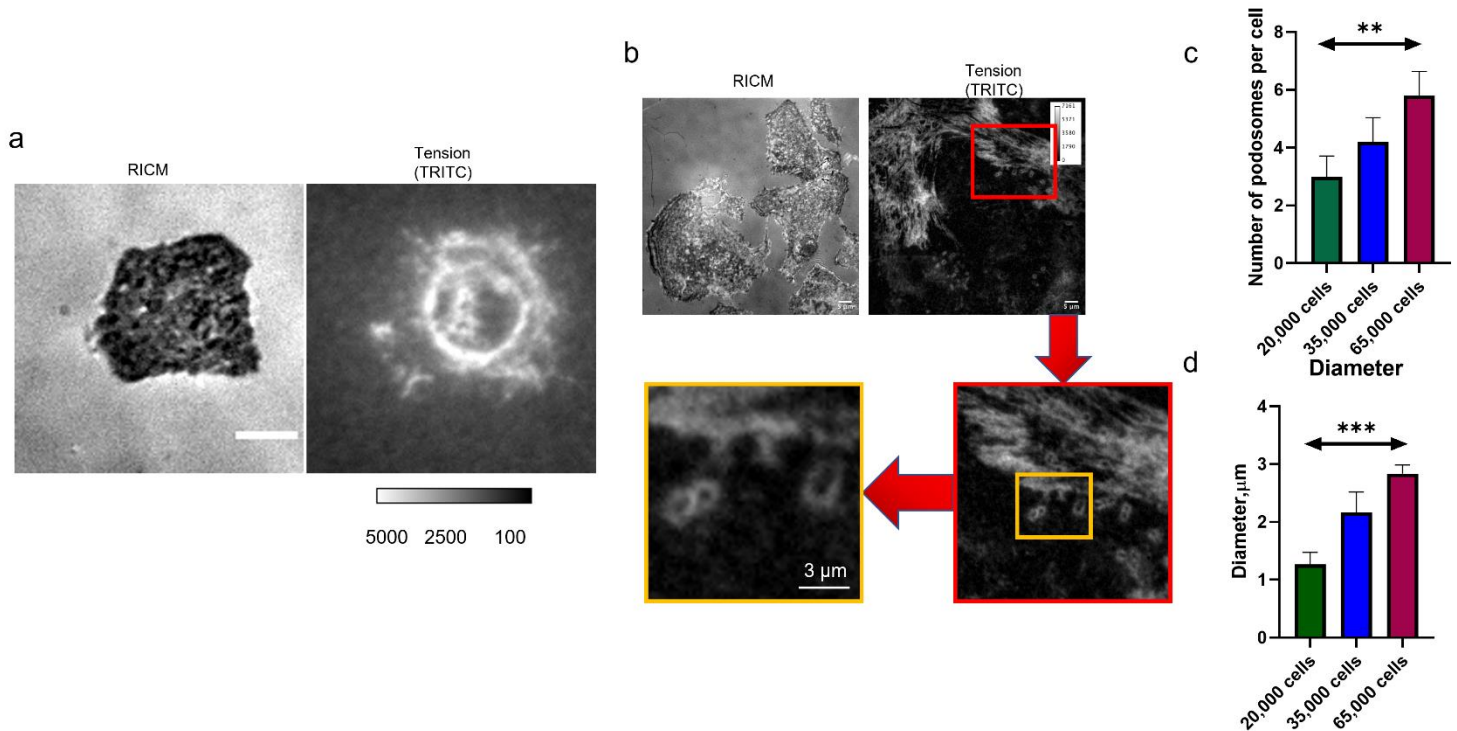
Supplementary Figure 20. Paxillin staining confirms podosome like puncta on 12 pN probes. Representative RICM, BF and DAPI+ FITC (paxillin) images of CMCs stained with phospho-paxillin antibody. CMCs on 12 pN had podosome like puncta on 12 pN probes compared to the 56 and 160 pN probes. Scale bar=12 μm.



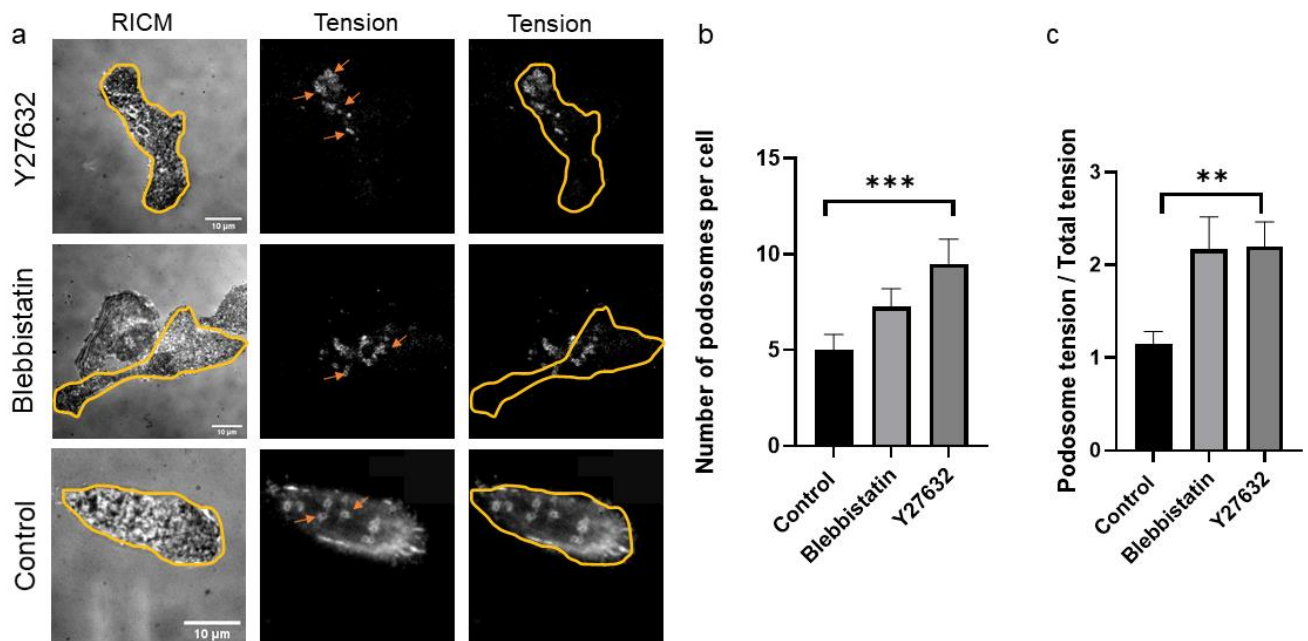
Supplementary Figure 21. Vinculin and Actin staining showing colocalized podosome like puncta on 12 pN probes. Representative RBCM, BF, tension, vinculin, actin, tension + vinculin and tension + actin respective images of CMC stained with phalloidin and vinculin antibody. Scale bar=20 μm .



Supplementary Figure 22. Pie chart quantifying podosome formation and beating myocytes on 12 pN probes. The chart shows most of the CMCs that had contractility also had podosomes like organization. (from $n > 3$, where cells were collected from three different isolation and three different sets of surface preparations).



Supplementary Figure 23. Podosome formation depends on the density of seeded cells. a. Representative RICM and tension images of podosome like structures that form under CMCs seeded on a 12 pN surface (2 hour after seeding). Scale bar= 5 μm b. Representative RICM and tension images of densely seeded (~65,000) CMCs on 12 pN surface forming multiple podosomes near intercellular junctions. The red box indicates a region of interest with number of podosome like structures and the zoom-ins highlight this region. c-d. Bar graph plotting the number of podosomes and diameter of podosomes as a function of cell seeding density on 12 pN surfaces. (** indicates $p < 0.01$ from one-way ANOVA. Error bars show standard error of the mean for $n=3$, where each experiment was obtained from unique cell isolations.



Supplementary Figure 24. Podosome formation depends on the density of seeded cells. a. Representative RICM and tension images of podosome like structures that form under CMCs seeded on a 12 pN surface (2 hour after seeding). Scale bar= 5 μ m b. Representative RICM and tension images of densely seeded (~65,000) CMCs on 12 pN surface forming multiple podosomes near intercellular junctions. The red box indicates a region of interest with number of podosome like structures and the zoom-ins highlight this region. c-d. Bar graph plotting the number of podosomes and diameter of podosomes as a function of cell seeding density on 12 pN surfaces. (** indicates $p < 0.01$ from one-way ANOVA. Error bars show standard error of the mean for $n=3$, where each experiment was obtained from unique cell isolations.

Author contributions

Sk A.R. and K.S. conceived of the project. SK A.R. designed and performed all of the experiments. A.B. assisted with automated calcium analysis. J.D.C helped with automated analysis of actinin staining. N. F. and H.C. helped with cell isolation and biological assay discussion. Y. D. helped with gel experiment. K.S and Sk A. R. wrote the manuscript. All the authors helped revise the manuscript.

Acknowledgement

This work is supported by NIH NIGMS R01GM124472 NIH NIGMS 1R01GM131099 NIH NHLBI R01HL142866. The authors especially want to thank Dr. Roxanne Glazier and Dr. Allison Ramey for discussion leading to planning of experiments. Also, to Dr. Hiroaki Ogasawara for assisting in acquiring mass spectrometry of oligo used in this project.

References

1. Ishii, Y.; Langberg, J.; Rosborough, K.; Mikawa, T., Endothelial cell lineages of the heart. *Cell Tissue Res* **2009**, *335* (1), 67-73.
2. Rochais, F.; Mesbah, K.; Kelly, R. G., Signaling pathways controlling second heart field development. *Circ Res* **2009**, *104* (8), 933-42.
3. Wu, S. M.; Chien, K. R.; Mummery, C., Origins and fates of cardiovascular progenitor cells. *Cell* **2008**, *132* (4), 537-43.
4. Guo, Y.; Pu, W. T., Cardiomyocyte Maturation: New Phase in Development. *Circ Res* **2020**, *126* (8), 1086-1106.
5. Cui, M.; Wang, Z.; Bassel-Duby, R.; Olson, E. N., Genetic and epigenetic regulation of cardiomyocytes in development, regeneration and disease. *Development* **2018**, *145* (24).
6. Mummery, C. L.; Zhang, J.; Ng, E. S.; Elliott, D. A.; Elefanty, A. G.; Kamp, T. J., Differentiation of human embryonic stem cells and induced pluripotent stem cells to cardiomyocytes: a methods overview. *Circ Res* **2012**, *111* (3), 344-58.
7. Iismaa, S. E.; Kaidonis, X.; Nicks, A. M.; Bogush, N.; Kikuchi, K.; Naqvi, N.; Harvey, R. P.; Husain, A.; Graham, R. M., Comparative regenerative mechanisms across different mammalian tissues. *NPJ Regen Med* **2018**, *3*, 6.
8. Kosmalska, A. J.; Casares, L.; Elosegui-Artola, A.; Thottacherry, J. J.; Moreno-Vicente, R.; Gonzalez-Tarrago, V.; Del Pozo, M. A.; Mayor, S.; Arroyo, M.; Navajas, D.; Trepate, X.; Gauthier, N. C.; Roca-Cusachs, P., Physical principles of membrane remodelling during cell mechanoadaptation. *Nat Commun* **2015**, *6*, 7292.

9. Zhao, M. T.; Ye, S.; Su, J.; Garg, V., Cardiomyocyte Proliferation and Maturation: Two Sides of the Same Coin for Heart Regeneration. *Front Cell Dev Biol* **2020**, *8*, 594226.
10. Scuderi, G. J.; Butcher, J., Naturally Engineered Maturation of Cardiomyocytes. *Front Cell Dev Biol* **2017**, *5*, 50.
11. Kannan, S.; Kwon, C., Regulation of cardiomyocyte maturation during critical perinatal window. *J Physiol* **2020**, *598* (14), 2941-2956.
12. Nguyen, P. K.; Neofytou, E.; Rhee, J. W.; Wu, J. C., Potential Strategies to Address the Major Clinical Barriers Facing Stem Cell Regenerative Therapy for Cardiovascular Disease: A Review. *JAMA Cardiol* **2016**, *1* (8), 953-962.
13. Denning, C.; Borgdorff, V.; Crutchley, J.; Firth, K. S.; George, V.; Kalra, S.; Kondrashov, A.; Hoang, M. D.; Mosqueira, D.; Patel, A.; Prodanov, L.; Rajamohan, D.; Skarnes, W. C.; Smith, J. G.; Young, L. E., Cardiomyocytes from human pluripotent stem cells: From laboratory curiosity to industrial biomedical platform. *Biochim Biophys Acta* **2016**, *1863* (7 Pt B), 1728-48.
14. Grskovic, M.; Javaherian, A.; Strulovici, B.; Daley, G. Q., Induced pluripotent stem cells--opportunities for disease modelling and drug discovery. *Nat Rev Drug Discov* **2011**, *10* (12), 915-29.
15. du Pre, B. C.; Doevendans, P. A.; van Laake, L. W., Stem cells for cardiac repair: an introduction. *J Geriatr Cardiol* **2013**, *10* (2), 186-97.
16. Bellin, M.; Marchetto, M. C.; Gage, F. H.; Mummery, C. L., Induced pluripotent stem cells: the new patient? *Nat Rev Mol Cell Biol* **2012**, *13* (11), 713-26.

17. Dambrot, C.; Passier, R.; Atsma, D.; Mummery, C. L., Cardiomyocyte differentiation of pluripotent stem cells and their use as cardiac disease models. *Biochem J* **2011**, *434* (1), 25-35.
18. McCain, M. L.; Parker, K. K., Mechanotransduction: the role of mechanical stress, myocyte shape, and cytoskeletal architecture on cardiac function. *Pflugers Arch* **2011**, *462* (1), 89-104.
19. Tallawi, M.; Rai, R.; Boccaccini, A. R.; Aifantis, K. E., Effect of substrate mechanics on cardiomyocyte maturation and growth. *Tissue Eng Part B Rev* **2015**, *21* (1), 157-65.
20. Zhu, R.; Blazeski, A.; Poon, E.; Costa, K. D.; Tung, L.; Boheler, K. R., Physical developmental cues for the maturation of human pluripotent stem cell-derived cardiomyocytes. *Stem Cell Res Ther* **2014**, *5* (5), 117.
21. Keung, W.; Boheler, K. R.; Li, R. A., Developmental cues for the maturation of metabolic, electrophysiological and calcium handling properties of human pluripotent stem cell-derived cardiomyocytes. *Stem Cell Res Ther* **2014**, *5* (1), 17.
22. Hughes, C. J. R.; Jacobs, J. R., Dissecting the Role of the Extracellular Matrix in Heart Disease: Lessons from the Drosophila Genetic Model. *Vet Sci* **2017**, *4* (2).
23. Jacot, J. G.; McCulloch, A. D.; Omens, J. H., Substrate stiffness affects the functional maturation of neonatal rat ventricular myocytes. *Biophys J* **2008**, *95* (7), 3479-87.
24. Boothe, S. D.; Myers, J. D.; Pok, S.; Sun, J.; Xi, Y.; Nieto, R. M.; Cheng, J.; Jacot, J. G., The Effect of Substrate Stiffness on Cardiomyocyte Action Potentials. *Cell Biochem Biophys* **2016**, *74* (4), 527-535.

25. Rodriguez, A. G.; Han, S. J.; Regnier, M.; Sniadecki, N. J., Substrate stiffness increases twitch power of neonatal cardiomyocytes in correlation with changes in myofibril structure and intracellular calcium. *Biophys J* **2011**, *101* (10), 2455-64.
26. Rodriguez, M. L.; Graham, B. T.; Pabon, L. M.; Han, S. J.; Murry, C. E.; Sniadecki, N. J., Measuring the contractile forces of human induced pluripotent stem cell-derived cardiomyocytes with arrays of microposts. *J Biomech Eng* **2014**, *136* (5), 051005.
27. Pandey, P.; Hawkes, W.; Hu, J.; Megone, W. V.; Gautrot, J.; Anilkumar, N.; Zhang, M.; Hirvonen, L.; Cox, S.; Ehler, E.; Hone, J.; Sheetz, M.; Iskratsch, T., Cardiomyocytes Sense Matrix Rigidity through a Combination of Muscle and Non-muscle Myosin Contractions. *Dev Cell* **2018**, *44* (3), 326-336 e3.
28. Lyon, R. C.; Zanella, F.; Omens, J. H.; Sheikh, F., Mechanotransduction in cardiac hypertrophy and failure. *Circ Res* **2015**, *116* (8), 1462-1476.
29. Hidalgo, C.; Donoso, P., Cell signaling. Getting to the heart of mechanotransduction. *Science* **2011**, *333* (6048), 1388-90.
30. Wang, X.; Ha, T., Defining single molecular forces required to activate integrin and notch signaling. *Science* **2013**, *340* (6135), 991-4.
31. Zhang, Y.; Qiu, Y.; Blanchard, A. T.; Chang, Y.; Brockman, J. M.; Ma, V. P.-Y.; Lam, W. A.; Salaita, K., Platelet integrins exhibit anisotropic mechanosensing and harness piconewton forces to mediate platelet aggregation. *Proceedings of the National Academy of Sciences* **2018**, *115* (2), 325-330.
32. Galie, P. A.; Khalid, N.; Carnahan, K. E.; Westfall, M. V.; Stegemann, J. P., Substrate stiffness affects sarcomere and costamere structure and electrophysiological function of isolated adult cardiomyocytes. *Cardiovasc Pathol* **2013**, *22* (3), 219-27.

33. Lammerding, J.; Kamm, R. D.; Lee, R. T., Mechanotransduction in cardiac myocytes. *Ann N Y Acad Sci* **2004**, *1015*, 53-70.
34. Liu, Y.; Galior, K.; Ma, V. P.; Salaita, K., Molecular Tension Probes for Imaging Forces at the Cell Surface. *Acc Chem Res* **2017**, *50* (12), 2915-2924.
35. Zhang, Y.; Ge, C.; Zhu, C.; Salaita, K., DNA-based digital tension probes reveal integrin forces during early cell adhesion. *Nat Commun* **2014**, *5*, 5167.
36. Paolini, P.; Pick, D.; Lapira, J.; Sannino, G.; Pasqualini, L.; Ludka, C.; Sprague, L. J.; Zhang, X.; Bartolotta, E. A.; Vazquez-Hidalgo, E.; Barba, D. T.; Bazan, C.; Hardiman, G., Developmental and extracellular matrix-remodeling processes in rosiglitazone-exposed neonatal rat cardiomyocytes. *Pharmacogenomics* **2014**, *15* (6), 759-74.
37. Israeli-Rosenberg, S.; Manso, A. M.; Okada, H.; Ross, R. S., Integrins and integrin-associated proteins in the cardiac myocyte. *Circ Res* **2014**, *114* (3), 572-586.
38. Ogawa, E.; Saito, Y.; Harada, M.; Kamitani, S.; Kuwahara, K.; Miyamoto, Y.; Ishikawa, M.; Hamanaka, I.; Kajiyama, N.; Takahashi, N.; Nakagawa, O.; Masuda, I.; Kishimoto, I.; Nakao, K., Outside-in signalling of fibronectin stimulates cardiomyocyte hypertrophy in cultured neonatal rat ventricular myocytes. *J Mol Cell Cardiol* **2000**, *32* (5), 765-76.
39. Neiman, G.; Scarafia, M. A.; La Greca, A.; Santin Velazque, N. L.; Garate, X.; Waisman, A.; Mobbs, A. M.; Kasai-Brunswick, T. H.; Mesquita, F.; Martire-Greco, D.; Moro, L. N.; Luzzani, C.; Bastos Carvalho, A.; Sevelever, G. E.; Campos de Carvalho, A.; Guberman, A. S.; Miriuka, S. G., Integrin alpha-5 subunit is critical for the early stages of human pluripotent stem cell cardiac differentiation. *Sci Rep* **2019**, *9* (1), 18077.

40. Terracio, L.; Rubin, K.; Gullberg, D.; Balog, E.; Carver, W.; Jyring, R.; Borg, T. K., Expression of collagen binding integrins during cardiac development and hypertrophy. *Circ Res* **1991**, *68* (3), 734-44.
41. Jurchenko, C.; Chang, Y.; Narui, Y.; Zhang, Y.; Salaita, K. S., Integrin-generated forces lead to streptavidin-biotin unbinding in cellular adhesions. *Biophys J* **2014**, *106* (7), 1436-46.
42. Estevez, B.; Shen, B.; Du, X., Targeting integrin and integrin signaling in treating thrombosis. *Arterioscler Thromb Vasc Biol* **2015**, *35* (1), 24-9.
43. Wang, S. Q.; Song, L. S.; Lakatta, E. G.; Cheng, H., Ca²⁺ signalling between single L-type Ca²⁺ channels and ryanodine receptors in heart cells. *Nature* **2001**, *410* (6828), 592-6.
44. Oyehaug, L.; Loose, K. O.; Jolle, G. F.; Roe, A. T.; Sjaastad, I.; Christensen, G.; Sejersted, O. M.; Louch, W. E., Synchrony of cardiomyocyte Ca(2+) release is controlled by T-tubule organization, SR Ca(2+) content, and ryanodine receptor Ca(2+) sensitivity. *Biophys J* **2013**, *104* (8), 1685-97.
45. Martewicz, S.; Serena, E.; Zatti, S.; Keller, G.; Elvassore, N., Substrate and mechanotransduction influence SERCA2a localization in human pluripotent stem cell-derived cardiomyocytes affecting functional performance. *Stem Cell Res* **2017**, *25*, 107-114.
46. Corbin, E. A.; Vite, A.; Peyster, E. G.; Bhoopalam, M.; Brandimarto, J.; Wang, X.; Bennett, A. I.; Clark, A. T.; Cheng, X.; Turner, K. T.; Musunuru, K.; Margulies, K. B., Tunable and Reversible Substrate Stiffness Reveals a Dynamic Mechanosensitivity of Cardiomyocytes. *ACS Appl Mater Interfaces* **2019**, *11* (23), 20603-20614.

47. Velayutham, N.; Alfieri, C. M.; Agnew, E. J.; Riggs, K. W.; Baker, R. S.; Ponny, S. R.; Zafar, F.; Yutzey, K. E., Cardiomyocyte cell cycling, maturation, and growth by multinucleation in postnatal swine. *J Mol Cell Cardiol* **2020**, *146*, 95-108.
48. Milliron, H. Y.; Weiland, M. J.; Kort, E. J.; Jovinge, S., Isolation of Cardiomyocytes Undergoing Mitosis With Complete Cytokinesis. *Circ Res* **2019**, *125* (12), 1070-1086.
49. Botting, K. J.; Wang, K. C.; Padhee, M.; McMillen, I. C.; Summers-Pearce, B.; Rattanatray, L.; Cutri, N.; Posterino, G. S.; Brooks, D. A.; Morrison, J. L., Early origins of heart disease: low birth weight and determinants of cardiomyocyte endowment. *Clin Exp Pharmacol Physiol* **2012**, *39* (9), 814-23.
50. Liu, Z.; Yue, S.; Chen, X.; Kubin, T.; Braun, T., Regulation of cardiomyocyte polyploidy and multinucleation by CyclinG1. *Circ Res* **2010**, *106* (9), 1498-506.
51. Landim-Vieira, M.; Schipper, J. M.; Pinto, J. R.; Chase, P. B., Cardiomyocyte nuclearity and ploidy: when is double trouble? *J Muscle Res Cell Motil* **2020**, *41* (4), 329-340.
52. Dupont, S., Role of YAP/TAZ in cell-matrix adhesion-mediated signalling and mechanotransduction. *Exp Cell Res* **2016**, *343* (1), 42-53.
53. Elbediwy, A.; Thompson, B. J., Evolution of mechanotransduction via YAP/TAZ in animal epithelia. *Curr Opin Cell Biol* **2018**, *51*, 117-123.
54. Yamashiro, Y.; Thang, B. Q.; Ramirez, K.; Shin, S. J.; Kohata, T.; Ohata, S.; Nguyen, T. A. V.; Ohtsuki, S.; Nagayama, K.; Yanagisawa, H., Matrix mechanotransduction mediated by thrombospondin-1/integrin/YAP in the vascular remodeling. *Proc Natl Acad Sci U S A* **2020**, *117* (18), 9896-9905.

55. Elosegui-Artola, A.; Andreu, I.; Beedle, A. E. M.; Lezamiz, A.; Uroz, M.; Kosmalska, A. J.; Oria, R.; Kechagia, J. Z.; Rico-Lastres, P.; Le Roux, A. L.; Shanahan, C. M.; Trepas, X.; Navajas, D.; Garcia-Manyes, S.; Roca-Cusachs, P., Force Triggers YAP Nuclear Entry by Regulating Transport across Nuclear Pores. *Cell* **2017**, *171* (6), 1397-1410 e14.
56. Mo, J. S.; Park, H. W.; Guan, K. L., The Hippo signaling pathway in stem cell biology and cancer. *EMBO Rep* **2014**, *15* (6), 642-56.
57. Boopathy, G. T. K.; Hong, W., Role of Hippo Pathway-YAP/TAZ Signaling in Angiogenesis. *Front Cell Dev Biol* **2019**, *7*, 49.
58. Vite, A.; Zhang, C.; Yi, R.; Emms, S.; Radice, G. L., alpha-Catenin-dependent cytoskeletal tension controls Yap activity in the heart. *Development* **2018**, *145* (5).
59. Shaul, Y. D.; Seger, R., The MEK/ERK cascade: from signaling specificity to diverse functions. *Biochim Biophys Acta* **2007**, *1773* (8), 1213-26.
60. Zhang, W.; Liu, H. T., MAPK signal pathways in the regulation of cell proliferation in mammalian cells. *Cell Res* **2002**, *12* (1), 9-18.
61. Li, L.; Wang, J.; Zhang, Y.; Zhang, Y.; Ma, L.; Weng, W.; Qiao, Y.; Xiao, W.; Wang, H.; Yu, W.; Pan, Q.; He, Y.; Sun, F., MEK1 promotes YAP and their interaction is critical for tumorigenesis in liver cancer. *FEBS Lett* **2013**, *587* (24), 3921-7.
62. Ramey-Ward, A. N.; Su, H.; Salaita, K., Mechanical Stimulation of Adhesion Receptors Using Light-Responsive Nanoparticle Actuators Enhances Myogenesis. *ACS Appl Mater Interfaces* **2020**, *12* (32), 35903-35917.

63. Zheng, M.; Jacob, J.; Hung, S. H.; Wang, J., The Hippo Pathway in Cardiac Regeneration and Homeostasis: New Perspectives for Cell-Free Therapy in the Injured Heart. *Biomolecules* **2020**, *10* (7).
64. Hilenski, L. L.; Terracio, L.; Borg, T. K., Myofibrillar and cytoskeletal assembly in neonatal rat cardiac myocytes cultured on laminin and collagen. *Cell Tissue Res* **1991**, *264* (3), 577-87.
65. Sit, B.; Feng, Z.; Xanthis, I.; Marhuenda, E.; Zingaro, S.; Shanahan, C.; Jones, G. E.; Yu, C.-h.; Iskratsch, T., Matrix stiffness and blood pressure together regulate vascular smooth muscle cell phenotype switching and cofilin dependent podosome formation. *bioRxiv* **2020**, 2020.12.27.424498.
66. Kaverina, I.; Stradal, T. E.; Gimona, M., Podosome formation in cultured A7r5 vascular smooth muscle cells requires Arp2/3-dependent de-novo actin polymerization at discrete microdomains. *J Cell Sci* **2003**, *116* (Pt 24), 4915-24.
67. Linder, S.; Wiesner, C., Tools of the trade: podosomes as multipurpose organelles of monocytic cells. *Cell Mol Life Sci* **2015**, *72* (1), 121-35.
68. Linder, S.; Kopp, P., Podosomes at a glance. *J Cell Sci* **2005**, *118* (Pt 10), 2079-82.
69. Zhu, X.; Efimova, N.; Arnette, C.; Hanks, S. K.; Kaverina, I., Podosome dynamics and location in vascular smooth muscle cells require CLASP-dependent microtubule bending. *Cytoskeleton (Hoboken)* **2016**, *73* (6), 300-15.
70. Bernadzki, K. M.; Rojek, K. O.; Proszynski, T. J., Podosomes in muscle cells and their role in the remodeling of neuromuscular postsynaptic machinery. *Eur J Cell Biol* **2014**, *93* (10-12), 478-85.

71. Burgstaller, G.; Gimona, M., Podosome-mediated matrix resorption and cell motility in vascular smooth muscle cells. *Am J Physiol Heart Circ Physiol* **2005**, *288* (6), H3001-5.
72. Cougoule, C.; Lastrucci, C.; Guiet, R.; Mascarau, R.; Meunier, E.; Lugo-Villarino, G.; Neyrolles, O.; Poincloux, R.; Maridonneau-Parini, I., Podosomes, But Not the Maturation Status, Determine the Protease-Dependent 3D Migration in Human Dendritic Cells. *Front Immunol* **2018**, *9*, 846.
73. Glazier, R.; Brockman, J. M.; Bartle, E.; Mattheyses, A. L.; Destaing, O.; Salaita, K., DNA mechanotechnology reveals that integrin receptors apply pN forces in podosomes on fluid substrates. *Nat Commun* **2019**, *10* (1), 4507.
74. Sit, B.; Gutmann, D.; Iskratsch, T., Costameres, dense plaques and podosomes: the cell matrix adhesions in cardiovascular mechanosensing. *J Muscle Res Cell Motil* **2019**, *40* (2), 197-209.
75. Garbern, J. C.; Lee, R. T., Cardiac stem cell therapy and the promise of heart regeneration. *Cell Stem Cell* **2013**, *12* (6), 689-98.
76. Duelen, R.; Sampaolesi, M., Stem Cell Technology in Cardiac Regeneration: A Pluripotent Stem Cell Promise. *EBioMedicine* **2017**, *16*, 30-40.
77. Ghioldi, A.; Piccoli, M.; Cirillo, F.; Monasky, M. M.; Ciconte, G.; Pappone, C.; Anastasia, L., Cell-Based Therapies for Cardiac Regeneration: A Comprehensive Review of Past and Ongoing Strategies. *Int J Mol Sci* **2018**, *19* (10).
78. Grijalva, S. I.; Gu, J. M.; Li, J.; Fernandez, N.; Fan, J.; Sung, J. H.; Lee, S. Y.; Herndon, C.; Buckley, E. M.; Park, S. J.; Fenton, F. H.; Cho, H. C., Engineered Cardiac

Pacemaker Nodes Created by TBX18 Gene Transfer Overcome Source-Sink Mismatch. *Adv Sci (Weinh)* **2019**, *6* (22), 1901099.

79. Karbassi, E.; Fenix, A.; Marchiano, S.; Muraoka, N.; Nakamura, K.; Yang, X.; Murry, C. E., Cardiomyocyte maturation: advances in knowledge and implications for regenerative medicine. *Nat Rev Cardiol* **2020**, *17* (6), 341-359.

80. Kapoor, N.; Liang, W.; Marban, E.; Cho, H. C., Direct conversion of quiescent cardiomyocytes to pacemaker cells by expression of Tbx18. *Nat Biotechnol* **2013**, *31* (1), 54-62.

81. Kapoor, N.; Galang, G.; Marban, E.; Cho, H. C., Transcriptional suppression of connexin43 by TBX18 undermines cell-cell electrical coupling in postnatal cardiomyocytes. *J Biol Chem* **2011**, *286* (16), 14073-9.

82. Cameron, M.; Kekesi, O.; Morley, J. W.; Tapson, J.; Breen, P. P.; van Schaik, A.; Buskila, Y., Calcium Imaging of AM Dyes Following Prolonged Incubation in Acute Neuronal Tissue. *PLoS One* **2016**, *11* (5), e0155468.

83. Bell, G. I., Models for the specific adhesion of cells to cells. *Science* **1978**, *200* (4342), 618-27.

84. Sedlak, S. M.; Bauer, M. S.; Kluger, C.; Schendel, L. C.; Milles, L. F.; Pippig, D. A.; Gaub, H. E., Monodisperse measurement of the biotin-streptavidin interaction strength in a well-defined pulling geometry. *PLOS ONE* **2017**, *12* (12), e0188722.

85. Mosayebi, M.; Louis, A. A.; Doye, J. P. K.; Ouldridge, T. E., Force-Induced Rupture of a DNA Duplex: From Fundamentals to Force Sensors. *ACS Nano* **2015**, *9* (12), 11993-12003.

86. Galush, W. J.; Nye, J. A.; Groves, J. T., Quantitative fluorescence microscopy using supported lipid bilayer standards. *Biophys J* **2008**, *95* (5), 2512-9.

Chapter 3. Mechanically sorting cells with TaCT (Tension-activated Cell Tagging) probes.

This chapter summarizes my contribution to the following manuscript. Dr. Rong Ma has primarily conducted the initial work. Arventh Velusamy has helped me with conducting the flow-cytometry experiment and analysis. Some of the shared data is preliminary. The manuscript that houses the initial work is currently under review in Nature Methods. It can also be found in the bio-archive.

Molecular Mechanocytometry Using Tension-activated Cell Tagging (TaCT) ¹

Rong Ma¹, Arventh Velusamy^{1, *}, Sk Aysha Rashid^{1, *}, Brendan R. Deal^{1, *}, Wenchun Chen², Brian Petrich², Renhao Li², Khalid Salaita^{1,3}

*These authors contributed equally.

Abstract

Single-cell gene expression measurement is a widely used technique in biological research, typically involving labeling cells with fluorescent antibodies and nucleic acids. In this chapter, I will share how the Tension activated Cell technique, introduced by Dr. Rong Ma, is a novel approach that enables the fluorescent labeling of cells based on the magnitude of molecular force transmitted through their adhesion receptors. As a proof-of-concept, we evaluated the efficacy of TaCT by applying it to fibroblasts with and without vinculin and then using conventional flow cytometry to analyze the results. I will also share where we incorporated the probes in primary cardiac cells.

Introduction

In biological and biomedical sciences, Fluorescence-activated Cell Sorting (FACS) is a critical technique for analyzing and sorting cells based on their molecular expression levels. This method typically involves using fluorescently labeled antibodies and complementary nucleic acids to label cells, followed by analysis and sorting using flow cytometry.

While flow cytometry is widely used for characterizing the biochemical profile of cells, it has limitations when assessing the mechanical properties of cells. To address this, we propose that the mechanical profile of cells can serve as a complementary biophysical marker intimately linked to their biochemical profile.

By combining mechanical phenotype with traditional flow cytometry techniques, we can gain a more comprehensive understanding of the properties of individual cells. Incorporating cell mechanics can have significant implications for understanding cellular dynamics and improving our ability to diagnose and treat diseases.^{2,3-5}

To investigate cell mechanics, a range of methods have been developed, including flow cytometry, which enables the measurement of cell deformation through processes such as hydrodynamic stretching or micro-constriction.⁶⁻⁸ One such technique is real-time deformability cytometry, which utilizes high-speed imaging to capture the deformation of cells as they pass through a narrow channel under shear flow.⁹ Although these methods have shown potential for detecting disease-specific changes, it can be challenging to interpret cell deformation due to multiple factors such as cell volume, membrane composition, cytoskeletal dynamics, and cell cycle.^{10, 11} To assess the gap in the current

field Rong Ma et al. developed mechanophenotyping platforms that use molecular markers to measure mechanotransduction, which is difficult with traditional high-resolution fluorescence microscopy.¹²⁻¹⁵ Unfortunately, recent flow cytometry and FACS-like techniques cannot tag cells based on the magnitude of molecular forces generated, making it necessary for further research and development.^{16, 17}

To overcome this limitation, we present a novel method called Tension-activated Cell Tagging (TaCT) (**Figure Appendix 3.6.1**), which enables the identification and sorting of mechanically active cells using flow cytometry based on the molecular forces transmitted by their surface adhesion receptors. The TaCT probes are designed as DNA duplexes that exhibit a precise digital response to pN force, releasing a cholesterol-modified strand that spontaneously incorporates into the membrane of force-generating cells. This innovative approach represents a significant step forward in understanding and analyzing cell mechanics. To show TaCT's functionality, we utilized the cardiac cell population and showed it could distinguish and sort cells by their mechanical properties.

3.3 Results and Discussion

3.3.1 Dose-dependent Tension inhibition experiment shows MEF cells have lower tension and tagging when treated with Rho kinase inhibitor (Y27632)

TaCT utilizes a unique property of double-stranded DNA, where it peels apart under force. When a short DNA duplex is pulled from both ends of one of the strands,¹⁸ becomes destabilized and denatures with sufficient force, leading to the separation of complementary DNA. This force-induced peeling can be characterized as a simple two-

state system, treating the DNA duplex as either being in dsDNA form or completely separated ssDNA form.¹⁹⁻²¹ The critical peeling force for a 24mer duplex was found to be 41 ± 2.8 pN using the ox DNA coarse-grained model.

The TaCT probe consists of a load bearing and 24mer peeling strand, immobilized on streptavidin-coated glass slides. The load-bearing strand displays an RGD integrin ligand at one terminus and an internal Cy3B dye. The complementary peeling strand releases when $F > F_{\text{peel}}$ and is labeled with Atto647N and cholesterol.²² The probe is initially in the dsDNA form, and when $F > F_{\text{peel}}$, the Atto647N strand peels and dissociates, while the Cy3B dye on the load-bearing strand is de-quenched.²³ This generates high-quality maps of integrin forces independent of cholesterol conjugation to the probe.

To demonstrate that cell-generated forces drive DNA duplex peeling, mouse embryonic fibroblasts (MEF) were plated on TaCT probe surfaces. The Cy3B signal confirmed integrin binding and engagement with RGD ligands on the load-bearing strands. **(Figure A1)**. The growth of the Cy3B signal corresponded to the loss of the Atto647N signal, establishing the force-induced peeling mechanism. This mechanism generated tension signals that colocalized with markers of focal adhesions and actin stress fibers, confirming that integrins primarily transmitted forces within focal adhesions. Control groups of cells treated with Latrunculin B (Lat B) showed a significantly reduced peeling signal, as expected. (Figure Appendix 1)

After establishing that DNA peeling can accurately map molecular traction forces, we investigated using cholesterol-DNA cell tagging for TaCT. Our previous work demonstrated that cholesterol-DNA could be integrated into the plasma membrane of

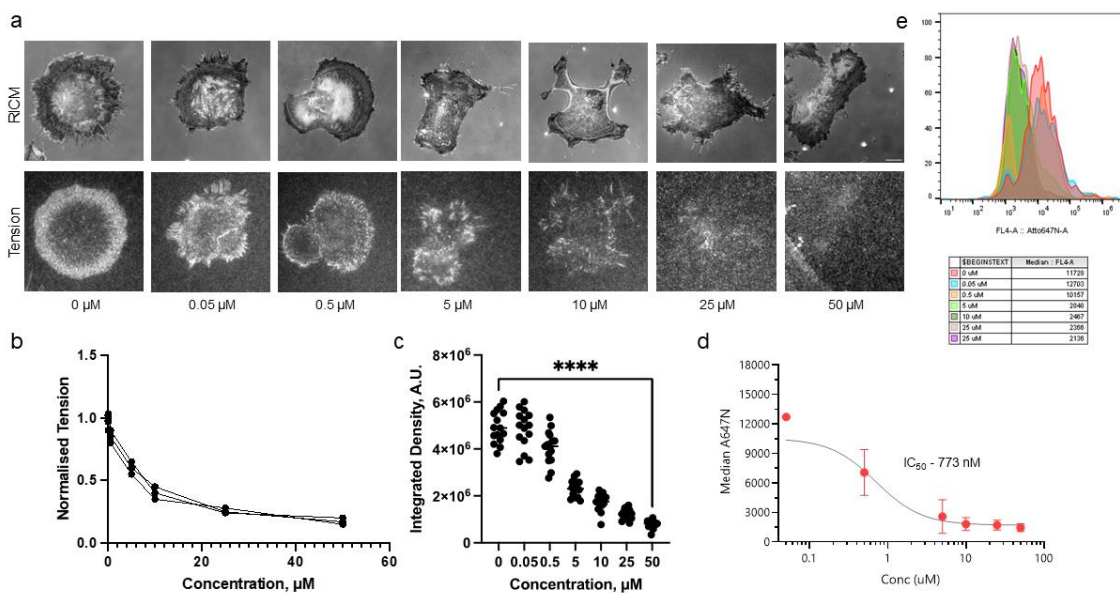


Figure 1. MEF cells were treated with various concentrations of Y27632. (a) RICM images show the spreading of the cells pretreated with Y27632 at $t = 60$ min. The tension signal in the Cy3B channel shows the irreversible tension over 60 min after plating the pretreated cells on peeling probe substrates. Scale bar = $10 \mu\text{m}$. (b,c) Plots showing MEF cells have dose-dependent tension signals where cells exert lower tension with increased drug treatment. (d,e) Flow cytometry data of treated MEF cells show lower uptake of Atto647 signal with increased drug treatment.

cells. However, we found that cholesterol-ssDNA conjugates were approximately 50 times more effective at tagging cells than cholesterol-dsDNA conjugates. This specificity enhancement was beneficial for TaCT, and we also confirmed that cholesterol-ssDNA membrane association was directly proportional to the concentrations tested. To ensure the stability of TaCT tags, we incubated cholesterol-ssDNA with cells and measured the loss of DNA over time. We determined that approximately 20-30% of the cholesterol-tethered DNA dissociated at 90 minutes, so we opted to incubate cells on the surface for

1 hour to allow for focal adhesion formation and TaCT to proceed while minimizing cholesterol dissociation.^{24, 25}

To demonstrate the effectiveness of TaCT as a method for reporting cell receptor forces, we utilized an inhibitor of Rho-associated protein kinase (ROCK) known as Y27632. By disrupting force transmission through the cytoskeleton and measuring the dose-dependent response in MEF cells, we could observe the impact of Y27632 on myosin activity, actin filament destabilization, and stress fiber formation (Figure Appendix 1). Y27632 functions by competing with ATP binding and inhibiting ROCK kinases. When MEF cells were pre-treated with Y27632, they exhibited a decrease in Cy3B tension signal (**Figure 1 a-c**). Furthermore, the TaCT signal, measured by flow cytometry, showed a precise dose-dependent curve with an IC₅₀ of 773 nM, consistent with microscopy measurements (**Figure 1d, e**). This result also aligned with the EC₅₀ values reported in the literature that range from hundreds of nM to low μ M.²⁶

3.3.2 Transient Transfection of Vinculin Ko cells show dose-dependent rescue of mechanical property.

In our study, we sought to explore the relationship between vinculin-GFP expression and tension, leveraging the power of the TaCT technique. To do so, we transiently transfected vinculin null cells with a plasmid encoding for vinculin-GFP, yielding a range of cells with varying levels of vinculin expression - a result commonly seen in transient transfection experiments. (**Figure Appendix 2**) Furthermore, by performing TaCT on these cells, we

measured both GFP and Atto647 intensity at the single cell level, allowing us to establish the correlation between vinculin expression and TaCT signal. (**Figure 2**)

Our results revealed a clear, dose-dependent relationship between vinculin expression

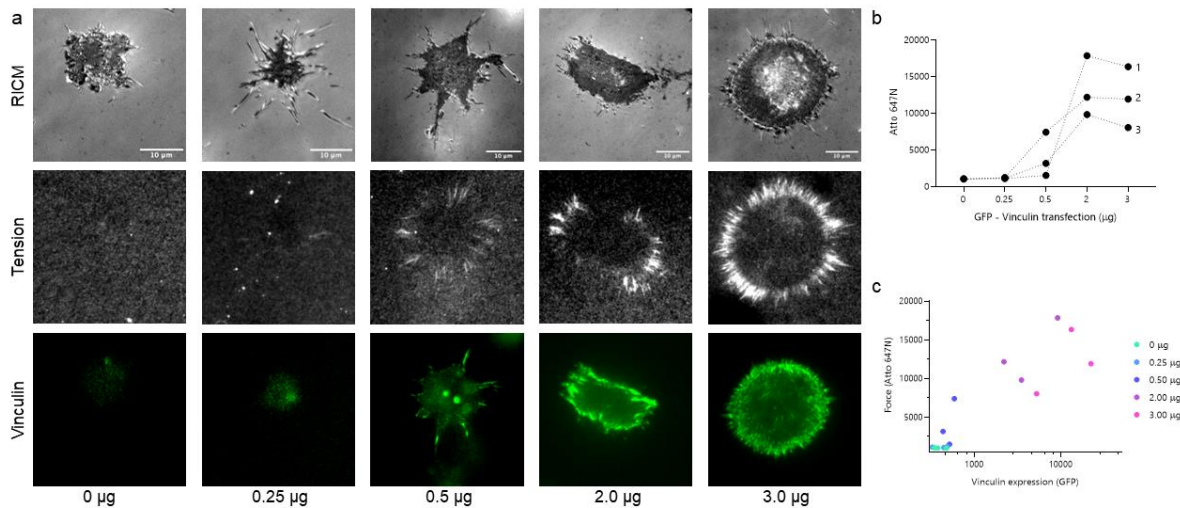


Figure 2. Transient transfection of Vinculin Ko MEF cells with various rescues of the plasmid. (a) RISM images show the spreading of Vinko with different amounts of plasmid. The tension signal in the Cy3B channel shows the irreversible tension over 60 min after plating the transfected cells on peeling probe substrates and FITC channel (GFP) shows the vinculin expression of the transfected cells. Scale bar = 10 μm. (b,c) Flow cytometry data of transfected Ko cells show higher uptake of Atto647 signal with increased plasmid concentration.

and TaCT signal, increasing as the amount of plasmid increased (Figure S9). Interestingly, we also observed that the TaCT signal recovered with relatively low levels of vinculin-GFP, suggesting a complex relationship between focal adhesion tension and vinculin expression. Specifically, we found that tension exhibited a linear regime at low levels of vinculin expression, followed by saturation at higher levels - a phenomenon may

be attributed to the interplay between vinculin and other tension-regulating proteins within the cell.

Our findings further emphasized the benefits of the TaCT technique, which allowed us to measure cellular tension with great precision and accuracy. Moreover, our study highlighted the potential utility of TaCT in the broader field of cell biology. The technique serves as a valuable tool for investigating the role of tension in cellular processes and signaling.

Our study provides valuable insights into the relationship between vinculin expression and cellular tension, underscoring the intricacies of tension regulation within cells. Furthermore, through TaCT, we were able to quantify this relationship with unprecedented accuracy, shedding light on a critical component of cellular mechanics that has implications for a wide range of biological and biomedical applications.

3.3.3 Preliminary experiments show TaCT probe can distinguish CFs and CMCs from the cardiac cell population.

We conducted preliminary measurements to analyze the mechanical forces generated by cells extracted from decellularized neonatal rat heart tissue using TaCT. Our decision to use TaCT on this type of tissue was motivated by the significance of mechanics to heart tissue physiology. In this experiment, we obtained hearts from 20-22 one to three-day-old rat pups, excising only the lower third of the organ from the apex to the midline to minimize the risk of contamination from nodal cells. Subsequently, the tissue was digested using collagenase and cultured in 2% serum for 24 hours to separate cardiac fibroblasts (CF)

and neonatal rat ventricular myocytes (NRVM) following standard procedures.^{27, 28} We validated the separation's success by using a vimentin antibody stain, a marker of CF cells, and brightfield microscopy, which showed the characteristic morphology of CFs.

With the validated isolated CF and NRVM populations, we cultured these cells onto the

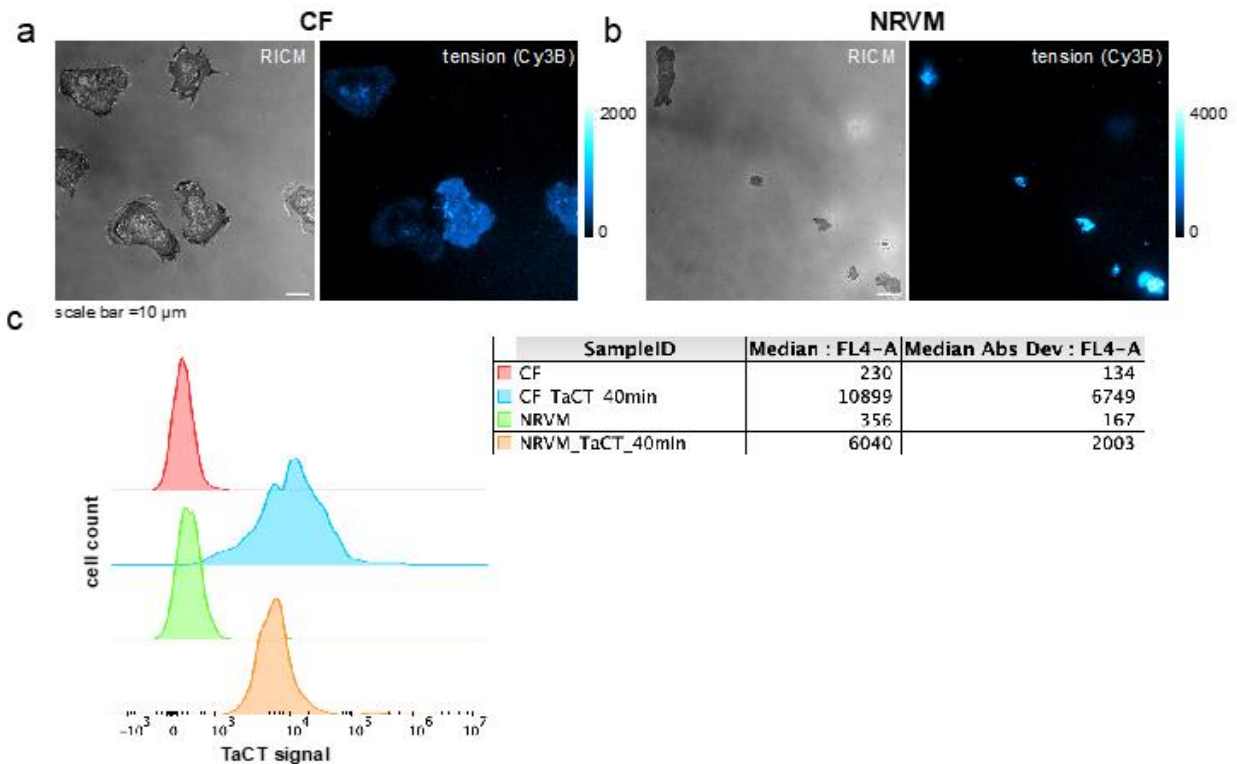


Figure 3. TaCT with Cardiac cells. (a, b) show representative images of cardiac fibroblasts (CFs) and neonatal rat ventricular myocytes (NRVMs) cultured on TaCT substrates. These images were obtained using reflection interference contrast microscopy (RISM) and force-induced peeling (Cy3B) microscopy after the cells were cultured for ~1hr in 2% serum-doped media. The image's scale bar is 10 μm, and the calibration bar shows the fluorescence intensity values. Notably, the RISM images reveal distinct morphological features of CFs. (c) displays flow cytometry histograms that measure the TaCT signal of NRVM and CF cells. The green and red curves represent control cells of NRVM and CF cells that were not exposed to the TaCT substrate, while the blue and orange curves indicate cells cultured on TaCT substrates. The data presented in this panel are representative of three independent biological replicates. The table summarizes the median fluorescent intensity (MFI) and median absolute standard deviation of the cell populations. The experiment was conducted in Collaboration with Dr. Rong Ma and the image is used with permission.

TaCT substrate. We performed flow analysis coupled with fluorescence microscopy analysis (**Figure 3**). A minimal autofluorescence signal was detected, with MFI values of 200-300 for the cells.

In comparison, the TaCT signal intensity for CFs was significantly higher at 10,900 MFI, exhibiting a broad distribution as evidenced by the Atto647N Median Abs Dev. On the other hand, NRVMs displayed a weaker TaCT signal at 6,040 MFI with a narrow distribution, as observed through microscopy. This intriguing result suggests that TaCT has the potential to effectively characterize complex primary cell populations obtained from tissue, revealing the varied mechano-heterogeneity of different cell types. However, it should be noted that the interpretation of these findings is still preliminary, and further single-cell analysis utilizing RNA or protein biomarkers is necessary to confirm individual cell types. In addition, decellularized tissue may still contain non-muscle cells, endothelial cells, stem cells, and other lineages, potentially contaminating the isolated cell populations.

Finally, it is essential to acknowledge that this experiment represents only the initial stages of a new thesis project. Future graduate students can expand upon these results to uncover more insights.

3.4 Conclusion

In summary, we have utilized 3'-5' mediated DNA peeling created by Dr. Rong Ma et al. as a novel set of DNA tension probes that can accurately track the molecular forces generated by cells. This development has enabled high-throughput flow cytometry to detect mechanically active cells. However, as with other DNA tension probes, the likelihood of mechanical dehybridization depends on the loading rate. Therefore, further studies are required to fully utilize this technique to investigate the impact of different loading rates and durations of applied force on duplex peeling, particularly for duplexes with varying lengths and GC%.

The TaCT signal indicates the total number of mechanical events exceeding F_{peel} , distinct from the biochemical analysis that employs antibodies and nucleic acids. In the future greater force magnitude detection can be created with duplexes with a higher F_{peel} . One thing also needs to be remembered to incorporate a cholesterol strand uptake calibration to account for potential variations in cholesterol insertion among different cell types. A negative control that is not mechanically active should also be included to eliminate the background uptake of cholesterol strands. Overall, the TaCT technique has the potential to provide a new class of tools for mechanobiology, enabling a connection between a single cell's mechanical characteristics and its biochemical properties. We have expanded the work using primary cardiac cells as a proof of principle experiment. Further validation and optimization of the technique can enhance the method utilized in a complex cell population.

3.5 Methods

ID	DNA Sequence (5'-3')
Load Bearing Strand	/5Thiol MC6-D/TTTTTTTTT TAGTGAGCTCTGAAGTCT TAGAACT/ iAmMC6T/TTT /3Bio/
24 mer Peeling strand	/5ATTO647NN/AGTTCTAAGACTTCAGAGCTCACT /3choITEG/
24 mer BHQ2 peeling strand	/5AmMC6/AGTTCTAAGACTTCAGAGCTCACT/3Bio/
24 mer NH ₂	/5BHQ_2/AGTTCTAAGACTTCAGAGCTCACT /3choITEG/

Table 1: List of Oligos used in the project.

3.5.1 Oligonucleotide preparation

3.5.1.1 Conjugation with dyes

The internal amine of the load-bearing strand was conjugated with Cy3B NHS, while the 5' amine of the 24mer peeling strand was conjugated with Atto647N NHS. The process involved reacting an excess amount of NHS dye (50 µg) with 10 nmol of amine oligonucleotide in 1×PBS containing 0.1 M NaHCO₃ at room temperature for one hour. The reaction mixture was then desalted with P2 gel and purified using HPLC with an Advanced oligonucleotide C18 column. Next, the product was eluted in Solvents A (0.1 M TEAA) and B (acetonitrile) using linear gradients of 10-35% Solvent B over 25 minutes, followed by 35-100% Solvent B over 5 minutes, with a flow rate of 0.5 mL/min. The oligo-dye conjugate was then dried overnight in a Vacufuge and reconstituted in water, and its concentration was determined by measuring its absorbance at 260 nm using Nanodrop.

3.5.1.2 Conjugation with cRGD

The thiol oligonucleotide (load-bearing strand) was conjugated with maleimide-cRGDfK. First, to achieve this, five nmol of thiol oligonucleotide was reduced to 200× molar excess TCEP for 15 min at room temperature. The mixture was then added to 0.5 mg (excess) of maleimide-cRGDfK in 1×PBS (pH = 6.8) and reacted for one hour at room temperature. Finally, as previously described, the reaction mixture was desalted with P2 gel and purified by HPLC with an advanced oligonucleotide column.

For the conjugation of azide-RGD with alkyne-DNA, stock solutions of CuSO₄ (20 mM in water), THPTA [Tris (3-hydroxypropyl triazolyl methyl) amine] (50 mM in water), and sodium ascorbate (100 mM in water) were prepared. A final mixture of 100 μM azide-RGD, 50 μM of alkyne-DNA, 0.1 mM CuSO₄, 0.5 mM THPTA, and 5 mM sodium ascorbate in 1X PBS was allowed to react at room temperature for 2 h. The product was then purified by P2 gel, followed by HPLC with an advanced oligonucleotide column, as previously described.

3.5.2 DNA substrates preparation

3.5.2.1 Preparation of glass slides with amine modification

We initially cleaned glass slides (25 × 75 mm) by placing them on a Wash-N-Dry rack and rinsing them with 18.2 MΩ water, followed by sonication in ethanol and water for 15 minutes, each rinsing them five-six times with water. To prepare the new piranha solution, concentrated sulfuric acid and hydrogen peroxide (30%) were mixed at a 3:1 ratio (v/v) in a total volume of 200 mL and then added to the slides for etching. Next, the slides were rinsed with copious amounts of water to remove the acid and then rinsed with ethanol to remove water. Next, 200 mL of 3% APTES in ethanol was prepared and added to the glass slides at room temperature, allowing them to react for 1 hour for amine modification. After the reaction, the glass slides were washed with copious amounts of ethanol and then bake-dried in an oven (80°C) for 20 minutes. Finally, the amine-modified glass slides were stored at -20°C until use.

3.5.2.2 Preparation of biotin substrate

We placed an amine-modified glass slide on a parafilm-lined petri dish to prepare for the experiment. Next, 1 mL of a 4 mg/mL solution of Biotin-NHS in DMSO was added to the glass slide and left to incubate overnight. The following day, the glass slide was washed thoroughly with ethanol and water and air-dried before being attached to either an ibidi sticky-slide imaging chamber or a bottomless adhesive 96-well plate. The wells were then passivated with 1% BSA in PBS for 10 minutes at room temperature and washed with PBS. Next, Streptavidin was added to each well at a concentration of 50 µg/mL in PBS and left to incubate for 30 minutes at room temperature before the excess was washed away with PBS.

Simultaneously, the TaCT/peeling probe with a load-bearing strand-to-peeling ratio of 1:1.5 was annealed at 50 nM by heating to 95°C for 5 minutes and gradually cooling to 20°C for 20 minutes. For TGT substrates, the BHQ2 top strand was annealed with the Cy3B bottom strand at a 1.1:1 ratio and 50 nM concentration. Finally, the probes were added to each streptavidin-coated well and left to incubate for 30 minutes before the excess was rinsed away with PBS in preparation for imaging.

3.5.3 Cell culture and transfection

NIH3T3 cells were cultured in DMEM (10% CCS, 1% P/S) at 37 °C with 5% CO₂. MEF and MEF vinculin null cells were cultured in DMEM (10% FBS, 1% P/S) at 37 °C with 5% CO₂. Cells were passaged at 80% confluency every two days by detaching using trypsin and replating at a lower density. A plasmid encoding full-length vinculin and GFP transfected MEF vinculin null cells. Cells were seeded in a 6-well plate and transfected

with 0, 0.25, 0.5, 2, or 3 µg of the plasmid for 24 h. The expression was validated by flow cytometry.

3.5.3.1 Cardiac Cell preparation

NRVMs were obtained from neonatal rats aged 1 to 2 days and cultured as a monolayer per previously published methods.^{29, 30} Only the lower one-third of the heart, from the apex to the midline, was excised to reduce contamination by atrioventricular nodal cells. One day after cell isolation, NRVMs were transduced with either Ad-Tbx18-IRES-GFP or Ad-GFP and cultured for 2-5 days. For all in vitro experiments, NRVMs were plated at a density of 210,000 cells per cm² of surface area.

3.5.4 Fluorescence microscopy Integrin tension imaging

Imaging was performed using a Nikon Ti2-E microscope. At first, all fibroblast cells were plated onto DNA probe substrates in DMEM (10% serum, 1% P/S) and given 15-20 minutes to attach in the 37 °C incubator. Afterward, the cells were allowed to spread at room temperature and imaged for up to 60 minutes after plating using RICM, Cy3B, and Atto647N channels with appropriate filter settings and an sCMOS detector.

In contrast, cardiac cells were plated onto DNA probe substrates in 1% serum medium (composed of 134 mM NaCl, 12 mM NaHCO₃, 2.9 mM KCl, 0.34 mM NaH₂PO₄, five mM glucose, five mM HEPES, pH 7.4-, and 1-mM Vitamin B12) for 1-2 hours in the cell culture

incubator. Then, they were imaged at room temperature for up to 30 minutes using RICM, Cy3B, and Atto647N channels.

3.5.5 Drug Treatment

Before seeding, MEF cells were pretreated with inhibitors for (>1hr @RT). Cells were treated with different concentrations of Y27632 dihydrochloride (Y0503, Millipore Sigma) for 30 min. We used PBS as a solvent vehicle for the control group.

3.5.6 Flow cytometry

To analyze TaCT signals, fibroblast cells were seeded at a density of $1-2 \times 10^4$ cells on the substrate and gently scraped after 60 minutes. Next, the collected cells were washed with Hank's buffer containing five mM EDTA and suspended in Hank's buffer without Ca^{2+} and Mg^{2+} but with five mM EDTA. Subsequently, the cells were immediately analyzed using a flow cytometer and were kept at a low temperature of 4C to obtain high TaCT signals.

As for cardiac cells, $1-2 \times 10^4$ cells were seeded on the TaCT substrate and collected by gentle scraping after 60 minutes. After 2-4 hours, the cardiac cells were carefully scraped and pipetted off the substrate, then washed before being analyzed with a flow cytometer for TaCT signals.

3.6 Appendix

3.6.1 TaCT Signal

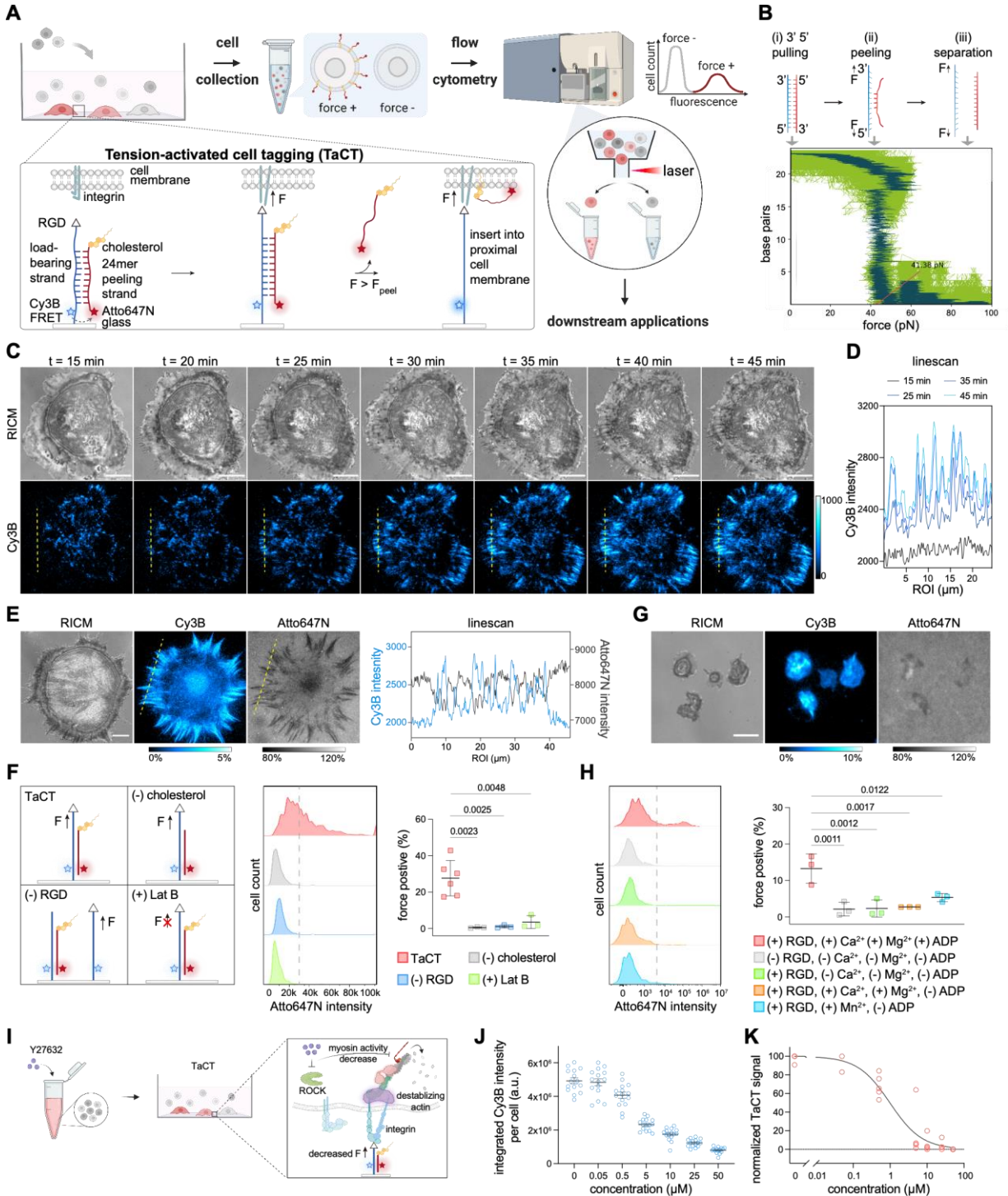
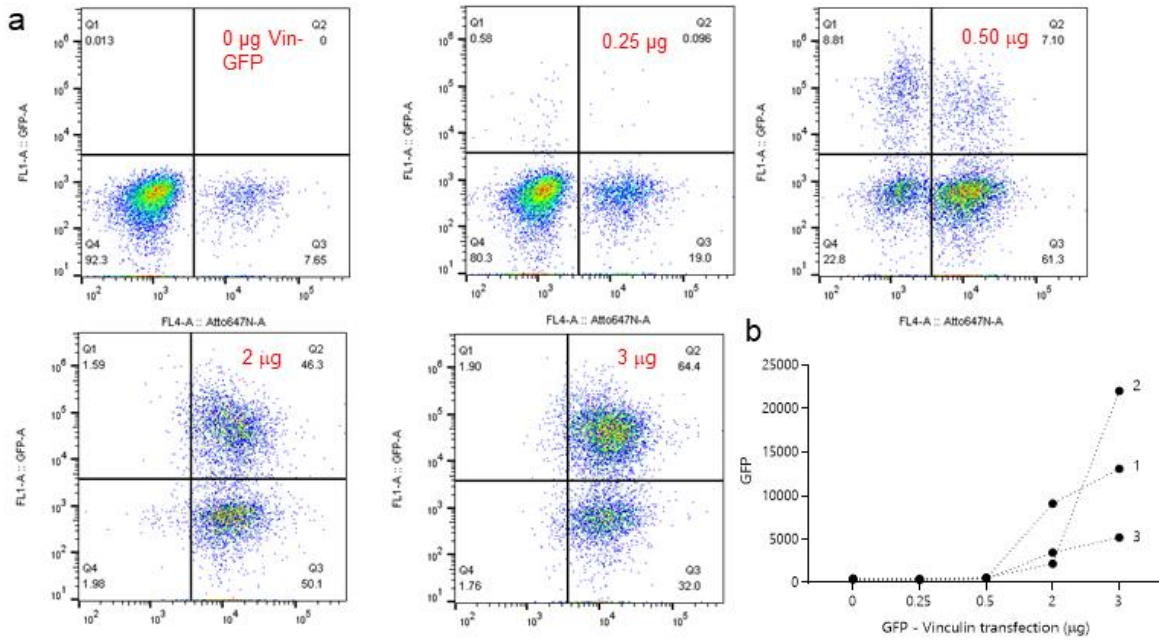


Figure Appendix 1. Tension-activated cell tagging (TaCT). (A) Schematic showing TaCT assay. (B) TaCT is based on the 3'-5' mechanical pulling of a DNA duplex that leads to its dehybridization. The plot of 24mer dsDNA stability as a function of applied force generated using oxDNA simulation with a loading rate of 2.81×10^3 nm/s (shown light green). Dark green shows the exponential moving average (EMA) and indicates a 41 pN dehybridization transition. (C) Time-lapse reflection interference contrast microscopy (RICM) and Cy3B fluorescence images of NIH3T3 cell spreading on TaCT surface 15-45 min after seeding. Scale bar = 10 μ m. (D) Line scan of Cy3B images noted by the yellow dashed line in (C). (E) Representative RICM, Cy3B, and Atto647N microscopy images of NIH3T3 cell cultured on TaCT substrate. The intensity bar for the Cy3B image indicates the % of TaCT probes that undergo force-triggered release, while the intensity bar for Atto647N shows the signal normalized to the background of intact TaCT probes. Scale bar = 10 μ m. Line scan shows anti-colocalization of Cy3B and Atto647N intensities. (F) Flow cytometry histograms of NIH3T3 cells cultured on TaCT substrates, as well as control surfaces with (-) cholesterol, (-) RGD, and (+) LatB. The plot displays the force-positive population from n=3-6 biological replicates (mean \pm SD, two-tailed student's t-test). The Grey dashed line indicates the gate for determining force-positive population. (G) Representative RICM, Cy3B, and Atto647N microscopy images of mouse platelets on TaCT substrates. Scale bar = 5 μ m. (H) Representative flow cytometry histograms of mouse platelets incubated on TaCT substrates. The Grey dashed line indicates the gate for determining force-positive population. Controls included experiments with TaCT probes -RGD (grey), -divalent cations -ADP agonist (green), -ADP agonist (orange), and -ADP/+Mn²⁺ (blue). Data plotted from n=3 animals (mean \pm

SD, two-tailed student's t-test). (I) Schematic showing Y27632 treatment decreases integrin forces. (J) Quantitative analysis of the integrated Cy3B signal per cell from microscopy images of MEF cells pretreated with 0, 0.05, 0.5, 5, 10, 25, and 50 μM of Y27632 and cultured on peeling probe substrate. The plot shows the result from $n=3$ biological replicates (mean \pm SEM). (K) TaCT signal of cells pretreated with different concentrations of Y27632. The plot shows the result from $n=2-4$ biological replicates. The figure is reused from reference 1 with permission.

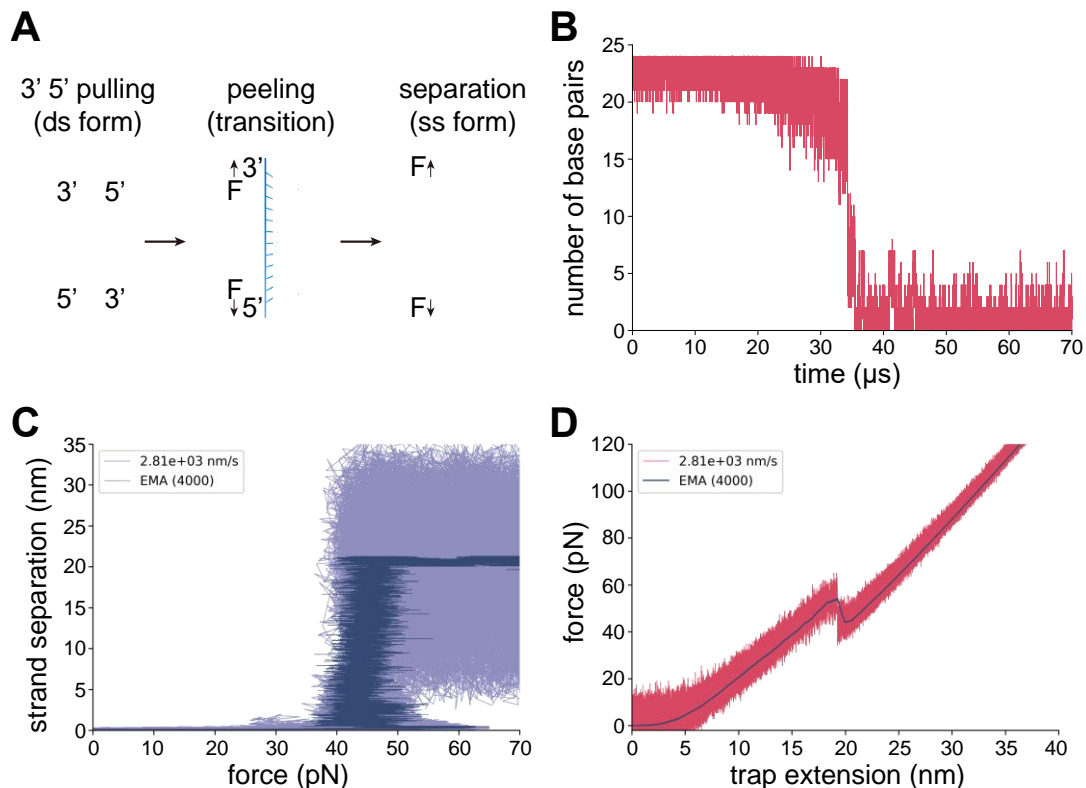
3.6.2 Transient Transfection of Vinculin Ko Cells

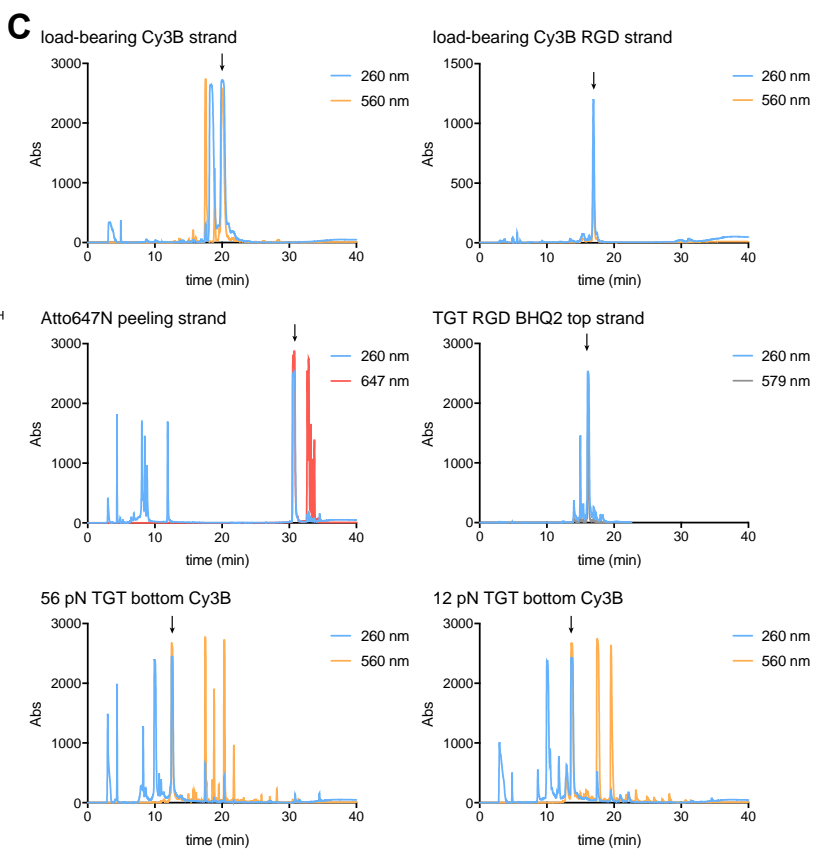
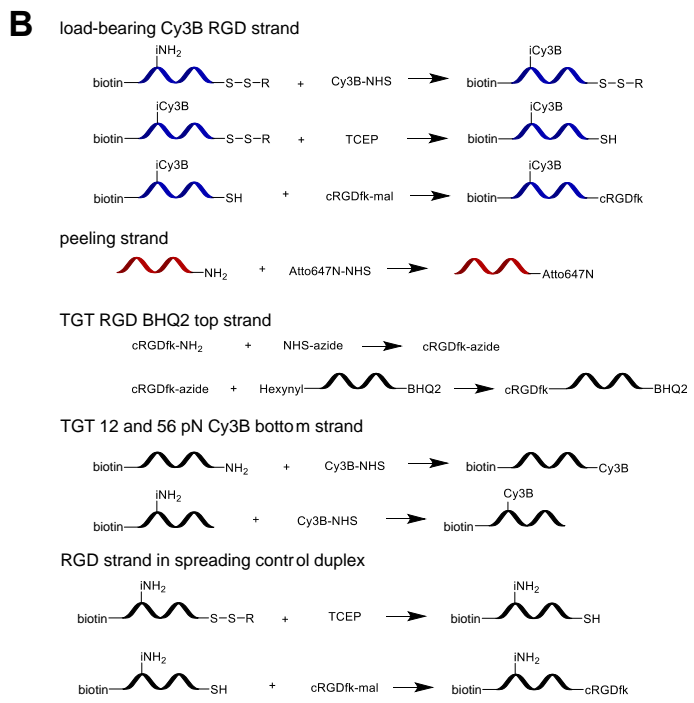
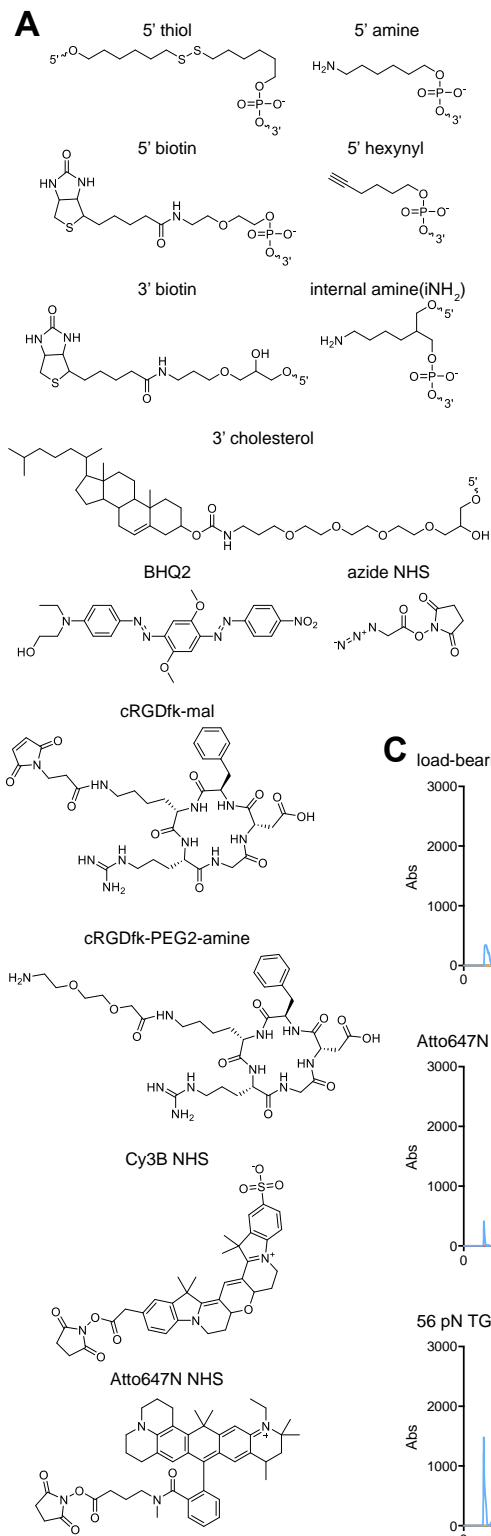
Flow cytometry experiments show vinculin is rescued in Vin Ko cells using different amount of vinculin- GFP plasmids. The plot shows the GFP signal increasing with an increased amount of the plasmid rescue. (0-3 μg).



3.6.3 Simulations with ox DNA.

(A) Schematic representation of the peeling mechanism of the 24 mer probes. (B) Simulation data of the transition state during force-induced peeling. The transition occurs on μs timescale, indicating that the peeling probe's transition state can be ignored using it as a digital tension sensor. (C) Simulation result of the strand separation distance versus force. (D) Simulated force-distance curve. Conditions used for simulation: loading rate = $2.81 \times 10^3 \text{ nm/s}$, ionic strength = 0.156 M Na^+ , and effective stiffness constant $k_{\text{eff}} = 5.71 \text{ pN/nm}$. The details of the simulation are further described in the methods section. The image is reused from reference 1 with permission. Arventh Velusamy prepared the simulation, and the data was prepared by Dr. Rong Ma.



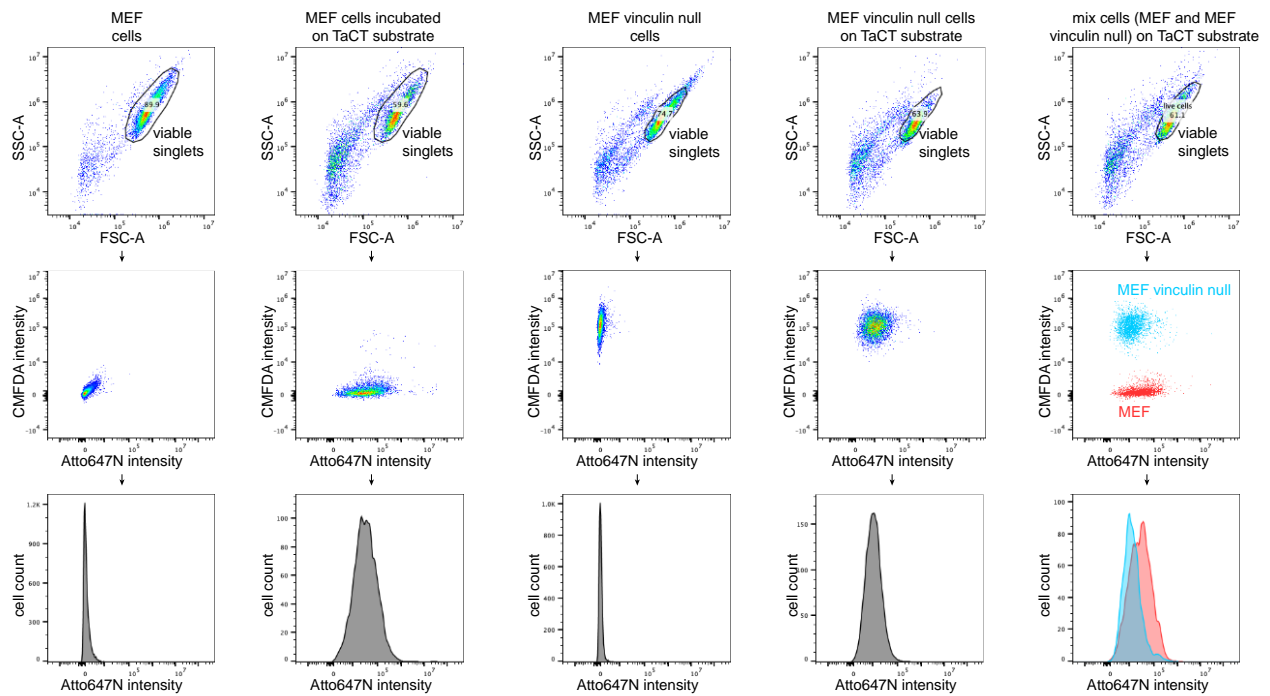


3.6.4 Peeling probe preparation purification

Structures of oligonucleotides and the different modifications. (B) Schematic representation of modified DNA strands. (C) HPLC chromatograms of modified and purified strands. The image was reused from the original work of Dr. Rong Ma with permission.

3.6.5 Flow cytometry data analysis workflow

For the flow cytometry analysis of TaCT, viable cells and singlets cells were identified using the forward scatter and side scatter. The histogram was used to show the fluorescence intensity of viable singlets. The image is reused from the original work of Dr. Rong ma et al.; with permission.



Author contributions in the original manuscript (reference 1)

R.M. and K.S. conceived the idea and wrote the manuscript. R.M., A.V., A.R., and B.R.D. carried out experiments and data analysis. A.V. performed oxDNA simulation. W.C., R.L., and B.P. provide mouse platelets.

References

1. Ma, R.; Velusamy, A.; Rashid, S. A.; Deal, B. R.; Chen, W.; Petrich, B.; Li, R.; Salaita, K., Molecular Mechanocytometry Using Tension-activated Cell Tagging (TaCT). *bioRxiv* **2023**, 2023.01.10.523449.
2. Sano, M.; Kaji, N.; Rowat, A. C.; Yasaki, H.; Shao, L.; Odaka, H.; Yasui, T.; Higashiyama, T.; Baba, Y., Microfluidic Mechanotyping of a Single Cell with Two Consecutive Constrictions of Different Sizes and an Electrical Detection System. *Anal Chem* **2019**, *91* (20), 12890-12899.
3. Di Carlo, D., A mechanical biomarker of cell state in medicine. *J Lab Autom* **2012**, *17* (1), 32-42.
4. Torrino, S.; Bertero, T., Metabo-reciprocity in cell mechanics: feeling the demands/feeding the demand. *Trends Cell Biol* **2022**.
5. Evers, T. M. J.; Holt, L. J.; Alberti, S.; Mashaghi, A., Reciprocal regulation of cellular mechanics and metabolism. *Nat Metab* **2021**, *3* (4), 456-468.
6. Belotti, Y.; Tolomeo, S.; Conneely, M. J.; Huang, T.; McKenna, S. J.; Nabi, G.; McGloin, D., High-Throughput, Time-Resolved Mechanical Phenotyping of Prostate Cancer Cells. *Sci Rep* **2019**, *9* (1), 5742.
7. Islam, M.; Mezencev, R.; McFarland, B.; Brink, H.; Campbell, B.; Tasadduq, B.; Waller, E. K.; Lam, W.; Alexeev, A.; Sulchek, T., Microfluidic cell sorting by stiffness to examine heterogenic responses of cancer cells to chemotherapy. *Cell Death Dis* **2018**, *9* (2), 239.
8. Lee, K. C. M.; Guck, J.; Goda, K.; Tsia, K. K., Toward Deep Biophysical Cytometry: Prospects and Challenges. *Trends Biotechnol* **2021**, *39* (12), 1249-1262.

9. Otto, O.; Rosendahl, P.; Mietke, A.; Golfier, S.; Herold, C.; Klaue, D.; Girardo, S.; Pagliara, S.; Ekpenyong, A.; Jacobi, A.; Wobus, M.; Topfner, N.; Keyser, U. F.; Mansfeld, J.; Fischer-Friedrich, E.; Guck, J., Real-time deformability cytometry: on-the-fly cell mechanical phenotyping. *Nat Methods* **2015**, *12* (3), 199-202, 4 p following 202.
10. Kozminsky, M.; Sohn, L. L., The promise of single-cell mechanophenotyping for clinical applications. *Biomeicrofluidics* **2020**, *14* (3), 031301.
11. Tse, H. T.; Gossett, D. R.; Moon, Y. S.; Masaeli, M.; Sohsman, M.; Ying, Y.; Mislick, K.; Adams, R. P.; Rao, J.; Di Carlo, D., Quantitative diagnosis of malignant pleural effusions by single-cell mechanophenotyping. *Sci Transl Med* **2013**, *5* (212), 212ra163.
12. They, M.; Bornens, M., Get round and stiff for mitosis. *HFSP J* **2008**, *2* (2), 65-71.
13. Fletcher, D. A.; Mullins, R. D., Cell mechanics and the cytoskeleton. *Nature* **2010**, *463* (7280), 485-92.
14. Sanyour, H. J.; Li, N.; Rickel, A. P.; Childs, J. D.; Kinser, C. N.; Hong, Z., Membrane cholesterol and substrate stiffness co-ordinate to induce the remodelling of the cytoskeleton and the alteration in the biomechanics of vascular smooth muscle cells. *Cardiovasc Res* **2019**, *115* (8), 1369-1380.
15. Guo, M.; Pegoraro, A. F.; Mao, A.; Zhou, E. H.; Arany, P. R.; Han, Y.; Burnette, D. T.; Jensen, M. H.; Kasza, K. E.; Moore, J. R.; Mackintosh, F. C.; Fredberg, J. J.; Mooney, D. J.; Lippincott-Schwartz, J.; Weitz, D. A., Cell volume change through water efflux impacts cell stiffness and stem cell fate. *Proc Natl Acad Sci U S A* **2017**, *114* (41), E8618-E8627.

16. Hang, X.; He, S.; Dong, Z.; Li, Y.; Huang, Z.; Zhang, Y.; Sun, H.; Lin, L.; Li, H.; Wang, Y.; Liu, B.; Wu, N.; Ren, T.; Fan, Y.; Lou, J.; Yang, R.; Jiang, L.; Chang, L., High-Throughput DNA Tensioner Platform for Interrogating Mechanical Heterogeneity of Single Living Cells. *Small* **2022**, *18* (12), e2106196.
17. Pushkarsky, I.; Tseng, P.; Black, D.; France, B.; Warfe, L.; Koziol-White, C. J.; Jester, W. F., Jr.; Trinh, R. K.; Lin, J.; Scumpia, P. O.; Morrison, S. L.; Panettieri, R. A., Jr.; Damoiseaux, R.; Di Carlo, D., Elastomeric sensor surfaces for high-throughput single-cell force cytometry. *Nat Biomed Eng* **2018**, *2* (2), 124-137.
18. Yang, Z.; Yuan, G.; Zhai, W.; Yan, J.; Chen, H., The kinetics of force-dependent hybridization and strand-peeling of short DNA fragments. *Science China Physics, Mechanics & Astronomy* **2016**, *59* (8).
19. Yang, Z. J.; Yuan, G. H.; Zhai, W. L.; Yan, J.; Chen, H., The kinetics of force-dependent hybridization and strand-peeling of short DNA fragments. *SCI CHINA PHYS MECH* **2016**, *59* (8).
20. Cocco, S.; Yan, J.; Leger, J. F.; Chatenay, D.; Marko, J. F., Overstretching and force-driven strand separation of double-helix DNA. *Physical Review E* **2004**, *70* (1 Pt 1), 011910.
21. Zhang, X.; Chen, H.; Fu, H.; Doyle, P. S.; Yan, J., Two distinct overstretched DNA structures revealed by single-molecule thermodynamics measurements. *Proceedings of the National Academy of Sciences* **2012**, *109* (21), 8103-8.
22. Snodin, B. E.; Randisi, F.; Mosayebi, M.; Sulc, P.; Schreck, J. S.; Romano, F.; Ouldridge, T. E.; Tsukanov, R.; Nir, E.; Louis, A. A.; Doye, J. P., Introducing improved

structural properties and salt dependence into a coarse-grained model of DNA. *J Chem Phys* **2015**, *142* (23), 234901.

23. Martino, F.; Perestrelo, A. R.; Vinarsky, V.; Pagliari, S.; Forte, G., Cellular Mechanotransduction: From Tension to Function. *Front Physiol* **2018**, *9*, 824.

24. Zhang, Y.; Ge, C.; Zhu, C.; Salaita, K., DNA-based digital tension probes reveal integrin forces during early cell adhesion. *Nat. Commun.* **2014**, *5*, 5167.

25. Galush, W. J.; Nye, J. A.; Groves, J. T., Quantitative fluorescence microscopy using supported lipid bilayer standards. *Biophys J* **2008**, *95* (5), 2512-9.

26. Uehata, M.; Ishizaki, T.; Satoh, H.; Ono, T.; Kawahara, T.; Morishita, T.; Tamakawa, H.; Yamagami, K.; Inui, J.; Maekawa, M.; Narumiya, S., Calcium sensitization of smooth muscle mediated by a Rho-associated protein kinase in hypertension. *Nature* **1997**, *389* (6654), 990-4.

27. Rashid, S. A.; Blanchard, A. T.; Combs, J. D.; Fernandez, N.; Dong, Y.; Cho, H. C.; Salaita, K., DNA Tension Probes Show that Cardiomyocyte Maturation Is Sensitive to the Piconewton Traction Forces Transmitted by Integrins. *ACS Nano* **2022**, *16* (4), 5335-5348.

28. Kapoor, N.; Liang, W.; Marban, E.; Cho, H. C., Direct conversion of quiescent cardiomyocytes to pacemaker cells by expression of Tbx18. *Nat Biotechnol* **2013**, *31* (1), 54-62.

29. Golden, H. B.; Gollapudi, D.; Gerilechaogetu, F.; Li, J.; Cristales, R. J.; Peng, X.; Dostal, D. E., Isolation of cardiac myocytes and fibroblasts from neonatal rat pups. *Methods Mol Biol* **2012**, *843*, 205-14.

30. Kapoor, N.; Galang, G.; Marban, E.; Cho, H. C., Transcriptional suppression of connexin43 by TBX18 undermines cell-cell electrical coupling in postnatal cardiomyocytes. *J Biol Chem* **2011**, 286 (16), 14073-9.

Chapter 4: Hydrogel-tethered DNA hairpin matrix to measure pN receptor forces.

This chapter is based on “Hydrogel-Based DNA Hairpin Probes to Measure Real-Time Cellular Tension” Sk Aysha Rashid, Yixiao Dong, Hiroaki Ogasawara, Mark Essien, and Khalid Salaita* manuscript that is currently under preparation to be submitted to ACS interfaces.

This project is a collaboration between Dr. Yixiao Dong and Dr. Hiroaki Ogasawara. Dr. Dong helped with the hydrogel characterization and collaborated on early design and troubleshooting experiments. Dr. Ogasawara helped with the DNA probe synthesis and characterization. Dr. Ogasawara also significantly contributed in preparation of the manuscript.

Abstract

Cells sense and respond to the physical properties of their environment through receptor-mediated signaling, a process known as mechanotransduction, which can modulate critical cellular functions such as adhesion, proliferation, differentiation, protein expression, and apoptosis. A vital aspect of this process is the ability of cells to exert forces on their extracellular matrix. Measuring these forces is crucial for understanding the impact of cellular tension on biological processes. We previously reported DNA hairpin probes for molecular tension fluorescence microscopy (MTFM) to map cell traction forces. HP probe is typically anchored to rigid glass slides, which are orders of magnitude stiffer than the extracellular matrix (ECM). Here, we developed chemical conjugation strategies and nuclease-resistant HP probes to image cell traction forces on hydrogels. Using HeLa cells as a model cell line, we show that cell traction forces are greater than 5.8 pN but less than 19 pN on 13 kPa gels. Forces are spatially localized with paxillin and pY118-paxilin. Additionally, cell traction forces are highly sensitive to the young's modulus of the substrate, and the 6 and 13 kPa gels produced a greater number of HP unfolding events compared to the 2 kPa substrates. The work provides a general strategy to integrate molecular tension probes into hydrogels, which better mimic the physiological stiffness.

Introduction

Mechanotransduction is the process by which cells sense and respond to the mechanical properties of their microenvironment. This signal transduction controls gene expressions and protein activations, resulting in the regulation of various cellular processes such as cell migration, proliferation, tissue development and repair, wound healing, and the maintenance of normal tissue architecture.^{1, 2} Disruptions in mechanotransduction can result in various physiological imbalances and diseases, including cardiovascular disease and cancer.³⁻⁵ Because mechanical cues in the cellular microenvironment can impact cell signaling, leading to cell behavior changes,⁶ understanding how the cellular microenvironment affects mechanotransduction is essential for elucidating the disease cascades and developing new therapeutic strategies.⁷

Although various factors are included in the cellular microenvironment including ECM protein, stiffness of substrate, pH, and surrounding cells, the stiffness of the substrate, or the material on which cells grow and differentiate, plays a vital role in determining cell fate.⁸⁻¹⁰ Increased ECM stiffness can promote tumor progression and inhibit wound healing, while decreased ECM stiffness can promote stem cell differentiation and improve heart function after injury.¹¹⁻¹³ Past studies have shown how global or local substrate stiffness can influence biological responses in a variety of cells.^{9, 14} The stiffness of polymeric substrates can be tuned by changing crosslinking density, using different hydrogel synthesis methods, and also by directly modulating the stiffness using external forces.¹⁵⁻¹⁷ These studies have shown that stem, neural, and muscle cells tend to have a “sweet spot” for stiffness, where cells behave poorly on too hard or soft substrates but behave optimally on primarily ~5-10 kPa substrates.^{9, 13, 18-20} On the contrary, cells

usually display non-physiological stress fiber formation when cultured on a stiff substrate such as glass (<100kPa), which is usually a sign of fibrosis. Past studies also revealed that cell-exerting tension levels are proportional to their substrate stiffness with greater stiffness leading to greater magnitudes of traction forces.²¹

Another critical interest in the field of mechanotransduction is to measure cell-exerted forces because receptor forces modulate cellular functions, including signaling, transcription, differentiation, and proliferation. Thus, scientists have utilized various techniques for measuring cellular forces. The most widely used technique to measure cell-generated forces is traction force microscopy (TFM).^{22, 23} This technique uses a soft polymer substrate coated with a fluorescent bead to measure the forces exerted by cells on the substrate. By tracking the displacement of the beads, TFM can measure the forces exerted by individual cells or groups of cells. One shortcoming of this technique is the forces measured by TFM are global, and the resolution is in the nN range, three orders of magnitude greater than the forces generated by individual receptors.²⁴ The micro-post array is another alternative technique that uses arrays of micrometer-scale pillars to apply forces to cells and measure the response of cells to the applied forces.^{25, 26} However, like TFM it lacks receptor force and spatial resolution.

To address the limitations of TFM and micropillar arrays, our group and others developed molecular tension probes.^{27, 28} These probes are comprised of a flexible linker such as PEG,^{29, 30} nucleic acids,³¹ polypeptides,^{32, 33} and proteins³⁴ and flanked by a fluorophore quencher pair to record mechanical extension. The probes are tethered to a glass slide or SLB present ligands that can engage cell surface proteins. Thus, molecular tension probes enable one to use a conventional fluorescence microscope to measure the

receptor forces with fairly low force threshold levels and high spatial resolution. Tension sensors integrating folded DNA hairpins (HPs) are the most sensitive class of probes reported thus far and are fairly facile to generate and use.²⁷ When the HP is exposed to tension, the stem-loop domain unfolds, separating a fluorophore and quencher and leading to an increase in fluorescence. These probes have been used in applications such as monitoring the mechanical properties of living cells and the study of immune cell mechanics.^{31, 35} However, almost all past examples of DNA HPs studying cell-ECM interaction were tethered onto a glass surface. Given the mechanical properties of cell ECM microenvironment, it is desirable to tether DNA HPs to hydrogels to mimic physiologically relevant substrates.

Typically, hydrogels or other polymers such as PDMS are used to investigate cell biology on compliant substrates. Several past studies by Ha and colleagues reported DNA probes tethered to such polymeric substrates.³⁶⁻³⁸ Typically, these studies utilized DNA duplex probe called tension gauge tether (TGT).³⁹ However, these are irreversible and cannot capture the dynamic ECM-receptor interactions. Additionally, the studies primarily utilized biotin-streptavidin as the gel tethering group, which has a small but present dissociation rate that is force-dependent and prone to degradation due to proteases released by cells.^{40, 41}

To overcome past barriers in integrin force measurement on soft substrates, we designed a hydrogel-tethered cellular tension sensing matrix. Because of the high biocompatibility and less cytotoxicity, we chose PEG-based hydrogel for the substrate.⁴²⁻⁴⁴ First, we tested various lengths of PEG precursors to prepare the different moduli of hydrogels that are more physiologically relevant. Next, we designed nuclease-resistant tension probes

consisting of single-stranded phosphorothioates (PS)-modified DNA HPs. Additionally, we covalently anchored the PS-HP to the hydrogels. Because of the single-stranded structure and covalent linkage, we have minimum probe degradation and dissociation induced by cell-secreted nuclease and cellular traction force. With the various moduli of hydrogel and nuclease-resistant tension probes in hand, we studied cellular traction force on hydrogel substrates. We found that the molecular traction force levels clearly correlated with the rigidity of the substrate. Interestingly, the fluorescent tension signal colocalized with pY118 paxillin signal, supporting the force-mediated focal adhesion formation. Finally, we tested different PS DNA HP constructs (22% and 100% GC content) and found that HeLa cells cultured on 13kPa hydrogel can open 22% GC PS-HP probe but cannot open the 100% GC PS-HP. This result confirms that cell receptor force is dependent on the rigidity of their substrate.

4.3 Results and discussions

Preparation and characterization of the hydrogel scaffold

Human tissues have a tensile strength spanning 100 kPa to 100 MPa, while the elastic modulus spans 1 kPa to 1 GPa.⁴⁵ To develop a generalized tool for cellular force

measurement, we synthesized PEG hydrogels with a controlled modulus that mimics the softer mechanical properties of biological tissues (**Figure 1a-e**).

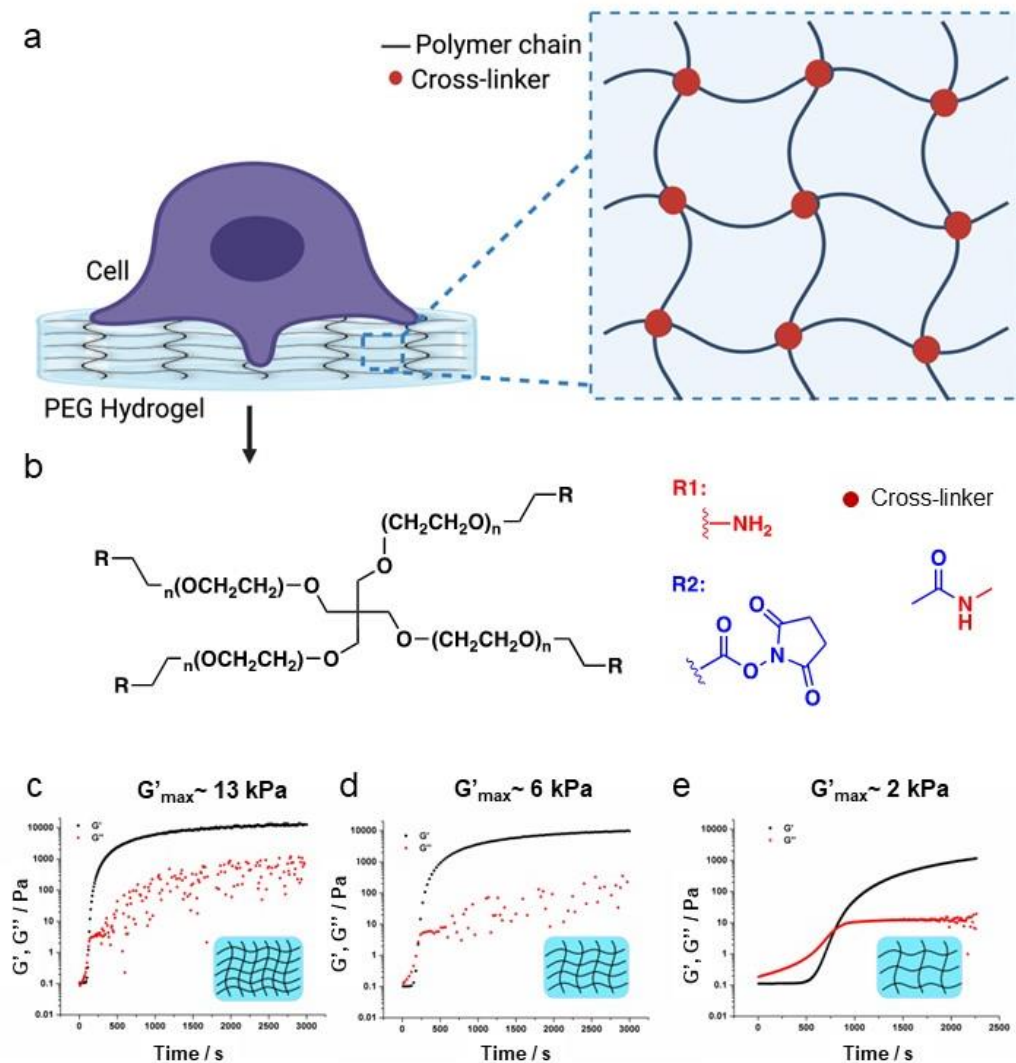


Figure 1. Preparation and characterization of PEG hydrogels. (a) Schematic design of working principle of hydrogel-tethered DNA tension matrix (b) Molecular structure of the hydrogel precursor molecule (tetra PEG-NH₂ and tetra PEG-NHS) (c-e) Time dependent rheology study of PEG hydrogel formed by 5 kDa PEG molecule (c), 10 kDa PEG molecule (d), and 20 kDa PEG molecule (e). Maximum elastic moduli (G'_{max}) were estimated at 50 min gelation time point.

We used PEG precursors with different molecular weights to synthesize hydrogels. Theoretically, with the same polymer weight content (~10 wt.%), the hydrogel synthesized from lower molecular weight precursors will have a greater elastic modulus than those synthesized from greater molecular weight. Briefly, three different hydrogels were synthesized with precursor molecules with 5 kDa, 10 kDa, and 20 kDa molecular weights. We chose NHS-amine reaction to construct the PEG hydrogel as it is spontaneous, does not require radical initiators, and shows appropriate reaction kinetics to mount the hydrogel on the glass surface. After mixing the precursor molecules 4-arm-PEG-NH₂ and 4-arm-PEG-NHS (5% (w/v) in potassium phosphate solution, pH 6.4), the mixture was quickly mounted on the rheometer, where we performed time-dependent rheology measurements to confirm the modulus tuning (**Figure 1c-e**). After allowing the two monomers to form a gel for 50 min, we found that the elastic modulus G'_{\max} of the 5, 10, and 20 kDa precursors were 13 kPa, 6 kPa, and 2 kPa, respectively. These moduli are on the softer range of physiologically relevant moduli and by happenstance are mechanically similar to tissues such as spleen, soft palate, and brain, respectively.⁴⁶ Note that the molecular weight of the precursor also affects the gelation kinetics, and the lower molecular weight precursors tend to gelate more rapidly than the greater molecular weight precursors (**Figure 1c-e**). The frequency scan in rheology indicates a classic hydrogel behavior which G' were significantly larger than G'' at all frequencies (**Figure S1**). We also studied the pore size both theoretically and experimentally (**Figure S2**). While the theoretical pore sizes of synthesized hydrogels are 60, 120, and 240 nm corresponding to 5, 10, and 20 kDa precursors, respectively, the SEM images show 160 and 7600 nm pore sizes for the hydrogels prepared by the 10 and 20 kDa precursors. These differences

between theoretical and experimental pore sizes are due to the hydrolysis of NHS groups under the gelation condition that results in the incomplete crosslinking reaction. Note that we utilized the unreacted amine group to introduce the DNA tension probe.

Design and synthesis of PS-modified DNA hairpin probes.

The starting materials to generate the PS DNA HP probes were single-stranded nucleic acids custom synthesized with a 5'-terminal alkyne and 3'-amine modification along with replacing the phosphodiester backbone with phosphorothioates (**Figure 1f**). The oligonucleotides were then chemically modified by a sequence of three reactions: 1) copper-catalyzed azide-alkyne cyclization (CuAAC), 2) NHS-amine coupling, and 3) strain-promoted azide-alkyne cycloaddition (SPAAC) (**Scheme S1**). Specifically, the 5' alkyne terminus was coupled using CuAAC to a trifunctionalized peptide containing the cyclic(Arg-Gly-Asp-D-Phe-Lys) (cRGD) peptide, Cy3B dye along with an N₃ group to introduce a cell-adhesive peptide and fluorophore to the 5' end of the HP. A DBCO group was installed on the 3' amine terminus, and this allowed for using a SPAAC reaction to couple the trifunctional BHQ2/tetrazine (Tz)-N₃ to the oligonucleotide terminus (**Figure 1f**). The PS DNA HP probes were purified by reversed phase HPLC and characterized by ESI-MS (**Figure S4**). The Gibbs free energies of hairpin unfolding for the PS-modified and -unmodified hairpin were evaluated by van't Hoff analysis using temperature-dependent fluorescence measurements in PBS (**Figure 1g**). As past studies have suggested, the PS-modified hairpin was less stable than that of conventional phosphodiester linked DNA (**Figure 1g and 1h**).⁴⁷ This is because PS-modifications

i

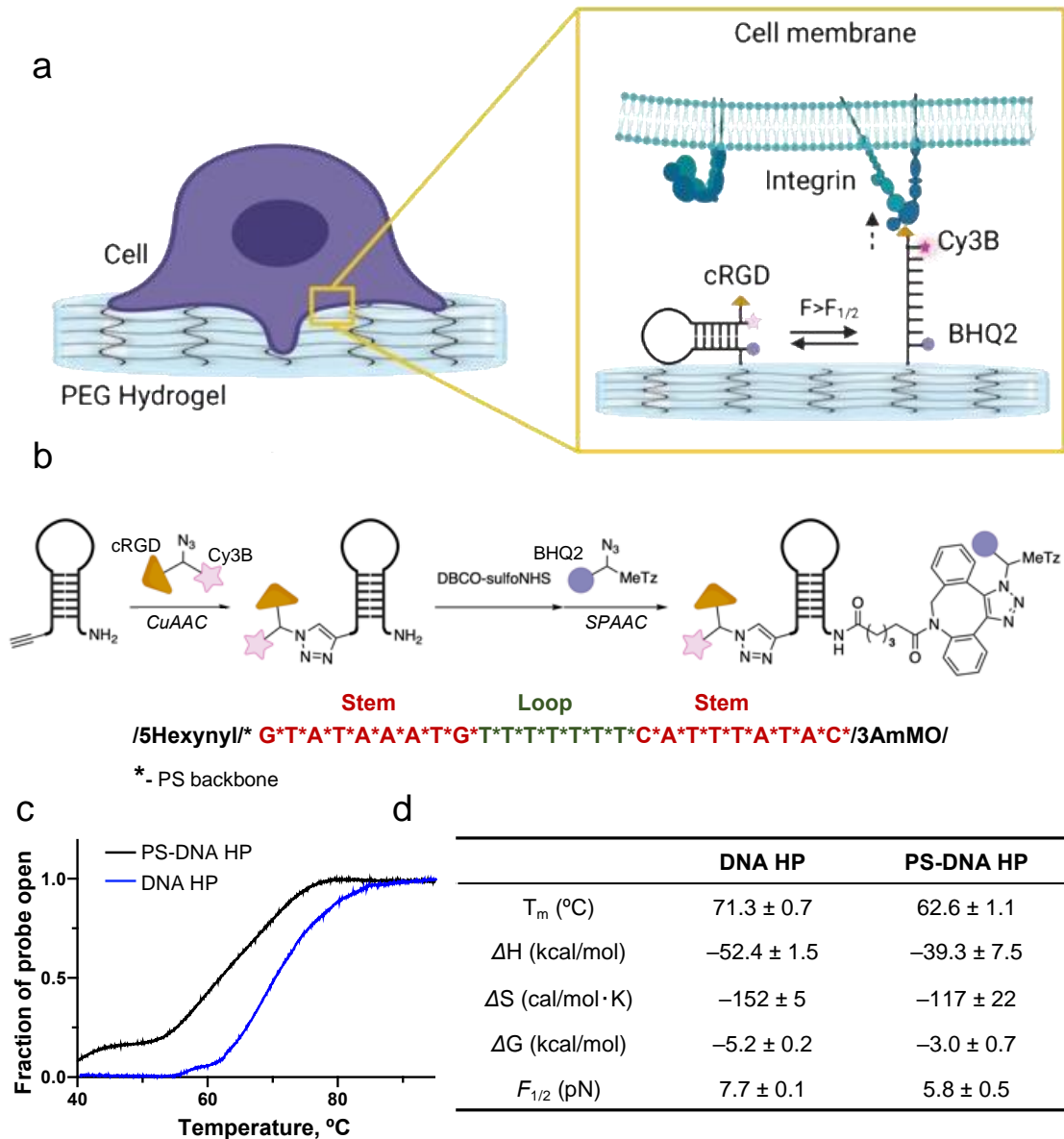


Figure 2. Design, synthesis, and characterization of PS modified HP probes. (a) Schematic design of working principle of hydrogel-tethered DNA tension matrix. (b) Synthetic scheme for preparing PS modified DNA HP probes. (c) Fluorescent thermal melting curve of DNA HP (22% GC) and PS modified DNA HP (22% GC) in PBS, (d) Table of the calculated T_m , ΔG , and $F_{1/2}$ for DNA HP and PS DNA HP (22% GC) probes in PBS at 37 °C.

modified DNA contains many diastereomers that weaken the duplex stability and broaden the melting transition under ensemble macroscopic analysis. Based on the thermodynamics of melting, the force at which 50% of hairpins unfold, $F_{1/2}$, was calculated

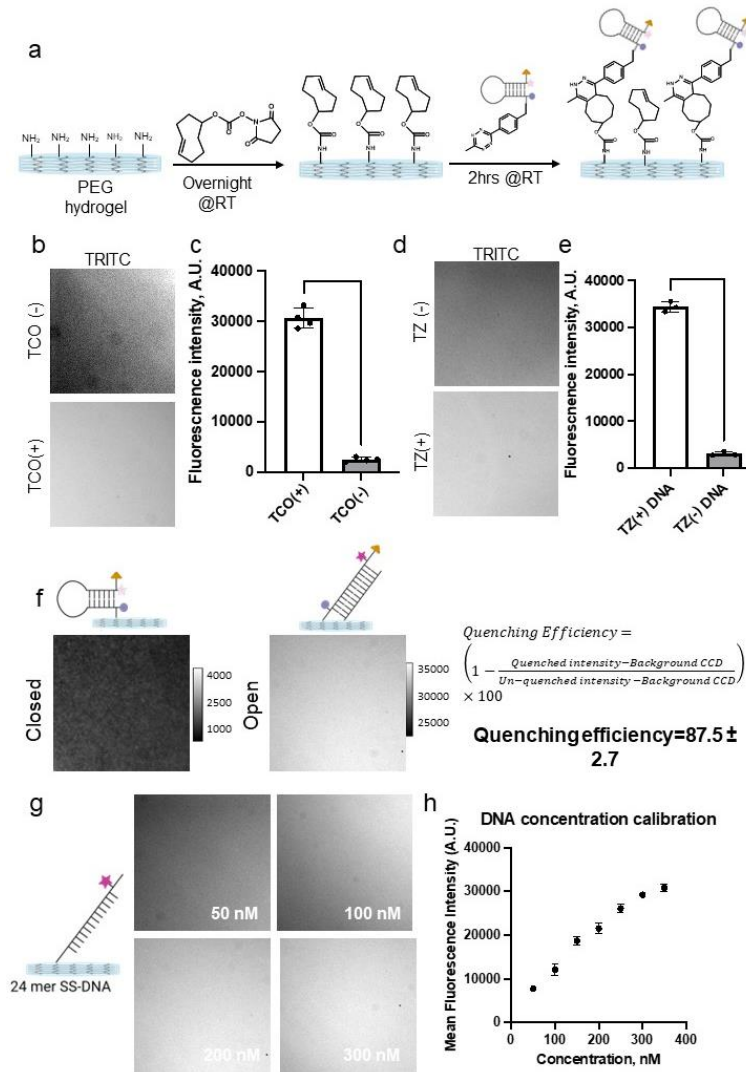


Figure 3. DNA Hairpin anchoring using TCO-Tz coupling. (a) Schematic representation of hydrogel-tethered tension sensing matrix preparation (b,c) fluorescent image and quantification of PS-DNA conjugated Cy3B in TRITC channel on the hydrogel. The gel was prepared with and without the TCO modification step. (d,e) fluorescent image and quantification of PS-DNA conjugated Cy3B in TRITC channel on the hydrogel. The PS-DNA was prepared with and without the Tz conjugation. These experiments with and without TCO or Tz were conducted to showcase specific binding of the DNA (f) Quenching efficiency measurement using DNA hybridization as fully open surface. (g-h) DNA concentration dependent fluorescent intensity shows 300 nM concentration is optimal for surface preparation ****, ***, **, * and ns indicate $p < 0.0001$, $p < 0.001$, $p < 0.01$, $p < 0.05$, and not significant respectively, as determined from one-way ANOVA. Error bars show the standard deviation for $N > 3$, three different sets of surface preparations.

hairpins, respectively. Note that the $F_{1/2}$ was inferred from the Gibbs free energy of unfolding and the free energy required to stretch single-strand DNA based on the worm-like chain model (**Figure 1h**).^{31, 48-50}

Hydrogel-tethered DNA HPs preparation and optimization.

Prior work by Ha³³, Leckband⁵¹, and Wang⁵² and colleagues reported the use of irreversible DNA-based TGT probes that were tethered to hydrogels using biotin-streptavidin chemistry.³⁸ We initially used this biotin-streptavidin strategy to anchor the DNA probes to the PEG hydrogel. However, in our hands, the probe density decreased dramatically (>75% loss) over 24 hrs, and seeded cells were poorly attached and spread (Figure S5). The lack of cell adhesion and tension signal is likely due to the k_{off} rate of biotin-streptavidin at 37 °C.^{40, 53} This led us to develop a covalent anchoring strategy using conventional DNA probes onto hydrogel; however, these probes showed significant nuclease- and traction force-mediated degradation over 6 hrs of cell seeding and then fluorophore internalization (Figure S6). Thus, we decided to employ a single-stranded DNA with PS modification rather than our original three-strand design as single-stranded PS DNA probes demonstrate high stability against traction force and nuclease activity.

We prepared 13kPa PEG hydrogels with/without TCO to validate the HP binding was specific and mediated by covalent coupling. The fluorescent images indicate that only a subset of the probes (<5%) are non-specifically bound to the hydrogel (Figure 3b and c). We also prepared oligos without Tz modification and observed a minimum nonspecific modification (<5%), confirming specific coupling through TCO-tetrazine chemistry (Figure 3d and e). Then, we measured the quenching efficiency of the closed hairpin probes. For

this experiment, we hybridized the quenched probe with a complementary oligonucleotide before reacting with the TCO-modified PEG hydrogel. Following the quenching efficiency (QE) calculation equation, we calculated the QE to be ~87.5%, which is slightly less efficient than our previous reports (Figure 3f).^{31, 54} This lower quenching efficiency can be derived from the less stability of PS DNA HP at 37 °C, resulting in a slightly higher probability of probe opening (Figure 2c melting). We used different DNA concentrations and incubation times to optimize the maximum probe density. We found that 300 nM DNA with an incubation time of 2 hrs (@RT) works best for preparing a hydrogel-tethered cellular tension sensing matrix (Figure 3g and h).

Cells can exert reversible pN tension on PEG hydrogel surfaces, and substrate stiffness modulates the total threshold of the exerted tension.

We used HeLa cells as a model system. Due to their high nuclease and protease activity and elevated mechanical activity, it is challenging to measure cellular tension using conventional (unmodified) DNA probes for extended durations beyond 1 hr. To address this issue, we prepared the PS modified hairpin-coated PEG hydrogel, and incubated HeLa cells for at 37 °C, 5% CO₂. The cell attachment and spreading were confirmed by brightfield imaging every 60 mins after 3 hrs incubation. Unlike cells cultured on RGD-DNA modified glass surfaces, which require 15-20 mins to show cell attachment and spreading, cells cultured on the 13 kPa hydrogels required 3-6 hrs to spread and exert sufficient traction force to open the PS DNA HP probe (**Figure 4a**). When HeLa cells were cultured on 13 kPa hydrogel presented with PS DNA HP probe for ~6 hrs, 100% increase in fluorescence intensity of the probe was observed in the peripheral region of the HeLa cells, confirmed by the bright field image.

Immunostaining with phospho-paxillin showed colocalization of tension signal confirming focal adhesion formation (**Figure S7**). To evaluate the impact of substrate stiffness on the cell traction force, we quantified the fluorescent tension signal and spreading area of the HeLa cells cultured on three hydrogels with different stiffness of 2, 6, and 13 kPa as described in **Figure 1**. The results showed a correlation between the spreading area, fluorescent tension signal, and gel stiffness. Indeed, we observed the lowest fluorescent tension signal on the 2 kPa hydrogel and the greatest tension signal on the 13 kPa hydrogel (**Figure 4a and b**). We also observed elongated f-actin expression on 13 kPa and 6 kPa substrates compared to 2 kPa substrates (**Figure S8**). To rule out differences in DNA/ligand density, we prepared stiffness-varying hydrogels similarly (with the same DNA concentration and incubation time). We confirmed this by measuring the similar background intensity before the cell experiments (**Figure S9**). To validate that the fluorescence signal is driven by specific forces between integrins and the probe-conjugated cRGD on the hydrogel, we created a control hydrogel substrate modified with the PS-DNA HP probe lacking cRGD as well as the cRGD peptide directly attached to the hydrogel (**Figure 4c**). Cells spread similarly on such control hydrogels, but the fluorescence intensity was diminished (10-fold decrease) and comparable to the

background intensity (**Figure 4d** and **S10**), thus confirming that the fluorescence signal is primarily mediated by specific integrin-cRGD interactions.

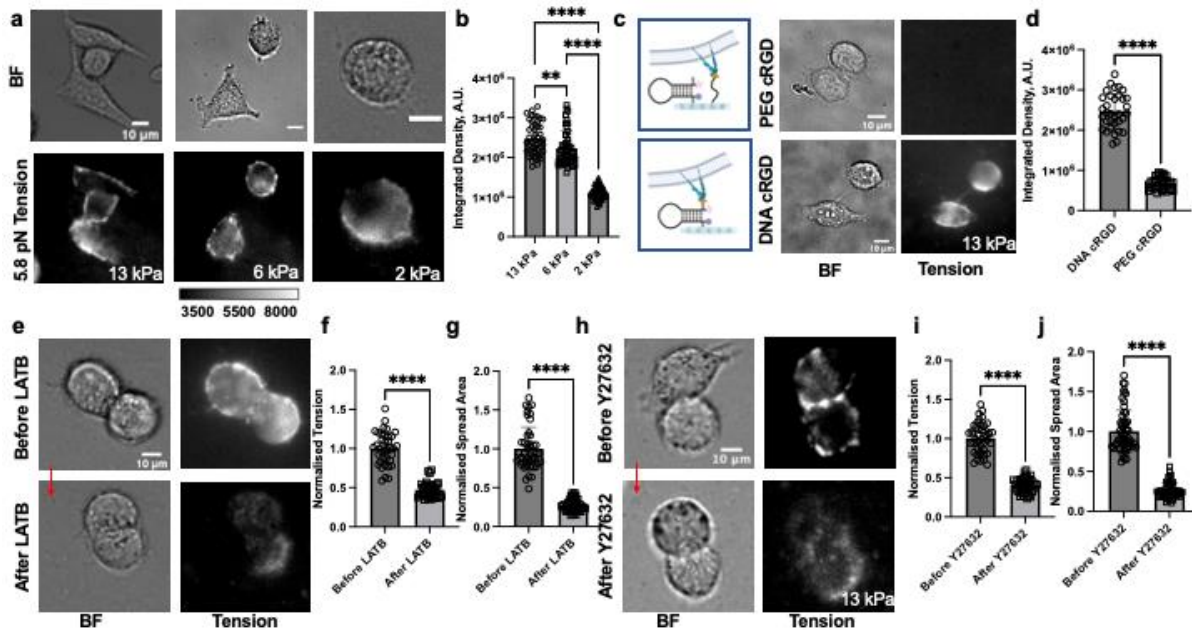


Figure 4. HeLa cells can sense matrix stiffness and differentiate the magnitude of force against 2, 6, and 13 kPa PEG gel (a) HeLa cells cultured on 13, 6, and 2 kPa substrate coated with PS DNA HP probe (22% GC content) (b) Total tension of HeLa cells on the different substrate (c) Schematic illustration of hydrogel (left) and BF and fluorescent tension images of HeLa cells cultured on hydrogel coated with PEG-cRGD and cRGD-lacked PS DNA HP probe (top) and hydrogel coated with PS DNA HP probe (bottom). (d) Quantification of total tension signal on the condition of (c). (e-g) BF and tension images of HeLa cells before and after treatment with LatB (20 μ M) and bar graph for the quantification of spread area and tension signal. (h-j) BF and tension images of HeLa cells before and after treatment with Y27632 (25 μ M) drug and bar graph for the quantification of spread area and tension signal. ****, ***, **, *, and ns indicate $p < 0.0001$, $p < 0.001$, $p < 0.01$, $p < 0.05$, and not significant respectively, as determined from one-way ANOVA. Error bars show the standard deviation for $N > 3$, where each experiment was averaged from three or more different cell passages with three different sets of surface preparations. Scale bar=10 μ m.

Finally, to demonstrate the reversibility of the tension signal, we treated the cells with either a cytoskeleton inhibitor (Latrunculin B) or a Rho kinase inhibitor (Y27632) (**Figure 4e-j**). The treated cells showed ~50% less spread area and ~80% less tension signal than untreated cells. This confirms that the reported tension is reversible and mediated by F-actin and myosin activity in alignment with prior literature.⁵⁵⁻⁵⁷

HeLa cells cannot unfold the stiff hairpin suggesting the tension threshold for each receptor is higher than 5.8 pN but smaller than 19 pN.

Previous work from our lab has shown that increasing the GC content in the stem region of DNA HPs can result in higher $F_{1/2}$.³⁵ Thus, we used 100% GC content for the stem region of the PS DNA HP probe to evaluate the magnitude of integrin-mediated traction force when cells are cultured on soft substrate. In contrast to PS DNA HP with 22% GC showing a fluorescent melting curve ($T_m = 62.6 \pm 1.1$ °C, **Figure 2c**), PS DNA HP with 100% GC did not show the full melting curve as higher GC content leads to high thermodynamic stability. Because our observation and previous work suggest that PS modification decreases the duplex stability, we expected the $F_{1/2}$ of PS DNA HP probe with 100% GC to be smaller than that of unmodified DNA HP probe ($F_{1/2} = 19$ pN).

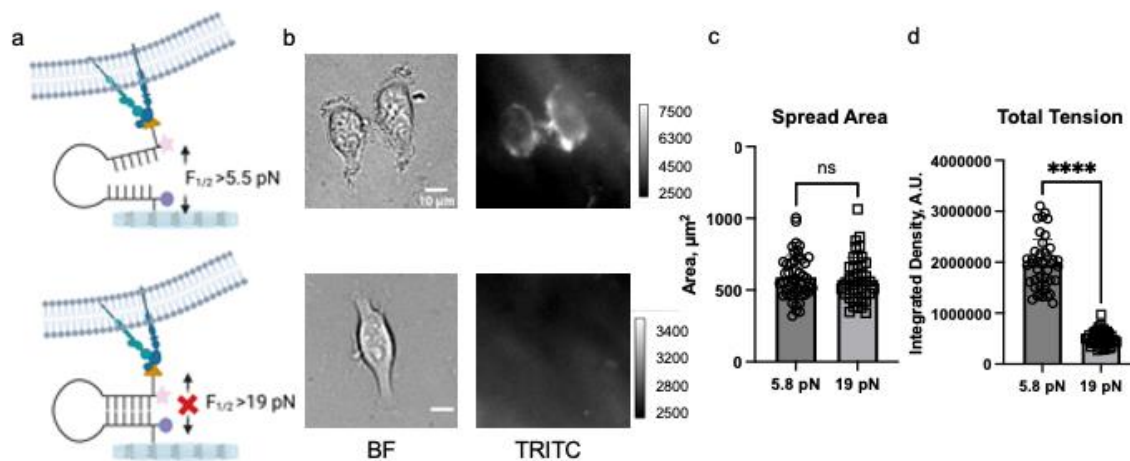


Figure 5. The force threshold of receptor forces exerted by HeLa cells are within $5.8 \text{ pN} < F_{1/2} < 19 \text{ pN}$ (a) Schematic representation of receptors pulling on to different force threshold of PS DNA HP probes (b) Bright Field and fluorescent tension (Cy3B) images of Hela cells on 5.8 pN and 19 pN surfaces. Images were taken after 3-4 hrs of incubation. (c) Bar graph showing spread area of cells on 5.8 and 19 pN hairpin surfaces. (d) Bar graphs plotting the integrated fluorescent tension signal of HeLa cells cultured on hydrogel-tethered 5.8 and 19 pN substrates. ****, ***, **, *, and ns indicate $p < 0.0001$, $p < 0.001$, $p < 0.01$, $p < 0.05$, and not significant respectively, as determined from one-way ANOVA. Error bars show the standard deviation for $N > 3$, where each experiment was averaged from three or more different cell passages with three different sets of surface preparations. Scale bar=10 μm .

When HeLa cells were cultured on 100% GC probes, cells could not unfold the hairpins and thus not observe the fluorescent tension signal. While the cell spreading areas were identical for the cells cultured on PS DNA HP probes (22% and 100% GC content), the quantified fluorescent tension signal for PS DNA HP probes (100% GC content) was

much smaller than that for the PS DNA HP probes (22% GC content) (**Figure 5 b and d**). These results suggest that the significant decrease in tension signal was not caused by poor spreading but caused by the lower magnitude of traction force when HeLa cells were cultured on soft substrates. Note that HeLa cells cultured on a glass substrate coated with PS DNA HP probe (100% GC) showed observable fluorescent tension signal (**Figure S11**).

4.4 Conclusions

Mechanical forces are crucial in cellular processes, such as cell adhesion, migration, and proliferation. As such, there is an increasing need for techniques that can accurately measure cellular traction force. Unfortunately, while existing tension sensing methods have shown promise, they are often limited by their inability to provide precise and localized measurements.

To address these limitations, we have developed a novel PEG hydrogel matrix that supports MTFM probes and responds to cellular traction force. In addition, the hydrogel matrix can provide several advantages over other tension-sensing techniques, including biocompatibility, elastic modulus tunability, and the ability to mimic the physiological conditions of living tissues.

Our experiments treated the hydrogel matrix with latrunculin B, which disrupts actin filaments and reduces cellular tension. As a result, we found that the fluorescence signals detected on the hydrogel surface were primarily indicative of cellular tension force rather than autofluorescence, confirming the effectiveness of our tension-sensing approach.

Furthermore, we investigated the effect of substrate stiffness on cellular behavior by culturing HeLa cells on hydrogels of varying stiffness. We discovered that HeLa cells exerted more potent mechanical force and exhibited a larger spreading area on stiffer substrates, highlighting the importance of substrate stiffness in regulating cellular behavior.

Moving forward, we plan to construct a 2.5D model as a step towards molecular tension sensing in a 3D environment where cells reside *in vivo*. Our findings provide valuable guidance for future developments in hydrogel-based tension sensing techniques and have the potential to advance our understanding of mechanical forces in cellular processes significantly.

4.5 Materials and methods

Synthesis of Phosphorothioates- (PS-) modified tension probes.

To synthesize PS-modified tension probes, we employed a three-step sequential process involving copper-mediated azide-alkyne cyclization reaction (CuAAC), NHS-Amine coupling reaction, and strain-promoted azide-alkyne cycloaddition reaction (SPAAC). Initially, we obtained 5' alkyne- and 3' amine-modified oligonucleotide with full PS-modification from Integrated DNA Technology (Coralville, IA). This oligonucleotide was then subjected to CuAAC reaction with cRGD/Cy3B-N₃ to introduce a cell-adhesive peptide and a fluorophore for tension signal. Subsequently, the amine group of the PS-modified oligonucleotide was reacted with DBCO-sulfo-NHS to introduce a strained alkyne group. Finally, the strained alkyne group was reacted with BHQ2/Tz-N₃, which acted as a quencher and surface anchoring moiety, forming the PS-modified tension probe. The detailed synthetic scheme can be found in Supporting Information.

Synthesis of hydrogel surface

To create the PEG hydrogel surface, two precursor solutions were mixed. In the case of the 5k molecular weight hydrogel, the first solution contained 55 mg of 4-arm-PEG-NH₂ (Mw 5k; Biopharma PEG, 10225) dissolved in 500 μ L potassium phosphate buffer (pH 6.4), while the second solution contained 50 mg of the 4-arm-PEG-NHS molecule (Mw5k; NOF America Corp. PTE05GS) dissolved in 500 μ L potassium phosphate buffer (pH6.4). The solutions were then cooled on ice for 15 minutes and mixed vigorously using a stir bar for 5 seconds at approximately 400 rpm. A 20 μ L mixture was then placed between a

parafilm strip and an APTES-treated glass surface to create a thin (80 μm) hydrogel layer, which was incubated for 1 hr at room temperature. Please note that the molecular weight given for 4-arm-PEG molecules refers to the overall molecular weight, not that of one arm. For example, a 4-arm-PEG molecule with a total molecular weight of 5k would have an M_w $5000/4=1250$ for each arm.

Gel stiffness characterization

The rheological properties of PEG hydrogel precursor mixtures were evaluated using an AR2000ex rheometer equipped with a temperature-controlled stage. The measurements were conducted between a 25 mm parallel plate and a stainless-steel stage using 100 μL of the liquid precursor mixture. The gap size was set to 0.1 mm. Oscillation mode was employed, where the top plate oscillated back and forth with a fixed amplitude and frequency. Time-dependent rheological experiments were performed at 25 $^{\circ}\text{C}$ with a constant strain of 1% and frequency of 1 Hz. Frequency sweep tests were performed on mixtures ranging from 0.01 Hz to 1000 Hz at 25 $^{\circ}\text{C}$ and a fixed strain of 1%.

Surface preparation

The parafilm strip was then removed using tweezers, and the gel was treated with DMSO for 5 minutes to wash and incubated overnight with 200 μL of 5 mg/mL NHS-TCO in DMSO. After thoroughly washing the TCO-coated PEG surface with DMSO (3 times), EtOH (3 times), Nano-pure water (3 times), and 1xPBS (3 times), 300 nM DNA was incubated on the surface for 2 hrs. The gel was washed thoroughly with PBS (3 times) and cell culture media (3 times) before seeding.

Cell imaging

The imaging of HeLa cells was performed in a 5% serum containing DMEM at a temperature of 25 °C, utilizing a Nikon Eclipse Ti microscope controlled by the Elements software package. This advanced microscope was equipped with various components, including an Evolve electron-multiplying charge-coupled device manufactured by Photometrics, an Intensilight epifluorescence source produced by Nikon, and a CFI Apo 40x objective, also made by Nikon.

Cell culture

We employed HeLa cells for our experiments. To provide optimal culture conditions, we used a culture medium with 10% Fetal Bovine Serum (FBS) supplemented with 2.2 mM L-glutamine and 1% antibiotic. To initiate cell adhesion and to spread, we added the cells to the substrate and incubated them for 3-6 hrs at 37 °C with 5% serum and 1% antibiotic. During this time, the cells attached to the surface and began to spread, allowing us to capture images and videos of their behavior. Our experiments required careful control of environmental conditions to ensure the viability and functionality of the cells.

Immunostaining

The cells were fixed by adding 2-4% formaldehyde in 1× PBS for 8-10 minutes. After fixation, cells were permeabilized with 0.1% Triton X-100 for 3 minutes and then blocked with BSA for 30 minutes. To perform staining, cells were exposed to 1:1000 Alexa 488-Phalloidin (Actin staining, ab176753, Abcam), 1:50 Vinculin Antibody SF9 647 (sc-73614

AF647, Santa Cruz Biotechnology), 1:50 Phospho-Paxillin (Tyr1888) Polyclonal Antibody (PA5-17828, Thermo Fisher). The cells were incubated with the primary antibodies for 1 hr at room temperature or refrigerated overnight followed by 1:3000 Alexa Fluor 555 goat anti-rabbit (A21147, Thermo Fisher), 1:1000 Alexa Fluor 647 or 488 goat anti-mouse IgG2b (γ 2b) (A28175 or A28181) or goat anti-rabbit secondary antibody (A27034 or A27080) from Thermo Fisher as indicated in the experiment details. The immunostained cells were imaged with fluorescent microscopy.

Drug treatment

Prior to seeding, the cells were subjected to pretreatment with various inhibitors for over 1 hr at room temperature. The cells were exposed to different treatments, including 25 μ M Y27632 dihydrochloride (Y0503, Millipore Sigma) for 30 minutes, 10 μ M eptifibatide (CAS No. 881997-860) for 30 minutes, 10 μ M Blebbistatin (18-521, Fisher Sci) for 30 minutes, or 25 μ M latrunculin B for 30 minutes. The control group was treated with 0.2% DMSO, which was used as a solvent vehicle.

Illustration and statistical analysis

All the illustrations of this manuscript were prepared by either adobe illustrator or BioRender.com. Statistical analyses were performed in GraphPad, imagej and MatLab.

Author contributions

Sk A.R. , Y. D. , and K.S. conceived of the project. SK A.R. and Y.D. designed and performed troubleshoot experiments. H. O. designed, prepared and characterized the probes for the study. M.E assisted in surface preparation. Sk A. R., H.O., and K.S. wrote the manuscript. All the authors helped revise the manuscript.

Acknowledgement

The authors especially want to thank Joseph D. Combs for assisting with manuscript review and discussions that led to experiments. Also, to Arventh Velusamy for discussions about surface preparation. Steven Narum assisted with the confocal imaging.

4.6 Appendix

1. SEM sample preparation.

A small PEG gel (1x1x0.2 cm) was synthesized at room temperature. The hydrogel was quickly dipped in liquid nitrogen for around 1min and then broken by tweezers to get the new cross-sections. After the sample was dried in a lyophilized overnight, the sample piece was mounted on a 90-degree aluminum SEM stub. Pt/Pd coating was also applied to the sample (~8 nm) to improve the image quality.

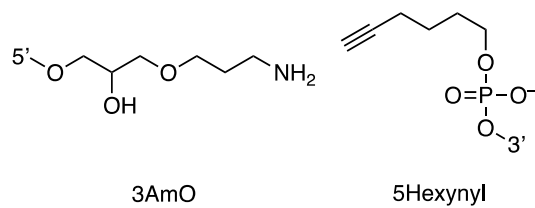
2. PEG pore size calculation.

The pore size is calculated based on previous studies.⁵⁸ Since the length of each PEG unit is ~0.28 nm, the pore size of hydrogels synthesized by 5 kDa/10 kDa/20 kDa PEG precursors are estimated to be 60/120/240 nm, respectively, in ideal conditions in which all the functional groups are reacted. Note that the PEG molecule is too soft at room temperature to maintain the original porous structure. Thus the SEM images can show different pore sizes when the samples are lyophilized. Because of this, the observed pore sizes did not match estimated sizes, while we observed a reduced pore size trend when the hydrogel was prepared with lower molecular weight PEG precursors.

Table 1: Sequence of DNA-HP probes used in this study.

Name	Sequence (5' to 3')
PS 22% GC	/5Hexynyl/*G*T* A*T*A* A*A*T* G*T*T* T*T*T* T*T*C* A*T*T* T*A*T* A*C*/3AmMO/
PS 100% GC	/5Hexynyl/*G*C* G*C*G* C*G*C* G*C*G* C*T*T* T*T*G* C*G*C* G*C*G* C*G*C* G*C*/3AmMO/

*Phosphorothioates (PS) modification



3. Copper-mediated azido-alkyne cyclization reaction for alkyne-modified oligonucleotides (22% GC hairpin & 100% GC hairpin)

cRGD-Lys(N₃)-Cy3B (cRGD/Cy3B-N₃) was ligated to the corresponding 5' alkyne-modified strand (IDT) via 1,3-dipolar cycloaddition reaction. Briefly, a solution of 10 nmol of phosphorothioate-modified DNA was reacted 1 hour at 50 °C with 20 nmol of azido reagents in the presence of sodium ascorbate (0.10 μmol), CuSO₄ (0.10 μmol), THPTA (0.75 μmol), and triethyl amine (4 μmol) in 45 μL (3: 2 = 18.2 MΩ MilliQ water: DMSO). The product was filtered through a microcentrifuge filter (0.22 μm). The filtrate was subjected to reverse-phase HPLC (AdvancedBio Oligonucleotides, Agilent, 4.6 × 150 mm, 0.5 mL min⁻¹ flow rate; solvent A: 0.1 M triethylammonium acetate (TEAA), solvent B: acetonitrile, solvent C: 50 mM EDTA, 100 mM triethylamine, hydrochloric acid was used to adjust pH 7.2, 90% 18.2 MΩ MilliQ water/ 10% methanol, HPLC condition: 100% C for 8 min to remove excess Cu ion, then 90% A + 10% B for 3 min, and then 1% per min gradient B for 16 min) to afford desired products.

Product **1**, 22% GC HP (5'- cRGD/Cy3B, 3'- NH₂): MS (ESI) calcd. For [M]⁺: 10006.7; deconvoluted: 10005.5

Product **2**, 100% GC HP (5'- cRGD/Cy3B, 3'- NH₂): MS (ESI) calcd. For [M]⁺: 11004.4; deconvoluted: 11004.4

4. NHS reaction for amine-modified oligonucleotides

A solution of 3'-amine modified oligonucleotide in 18.2 MΩ MilliQ water (10 μL) was added 10 μL of 10X PBS and 10 μL of an aqueous solution of 1 M NaHCO₃. The mixture was then added sulfoNHS-DBCO or NHS-DBCO (Click Chemistry Tools, 300 μg) for 22% HP and 100% HP,

respectively, in DMSO (70 μL) and left for 1.5 hour. The product was filtered through a microcentrifuge filter (0.22 μm) with 50 μL of 18.2 M Ω MilliQ water. The filtrate was subjected to reverse-phase HPLC (AdvancedBio Oligonucleotides, Agilent, 4.6 \times 150 mm, 0.5 mL min⁻¹ flow rate; solvent A: 0.1 M triethylammonium acetate (TEAA), solvent B: acetonitrile; starting condition: 82% A + 18% B, 0.83% per min gradient B) to desired products.

Product **3**, 22% GC HP (5'- cRGD/Cy3B, 3'- DBCO): MS (ESI) calcd. For [M]⁺: 10320.1; deconvoluted: 10312.2

Product **4**, 100% GC HP (5'- cRGD/Cy3B, 3'- DBCO): MS (ESI) calcd. For [M]⁺: 11291.8; deconvoluted: 11291.6

5. Strain-promoted azido-alkyne cyclization reaction for alkyne-modified oligonucleotides (22% GC hairpin & 100% GC hairpin)

To a solution of DBCO modified oligonucleotides in 18.2 M Ω MilliQ water (20 μL) was added large excess amount of BHQ2/MeTz-N₃ or MeTz-PEG₄-N₃ (Click Chemistry Tools) in DMSO (80 μL) and left for 3 hour. The resulting solution was filtered through a microcentrifuge filter (0.22 μm). The filtrate was subjected to reverse-phase HPLC (AdvancedBio Oligonucleotides, Agilent, 4.6 \times 150 mm, 0.5 mL min⁻¹ flow rate; solvent A: 0.1 M triethylammonium acetate (TEAA), solvent B: acetonitrile; starting condition: 75% A + 25% B, 1% per min gradient B for 30 min) to PS modified tension probes.

Product **5**, 22% GC HP Probe (5'- cRGD/Cy3B, 3'- BHQ2/MeTz): MS (ESI) calcd. For [M]⁺: 11328.2; deconvoluted: 11327.1

Product **6**, 100% GC HP (5'- cRGD/Cy3B, 3'- BHQ2/MeTz): MS (ESI) calcd. For [M]⁺: 12297.9; deconvoluted: 12297.2

Product **7**, 22% GC HP Probe (5'- cRGD/Cy3B, 3'- MeTz): HPLC starting condition: 75% A + 25% B, 0.5% per min gradient B for 25 min: MS (ESI) calcd. For [M]⁺: 10711.5; deconvoluted: 10710.8

6. Synthesis of oligonucleotides for control experiments(22% GC hairpin)

A solution of 3'-amine modified oligonucleotide in 18.2 MΩ MilliQ water (10 μL) was added 2.5 μL of 10X PBS, 2.5 μL of an aqueous solution of 1 M NaHCO₃, and 5 μL of 18.2 MΩ MilliQ water. The mixture was then added NHS-QSY9 (50 μg) or NHS-Cy3B (50 μg) for Product **1** or 22% HP, respectively, in DMSO (5 μL) and left for 1 hour. The product was filtered through a P2 gel with 75 μL of 18.2 MΩ MilliQ water. The filtrate was subjected to reverse-phase HPLC (AdvancedBio Oligonucleotides, Agilent, 4.6 × 150 mm, 0.5 mL min⁻¹ flow rate; solvent A: 0.1 M triethylammonium acetate (TEAA), solvent B: acetonitrile) to desired products.

Product **8**, 22% GC HP Probe (5'- cRGD/Cy3B, 3'- QSY9): HPLC starting condition: 82.5% A + 17.5% B, 0.5% per min gradient B for 20 min: MS (ESI) calcd. For [M]²⁺: 10807.6; deconvoluted: 10807.8

Product **9**, 22% GC HP Probe (5'- Alkyne, 3'- Cy3B): HPLC starting condition: 83% A + 17% B, 1% per min gradient B for 23 min: MS (ESI) calcd. For [M]⁺: 8957.9; deconvoluted: 8958.7

MeTz-Lys(N₃)-BHQ2 (BHQ2/MeTz-N₃) was ligated to the corresponding 5' alkyne-modified strand (Product **9**) via 1,3-dipolar cycloaddition reaction. Briefly, a solution of Product **9** was reacted 1 hour at 50 °C with 20 nmol of azido reagents in the presence of sodium ascorbate (0.10 μmol), CuSO₄ (0.10 μmol), THPTA (0.15 μmol), and triethyl amine (4 μmol) in 45 μL (1: 4 = 18.2 MΩ

MilliQ water: DMSO). The product was filtered through a microcentrifuge filter (0.22 μm). The filtrate was subjected to reverse-phase HPLC (AdvancedBio Oligonucleotides, Agilent, 4.6 \times 150 mm, 0.5 mL min^{-1} flow rate; solvent A: 0.1 M triethylammonium acetate (TEAA), solvent B: acetonitrile, solvent C: 50 mM EDTA, 100 mM triethylamine, hydrochloric acid was used to adjust pH 7.2, 90% 18.2 M Ω MilliQ water/ 10% methanol, HPLC condition: 100% C for 8 min to remove excess Cu ion, then 90% A + 10% B for 3 min, and then 2% per min gradient B for 16 min,) to afford desired products.

Product **10**, 22% GC HP Probe (5'- BHQ2/MeTz, 3'- Cy3B): HPLC condition: 100% C for 8 min to remove excess Cu ion, then 85% A + 15% B for 3.5 min, and then 2% per min gradient B for 25 min, MS (ESI) calcd. For $[\text{M}]^+$: 9964.0; deconvoluted: 9965.1

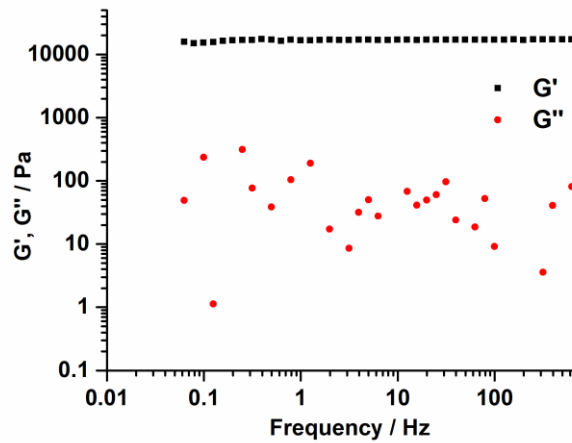
7. Thermal Melting Analysis

For the experimental thermal melting curve, 100 μL solutions of compound **8** at 20 μM was prepared in 1X PBS in qPCR tubes. The probe solutions were heated to 70 $^{\circ}\text{C}$ for 3 minutes and then cooled at a rate of 1.3 $^{\circ}\text{C min}^{-1}$ to 25 $^{\circ}\text{C}$ to hybridize. The solutions were then transferred to the 4 wells of a 96-well qPCR plate in 20 μL each for three individual measurements for a condition. Using the qPCR instrument (LightCycler 96), the plate was incubated at 37 $^{\circ}\text{C}$ for 5 min and then heated to 95 $^{\circ}\text{C}$ over 1900 seconds with Cy3B fluorescent measurements.

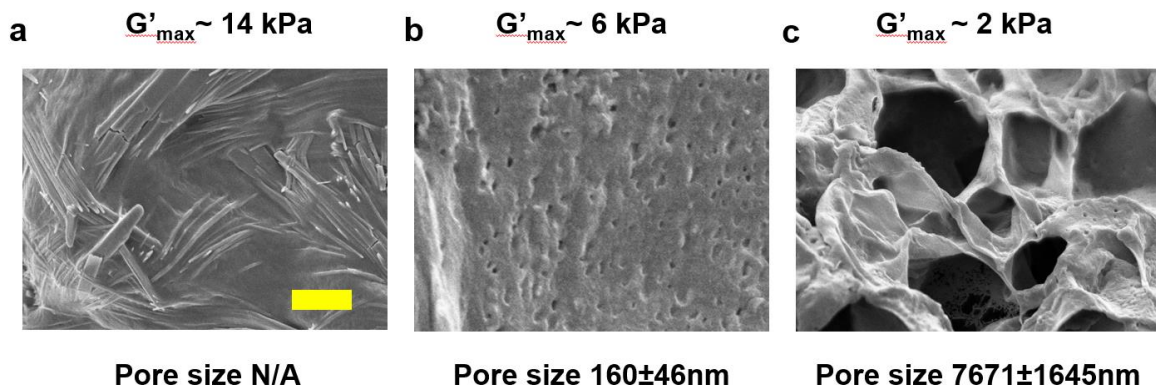
Because the thermodynamic equilibrium of DNA folded structure is an intramolecular transition, their thermodynamic parameters, including ΔG , ΔH , and ΔS , are concentration-independent.⁵⁹ Thus, the probe's van't Hoff equation for thermodynamic analysis can be adopted from the definition of Gibbs free energy equation.

8. Electron Spray Ionization (ESI) mass spectroscopy

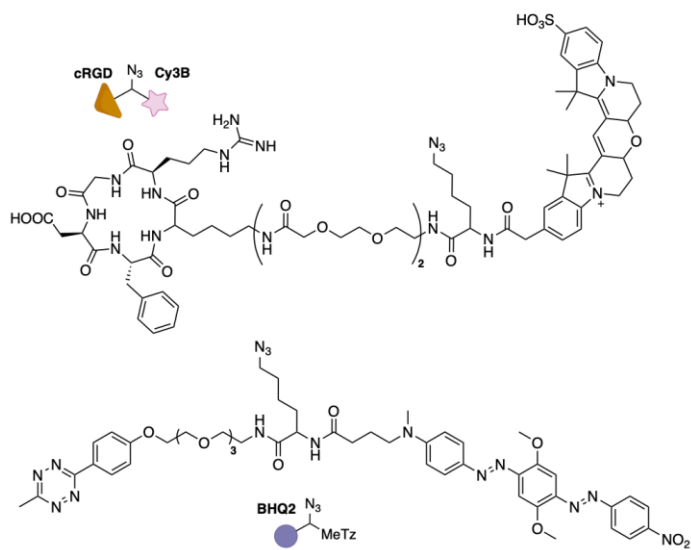
The molecular weight of the products was evaluated with an electron spray ionization (ESI) method using a Thermo Fisher Scientific Orbitrap. For the small molecules, the samples were prepared in the 18.2 MΩ MilliQ water and recorded the spectra in positive charge mode eluted with a mixture of 60% of 18.2 MΩ MilliQ water and 40% of acetonitrile containing 0.05% formic acid. For oligonucleotides, the samples were prepared in the mixture of 70% 18.2 MΩ MilliQ water and 30% methanol containing 10 μM ethylenediaminetetraacetic acid (EDTA), 0.0375% triethylamine, and 0.75% of 1,1,1,3,3,3-hexafluoro-2-propanol (HFIP) and recorded the spectra with negative charge mode eluted with same solution.⁶⁰ The obtained ESI-MS spectrum (m/z) was then deconvoluted for the main peak to obtain average molecular weight for the oligonucleotides.



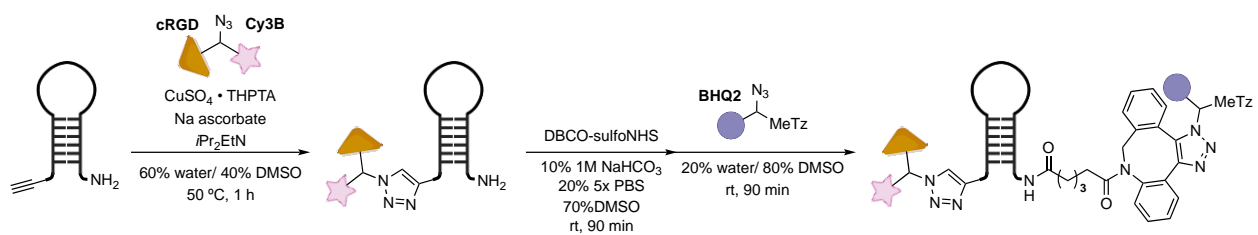
Supplementary figure 1. Frequency scan (0.1-1000 Hz) in rheology characterization of a PEG hydrogel that has 13 kPa modulus. Note that $G' > G''$ in all frequencies, which represents



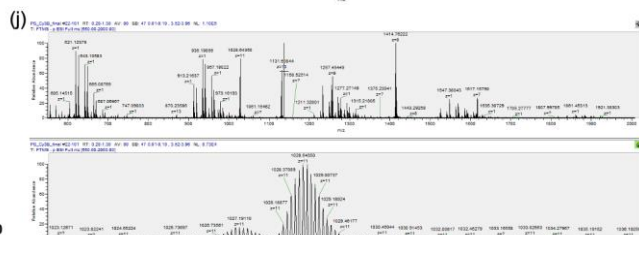
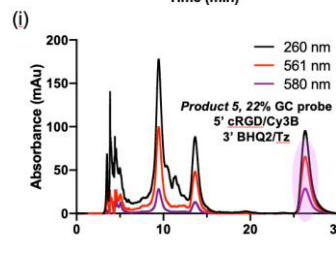
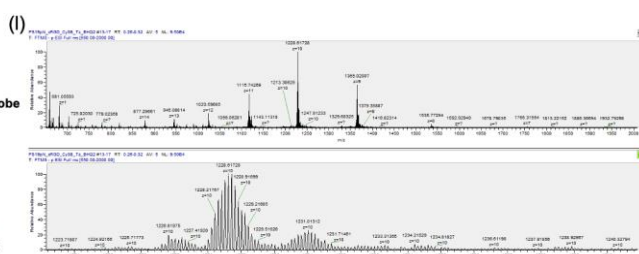
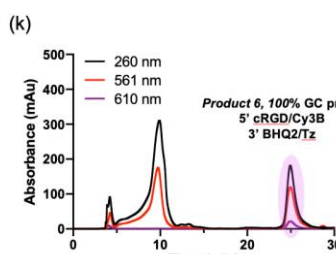
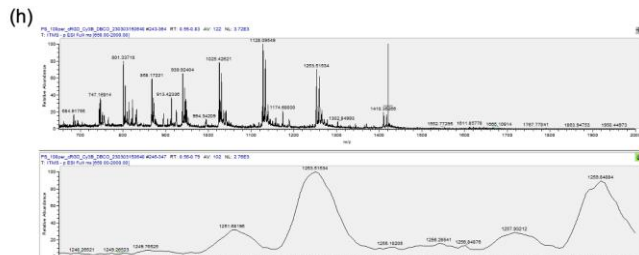
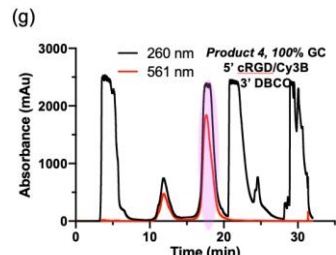
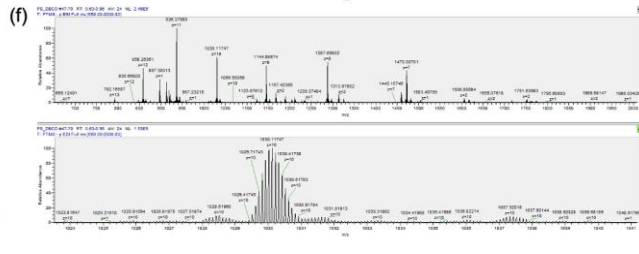
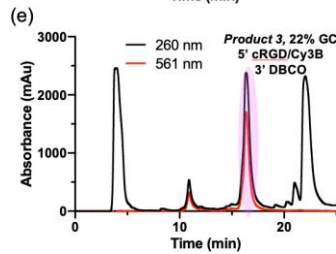
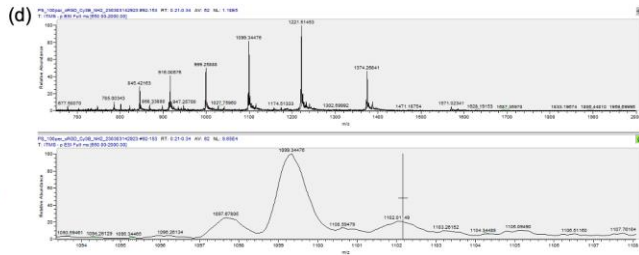
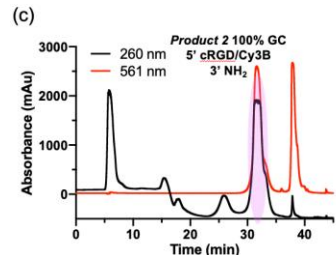
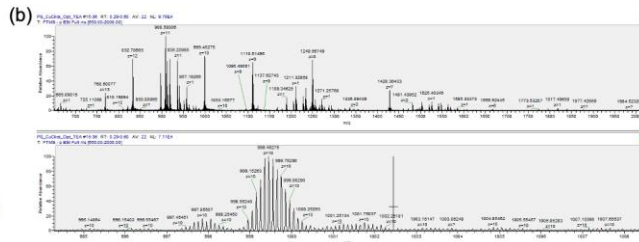
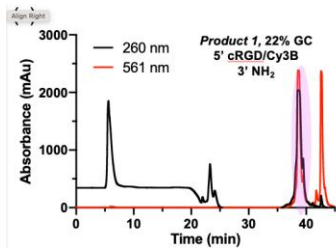
Supplementary figure 2. SEM images and pore size calculation for PEG hydrogels with different elastic modulus. **a.** hydrogel synthesized from 5 kDa PEG precursors. **b.** hydrogel synthesized from 10 kDa PEG precursors. **c.** hydrogel synthesized from 20 kDa PEG precursors. Scale bar: 4 μm

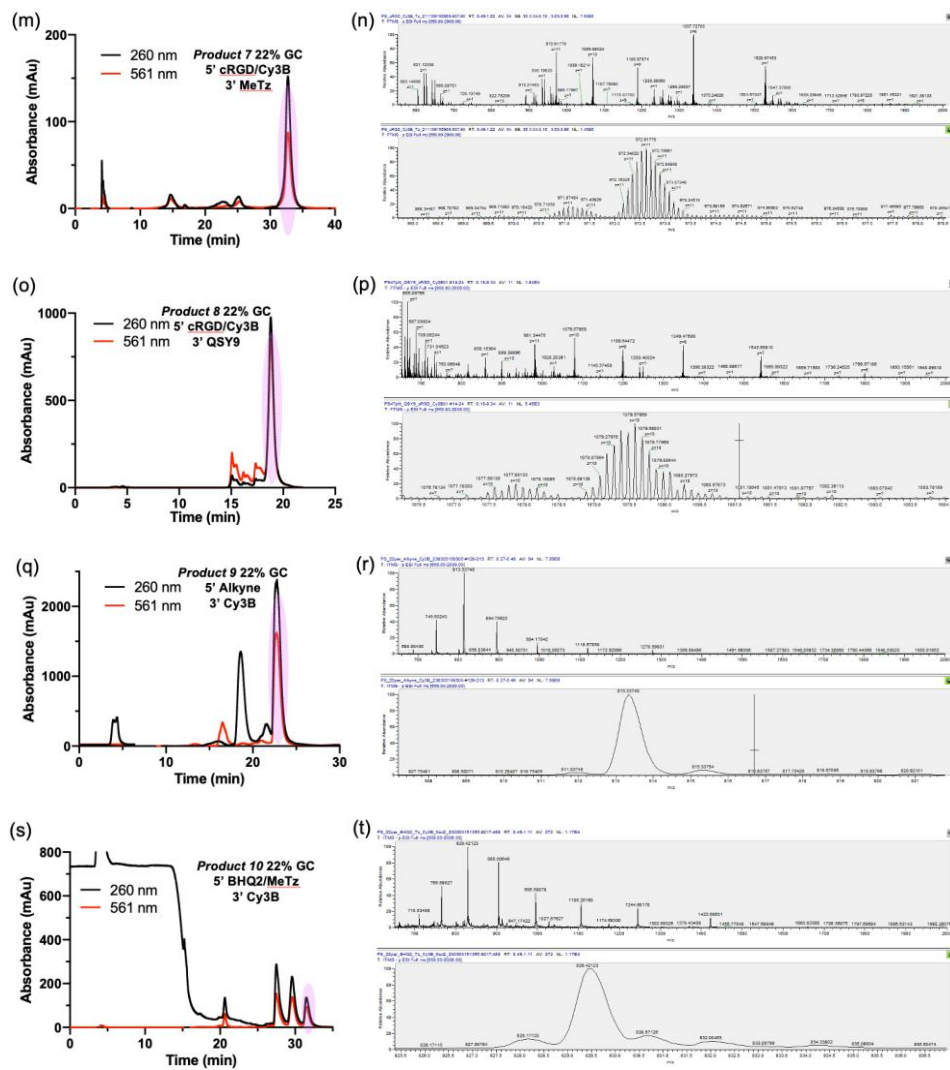


Supplementary figure 3. Chemical structures of **(top)** cRGD/Cy3B-N₃ and **(bottom)** BHQ2/MeTz-N₃ conjugates.

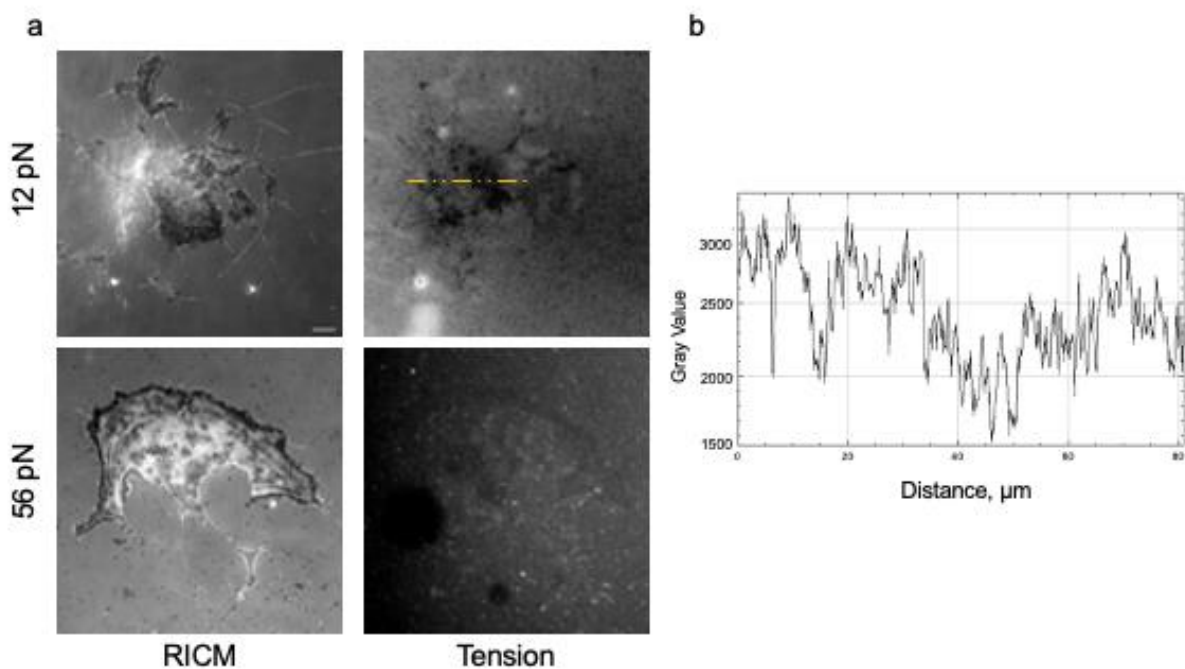


Supplementary scheme 1. Synthetic scheme of PS-modified DNA HP probes

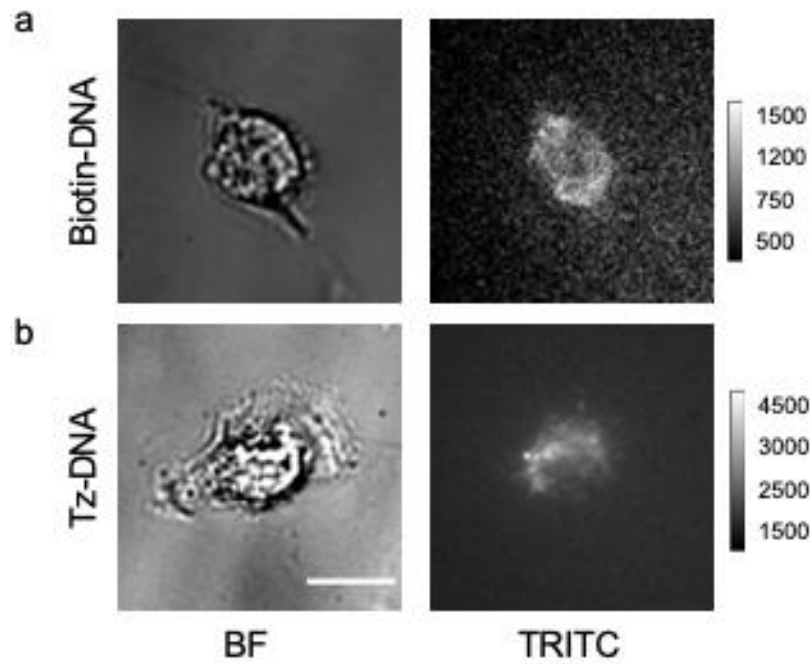




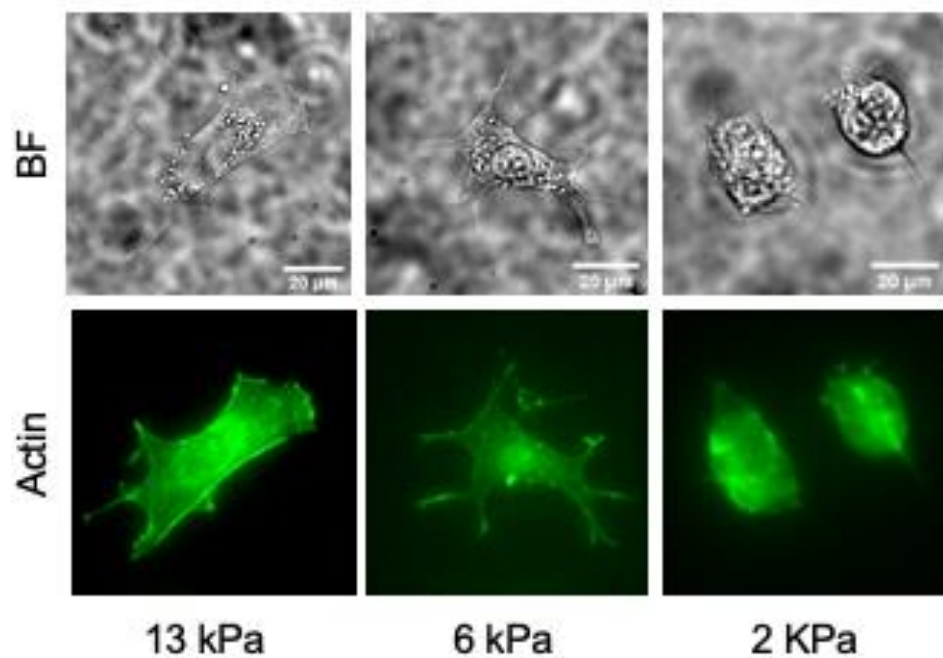
Supplementary figure 4. HPLC chromatogram and ESI-MS characterization of synthesized product.



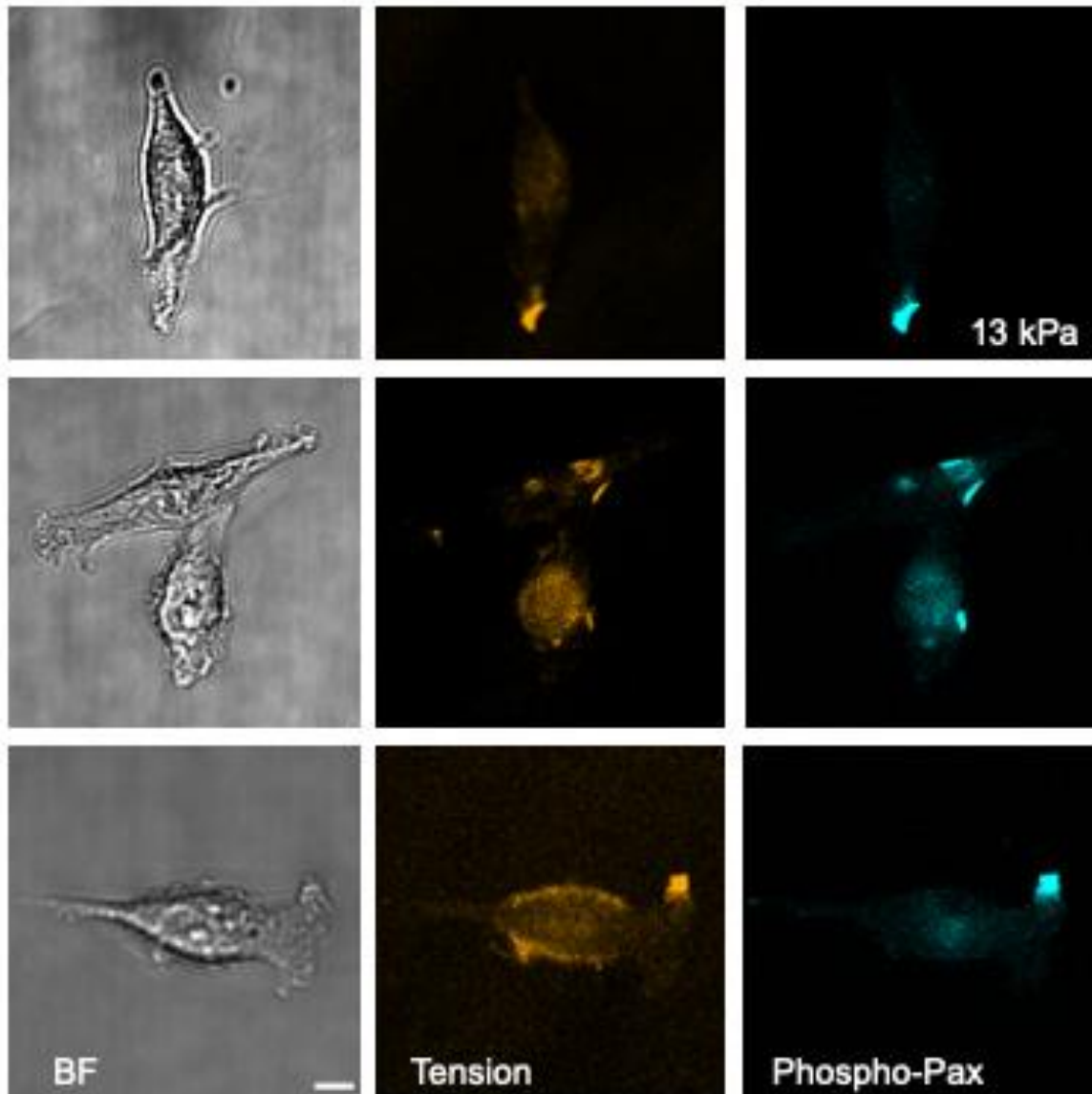
Supplementary figure 5. Conventional DNA duplex probes (TGT) showed HeLa cell-induced probe degradation on the glass surface. a. Representative RICM and fluorescent tension images of HeLa cells cultured on glass surface coated with TGT. Images were taken 3 hrs after cell seeding on biotin-tethered 12 and 56 pN TGT probes. **b.** Line scan of fluorescent tension image. Loss of fluorescent signal intensity indicates HeLa cells degrade the TGT probes due to nuclease and protease activities. Scale bar- 10 μm .



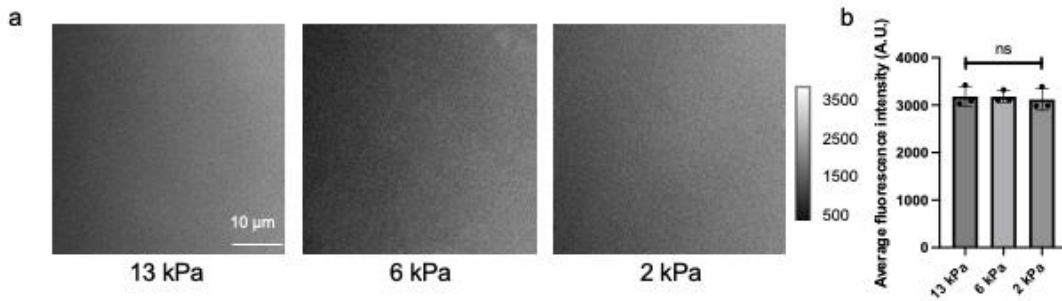
Supplementary figure 6. HeLa cells internalized the fluorescent tension probes when cells are cultured on the conventional DNA HP probe-tethered hydrogel surface. a, b. Representative BF and TRITC images of HeLa cells cultured on conventional DNA probes tethered with Biotin-streptavidin interaction or anchored covalently using TCO-Tz coupling. Scale bar- 10 μ m.



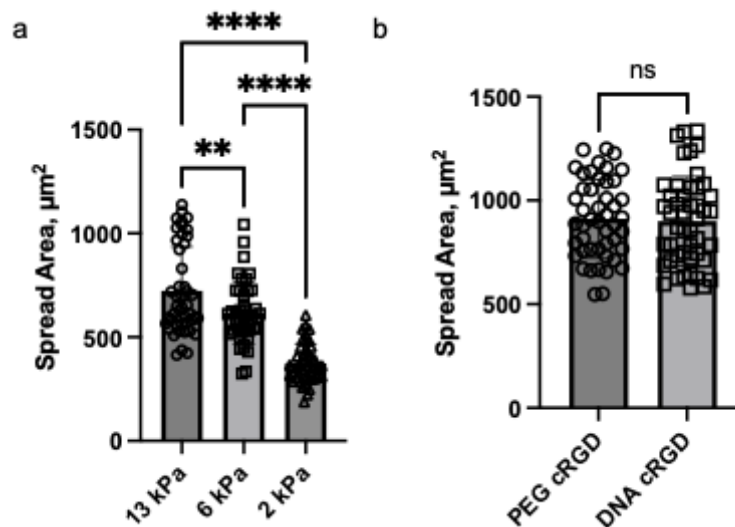
Supplementary figure 7. F-actin expression of HeLa cells. a. Representative BF and Actin images of HeLa cells cultured on 13, 6 and, 2 kPa hydrogels with PS DNA HP probe (22% GC content). F-actin was stained with Phalloidin-Alexa Fluor 488. Scale bar- 20 μm



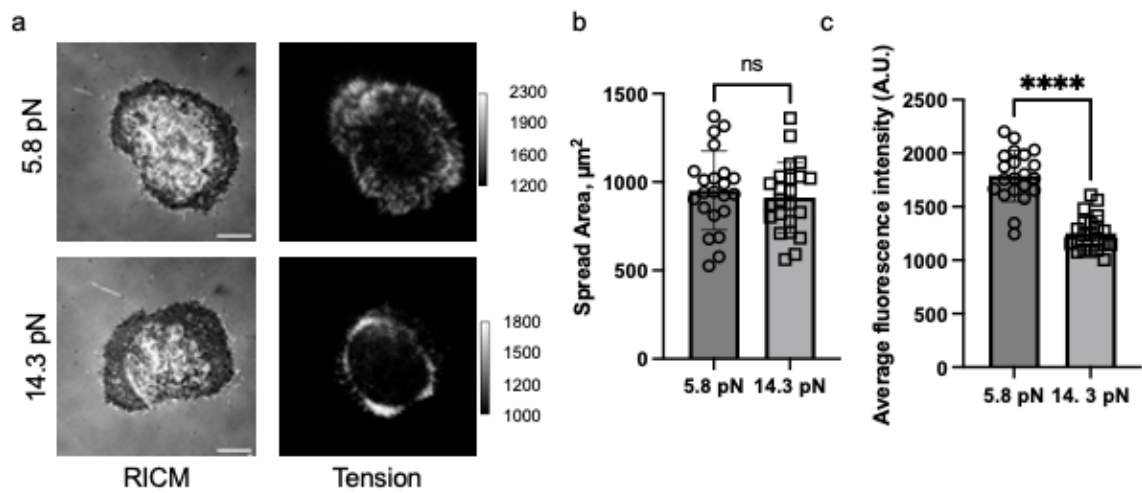
Supplementary figure 8. P-Tyr118 paxillin and fluorescent tension signal (PS DNA HP probe, 22% GC content) showed good colocalization. Three representative images of Immunostained HeLa cells cultured on 13 kPa hydrogels coated with PS DNA HP probes show tension signal is colocalized with phospho-paxillin signals, suggesting the focal adhesion formation under tension signal. Scale Bar- 10 μ m.



Supplementary figure 9. DNA density confirmation on 13, 6, and 2 kPa hydrogels. a. Representative TRITC images of 13, 6, and 2 kPa hydrogels. b. Bar graph showing average fluorescent intensity of PS DNA HP probe tethered hydrogels. The data with identical background intensity indicates similar DNA density for all hydrogels used in this study. ns indicate not significant with $p > 0.5$, as determined from one-way ANOVA. Error bars show the standard deviation for $N=3$.



Supplementary figure 10. Spread area of HeLa cells cultured on different types of hydrogel surfaces. a. Bar graph plotting spread area of HeLa cells on 13, 6, and 2 kPa hydrogels coated with PS DNA HP probe (22% GC content). b. Bar graph showing HeLa cells show comparable spreading area when cultured on the hydrogel coated with PS DNA HP probe or coated with cRGD and cRGD-lacked PS DNA HP. ****, ***, **, * and ns indicate $p < 0.0001$, $p < 0.001$, $p < 0.01$, $p < 0.05$, and not significant, respectively, as determined from one-way ANOVA. Error bars show the standard deviation for $N=3$.



Supplementary figure 11. HeLa cells cultured on PS DNA HP probes (22% and 100% GC content) tethered to glass substrate showed fluorescent tension signal. a. Representative RICM and fluorescent tension signals of heLa cells cultured on 22% and 100% GC content probes. **b, c.** Bar graphs plotting spread area and average tension signals of HeLa cells on two different HP probes show cells have similar spread area, but HeLa cells have greater tension on 5.8 pN probes.****, and ns indicate $p < 0.0001$, and not significant respectively, as determined from one-way ANOVA. Scale Bar- 10 μm

References

1. Mohammed, D.; Versaevel, M.; Bruyère, C.; Alaimo, L.; Luciano, M.; Vercruysse, E.; Procès, A.; Gabriele, S., Innovative Tools for Mechanobiology: Unraveling Outside-In and Inside-Out Mechanotransduction. *Front Bioeng Biotechnol* **2019**, *7*, 162.
2. Martino, F.; Perestrelo, A. R.; Vinarský, V.; Pagliari, S.; Forte, G., Cellular Mechanotransduction: From Tension to Function. *Front Physiol* **2018**, *9*, 824.
3. Jaalouk, D. E.; Lammerding, J., Mechanotransduction gone awry. *Nat Rev Mol Cell Biol* **2009**, *10* (1), 63-73.
4. Chin, L.; Xia, Y.; Discher, D. E.; Janmey, P. A., Mechanotransduction in cancer. *Curr Opin Chem Eng* **2016**, *11*, 77-84.
5. Jansen, K. A.; Atherton, P.; Ballestrem, C., Mechanotransduction at the cell-matrix interface. *Semin Cell Dev Biol* **2017**, *71*, 75-83.
6. Dombroski, J. A.; Hope, J. M.; Sarna, N. S.; King, M. R., Channeling the Force: Piezo1 Mechanotransduction in Cancer Metastasis. *Cells* **2021**, *10* (11).
7. Jiang, Y.; Zhang, H.; Wang, J.; Liu, Y.; Luo, T.; Hua, H., Targeting extracellular matrix stiffness and mechanotransducers to improve cancer therapy. *J Hematol Oncol* **2022**, *15* (1), 34.
8. Riehl, B. D.; Kim, E.; Bouzid, T.; Lim, J. Y., The Role of Microenvironmental Cues and Mechanical Loading Milieus in Breast Cancer Cell Progression and Metastasis. *Front Bioeng Biotechnol* **2020**, *8*, 608526.

9. Ge, H.; Tian, M.; Pei, Q.; Tan, F.; Pei, H., Extracellular Matrix Stiffness: New Areas Affecting Cell Metabolism. *Front Oncol* **2021**, *11*, 631991.
10. Chaudhuri, O.; Cooper-White, J.; Janmey, P. A.; Mooney, D. J.; Shenoy, V. B., Effects of extracellular matrix viscoelasticity on cellular behaviour. *Nature* **2020**, *584* (7822), 535-546.
11. Wang, M.; Yang, Y.; Han, L.; Han, S.; Liu, N.; Xu, F.; Li, F., Effect of three-dimensional ECM stiffness on cancer cell migration through regulating cell volume homeostasis. *Biochem Biophys Res Commun* **2020**, *528* (3), 459-465.
12. Frangogiannis, N. G., The extracellular matrix in myocardial injury, repair, and remodeling. *J Clin Invest* **2017**, *127* (5), 1600-1612.
13. Smith, L. R.; Cho, S.; Discher, D. E., Stem Cell Differentiation is Regulated by Extracellular Matrix Mechanics. *Physiology (Bethesda)* **2018**, *33* (1), 16-25.
14. Yi, B.; Xu, Q.; Liu, W., An overview of substrate stiffness guided cellular response and its applications in tissue regeneration. *Bioact Mater* **2022**, *15*, 82-102.
15. Guo, J.; Shu, X.; Deng, H.; Zhang, J.; Wang, Y.; Meng, G.; He, J.; Wu, F., Stiff and Tough Hydrogels Prepared Through Integration of Ionic Cross-linking and Enzymatic Mineralization. *Acta Biomater* **2022**, *149*, 220-232.
16. Luo, T.; Tan, B.; Zhu, L.; Wang, Y.; Liao, J., A Review on the Design of Hydrogels With Different Stiffness and Their Effects on Tissue Repair. *Front Bioeng Biotechnol* **2022**, *10*, 817391.
17. Ting, M. S.; Travas-Sejdic, J.; Malmstrom, J., Modulation of hydrogel stiffness by external stimuli: soft materials for mechanotransduction studies. *J Mater Chem B* **2021**, *9* (37), 7578-7596.

18. Boothe, S. D.; Myers, J. D.; Pok, S.; Sun, J.; Xi, Y.; Nieto, R. M.; Cheng, J.; Jacot, J. G., The Effect of Substrate Stiffness on Cardiomyocyte Action Potentials. *Cell Biochem Biophys* **2016**, *74* (4), 527-535.
19. Corbin, E. A.; Vite, A.; Peyster, E. G.; Bhoopalam, M.; Brandimarto, J.; Wang, X.; Bennett, A. I.; Clark, A. T.; Cheng, X.; Turner, K. T.; Musunuru, K.; Margulies, K. B., Tunable and Reversible Substrate Stiffness Reveals a Dynamic Mechanosensitivity of Cardiomyocytes. *ACS Appl Mater Interfaces* **2019**, *11* (23), 20603-20614.
20. Zhang, C.; Tan, Y.; Feng, J.; Huang, C.; Liu, B.; Fan, Z.; Xu, B.; Lu, T., Exploration of the Effects of Substrate Stiffness on Biological Responses of Neural Cells and Their Mechanisms. *ACS Omega* **2020**, *5* (48), 31115-31125.
21. Liu, B.; Kilpatrick, J. I.; Lukasz, B.; Jarvis, S. P.; McDonnell, F.; Wallace, D. M.; Clark, A. F.; O'Brien, C. J., Increased Substrate Stiffness Elicits a Myofibroblastic Phenotype in Human Lamina Cribrosa Cells. *Invest Ophthalmol Vis Sci* **2018**, *59* (2), 803-814.
22. Califano, J. P.; Reinhart-King, C. A., Substrate Stiffness and Cell Area Predict Cellular Traction Stresses in Single Cells and Cells in Contact. *Cell Mol Bioeng* **2010**, *3* (1), 68-75.
23. Hur, S. S.; Jeong, J. H.; Ban, M. J.; Park, J. H.; Yoon, J. K.; Hwang, Y., Traction force microscopy for understanding cellular mechanotransduction. *BMB Rep* **2020**, *53* (2), 74-81.
24. Lekka, M.; Gnanachandran, K.; Kubiak, A.; Zielinski, T.; Zemla, J., Traction force microscopy - Measuring the forces exerted by cells. *Micron* **2021**, *150*, 103138.

25. Plotnikov, S. V.; Sabass, B.; Schwarz, U. S.; Waterman, C. M., High-resolution traction force microscopy. *Methods Cell Biol* **2014**, *123*, 367-94.
26. Beussman, K. M.; Rodriguez, M. L.; Leonard, A.; Taparia, N.; Thompson, C. R.; Sniadecki, N. J., Micropost arrays for measuring stem cell-derived cardiomyocyte contractility. *Methods* **2016**, *94*, 43-50.
27. Shi, Y.; Sivarajan, S.; Crocker, J. C.; Reich, D. H., Measuring Cytoskeletal Mechanical Fluctuations and Rheology with Active Micropost Arrays. *Curr Protoc* **2022**, *2* (5), e433.
28. Liu, Y.; Galior, K.; Ma, V. P.; Salaita, K., Molecular Tension Probes for Imaging Forces at the Cell Surface. *Acc Chem Res* **2017**, *50* (12), 2915-2924.
29. Ma, V. P.; Salaita, K., DNA Nanotechnology as an Emerging Tool to Study Mechanotransduction in Living Systems. *Small* **2019**, *15* (26), e1900961.
30. Stabley, D. R.; Jurchenko, C.; Marshall, S. S.; Salaita, K. S., Visualizing mechanical tension across membrane receptors with a fluorescent sensor. *Nat Methods* **2012**, *9* (1), 64-67.
31. Liu, Y.; Yehl, K.; Narui, Y.; Salaita, K., Tension Sensing Nanoparticles for Mechano-Imaging at the Living/Nonliving Interface. *J Am Chem Soc* **2013**, *135* (14), 5320-5323.
32. Zhang, Y.; Ge, C.; Zhu, C.; Salaita, K., DNA-based digital tension probes reveal integrin forces during early cell adhesion. *Nat Commun* **2014**, *5*, 5167.
33. Morimatsu, M.; Mekhdjian, A. H.; Adhikari, A. S.; Dunn, A. R., Molecular Tension Sensors Report Forces Generated by Single Integrin Molecules in Living Cells. *Nano Lett* **2013**, *13* (9), 3985-3989.

34. Chang, A. C.; Mekhdjian, A. H.; Morimatsu, M.; Denisin, A. K.; Pruitt, B. L.; Dunn, A. R., Single Molecule Force Measurements in Living Cells Reveal a Minimally Tensioned Integrin State. *ACS Nano* **2016**, *10* (12), 10745-10752.
35. Galior, K.; Liu, Y.; Yehl, K.; Vivek, S.; Salaita, K., Titin-Based Nanoparticle Tension Sensors Map High-Magnitude Integrin Forces within Focal Adhesions. *Nano Lett* **2016**, *16* (1), 341-8.
36. Liu, Y.; Blanchfield, L.; Ma, V. P.; Andargachew, R.; Galior, K.; Liu, Z.; Evavold, B.; Salaita, K., DNA-based nanoparticle tension sensors reveal that T-cell receptors transmit defined pN forces to their antigens for enhanced fidelity. *Proc Natl Acad Sci U S A* **2016**, *113* (20), 5610-5.
37. Zhao, B.; O'Brien, C.; Mudiyansele, A.; Li, N.; Bagheri, Y.; Wu, R.; Sun, Y.; You, M., Visualizing Intercellular Tensile Forces by DNA-Based Membrane Molecular Probes. *J Am Chem Soc* **2017**, *139* (50), 18182-18185.
38. Humphrey, J. D.; Dufresne, E. R.; Schwartz, M. A., Mechanotransduction and extracellular matrix homeostasis. *Nat Rev Mol Cell Biol* **2014**, *15* (12), 802-12.
39. Wang, X.; Rahil, Z.; Li, I. T.; Chowdhury, F.; Leckband, D. E.; Chemla, Y. R.; Ha, T., Constructing modular and universal single molecule tension sensor using protein G to study mechano-sensitive receptors. *Sci Rep* **2016**, *6*, 21584.
40. Chowdhury, F.; Li, I. T. S.; Leslie, B. J.; Doganay, S.; Singh, R.; Wang, X.; Seong, J.; Lee, S. H.; Park, S.; Wang, N.; Ha, T., Single molecular force across single integrins dictates cell spreading. *Integr Biol* **2015**, *7* (10), 1265-1271.

41. Jo, M. H.; Li, J.; Jaumouille, V.; Hao, Y.; Coppola, J.; Yan, J.; Waterman, C. M.; Springer, T. A.; Ha, T., Single-molecule characterization of subtype-specific beta1 integrin mechanics. *Nat Commun* **2022**, *13* (1), 7471.
42. Wang, X.; Ha, T., Defining Single Molecular Forces Required to Activate Integrin and Notch Signaling. *Science* **2013**, *340* (6135), 991-994.
43. Jurchenko, C.; Chang, Y.; Narui, Y.; Zhang, Y.; Salaita, K. S., Integrin-generated forces lead to streptavidin-biotin unbinding in cellular adhesions. *Biophys J* **2014**, *106* (7), 1436-46.
44. Rashid, S. A.; Blanchard, A. T.; Combs, J. D.; Fernandez, N.; Dong, Y.; Cho, H. C.; Salaita, K., DNA Tension Probes Show that Cardiomyocyte Maturation Is Sensitive to the Piconewton Traction Forces Transmitted by Integrins. *ACS Nano* **2022**, *16* (4), 5335-5348.
45. Bjugstad, K. B.; Lampe, K.; Kern, D. S.; Mahoney, M., Biocompatibility of poly(ethylene glycol)-based hydrogels in the brain: An analysis of the glial response across space and time. *Journal of Biomedical Materials Research Part A* **2010**, *95A* (1), 79-91.
46. Zhu, J., Bioactive modification of poly(ethylene glycol) hydrogels for tissue engineering. *Biomaterials* **2010**, *31* (17), 4639-56.
47. Gao, R.; Yu, C. J.; Gao, L.; Piatkevich, K. D.; Neve, R. L.; Munro, J. B.; Upadhyayula, S.; Boyden, E. S., A highly homogeneous polymer composed of tetrahedron-like monomers for high-isotropy expansion microscopy. *Nat Nanotechnol* **2021**, *16* (6), 698-707.

48. Singh, G.; Chanda, A., Mechanical properties of whole-body soft human tissues: a review. *Biomedical Materials* **2021**, *16* (6), 062004.
49. Kibler-Herzog, L.; Zon, G.; Uznanski, B.; Whittier, G.; Wilson, W. D., Duplex stabilities of phosphorothioate, methylphosphonate, and RNA analogs of two DNA 14-mers. *Nucleic Acids Res* **1991**, *19* (11), 2979-86.
50. Du, Q.; Smith, C.; Shiffeldrim, N.; Vologodskaia, M.; Vologodskii, A., Cyclization of short DNA fragments and bending fluctuations of the double helix. *Proc Natl Acad Sci U S A* **2005**, *102* (15), 5397-402.
51. Brockman, J. M.; Su, H.; Blanchard, A. T.; Duan, Y.; Meyer, T.; Quach, M. E.; Glazier, R.; Bazrafshan, A.; Bender, R. L.; Kellner, A. V.; Ogasawara, H.; Ma, R.; Schueder, F.; Petrich, B. G.; Jungmann, R.; Li, R.; Mattheyses, A. L.; Ke, Y.; Salaita, K., Live-cell super-resolved PAINT imaging of piconewton cellular traction forces. *Nat Methods* **2020**, *17* (10), 1018-1024.
52. Woodside, M. T.; Behnke-Parks, W. M.; Larizadeh, K.; Travers, K.; Herschlag, D.; Block, S. M., Nanomechanical measurements of the sequence-dependent folding landscapes of single nucleic acid hairpins. *Proc Natl Acad Sci U S A* **2006**, *103* (16), 6190-5.
53. Rahil, Z.; Pedron, S.; Wang, X.; Ha, T.; Harley, B.; Leckband, D., Nanoscale mechanics guides cellular decision making. *Integr Biol (Camb)* **2016**, *8* (9), 929-35.
54. Sarkar, A.; LeVine, D.; Zhao, Y.; Mollaeian, K.; Ren, J.; Wang, X., Tandem tension sensor reveals substrate rigidity-dependence of integrin molecular tensions in live cells. *bioRxiv* **2020**, 2020.01.24.918946.

55. Deng, L.; Kitova, E. N.; Klassen, J. S., Dissociation Kinetics of the Streptavidin–Biotin Interaction Measured Using Direct Electrospray Ionization Mass Spectrometry Analysis. *J Am Soc Mass Spectrom* **2013**, *24* (1), 49-56.
56. Glazier, R.; Shinde, P.; Ogasawara, H.; Salaita, K., Spectroscopic Analysis of a Library of DNA Tension Probes for Mapping Cellular Forces at Fluid Interfaces. *ACS Appl Mater Interfaces* **2021**, *13* (2), 2145-2164.
57. Doss, B. L.; Pan, M.; Gupta, M.; Greci, G.; Mege, R. M.; Lim, C. T.; Sheetz, M. P.; Voituriez, R.; Ladoux, B., Cell response to substrate rigidity is regulated by active and passive cytoskeletal stress. *Proc Natl Acad Sci U S A* **2020**, *117* (23), 12817-12825.
58. Ghabache, E.; Cao, Y.; Miao, Y.; Groisman, A.; Devreotes, P. N.; Rappel, W. J., Coupling traction force patterns and actomyosin wave dynamics reveals mechanics of cell motion. *Mol Syst Biol* **2021**, *17* (12), e10505.
59. Ellefsen, K. L.; Holt, J. R.; Chang, A. C.; Nourse, J. L.; Arulmoli, J.; Mekhdjian, A. H.; Abuwarda, H.; Tombola, F.; Flanagan, L. A.; Dunn, A. R.; Parker, I.; Pathak, M. M., Myosin-II mediated traction forces evoke localized Piezo1-dependent Ca(2+) flickers. *Commun Biol* **2019**, *2*, 298.
60. López-Otín, C.; Bond, J. S., Proteases: multifunctional enzymes in life and disease. *J Biol Chem* **2008**, *283* (45), 30433-30437.
61. Lee, M.; Fridman, R.; Mobashery, S., Extracellular proteases as targets for treatment of cancer metastases. *Chem Soc Rev* **2004**, *33* (7), 401-409.

Chapter 5: Summary, Perspective and Outlook.

5.1 Summary

Traction force microscopy is limited in its ability to display the localized effect of receptor forces on cell mechanics due to a lack of spatial and force resolution. To overcome the limitations of TFM, molecular force sensors have been utilized to depict the impact of molecular force influences on cellular behavior. However, these techniques often require specialized equipment and trained data collection and analysis personnel. In response to these challenges, we have developed a high-throughput assay that mechanically tags and sorts cells based on their mechanical phenotype. Additionally, current techniques incorporating molecular force sensors often rely on rigid substrates, which are not representative of the physiological microenvironment. In this study, we have utilized various DNA-based force measurement techniques, incorporating soft substrates, to investigate the role of receptor forces in different biological systems.

Chapter 2 described how pN forces transmitted by ligand- ECM interaction can affect cardiac muscle cells' functional maturation. Cardiac muscle cells (CMCs) are crucial in heart function as the primary unit cells that make up the heart. During their development, CMC undergoes differentiation and maturation processes, which are influenced by mechanical cues sensed through receptors such as integrins. Cell traction forces, for instance, are vital for the differentiation and maturation of functional CMCs, as the substrate stiffness on which they are cultured affects their function. Previous studies have mainly focused on the impact of bulk ECM stiffness on CMC function. Still, a crucial question remains regarding the specific integrin piconewton (pN) forces that trigger CMC functional maturation. To answer this question, we used DNA adhesion tethers that break

at specific force levels (~12, ~56, and ~160 pN) to test if limiting integrin tension to specific magnitudes affects CMC function. Our results show that tethers with greater force tolerance resulted in functionally mature CMCs, as indicated by morphological changes, twitching frequency, transient calcium flux measurements, and protein expression (F-actin, vinculin, α -actinin, YAP, and SERCA2). Additionally, the mechanical tolerance of integrin tethers was seen to enhance sarcomeric actinin alignment and multinucleation significantly. In conclusion, our study highlights that CMCs use defined pN integrin forces to drive early-stage differentiation and maturation. This research represents an essential step towards biophysically characterizing the role of pN forces in early-stage cardiac differentiation.

Next, in **Chapter 3**, we developed and incorporated a mechanical phenotyping assay with the collaboration of Dr. Rong Ma. Flow cytometry is a widely utilized tool in cellular biology to analyze single-cell gene expression. This is typically achieved through staining cells with fluorescent probes such as antibodies and nucleic acids. However, here we introduce a novel approach called Tension-activated Cell Tagging (TaCT), which fluorescently labels cells based on the magnitude of mechanical force transmitted through cell adhesion receptors. This innovative method significantly advances our understanding of cellular function and biophysics. As a demonstration of its utility, we applied TaCT to analyze fibroblasts and mouse platelets and analyzed the results using conventional flow cytometry techniques. Our results prove that TaCT can effectively and accurately label cells based on the amount of force transmitted through cell receptors. We also show that TaCT can identify and differentiate between various muscle cell types from a complex primary cardiac cell mixture. This new approach opens exciting possibilities for further

exploring the relationship between cell adhesion, force transmission, and gene expression.

Furthermore, we expanded the technique by developing a hydrogel-based DNA tension matrix in **Chapter 4**. Various techniques have been used to measure and manipulate cell-receptor forces, including traction force microscopy, optical tweezers, atomic force microscopy, and micro post arrays to understand the impact of single receptor-mediated forces on cell biology. However, these techniques either lack the necessary pN force resolution or are not suitable for studying the regulation of cell biology by single receptor force. Our lab has developed Molecular traction force microscopy (MTFM) to overcome this limitation, but this method still faces challenges in mimicking the natural extracellular environment.

We have employed a new approach using hydrogel-based DNA tension surfaces to address this issue. This study involved the integration of a single molecular mechanofluorescence probe into a PEG-based hydrogel matrix, allowing us to both measure and manipulate mechanical forces and storage modulus. The results show how single receptor forces behave on soft hydrogel surfaces. We have also investigated the effects of substrate stiffness on focal adhesion by altering the crosslinking peg density. This study provides a valuable contribution to understanding the role of single receptor-mediated forces in cellular biology.

5.2 Perspective

The advancement of new DNA probes and matrices has introduced innovative opportunities to study the mechanics of cells and measure molecular forces in physiologically relevant environments using high-throughput assays. These methods exhibit robustness, speed, and sensitivity yet still have room for improvement. The ultimate tension detection method should be versatile and applicable to any protein or cell type, delivering results with heightened sensitivity to detect single-cell mechanics in a matter of minutes. It should also be automated and specific to the target protein to eliminate human error and maximize efficiency. However, using a rigid matrix impedes the proper replication of biological substrates. Despite these obstacles, the continued progress in science and technology has created exciting prospects for molecular mechano-sensing.

5.3 Other contributions

5.3.1 Carfilzomib Treatment Causes Molecular and Functional Alterations of Human-Induced Pluripotent Stem Cell-Derived Cardiomyocytes

This project discusses the cardiotoxicity of proteasome inhibitors, particularly carfilzomib, in treating cancer. Proteasome inhibitors inhibit the proteasome, which degrades and recovers proteins within cells. This mechanism is often exploited in cancer therapy because cancer cells have a high turnover of proteins and are more sensitive to proteasome inhibition than normal cells. However, proteasome inhibitors are associated with an increased risk of cardiac adverse events, such as arrhythmias and heart failure.

To better understand the molecular mechanisms underlying carfilzomib-induced cardiotoxicity, we used human-induced pluripotent stem cell-derived cardiomyocytes (hiPSC-CMs) as a model system. These cells are generated by reprogramming adult cells, such as skin cells, back into a pluripotent state and then differentiating them into cardiomyocytes. hiPSC-CMs are a sound model for studying drug-induced cardiotoxicity because they can be derived from human cells and exhibit similar characteristics to native cardiomyocytes.

We found that carfilzomib induced dose-dependent cytotoxicity in hiPSC-CMs and targeted mitochondria at physiologically relevant doses, disrupting cellular energy and contractility. We also examined cellular function at the single-cell level through traction force measurements using a nucleic acid-based tension sensor and Ca²⁺ transient imaging. Our findings on reduction in traction forces, abnormal Ca²⁺ transients, mitochondrial dysfunction, and contractility impairment, combined with comprehensive

transcriptome and proteome analyses, illustrate the possible molecular mechanisms in cardiomyocyte functional alteration after carfilzomib treatment.

Overall, the study highlights the importance of understanding the molecular mechanisms underlying drug-induced cardiotoxicity and the potential of hiPSC-CMs as a model system for studying this phenomenon. In addition, the findings could contribute to developing biomarkers associated with cardiomyocyte dysfunction and arrhythmias following carfilzomib therapy and ultimately lead to the development of safer and more effective cancer treatments.

5.3.2 An outside-in switch in integrin signaling caused by chemical and mechanical signals in reactive astrocytes.

After brain injury, the ability of astrocytes to repair the damaged tissue after brain injury is hindered due to their reactive state, characterized by the upregulation of surface proteins and the release of pro-inflammatory molecules and extracellular matrix proteins. The integrin protein, particularly $\alpha_v\beta_3$ Integrin, is crucial in triggering this reactive phenotype and increasing astrocyte contractility and motility. However, it is still unclear how $\alpha_v\beta_3$ Integrin mechanoreceptor response in astrocytes affects their reactive phenotype. Astrocytes were exposed to chemical and mechanical stress to study this response by stimulating them with Thy-1-Protein A-coated magnetic beads and applying a magnetic field to generate mechanical tension. The results showed that mechanical stress accelerated the response of astrocytes to Thy-1 engagement of integrin receptors, resulting in cell adhesion and contraction. This contraction exerted traction forces onto the ECM, inducing faster cell contractility and higher traction forces than Thy-1 alone.

Therefore, cell-extrinsic chemical and mechanical signals regulate astrocyte reactivity by inducing integrin upregulation, ligation, and signaling events that promote cell contraction. Furthermore, these changes generate cell-intrinsic signals that increase traction forces exerted onto the ECM. In conclusion, the study suggests that $\alpha_v\beta_3$ Integrin mechanoreceptor can be targeted to regulate the harmful effects of reactive astrocytes in neuronal healing.

5.3.3 Diffraction-limited mapping of integrin force vector fields with VALiD-MFM

In recent years, a new imaging technique called molecular tension fluorescence microscopy (MTFM) has emerged, allowing researchers to map the small receptor forces exerted by live cells with high precision. However, MTFM needs to provide more information on the orientation of these forces. To overcome this limitation, we have developed a new method using a polarized, variable incidence angle fluorescence excitation laser.

With this new technique, the team could create vector maps of receptor forces with the highest resolution. In addition, by studying platelet integrin forces, we discovered that the forces are more lateral and locally heterogeneous than previously thought. These findings provide a potential explanation for discrepancies in previous literature on this topic.

The results of this study are particularly significant as understanding the orientation of receptor forces is crucial for gaining insights into how cells interact with their environment. This new technique could revolutionize the field of cellular biomechanics and provide a deeper understanding of how cells respond to mechanical stimuli. Furthermore, this

technique could be applied further to study other cell types and shed light on the mechanics of various biological processes.

5.3.4 DNA mechanocapsules for programmable piconewton(pN) responsive drug delivery

Traditional biochemical markers cannot depict and measure the mechanical forces exerted by cells. The abnormal mechanical behavior of cells is linked to various disease states, making it crucial to develop drug delivery strategies based on cellular mechanical phenotypes. We created and characterized DNA tetrahedrons responsive to mechanical force to address this issue. We also utilized computational modeling to predict how force-induced rupture would occur and how the applied force's spatial position and orientation can fine-tune the threshold for force response. These DNA mechanocapsules (DMCs) were functionalized with adhesion ligands and demonstrated mechanical denaturation in vitro when exposed to cell receptor forces. The DMCs were engineered to encapsulate macromolecular cargos, such as dextran and oligonucleotide drugs, with minimal cargo leakage and high resistance to nuclease degradation. We observed that DMCs released their cargo in response to force, followed by cellular uptake, which was validated by flow cytometry analysis. Finally, we demonstrated that DMCs could selectively knock down HIF1 α mRNA and reduce the viability of cancer cells in a traction force-dependent manner. These findings suggest that DMCs can effectively target biophysical phenotypes, with potential applications in fields such as immunology, regenerative medicine, and cancer biology.

5.3.5 Mechanically triggered hybridization chain reaction

Cells utilize mechanical forces in essential processes such as immune recognition and cell migration. However, measuring these forces is challenging due to their sparsity. High-resolution fluorescence microscopy is commonly used to quantify molecular tension, but it has limited widespread adoption and application. To address this issue, we have developed a new approach called the mechanically triggered hybridization chain reaction (mechanic-HCR). This technique enables chemical amplification of mechanical events started by the mechanical denaturation of a duplex that exposes a cryptic initiator, leading to in situ activation of the HCR reaction. Importantly, mechano-HCR allows direct measurement of piconewton forces using a plate reader. We used this method to measure mechano-IC₅₀ values for aspirin, Y-27632, and eptifibatide. This capability could be helpful in drug discovery, personalized medicine, and disease diagnosis, particularly in the context of the clinical importance of cell mechanical phenotypes.

5.3.6 Supramolecular DNA photonic hydrogels for on-demand control of coloration with a high spatial and temporal resolution.

Hydrogels that contain regular arrangements of nanoparticles exhibit a striking photonic crystal coloration, which could be helpful for various applications, including camouflage, anticounterfeiting, and chemical sensing. However, dynamically generating color patterns requires precise nanoparticle organization control within a polymer network, which poses a significant challenge. To overcome this challenge, we have developed a DNA hydrogel system demonstrating a substantial reduction in modulus (by approximately 50,000-fold)

upon heating by around 10°C. The magnetic nanoparticles entrapped within these DNA gels generate a structural color only when the gel is heated, and a magnetic field is applied. Using photopatterning with near-infrared illumination, we achieved a spatially controlled photonic crystal coloration. The color can be "erased" by illuminating or heating the gel without an external magnetic field. This technology allows for on-demand assembly and may help develop new innovative materials for applications such as erasable lithography, encryption, and sensing.

5.4 Future Outlook

5.4.1 Influence of substrate stiffness on electrochemical properties of CMCs

Mitochondria are crucial in maintaining cardiac health by providing energy for the heart's contractions and regulating critical cellular pathways. These tiny organelles generate ATP through oxidative phosphorylation, which can be disrupted during a heart attack, leading to an overproduction of harmful reactive oxygen species and bioenergetic insufficiency. Promoting mitochondrial biogenesis and quality control mechanisms that remove damaged mitochondria is essential to maintain proper mitochondrial function. Quality control components are activated when the mitochondrial network is compromised to identify and remove unhealthy mitochondria and their proteins. However, if mitochondrial quality control fails, it can accumulate abnormal mitochondria and contribute to the development of various cardiovascular diseases and heart failure. Future studies on how receptor forces can influence mitochondrial activity in cardiac cells could be helpful.

5.4.2 Effect of receptor forces on cardiomyocyte maturation in 3D gel environment

How biochemical and mechanical signaling interact is essential for various cellular processes, including wound healing, embryogenesis, metastasis, and cell migration. While traditional methods of measuring traction forces have provided helpful information about cell interactions with the extracellular matrix in two dimensions, recent studies have shown significant differences in cell behavior and morphology in three-dimensional environments. Two new techniques based on laser scanning confocal microscopy have emerged to address this need for accurate three-dimensional measurements of cell traction forces. In the future, incorporating MTFM in 3D gels can help scientists highlight

the implementation and advantages of a newly developed three-dimensional molecular traction force microscopy (3D MTFM) methodology, which allows for the dynamic computation of cellular traction forces during cell migration and locomotion. The 3D MTFM technique can provide a new quantitative vantage point for exploring cell-ECM interactions in three dimensions.

5.4.3 Understanding the effect of receptor forces in stem cell differentiation.

Stem cells can transmit mechanical forces to their microenvironment, regulating cell fate and behavior to guide developmental processes. Mechanical forces play a crucial role in patterning and organogenesis during embryonic development. In pluripotent stem cells, their physical environment regulates their differentiation and self-renewal. Additionally, mechanical and physical cues are essential in matured tissues, where differentiated stem cells require physical interactions with the extracellular matrix to maintain their potency.

In vitro, synthetic models of stem cell mechanotransduction can be used to manipulate and precisely control the biophysical and biochemical properties of the stem cell microenvironment. Researchers have examined mechanical cues, such as matrix stiffness or applied forces, direct stem cell differentiation and function. Insights gained from understanding the mechanobiology of stem cells using MTFM can inform the design of artificial microenvironments for regenerative therapies. Understanding how mechanical cues regulate stem cells can affect the development of new regenerative therapies. We can also utilize the TaCT probes to efficiently tag and sort the cells based on their mechanical phenotypes.